

Molecular imaging of abdominal aortic aneurysms

Richa Gandhi

**Submitted in accordance with the requirements for the degree of
Doctor of Philosophy**



**The University of Leeds
School of Mechanical Engineering
Institute of Medical and Biological Engineering**

April 2020

The candidate confirms that the work submitted is her own, except where work which has formed part of jointly authored publications has been included, and that appropriate credit has been given within the thesis where reference has been made to the work of others. The contributions of the candidate and other authors to this work is explicitly indicated in the Preface.

This copy has been supplied on the understanding that it is copyright material and that no quotation from the thesis may be published without proper acknowledgement.

The right of Richa Gandhi to be identified as Author of this work has been asserted by her in accordance with the Copyright, Designs and Patents Act 1988.

© 2020 The University of Leeds and Richa Gandhi

Acknowledgements

This PhD has completely changed my life in more ways than one, and I have so many people to thank for it. Firstly, my deepest gratitude goes to my supervisors Harry Tsoumpas and Marc Bailey. Thank you for your invaluable support, professional guidance, and endless constructive feedback, without which this thesis would not have been possible. I would like to profoundly thank the preclinical imaging team at the University of Hull, particularly Chris Cawthorne and Steve Archibald; it would have been impossible for me to achieve such significant data so early in my PhD without our collaboration.

A massive thank you goes to Lucy Craggs and Parkavi Kandavelu, whom I pestered relentlessly throughout my PhD. Thank you for being so incredibly patient with me as I learned all the basics of lab-based experiments and animal handling. I would not have been able to achieve such a high level of independence without your generous guidance. A huge thank you also goes to John Wright for overseeing all the experiments in ePIC; I have learned so much about the PET world from you. Thank you to all my other colleagues in LICAMM throughout the LIGHT and Worsley buildings who I was fortunate to interact with through my PhD journey; there are just too many names to list here. Whether it was to help me find an elusive piece of equipment, figure out why something was not working the way I had expected it to, or make lunch and coffee breaks more pleasant, I consider myself so lucky to have found myself in such a large friendly institute that has made my time in Leeds so enjoyable. I have made many friends over these years who I will treasure immensely going forward.

I would like to express my eternal gratefulness to my partner and best friend Shivam. You have been my pillar of strength and have saved me from many emotional breakdowns throughout this journey; I am beyond appreciative of you in my life. Thanks to my brother Rahul for being a constant encouragement, even when I started using excessive scientific jargon when I told you about my research; your thoughtfulness has always meant so much to me. Finally, I would like to thank my parents Mukesh and Arti for your unwavering support and love. You have worked so hard to give me the opportunity to be independent and find my own path, and my heart is filled with the deepest love and appreciation for you, beyond what I could express in words.

Abstract

Abdominal aortic aneurysm (AAA) disease is characterised by an asymptomatic, permanent, focal dilatation of the abdominal aorta progressing towards rupture, which confers significant mortality. Patient management and surgical decisions currently rely on aortic diameter measurements via abdominal ultrasound screening. However, AAA rupture can occur at small diameters or may never occur at large diameters. Therefore, there is a need to develop molecular imaging-based biomarkers independent of aneurysm diameter that may help stratify patients with early-stage AAA to reduced surveillance. AAA uptake of [^{18}F]fluorodeoxyglucose on positron emission tomography (PET) has been demonstrated previously; however, its glucose-dependent uptake may overlook other key mechanisms. The cell proliferation marker [^{18}F]fluorothymidine ([^{18}F]FLT) is primarily used in tumour imaging. The aim of the overall study for this thesis was to explore the feasibility of [^{18}F]FLT PET / computed tomography (CT) to visualise and quantify AAA in the angiotensin II (AngII)-infused mouse model. The experiments presented in this thesis revealed increased uptake of [^{18}F]FLT in the 14-day AngII AAA model than in saline controls, followed by a decrease in this uptake at 28 days. Moreover, in line with the *in vivo* PET/CT findings, Western blotting of aortic tissue revealed increased levels of thymidine kinase-1 (the substrate of [^{18}F]FLT) and nucleoside transporters in the 14-day AngII AAA model than in saline controls, followed by decreased expression levels at 28 days. A pilot experiment further demonstrated that [^{18}F]FLT PET/CT could be used to detect an early therapeutic response to oral imatinib treatment in the AngII AAA model. Therefore, [^{18}F]FLT PET/CT may be a feasible modality to detect and quantify cell proliferation in the AngII AAA murine model. The findings of this thesis are encouraging for the application of [^{18}F]FLT PET/CT in patients with small AAA.

Table of Contents

Acknowledgements	i
Abstract	ii
Table of Contents	iii
List of Tables	vi
List of Equations	vii
List of Figures	viii
List of Abbreviations	xi
Preface	1
Historical context: The mystery that outsmarted Albert Einstein	1
Motivation.....	2
Thesis overview	2
Key contributions.....	3
Dissemination.....	4
Journal articles.....	4
Conference presentations	5
Funding sources.....	6
Chapter 1 Background	7
1.1 Aneurysms.....	7
1.2 Aortic aneurysms	7
1.3 Abdominal aortic aneurysms.....	10
1.3.1 Clinical features.....	10
1.3.2 Screening and monitoring.....	11
1.3.3 Intervention thresholds	12
1.3.4 Interventions.....	14
1.3.5 AAA development.....	15
1.3.6 Clinical imaging of AAA	19
1.4 Preclinical imaging of AAA.....	22
1.4.1 Preclinical models of AAA	22
1.4.1.1 AngII infusion model	23
1.4.1.2 PPE application model.....	24
1.4.1.3 CaCl ₂ application model.....	25
1.4.2 USS.....	25
1.4.3 MRI.....	26
1.4.4 CT.....	27

1.4.5	Single-photon emission computed tomography.....	27
1.5	PET.....	27
1.5.1	Data analysis.....	28
1.5.2	PET radiotracers.....	31
1.5.3	[¹⁸ F]FLT and thymidine.....	42
1.6	Research hypotheses, aims, and objectives.....	44
Chapter 2 Methods.....		45
2.1	Animal models.....	45
2.2	Histological staining.....	46
2.3	<i>In vivo</i> USS.....	47
2.4	<i>In vivo</i> [¹⁸ F]FLT PET/CT.....	48
2.4.1	PET/CT image analysis.....	50
2.4.2	Generation of different ROI definitions for SUV analyses.....	51
2.5	<i>Ex vivo</i> [¹⁸ F]FLT gamma counting.....	52
2.6	<i>Ex vivo</i> [¹⁸ F]FLT autoradiography.....	53
2.7	Western blotting.....	53
2.8	Statistical analyses.....	54
Chapter 3 Results.....		55
3.1	Cell proliferation is detectable in murine AAA models.....	57
3.2	AngII AAA volume correlates with the proportion of Ki67-positive nuclei.....	59
3.3	Cell proliferation can be visualised and quantified using [¹⁸ F]FLT PET/CT in the AngII AAA model.....	63
3.3.1	Animal survival decreased over the course of the experiment.....	63
3.3.2	[¹⁸ F]FDG uptake differs between saline controls and AngII AAA mice.....	66
3.3.3	[¹⁸ F]FLT localises to expected regions of cell proliferation in control mice.....	74
3.3.4	[¹⁸ F]FLT uptake is observed in regions of cell proliferation in the AngII model of AAA.....	79
3.3.5	[¹⁸ F]FLT uptake is observed in AngII AAA.....	83
3.3.6	Different ROI definitions may affect resultant SUVs.....	91
3.3.7	[¹⁸ F]FLT uptake in the AngII AAA model may be localised to the aortic wall.....	93
3.4	<i>Ex vivo</i> [¹⁸ F]FLT uptake is greater in AngII AAA than in saline control aortae.....	95
3.4.1	Aortic [¹⁸ F]FLT uptake is correlated with aortic volume.....	95

3.5	Expression of key molecules involved in [¹⁸ F]FLT metabolism are upregulated in the AngII AAA model.....	98
3.5.1	Expression of the substrate of [¹⁸ F]FLT is increased in the AngII AAA model	98
3.5.2	Expression of [¹⁸ F]FLT transporters is increased in the AngII AAA model	100
3.6	Cell proliferation is difficult to visualise and quantify using [¹⁸ F]FLT PET/CT in the PPE AAA model	105
3.6.1	Aortic volumes and diameters in the PPE AAA model are larger than those in sham controls	105
3.6.2	<i>In vivo</i> [¹⁸ F]FLT uptake is variable in the PPE AAA model ..	107
3.6.3	<i>Ex vivo</i> [¹⁸ F]FLT uptake in PPE AAA is similar to that in sham control aortae.....	107
3.7	[¹⁸ F]FLT PET/CT might be useful to assess a therapeutic response in the AngII AAA model.....	110
3.8	Summary and conclusions.....	113
Chapter 4 Discussion.....		114
4.1	Histological evidence of cell proliferation in AAA	115
4.2	Expression of key players in the [¹⁸ F]FLT mechanistic pathway..	116
4.3	[¹⁸ F]FLT uptake in the AngII AAA model.....	117
4.4	PET image analysis	121
4.5	Anti-proliferative treatment for AAA	123
4.6	Future directions	125
4.6.1	Considerations of the AngII AAA mouse model.....	126
4.6.2	Future studies of calcification	127
4.6.3	Prospective studies based on genetic pathways	128
4.6.4	Potential studies related to angiogenic and immune mechanisms in AAA	129
4.6.5	Clinical translation	130
4.7	Conclusion	131
References.....		133
Appendix A		163
Appendix B		166

List of Tables

Table 1.1 Estimated annual risk of AAA rupture.	13
Table 1.2 Studies using PET imaging to investigate AAA published in the most recent decade.	36

List of Equations

Equation 1.1 Incremental cost-effectiveness ratio	11
Equation 1.2 Standardised uptake value.....	29
Equation 1.3 Target-to-background ratio	31
Equation 2.1 Normalised percentage of injected dose per gram of sample (%ID/g).	53

List of Figures

Figure 1.1 Anatomy of the aorta.....	9
Figure 1.2 Flow diagram of the mechanisms contributing to AAA formation and progression.....	18
Figure 1.3 Schematic of the metabolic pathway of glucose and its analogue [¹⁸ F]FDG.....	33
Figure 1.4 Schematic of the metabolic pathway of thymidine and its analogue [¹⁸ F]FLT.....	43
Figure 3.1 Different cohorts of ApoE ^{-/-} mice were used for different experiments.....	56
Figure 3.2 Aneurysm tissues show greater Ki67 staining than control aortic tissue.....	58
Figure 3.3 PPE and AngII AAA tissue reveal the greatest proportions of Ki67-positive nuclei.....	60
Figure 3.4 Aortic volumes and diameters are larger in the AngII AAA model than in saline controls.....	61
Figure 3.5 AngII AAA volume and the proportion of Ki67-positive nuclei are positively correlated.....	62
Figure 3.6 Number of surviving animals decreased from 13 to 18 weeks of age.....	64
Figure 3.7 Number of surviving animals decreased from 13 to 18 weeks of the study period.....	65
Figure 3.8 [¹⁸ F]FDG uptake was visualised in the IVC at the beginning of each scan.....	67
Figure 3.9 [¹⁸ F]FDG uptake was visualised in the myocardium of all mice.....	68
Figure 3.10 [¹⁸ F]FDG uptake in the myocardium increased from 0 to 90 min post-[¹⁸ F]FDG injection.....	69
Figure 3.11 [¹⁸ F]FDG uptake was visualised in the paraspinal region of most mice.....	71
Figure 3.12 [¹⁸ F]FDG uptake in the abdominal aorta was greater but variable in the 28-day AngII AAA model than in 28-day saline controls.....	72
Figure 3.13 [¹⁸ F]FDG uptake in the abdominal aorta was variable in the 28-day AngII AAA model than in saline controls.....	73
Figure 3.14 [¹⁸ F]FLT uptake was visualised in the IVC at the beginning of each PET scan.....	75
Figure 3.15 [¹⁸ F]FLT uptake was visualised in the spleen of all healthy controls.....	76
Figure 3.16 [¹⁸ F]FLT uptake in the spleen increased from 0 to 90 min post-[¹⁸ F]FLT injection.....	77

Figure 3.17 <i>Ex vivo</i> [¹⁸ F]FLT uptake in the spleen was greater than that in the heart and abdominal aorta in healthy control mice.	78
Figure 3.18 [¹⁸ F]FLT uptake was visualised in the IVC at the beginning of each PET scan.	80
Figure 3.19 [¹⁸ F]FLT uptake was visualised in the spleen of all mice...	81
Figure 3.20 [¹⁸ F]FLT uptake in the spleen increased from 0 to 90 min post-[¹⁸ F]FLT injection.....	82
Figure 3.21 [¹⁸ F]FLT uptake in the abdominal aorta was visualised late in the 90-min scan.....	84
Figure 3.22 [¹⁸ F]FLT uptake in the abdominal aorta was greater in the 14-day AngII AAA model than in saline controls.....	85
Figure 3.23 Abdominal aortic ROIs for SUV analysis were constructed avoiding adjacent organs.	86
Figure 3.24 [¹⁸ F]FLT uptake in the abdominal aorta was consistently greater in the 14-day AngII AAA model than in saline controls....	87
Figure 3.25 [¹⁸ F]FLT uptake in the abdominal aorta was greater in the 28-day AngII AAA model than in the saline control.	89
Figure 3.26 [¹⁸ F]FLT uptake in the abdominal aorta was consistently greater in the 28-day AngII AAA model than in the saline control.....	90
Figure 3.27 SUV ₇₀ corresponding to both fixed-size and manually drawn aortic ROIs exhibited no significant differences.	92
Figure 3.28 [¹⁸ F]FLT uptake in the AngII AAA model may occur in the aortic wall.	94
Figure 3.29 <i>Ex vivo</i> [¹⁸ F]FLT uptake in the abdominal aorta was greater in the 14-day AngII AAA model than in 14-day saline controls.....	96
Figure 3.30 Aortic volume is positively correlated with [¹⁸ F]FLT uptake.	97
Figure 3.31 TK-1 expression was the greatest in 14-day AngII AAA. ...	99
Figure 3.32 ENT-1 expression was the greatest in 14-day AngII AAA.	101
Figure 3.33 ENT-2 expression was the greatest in 14-day AngII AAA.	102
Figure 3.34 CNT-1 expression was the greatest in 14-day AngII AAA.	103
Figure 3.35 CNT-3 expression was the greatest in 14-day AngII AAA.	104
Figure 3.36 Aortic volume and AP diameters were greater in the 14-day PPE AAA model than in sham controls.	106
Figure 3.37 [¹⁸ F]FLT uptake in the abdominal aorta was difficult to visualise in the 14-day PPE AAA model.....	108
Figure 3.38 <i>Ex vivo</i> [¹⁸ F]FLT uptake in the abdominal aorta was similar in PPE AAA and sham control aortae.....	109

Figure 3.39 [¹⁸F]FLT uptake in AngII AAA decreased following imatinib treatment.	111
Figure 3.40 <i>Ex vivo</i> [¹⁸F]FLT uptake in AngII AAA was reduced following imatinib treatment than that following vehicle treatment.....	112

List of Abbreviations

- 3D: three-dimensional
- AAA: abdominal aortic aneurysm
- AngII: angiotensin II
- ApoE^{-/-}: apolipoprotein E-knockout
- CaCl₂: calcium chloride
- CD: cluster of differentiation
- CT: computed tomography
- CNT: concentrative nucleoside transporter
- CTA: computed tomography angiography
- EVAR: endovascular aneurysm repair
- ENT: equilibrative nucleoside transporter
- ECM: extracellular matrix
- [¹⁸F]FDG: [¹⁸F]fluorodeoxyglucose
- [¹⁸F]FES: [¹⁸F]-fluoro-17 β -estradiol
- [¹⁸F]FLT: [¹⁸F]fluorothymidine
- GLUT: glucose transporter
- HPLC: high-performance liquid chromatography
- ICER: incremental cost-effectiveness ratio
- %ID/g: percentage of injected dose per gram of tissue
- IVC: inferior vena cava
- MRA: magnetic resonance angiography
- MRI: magnetic resonance imaging
- MMP: matrix metalloproteinase
- MASS: Multicentre Aneurysm Screening Study
- [¹⁸F]NaF: [¹⁸F]sodium fluoride
- NHS: National Health Service
- ER: oestrogen receptor
- OAR: open aneurysm repair

PDGF: platelet-derived growth factor

PPE: porcine pancreatic elastase

PET: positron emission tomography

QALY: quality-adjusted life year

ROI: region of interest

SPECT: single-photon emission computed tomography

SMC: smooth muscle cell

SoFIA³: Sodium Fluoride Imaging of AAA

SD: standard deviation

SEM: standard error of the mean

SUV: standardised uptake value

SUV_{max}: maximum standardised uptake value

SUV_{mean}: mean standardised uptake value

TBR: target-to-background ratio

TAA: thoracic aortic aneurysm

TK: thymidine kinase

TAC: time–activity curve

USS: ultrasound scanning

VEGF: vascular endothelial growth factor

VSMC: vascular smooth muscle cell

Preface

Historical context: The mystery that outsmarted Albert Einstein

Albert Einstein, one of the most influential scientists of the 20th century and father of the revolutionary Theory of Relativity, was faced with a puzzle that was daunting even for someone of his calibre. For years, he had suffered from attacks of upper abdominal pain every 2–3 months, each lasting for 2–3 days and often accompanied by bouts of vomiting. He was nearing 70 years of age, slightly overweight, and a regular pipe smoker; the rest of his history was unremarkable. In late 1948, he finally consulted with Dr Rudolph Nissen, a thoracic surgeon at the Brooklyn Jewish Hospital. Physical examination revealed a pulsating mass deep in his abdomen. Further assessment revealed a weakened, dilated span of the largest artery in the body: the aorta. Einstein, the brilliant theoretical physicist, was diagnosed with an abdominal aortic aneurysm (AAA).

Patients with AAA exhibit a focal ballooning of the abdominal portion of the aorta. Individuals who are male, are older than 60 years of age, are former or current smokers, have a positive familial history, and have high blood pressure fulfil the criteria for being at risk of developing AAA. Most cases of AAA remain clinically silent until they progress to a more critical stage. Aneurysms grow in size over time and eventually rupture, an event that causes profound internal bleeding and inevitable patient death (Sakalihan et al., 2018). Nissen aimed to prevent Einstein's aneurysm from rupturing by wrapping the aneurysm of arguably the most intelligent man in the world with a common kitchen item: cellophane. This was a ground-breaking procedure implemented in 1948, with the rationale that the tightly wrapped cellophane would elicit an immune response to the 'foreign body'. Immune cells would tackle the perceived intruder and, by proximity, the cells within the wrapped aortic section, which would trigger a full-blown immune attack and eventually narrow the aneurysmal aorta. This pioneering measure was an ingenious approach at the time, as a bit of cellophane sufficed to keep Einstein symptom-free and able to continue with his physics research for roughly 7 years. Currently, the wrapping of cellophane has been replaced by the more sophisticated removal of the aneurysmal section and insertion of a specialised graft to conjoin the gap.

In 1955, however, Einstein developed severe abdominal and back pain, which are also common acute signs of worsening prognosis, as the

cellophane was no longer sufficient to restrict the AAA expansion. At this point, he was offered another exploratory surgery that might have added a few more years to his life. Aneurysms tend to exhibit prolonged courses of progression and can be detected well before they rupture. As the risk of AAA rupture and internal bleeding increases with aortic size, early AAA detection combined with the ability to stratify patients according to rupture risk is crucial. Einstein, who at 76 years of age was content with his long and gratifying life, refused the additional life-extending surgery, as he parted with the famous wise words, 'I have done my share, it is time to go. I will do it elegantly' (Zimmermann, 2018).

Motivation

AAA has long represented a significant clinical burden, owing to the lack of effective risk stratification methods and inability to confidently predict the incidence of post-surgical complications. The selection of patients to undergo surgical intervention is based on aneurysm size and growth rate revealed through abdominal ultrasound scanning (USS)-based screening, which is currently implemented in the UK for all men older than 65 years of age. However, the traditional anatomy-based screening of AAA fails to comprehensively elucidate the risk of aneurysm rupture and predisposition to surgery-related complications. Molecular imaging of biological events that are involved in AAA formation and rupture is likely to improve patient risk stratification and help distinguish between patients who would benefit from different therapies by dividing them into 'watchful waiting' and 'imminent surgery' groups, for example, eventually resulting in decreased AAA morbidity and mortality.

This thesis focusses on the novel application of positron emission tomography (PET) / computed tomography (CT) with a radiotracer that is predominantly used for tumour imaging: [¹⁸F]fluorothymidine ([¹⁸F]FLT). [¹⁸F]FLT is a marker of cell proliferation, thus being a suitable indicator of cancer progression. Meanwhile, there is emerging evidence of early-stage cell proliferation in the pathophysiology of AAA that proceeds to a late-stage process characterised by apoptosis and senescence; therefore, cell proliferation is an interesting molecular target for imaging. The overarching emphasis in this thesis is placed on assessing the feasibility of using [¹⁸F]FLT PET/CT to visualise and quantify cell proliferation in a classical murine model of AAA.

Thesis overview

Four main chapters comprise this thesis to convey the journey of implementing [¹⁸F]FLT PET/CT in a AAA mouse model. An overview of the chapters is presented below.

Chapter 1 (Background): This chapter provides a comprehensive introduction to the basic concepts underlying AAA in terms of its pathophysiology and clinical issues. Clinical and preclinical imaging is discussed, followed by a particular focus on PET and radionuclide-based tracers. This then sets the stage for the introduction of the overall hypothesis, aim, and research objectives of the thesis.

Chapter 2 (Methods): The methods implemented for the experiments described in this thesis and their rationale are outlined in this chapter. Descriptions of the different mouse models used in the overall study are provided, following by details of the methodologies implemented, including histological staining, *in vivo* USS and PET/CT, *ex vivo* gamma counting and autoradiography, and Western blotting. The methods adopted for statistical analyses are also outlined.

Chapter 3 (Results): All the key findings of the overall research are systematically reported in this chapter. The presence of cell proliferation in different murine models of AAA was first investigated to prioritise a model to implement for the *in vivo* PET/CT experiments. The uptake of the gold-standard radiotracer [¹⁸F]fluorodeoxyglucose ([¹⁸F]FDG) was first tested, followed by [¹⁸F]FLT uptake in healthy control mice, before finally assessing [¹⁸F]FLT uptake in AAA models. The results of a pilot therapeutic-based PET/CT study are also presented in this chapter.

Chapter 4 (Discussion): A general discussion of the key results arising from the overall research is included in this chapter, starting with the histological evidence of cell proliferation in AAA and expression of key players in the [¹⁸F]FLT mechanistic pathway. A comprehensive discussion of [¹⁸F]FLT uptake in the AngII AAA model and PET image analysis is then provided, followed by a discussion of anti-proliferative treatment for AAA. The chapter then ends with potential future directions of AAA research and concluding thoughts.

Key contributions

The following are the specific achievements of this thesis:

- (i) [¹⁸F]FLT uptake on *in vivo* PET/CT and *ex vivo* gamma counting has been characterised for the first time in a classical murine model of AAA, revealing a peak in abdominal aortic uptake in the early stage of the disease;
- (ii) the expression levels of key players in the thymidine mechanistic pathway were found to be increased in the early stage of AAA, mirroring the pattern of [¹⁸F]FLT uptake;
- (iii) [¹⁸F]FLT PET/CT was identified as a feasible modality to evaluate the response to an anti-proliferative agent in a classical murine model of AAA, a finding that would benefit from further validation using large sample sizes; and
- (iv) an optimised quantification approach was identified for PET image analysis, which may have implications for future analyses of PET data.

Dissemination

The following jointly authored publications and presentations are associated with the research presented in this thesis.

Journal articles

- **Richa Gandhi**, Christopher Cawthorne, Lucinda J. L. Craggs, John D. Wright, Juozas Domarkas, Ping He, Joanna Koch-Paszkowski, Michael Shires, Andrew F. Scarsbrook, Stephen J. Archibald, Charalampos Tsoumpas & Marc A. Bailey. 2019. Cell proliferation detected using [¹⁸F]FLT PET/CT as an early marker of abdominal aortic aneurysm. *Journal of Nuclear Cardiology*, 18 Nov 2019, doi: 10.1007/s12350-019-01946-y. [Epub ahead of print] (Journal article (Gandhi et al., 2019))

The candidate performed experiments and collected data, analysed data from experiments, wrote the manuscript, and obtained funding. The co-authors jointly performed experiments and collected data, edited the manuscript, produced critical reagents for experiments, provided intellectual input, obtained funding, conceived the idea, and had overall responsibility for the study.

In addition, attention is drawn to the following editorial article that focussed exclusively on (Gandhi et al., 2019):

- Maaz B. J. Syed, Alexander J. Fletcher & Marc R. Dweck. 2019. Imaging cellular activity and proliferation in the aortic wall. *Journal of Nuclear Cardiology*, 12 Dec 2019, doi: 10.1007/s12350-019-01987-3. [Epub ahead of print]:

This is the first study to confirm that cellular proliferation is indeed elevated within the aorta of AngII-infused ApoE^{-/-} mice and that ¹⁸F-FLT can non-invasively quantify this process. Moreover, the timing of ¹⁸F-FLT uptake closely mirrored histological and proteomic analysis of aneurysmal tissue, with cellular proliferation appearing to be higher in the early stages of aneurysm development before later tailing off. This study has therefore provided novel insight into the cellular mechanisms observed in maturing aneurysmal tissue, and demonstrated ¹⁸F-FLT PET as a useful technique to detect these cellular changes (Syed et al., 2019).

- **Richa Gandhi** & Charalampos Tsoumpas. 2019. Preclinical imaging biomarkers for postischaemic neurovascular remodelling. *Contrast Media & Molecular Imaging*, 03 Feb 2019, 3128529, doi: 10.1155/2019/3128529. eCollection 2019. (Journal article (Gandhi and Tsoumpas, 2019))

The candidate conducted the systematic review, analysed data, wrote the manuscript, obtained funding, and conceived the idea. The co-author edited the manuscript, provided intellectual input, obtained funding, and had overall responsibility for the study.

Conference presentations

- **Richa Gandhi**, John D. Wright, Joanna Koch-Paszkowski, Parkavi Kandavelu, Christopher Cawthorne, Stephen J. Archibald, Marc A. Bailey, Charalampos Tsoumpas. Assessing abdominal aortic aneurysm response to imatinib treatment using [¹⁸F]fluorothymidine positron emission tomography / computed tomography. *European Molecular Imaging Meeting 2020*, Thessaloniki, Greece (Poster presentation)

The candidate performed experiments and collected data, analysed data from experiments, obtained funding, plans to create the poster, and plans to present the poster at the conference.

- Bashair Alhummiyany, **Richa Gandhi**, Stephen J. Archibald, Christopher Cawthorne, Marc A. Bailey, Charalampos Tsoumpas. Effect of different ROI definitions on the quantification of SUV. *European Molecular Imaging Meeting 2019*, Glasgow, Scotland, UK (Poster presentation)

The candidate supervised the MSc student (Bashair Alhummiyany), conceived the idea for the project, collected data, provided intellectual input, edited the poster, and presented the poster at the conference. A copy of the poster is provided in Appendix A.

- **Richa Gandhi**, John D. Wright, Joanna Koch-Paszkowski, Stephen J. Archibald, Christopher Cawthorne, Marc A. Bailey, Charalampos Tsoumpas. [¹⁸F]fluorothymidine positron emission tomography/computed tomography of experimental abdominal aortic aneurysms in murine models. *European Molecular Imaging Meeting 2019*, Glasgow, Scotland, UK (Poster presentation)

The candidate performed experiments and collected data, analysed data from experiments, obtained funding, created the poster, and presented the poster at the conference. A copy of the poster is provided in Appendix A.

- **Richa Gandhi**, Michael Shires, Stephen J. Archibald, Marc A. Bailey Christopher Cawthorne & Charalampos Tsoumpas. Uptake of ¹⁸F-fluorothymidine in experimental abdominal aortic aneurysms of small rodents detected using PET/CT. *European Association of Nuclear Medicine 2018*, Dusseldorf, Germany (ePoster presentation)

The candidate performed experiments and collected data, analysed data from experiments, obtained funding, created the poster, and presented the poster at the conference. A copy of the poster is provided in Appendix A.

Funding sources

This research was funded by the EPSRC Centre for Doctoral Training in Tissue Engineering and Regenerative Medicine – Innovation in Medical and Biological Engineering, multidisciplinary collaboration of Faculties at the University of Leeds (grant number EP/L014823/1), and in part by the David Gamble Award for Secondments in PET-CT Imaging, a charitable donation from the James Ellis charitable trust, and The Academy of Medical Sciences (Clinical Lecturer Starter Grant to Dr Bailey, SGL017\1056).

Chapter 1 Background

This chapter presents a general introduction to aneurysms, before narrowing down to aortic aneurysms. A brief comparison between AAA and thoracic aortic aneurysms (TAA) is presented in terms of cellular biology and genetics. The spotlight then turns to AAA with a focus on important clinical aspects related to screening and diagnosis, along with pathophysiological and biomechanical characteristics that contribute to AAA formation. Next, the importance of preclinical imaging is highlighted with a brief overview of different imaging modalities in the context of AAA, followed by a discussion of PET and quantitative image analysis. Finally, [¹⁸F]-based PET radiotracers are discussed with a particular emphasis on [¹⁸F]FLT, in addition to literature focussing on recent studies investigating AAA using PET. Finally, the overall hypothesis, aim, and research objectives of the thesis are presented.

1.1 Aneurysms

The word ‘aneurysm’ is derived from the Greek word *aneurysma*, meaning dilation. An aneurysm is a focal dilation of a blood vessel to greater than 1.5 times its normal size, predominantly due to weakening of the arterial wall. Aneurysms can develop in various arteries throughout the body, with the most common sites being branches of the Circle of Willis in the brain and the aorta. Aneurysms that develop in the cerebral vasculature are referred to as intracranial aneurysms. Rupture of these aneurysms commonly causes subarachnoid haemorrhage, a severe type of stroke that involves bleeding into the area between the arachnoid membrane and pia mater surrounding the brain (Keedy, 2006). Meanwhile, the aorta is the largest artery in the body that originates in the left ventricle of the heart and passes through the chest and abdomen. AAA, which develops in the part of the aorta that passes through the abdominal cavity, is the most common type of aortic aneurysm. TAA develops in the part of the aorta that passes through the chest (Harris et al., 2016). Aneurysms can also occur in peripheral arteries, which are less likely to rupture than aortic aneurysms. Some examples include aneurysms of the popliteal artery in the leg behind the knee, carotid artery in the neck, splenic artery near the spleen, femoral artery in the groin, and mesenteric artery that supplies the intestines.

1.2 Aortic aneurysms

Aortic aneurysms can occur at different sites, which are named accordingly, such as ascending aortic aneurysms, aortic arch aneurysms, descending TAA, thoracoabdominal aortic aneurysms, and AAA (Figure 1.1). Increasing evidence suggests that TAA and AAA are unique pathophysiological entities with different characteristics (Ruddy et al., 2008, Kuivaniemi et al., 2015). The aorta contains intimal, medial, and adventitial layers; however, these layers in the thoracic aorta are structurally different from those in the abdominal aorta. Essential components of the medial layer include lamellar units, which are unique fibromuscular layers of smooth muscle cells (SMCs) enveloped by structural proteins such as collagen, elastin, and proteoglycans that facilitate the dispersal of stress and supply elasticity. The media of the thoracic aorta contains approximately 60 lamellar units that are further distributed across avascular and vascular regions. Meanwhile, the abdominal aorta contains roughly 30 lamellar units and is exclusively avascular (Kuivaniemi et al., 2015). Variations in the delivery of oxygen, growth factors, and nutrients to cells of the thoracic and abdominal aortic media are likely to play a role in the variations observed in vascular remodelling between the two aortic regions. The smaller number of lamellar units, avascular form, and thinner wall of the abdominal aorta in comparison to the thoracic aorta may also contribute to the greater incidence of AAA than of TAA (Guo et al., 2006, Ruddy et al., 2008).

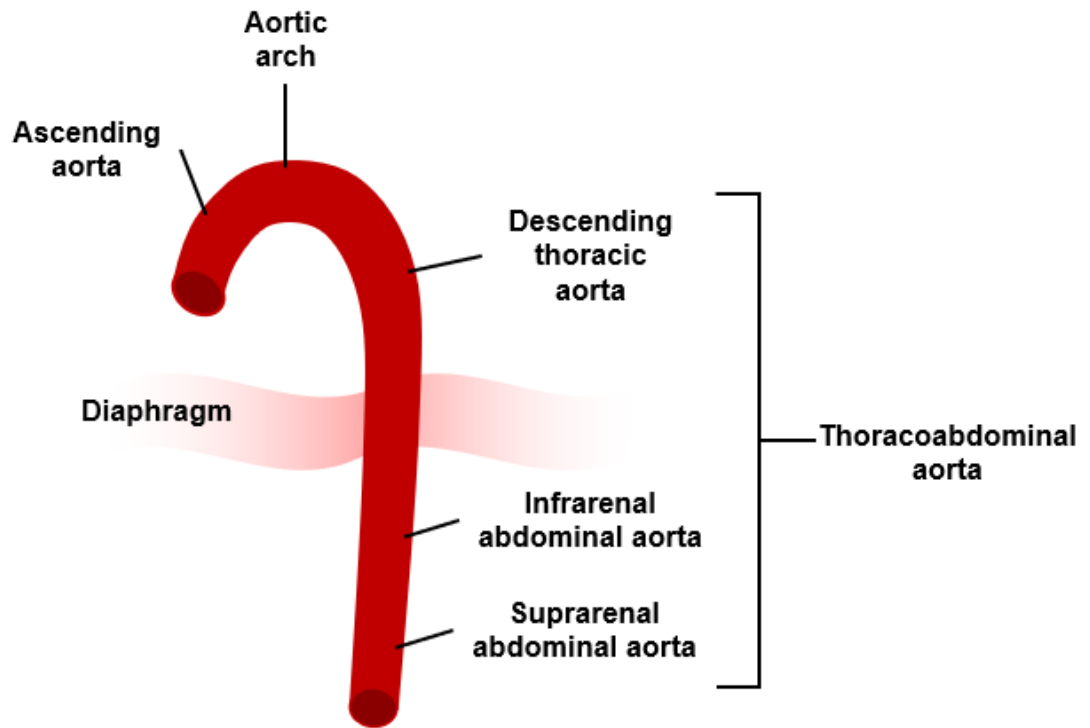


Figure 1.1 Anatomy of the aorta.

The role of genetics in TAA and AAA is well studied. Many cases of TAA are associated with genetic syndromes, such as Marfan syndrome due to mutations in fibrillin-1, Ehlers–Danlos syndrome caused by mutations in type III collagen, and Loeys–Dietz syndrome caused by mutations in transforming growth factor- β receptors 1 and 2 (Elefteriades and Pomianowski, 2013). TAA may also occur in individuals with genetic predispositions in the form of familial TAA and aortic dissection, the risk of which is also increased with mutations in vascular smooth muscle cell (VSMC) contractile proteins (Pannu et al., 2006, Guo et al., 2007). Meanwhile, specific mutations in relation to genetic predispositions in AAA are not entirely clear, although AAA is associated with a first-degree familial history of aneurysmal disease (Guo et al., 2006, Harris et al., 2016). A meta-genome-wide association study by Jones *et al.*, to which Leeds contributed more than 500 patient samples, verified the roles of a number of risk loci that appear to exhibit particular specificity for AAA: *BCAR3*, *SORT1*, *NOTCH2*, *TDRD10*, *UBE2W*, *CDKN2B-AS1/ANRIL*, *LRP1*, *NAB2*, *FGF9*, and *PLTP* (Jones et al., 2017). The formation of both TAA and AAA are complex processes resulting from the interaction of various contributory factors. Whilst TAA is primarily a genetic condition with a single gene mutation resulting in aneurysm development in a specific patient, AAA is a more degenerative disease of older age with a polygenic footprint of an array of susceptibility genes. More studies are needed to build a more complete understanding of the differences in aetiologies and pathogeneses of aortic aneurysms. The remainder of this chapter lays the foundation for the AAA-centred experiments presented in this thesis, which were conducted to elucidate the molecular mechanisms of AAA.

1.3 Abdominal aortic aneurysms

1.3.1 Clinical features

AAA disease is characterised by localised dilatation of the abdominal aorta from a normal diameter of approximately 10–20 mm to an aneurysmal diameter of 30 mm or greater. AAA is asymptomatic, yet simultaneously progressive towards rupture and profound internal bleeding, resulting in a high mortality rate in the range of 59–83% for patients with ruptured AAA who either cannot make it to the hospital in time or do not undergo surgery (Blanchard et al., 2000, National Institute for Health and Clinical Excellence, 2008, Kumar et al., 2017). From 2005 to 2012, 39,740 aneurysm-associated deaths occurred in England (Karthikesalingam et al., 2016). Ruptured

aneurysms manifest with severe abdominal or back pain, hypotension, and shock. Various environmental and genetic risk factors contribute to the development and progression of AAA; the predominant risk factors of AAA include increased age, male gender, cigarette smoking, and elevated diastolic blood pressure (Blanchard et al., 2000, Thompson et al., 2002, Sakalihan et al., 2018). Meanwhile, the risk of aneurysm rupture may be enhanced by rapid aortic expansion, female gender, cigarette smoking, and hypertension. Although it is suggested that patients with AAA undergo interventions that lower cardiovascular risk, in addition to smoking cessation, there remains limited evidence that these approaches reduce AAA-associated morbidity and mortality (Toczek et al., 2016). Therefore, there is an unmet clinical need for interventions that specifically target AAA.

1.3.2 Screening and monitoring

Early-stage AAA does not manifest with any apparent signs or symptoms; therefore, it is usually diagnosed incidentally during unrelated medical check-ups or more recently through screening programmes, which have been formally launched in several countries including the US, the UK, and Sweden (Davis et al., 2013, Guirguis-Blake et al., 2014, Johansson et al., 2015, Zarrouk et al., 2016). The National Health Service (NHS) AAA Screening Programme was fully implemented in 2013 in England to offer routine USS-based screening for all men aged older than 65 years. This programme was established based on the results of the UK Multicentre Aneurysm Screening Study (MASS), which demonstrated a nearly 50% reduction in AAA-related mortality risk after 13 years in men invited for screening compared with that in men who did not undergo screening (0.66% vs. 1.12%). The UK MASS further showed that this reduction was associated with an incremental cost-effectiveness ratio of £7600 per quality-adjusted life years (QALYs) gained at 10 years (Ashton et al., 2002, Thompson et al., 2012).

Cost-effectiveness is an important aspect to consider when implementing AAA screening programmes in the general population. If health benefits are assessed in terms of QALYs, then the cost-effectiveness of AAA screening may be evaluated based on the incremental cost-effectiveness ratio (ICER) of screening vs. no screening (Equation 1.1):

$$ICER = \frac{cost_{screening} - cost_{no_screening}}{QALYs_{screening} - QALYs_{no_screening}}$$

Equation 1.1 Incremental cost-effectiveness ratio

Based on economic modelling that incorporates AAA prevalence, size distribution at initial screening, and screening attendance to determine the ICER, AAA USS-based screening implemented in England for men aged 65 years and older remains highly cost-effective per QALYs gained (Glover et al., 2014, Zarrouk et al., 2016). The gain in QALYs is attributed to screening being used to detect when AAA reaches the intervention threshold, i.e. the point at which the risk of intervention no longer outweighs the risks of intervention.

1.3.3 Intervention thresholds

AAA is currently managed through careful monitoring of aortic diameter based on USS; the frequency of surveillance in patients reflects AAA size. Small AAA (30–49 mm in diameter) typically grow at a rate of 2–4 mm/year; this growth rate increases to >7 mm/year beyond a diameter of 55 mm (Vega de Céniga et al., 2006, Huang et al., 2019). Patients with small AAA are regularly monitored (e.g. annually for AAA with diameters of 30–45 mm and every 3 months for AAA with diameters of 45–55 mm) until the (a) diameter exceeds 55 mm or (b) growth rate exceeds 10 mm/year; when either of these criteria are fulfilled, patients are referred for surgery. International guidelines, however, suggest a diameter threshold of 50 mm in women, based on the observations that women have a three-fold higher risk of AAA rupture than men and the mean aortic diameter preceding AAA rupture is larger in men than in women (Powell et al., 1996, Brown and Powell, 1999, Moxon et al., 2010). Aortic size has been shown to be correlated with rupture risk. Oliver-Williams *et al.* recently reported rupture risks of less than 0.5% for men with AAA less than 55 mm in diameter (Table 1.1) (Oliver-Williams et al., 2019).

Table 1.1 Estimated annual risk of AAA rupture. Sources: (Kent, 2014, Ullery et al., 2018)

AAA Diameter (mm)	Rupture Risk (%/y)
30–44	0.03
45–49	<0.3
50–54	0.40
55–59	<10
60–69	10–20
70–79	20–40
≥80	30–50

Furthermore, for each 5-mm increase in AAA diameter, the mean aortic growth rate increases by 0.59 mm/y, with an increase in the AAA rupture rate by a factor of 1.91. These values work out to more than 7 years of surveillance for a 30-mm AAA and about 8 months of surveillance for a 50-mm AAA to reduce the risk of AAA exceeding 55 mm in diameter to less than 10% in men (RESCAN Collaborators et al., 2013). These results indicate that a watchful waiting period of several years is suitable for patients with small AAA. Surgical intervention is offered once the aortic diameter exceeds 55 mm; adoption of this threshold in the clinic is supported by evidence from four different trials (the UKSAT, ADAM, CAESAR, and PIVOTAL studies) that demonstrates no significant advantage to early surgical intervention for small AAA (Filardo et al., 2015). Whether non-surgical options may be effective for small AAA is currently unknown.

The important point to note here is that although there is extensive ongoing research to establish more reliable and informative risk markers of AAA, the only indicator that is used consistently in the clinic is aortic size. This is the simplest and most convenient parameter to extract using USS, but may not always accurately reflect prognosis, as small AAA have been reported to rupture, whilst large AAA have been reported as remaining stable (McGloughlin and Doyle, 2010). Some other proposed risk markers that are under ongoing validation are aortic wall stress, the finite element analysis rupture index, vessel asymmetry, intraluminal thrombus growth, and the rupture potential index; in addition, aortic wall stress and intraluminal thrombi have been demonstrated to be independent of aortic diameter, hence justifying the notion of utilising more than aortic size alone when evaluating AAA rupture risk (Stenbaek et al., 2000, Fillinger et al., 2003, Vande Geest et al., 2006, Doyle et al., 2009, Zhu et al., 2020). However, these potential markers require substantial investigation before being introduced into clinical practice.

1.3.4 Interventions

Surgical intervention for AAA is currently offered once the aortic diameter reaches 55 mm in maximal diameter. The exact timing of surgery is often difficult to determine due to the risks associated with AAA progression and surgery invasiveness; the 55-mm aortic diameter acts as a threshold at which point the annual risk of AAA rupture is similar to the mortality risk of surgery (Moxon et al., 2010, Cafueri et al., 2012). It is well established that the low rupture rate in small aneurysms and risks correlated with surgical

intervention do not sufficiently justify routine repair of small AAA (Filardo et al., 2015, Chuen and Theivendran, 2018).

The two main types of surgical intervention currently offered are open aneurysm repair (OAR) and endovascular aneurysm repair (EVAR). OAR has been performed since the mid-1950s and involves making a large abdominal incision to expose the abdominal aorta, followed by insertion of a synthetic graft that is sewn in place to replace the weakened portion of the aorta. OAR is a highly invasive procedure that confers considerable mortality and morbidity risks due to which many patients are denied for surgery. On the other hand, EVAR involves making an incision in the groin area, followed by insertion of a collapsed synthetic graft through the femoral artery that is opened inside the aneurysm with X-ray guidance and fixed in place with a stent. EVAR was introduced with the promise of being a solution to the pitfalls of OAR and comes with the advantages of requiring smaller incisions, conferring fewer perioperative complications, being less painful for the patient, being associated with lower mortality and morbidity rates, and requiring less hospitalisation in comparison to OAR (Greenhalgh, 2004, Prinssen et al., 2004, Kontopodis et al., 2020). However, EVAR is also reported to be associated with an increased frequency of readmissions due to the lack of long-term durability (Sandford et al., 2014). The short-term (i.e. 0–6 months following surgery) survival benefits of EVAR compared to those of OAR (4.6 vs. 10.0%/person-years) appear to be reduced beyond 8 years following surgery (1.3 vs. 0.2%/person-years) (Patel et al., 2016). The National Institute for Health and Care Excellence guidelines have previously suggested removing EVAR as an option from the NHS for elective cases (National Institute for Health and Clinical Excellence, 2018); however, these have since been updated to include EVAR in cases wherein OAR is contraindicated (National Institute for Health and Clinical Excellence, 2020). Nonetheless, the implementation of EVAR in AAA management remains controversial, and its effects on the long-term prognosis of patients with AAA remain under scrutiny to facilitate improvements in the procedure.

1.3.5 AAA development

The pathophysiology of AAA involves active and dynamic pathological remodelling of the connective tissue within the aortic wall; however, the exact sequence of events remains largely unclear (Davies, 1998, Kuivaniemi et al., 2015, Petsophonsakul et al., 2019). During early-stage AAA formation, changes in haemodynamic stress and aortic wall elasticity occur, likely in response to one or more of the causal risk factors described in section 1.3.1,

such as cigarette smoking and increased diastolic blood pressure. Macrophages also infiltrate the vessel wall due to increased oxidative stress, leading to protease secretion that deteriorates the vessel wall via extracellular matrix (ECM) degradation; the upregulation of pro-inflammatory cytokines and chemokines further contributes to compromised aortic wall integrity (Henderson et al., 1999, Thompson et al., 2002, Cafueri et al., 2012, Kuivaniemi et al., 2015, Sun et al., 2018). Although extensive research has focussed on the role of inflammation in AAA, inflammatory mechanisms only account for part of the overall story (Patel et al., 1996). This is further evidenced by the lack of definitive findings of anti-inflammatory therapy attenuating AAA growth, with some enhancing AAA growth (Yoshimura et al., 2018, Tedjawirja and de Waard, 2019).

It is increasingly recognised that the proliferation of VSMCs, which reside in the tunica media and are responsible for controlling blood pressure and flow distribution, contributes to AAA development (Owens et al., 2004, Chasman and Lawler, 2017). An early study in this field demonstrated that VSMC migration and proliferation are enhanced in AAA tissues compared to that in aortic occlusive disease and normal inferior mesenteric artery tissues (Patel et al., 1996). The same team also showed that these aortic SMCs produce increased levels of matrix metalloproteinases (MMPs) compared to those produced in control arterial tissues (Patel et al., 1996); these MMPs contribute to the degradation of elastin and various ECM proteins, progressively leading to degradation of the aortic wall. In the following year, another study revealed that the SMC density in the medial layer is significantly decreased in AAA tissues in association with SMC apoptosis, reflecting its role in aortic wall degradation (Lopez-Candales et al., 1997). VSMCs usually exhibit a contractile, quiescent phenotype, characterised by the expression of proteins such as α -smooth muscle actin, smooth muscle myosin heavy chain, and smooth muscle-22 α ; however, when stimulated by injury or stress, they undergo a phenotypic switch to a proliferative and migratory state (Owens et al., 2004, Ailawadi et al., 2009, Michel et al., 2018, Petsophonsakul et al., 2019). In 2009, Ailawadi et al. demonstrated that this phenotypic switching is an early event in AAA, based on the downregulation of SMC marker genes and upregulation of MMPs (Ailawadi et al., 2009). One of the histopathological characteristics of AAA is extensive degradation of the aortic ECM, which is facilitated by elastolytic enzymes that are produced by VSMCs when they exhibit the proliferative phenotype. The ECM is a fundamental component of blood vessels that is produced by the cells located in vessel walls and contains fibrous proteins such as

collagen and elastin, proteoglycans such as versican, and glycoproteins such as thrombospondins and fibronectin. There are numerous kinds of ECM with varying compositions that each play different roles in facilitating different pathophysiological processes. Proteomics-based approaches have revealed distinct differences in the ECM composition between AAA and non-AAA tissues (Didangelos et al., 2011). Some proteins that have been identified to exhibit changes in AAA include collagen XII, which is found in tissues subject to high tensile forces; versican, a major extracellular proteoglycan; periostin and thrombospondins, which contribute to cellular adhesion and spreading; ACLP, which is known to be associated with collagen and fibrosis; and tenascin, which is correlated with macrophage accumulation (Satta et al., 1997, Layne et al., 1998, Theocharis et al., 2001, Didangelos et al., 2011). These ECM proteins significantly modulate VSMC phenotypic switching, and their reduction reflects the pathological remodelling of the ECM and VSMCs in the AAA disease course. Finally, calcification—the deposition of calcium phosphate crystals in the medial layer of the vessel wall—further contributes to vessel stiffening, and hence, VSMCs have been shown to contribute to vascular calcification (Proudfoot et al., 2000, Shanahan et al., 2011, Wu et al., 2013). Overall, synthetic VSMCs are associated with a loss of contractile proteins, greater production of elastolytic enzymes that degrade the ECM, the release of extracellular vesicles that promote inflammation and calcification, and presence of reactive oxygen species (Kapustin and Shanahan, 2016, Schurgers et al., 2018). These key biological processes thus collectively contribute to inducing vessel dilatation and aneurysm progression.

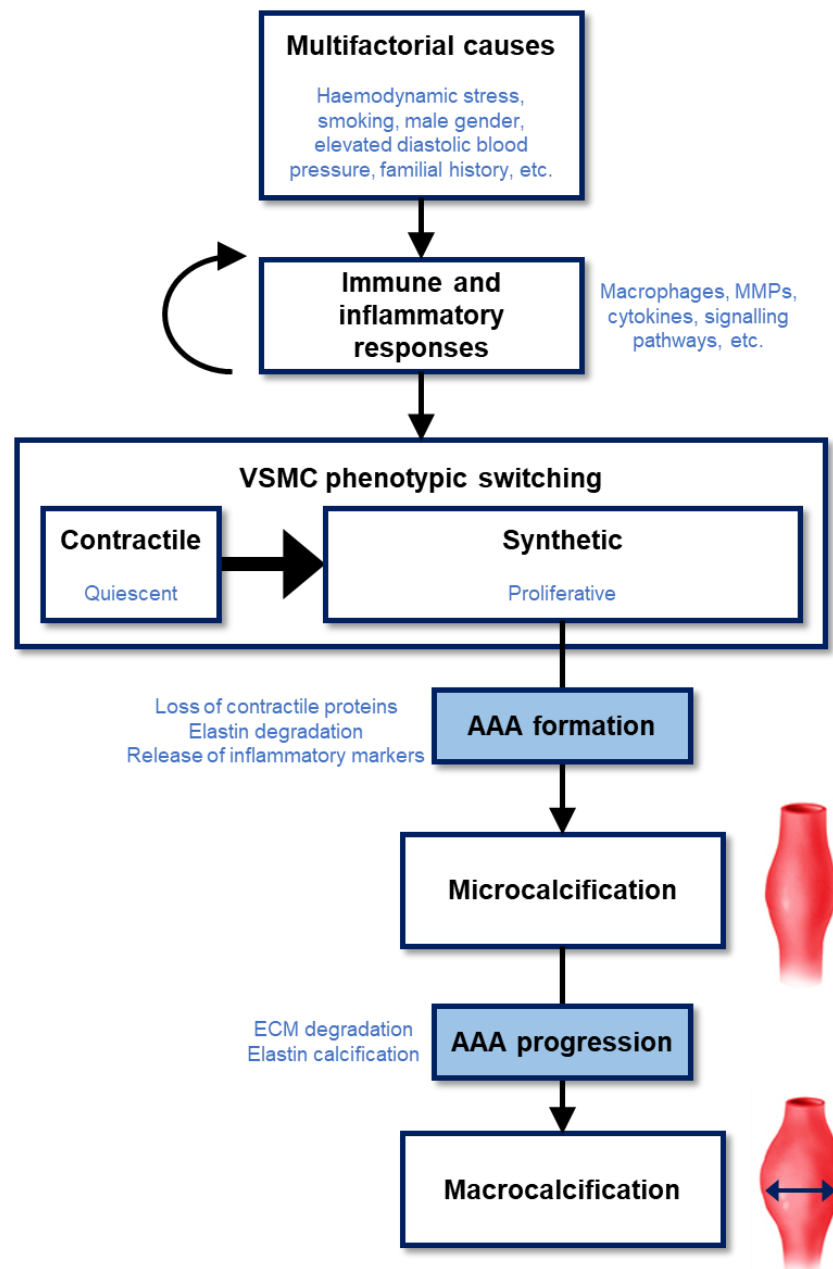


Figure 1.2 Flow diagram of the mechanisms contributing to AAA formation and progression.

Late-stage AAA is understood to involve an amalgamation of VSMC apoptosis, upregulated inflammatory cell infiltration, thinning of the aortic wall due to an imbalance between the concentrations of collagen and elastin, and calcification; these components collectively exacerbate focal aortic wall weakening, eventually resulting in rupture (MacSweeney et al., 1994, Wills et al., 1996, Lopez-Candales et al., 1997, Proudfoot et al., 2000, Rowe et al., 2000, Clement et al., 2019, Quintana and Taylor, 2019). The prediction of rupture risk is an important area of research, and in this context, mechanical properties of the aorta in relation to breaking stress and stiffness are well studied. Per the Law of Laplace, intraluminal pressure, wall thickness, and vessel diameter affect the wall tension necessary to counter a given internal fluid pressure, which in turn affects wall stress. Aneurysm rupture occurs when the wall stress exceeds wall tension (Vorp, 2007). Studies of the biomechanical properties of aortic aneurysms typically involve computational modelling and finite element methods to apply an array of proposed criteria that may help predict rupture risk: expansion rate, wall tension, wall stiffness, peak wall stress, intraluminal thrombus thickness, and surface area (Hall et al., 2000, Hatakeyama et al., 2001, Metaxa et al., 2017, van Disseldorp et al., 2019). For example, Conlisk *et al.* demonstrated that sites of greater curvature exhibit increased stress, which then corresponds with a greater susceptibility of rupture (Conlisk et al., 2017). Importantly, some AAA that are smaller in diameter than the surgical intervention threshold exhibit high peak wall stress (van Disseldorp et al., 2019). Recent data have suggested that biomechanical assessment may be superior to using only the aortic diameter to evaluate rupture risk (Polzer et al., 2020). Basing clinical assessments on biochemical parameters in this way may be a promising adjunctive tool for precise diagnosis and disease course prediction, although their application in the clinic is likely to be hampered by the logistical difficulties of obtaining these measurements at repeated time points to suffice precise risk prediction as an aneurysm grows and remodels. In this case, more subtle stratification biomarkers based on underlying molecular mechanisms that come into play before physical appearance of the disease may be more feasible to implement in the clinic to predict whether patients have a high or low risk of rapidly progressive disease.

1.3.6 Clinical imaging of AAA

Current clinical interventions for AAA focus on physically excluding the aneurysm, which themselves are associated with significant risks. Therapies that instead inhibit the progressive deterioration and molecular dysfunction

of the aortic wall would decrease the necessity for surgery. Medical imaging plays a key role in better understanding the adverse molecular mechanisms underlying early AAA formation. Currently, USS is used in the clinic to screen for AAA and monitor disease progression over time. Whilst it is effective in revealing changes in aortic size and shape over time, the technique is not without its limitations. The most salient limitation is that USS is operator-dependent; therefore, results from USS depend on a sonographer's experience and accuracy. This creates a two-variable problem: individual patient factors and sonographer accuracy. Implementing quality control is inevitably difficult, having to rely on standardised guidelines to reduce inter-patient and inter-operator variability. An increasingly common problem in Western societies is patient size. Larger patients are difficult to image via USS due to their greater mass and depth of tissue, which attenuates the sound waves reflecting from deeper structures in the body, such as the aorta, and back to the transducer. Ironically, it is overweight and obese patients who tend to carry a greater risk of developing AAA and would most benefit from screening and monitoring. Trapped air and gas can further obstruct the findings of USS; therefore, imaging of regions that are close to the air-filled bowel is not always ideal (Kornezos et al., 2010, Dobrucki and Sinusas, 2020). That being said, with a sensitivity of 95% and specificity of nearly 100%, USS is predominantly used in the clinic to screen for AAA because of its ease of operability, low costs, low post-imaging workload and instantaneous results, and widespread availability (Kumar et al., 2017).

Abdominal CT without contrast enhancement is equivalent to USS in terms of detecting AAA and is typically recommended in patients who cannot undergo USS. Meanwhile, CT with contrast enhancement can provide information on the presence of thrombus or dissection flaps, but may not provide as much information about branch vessel involvement and smooth three-dimensional (3D) rendering that CT angiography (CTA) may offer (Reis et al., 2017). CTA is another commonly used modality in the clinic for AAA. It is notably valuable in pre-intervention planning, such as in assessing aortic size, the presence of intraluminal thrombus, the involvement of visceral arteries, and extension to other parts of the aorta, and is even superior to USS in identifying and measuring the size of aneurysms (Kumar et al., 2017, Kyriakou et al., 2020). Use of CTA for maximum diameter measurements has been shown to be associated with high intra-observer reproducibility (Mora et al., 2014). However, CTA confers high radiation doses (Kumar et al., 2017).

Magnetic resonance imaging (MRI) has the ability to provide accurate anatomical information of AAA with excellent soft-tissue contrast and reduced exposure to ionising radiation compared to CT. MRI has previously been used to confirm the diagnosis of thrombus and assess blood flow in aortic diseases in patients with aortic aneurysms and dissection (Honda et al., 1999). Four-dimensional flow MRI has further been utilised to analyse changes in blood flow patterns in the abdominal aorta (Liu et al., 2018). Although long scan durations are a notable challenge with the use of MRI, advances in MRI-based approaches have revealed that 3D non-contrast black-blood MRI is associated with decreased scan durations with retention of image quality (Zhu et al., 2019). In a prospective study, this method was shown to reveal intraluminal thrombi in patients with AAA, with the finding that active changes in intraluminal thrombi are associated with large aortic diameters and rapid AAA growth (Zhu et al., 2019). Furthermore, magnetic resonance angiography (MRA) has a similar sensitivity to that of CTA and has also been shown to reveal endoleaks that could not be visualised using CT angiography (Wicky et al., 2003). MRA is particularly useful in cases wherein intravenous contrast is contraindicated, such as in cases of allergic responses or renal dysfunction, and is associated with a lack of ionising radiation (Kumar et al., 2017). However, the benefits of MRI and MRA are hampered by key disadvantages such as higher associated costs, reduced availability of scanners, motion artefacts and patient claustrophobia due to long scanning durations, and contraindications in patients harbouring pacemakers and metal clips.

Meanwhile, PET imaging has the potential to offer more precise functional information at the molecular level for risk stratification purposes as an adjunctive tool to USS-based screening and surveillance. As the primary focus of this thesis, section 1.5 is dedicated to a discussion of PET imaging in the context of AAA. The use of PET with a suitable radiotracer may be beneficial when applied at the time of AAA detection to help personalise a surveillance regimen or intervention threshold. Furthermore, there is currently no pharmacological treatment for AAA, and the indication for surgery is based solely on aortic size from USS. Establishing a pharmacological treatment that could slow or even reverse AAA progression is the ultimate aim of AAA research, but this necessitates a stratification imaging biomarker that could (a) help select patients who would benefit from such a treatment, (b) predict AAA growth and refine watchful waiting regimens, (c) determine patient-specific intervention thresholds, or (d) be applied in all of the aforementioned applications. Much of the dated

understanding of late-stage AAA is based on aortic tissue acquired during surgery; hence, theories derived from these samples may not accurately represent the mechanisms of early-stage disease, when a novel pharmacological therapy may be administered. Preclinical studies of AAA are the first step in achieving a more thorough understanding of early-stage AAA pathophysiology. Understanding the molecular workings of AAA in preclinical models can then lead to the development of stratification biomarkers that could be translated to the clinic. Following on from this, a preclinical model of AAA has been used to investigate a candidate radiotracer for PET imaging in this thesis.

1.4 Preclinical imaging of AAA

In vivo imaging modalities are the central focus of preclinical research and confer the advantage of visualising biological processes in live animals non-invasively. The multifactorial contributors to the underlying AAA pathobiology each act as attractive molecular-level imaging targets to further our understanding of the early-stage changes that precede anatomical changes in aneurysmal aortae.

1.4.1 Preclinical models of AAA

For any disease, the use of clinically relevant animal models is essential to shed light on mechanisms of disease progression before clinical testing. That being said, no single model is a perfect representative of human AAA pathology; therefore, it is ideal to test hypotheses in multiple models. Rabbits, pigs, mice, and rats have been used previously to investigate AAA (Patelis et al., 2017). Mice are invaluable in studies of AAA for numerous reasons. They are small in size and thus convenient as model species; they can be easily housed and maintained, and they adapt well to changes in their surroundings. Mice are also relatively cost-effective, as large batches can be purchased from mass-producers that breed rodents specifically for research purposes (Daugherty and Cassis, 2004, Poulsen et al., 2016). Furthermore, the mouse genome is very similar to the human genome and can be easily modified to study genes of interest. Inbreeding of different mouse strains is a standard means to achieve gene knockout or knock-in models, the physiological and phenotypic implications of which can then be explored. For example, in the context of AAA, hyperlipidaemic mice are achieved via the knockout of apolipoprotein E or low-density lipoprotein receptors, and mice deficient in lysyl oxidase (resulting in a failure to crosslink elastin and collagen) and MMP genes have also been utilised to

better understand the role of the ECM (Daugherty and Cassis, 2004, van der Weyden et al., 2011). Herein, three commonly used murine models of AAA are described: angiotensin II (AngII) infusion in apolipoprotein E-knockout (ApoE^{-/-}) mice, aortic application of calcium chloride (CaCl₂), and aortic application of porcine pancreatic elastase (PPE).

1.4.1.1 AngII infusion model

The AngII model is the most commonly used AAA model in mice (Poulsen et al., 2016). The result of AngII infusion leading to the development of AAA was an unexpected finding of a study conducted to assess the effect of increased plasma concentrations of AngII on atherogenesis in ApoE^{-/-} mice (Daugherty et al., 2000). AngII is a vasoconstrictor that mediates a variety of growth processes, including proliferation. The proliferative effects of AngII have long been established in adrenocortical cells (Gill et al., 1977), mesangial cells (Bakris and Re, 1993), endothelial cells (Wolf et al., 1996), hematopoietic stem cells (Kim et al., 2016), and VSMCs (Johnson et al., 1992, Yaghini et al., 2010), among other cell types. To study AAA, ApoE^{-/-} mice are classically used for this model because of their inherent atherosclerotic susceptibility. AngII infusion in wildtype C57BL6/J mice will also produce aneurysms, but only in about 10% of animals compared to 80% of animals with an ApoE^{-/-} background. Low-density lipoprotein receptor-deficient mice also exhibit an increased incidence of AAA following AngII infusion and are an alternative, as is a prolonged period of high-fat diet feeding. Therefore, although an underlying ApoE^{-/-} condition is not necessary for AAA development, it appears to significantly enhance the incidence with which AAA develops in this model (Deng et al., 2003, Manning et al., 2003). In this model, AAA occurs spontaneously in the suprarenal abdominal aorta following 28 days of continuous AngII infusion at a dose of 500–1000 ng/kg/min via an osmotic mini-pump that has been subcutaneously implanted laterally into the flank through a midline neck incision without conferring an effect on the thoracic aorta (Rateri et al., 2011). Along with dilatation of the suprarenal aorta, the aneurysms in this model present with atherosclerosis, macrophage accumulation in the elastic lamina, leukocyte infiltration, and medial hypertrophy. There is also a predominance of AAA development in male mice, with roughly double the incidence than that in female mice. These features are similar to those observed in human AAA disease (Daugherty et al., 2000). This model is also popular because the AAA is progressive, i.e. it continues to grow as long as AngII continues to be infused (Tedjawirja and de Waard, 2019). The timeline of biological events in

this model is well established, initiating with macrophage infiltration into the medial layer of the susceptible aortic region, transmural dissection that results in rapid luminal expansion within the first week of AngII infusion, and additional inflammatory mechanisms, such as the formation of an intramural thrombus, degradation of elastin, and significant vascular remodelling (Cao et al., 2010). It is important to acknowledge that this model is regarded by many as an aortic dissection and dissecting aneurysm model; this is because the aneurysms that form in this model have been found to be preceded by an intramural rather than intraluminal thrombus, medial tears at specific side branches instead of circumferential medial degradation, and aortic dissection, which are not typical features of human AAA (Trachet et al., 2017). This was the main model used for the experiments in this thesis for its procedural simplicity and characteristic similarities to AAA disease in humans. The most salient difficulty encountered in this model is the high AAA rupture rate (rates of 30–50% have been reported previously); most ruptures occur within the first week of AngII infusion, thus necessitating a greater starting number of animals for experiments involving this model (Cao et al., 2010, Nguyen et al., 2011, English et al., 2015).

1.4.1.2 PPE application model

The PPE perfusion model was first described by Anidjar *et al.* in 1990 and has been widely used as a murine model of AAA since then. This model entails *in vivo* isolation and cannulation of the abdominal aorta to administer elastase, followed by careful repair of the surgical incision. This model is technically demanding; murine aortic isolation from the adjacent inferior vena cava (IVC) and small lumbar branch vessels can prove to be difficult. In addition, there may be differences in the extent of vascular injury due to differences in perfusion pressure. Moreover, careful closure of the aortotomy whilst avoiding stenosis is imperative to restore antegrade blood flow (Anidjar et al., 1990).

More than two decades later, a modified version of this model wherein PPE is applied to the peri-adventitial aorta was introduced by Bhamidipati *et al.* to overcome the complexities associated with the PPE perfusion model. Their model can be achieved without individual vessel manipulation and generates aneurysms that involve greater accumulation of activated macrophages, elastic lamina degradation, decreased expression of smooth muscle protein, and enhanced matrix metalloproteinase activity, similar to that observed in other experimental AAA models (Bhamidipati et al., 2012). This modified

model was implemented for the research presented in this thesis for its technical simplicity.

The PPE model rarely if ever demonstrates rupture in comparison to the AngII model. Atherosclerosis is not a feature of the PPE model, whilst AAA in this model is associated with medial degeneration, leukocyte infiltration, and formation in the infra-renal abdominal aorta as the key features resembling human AAA. However, the PPE model is a non-progressive model of AAA, as the disease stabilises after a period of several days or weeks due to healing of the biological process (Senemaud et al., 2017).

1.4.1.3 CaCl₂ application model

The CaCl₂ model is another non-progressive model of AAA that involves peri-aortic application of CaCl₂ to the infra-renal aorta, which induces AAA. In 1988, Gertz *et al.* first demonstrated that the application of CaCl₂ to the adventitia of a carotid artery resulted in the formation of an aneurysm. This aneurysm was accompanied by a decrease in VSMCs, elastin calcification, and inflammatory cell infiltration (Gertz et al., 1988). In 1997, this approach was reported to induce AAA in New Zealand rabbits (Freestone et al., 1997). Finally, this model was first described in mice by Chiou et al. who reported a 110% increase in diameter 3 weeks after CaCl₂ treatment. This model is based on the high affinity of calcium for elastin; disrupting this affinity weakens the vascular wall, activates inflammatory processes, and eventually leads to aneurysm development. Furthermore, AAA in this model is accompanied by the depletion of VSMCs, degradation of elastin, infiltration of inflammatory cells, and high circulating levels of inflammatory markers (Chiou et al., 2001, Wang et al., 2013). Disruption of elastic tissue by calcium depositions has been demonstrated in human atherosclerosis; in addition, calcification of the human aorta is observed in older adults, and approximately 80% of human AAA exhibit calcification of the aortic wall (Jayalath et al., 2005, Maier et al., 2010, Kamenskiy et al., 2018). These findings make the CaCl₂ model a relevant model of human AAA. However, thrombus and rupture, which are observed in human AAA, are not features of CaCl₂-induced AAA (Wang et al., 2013).

1.4.2 USS

As the imaging modality of choice in the clinic, USS has also been used extensively in preclinical research to investigate morphological aspects of AAA. The feasibility of 3D micro-USS in monitoring aneurysm growth has been demonstrated in mice via comparisons with histological images

(Goldberg et al., 2007). High-frequency USS, which is better suited to visualise superficial body structures and can produce images of high axial resolution compared to low-frequency USS, has also been used extensively to detect AAA in mice based on measurements of luminal diameter and aortic wall thickness (Martin-McNulty et al., 2005, Barisione et al., 2006, Azuma et al., 2011). USS is a feasible modality to assess changes in aortic strain (Favreau et al., 2012). Moreover, preclinical USS combined with a semi-automatic image processing algorithm has been shown to reveal changes in arterial distension, which may prove to be informative as an early marker of arterial disease in animal models (Janus et al., 2018). USS can be challenging in mice with AAA; aortic rupture has been reported to occur during USS, implying that pressure from the probe on the abdominal region may be sufficient to induce rupture.

1.4.3 MRI

MRI uses strong magnetic fields and radiofrequency pulses to produce high-resolution images without the need for ionising radiation (Brangsch et al., 2017). MRI can be implemented with various probes that have different targets to elucidate AAA mechanisms and potentially act as distinct biomarkers supplemental to aortic diameter. Botnar *et al.* demonstrated the feasibility of using a fibrin-specific MRI probe to investigate fibrin content in the AngII AAA mouse model (Botnar et al., 2018). Bazeli *et al.* used contrast-enhanced MRI to detect MMPs in the rat elastase model of AAA, demonstrating a correlation between MMP activity and inflammation (Bazeli et al., 2010). Furthermore, a newly developed smart MRI nanoprobe has recently been demonstrated to be useful in detecting MMP activity in the AngII AAA mouse model and potentially correlating with severe progression or rupture (Yao et al., 2020). Brangsch *et al.* demonstrated the use of dual-probe MRI to evaluate ECM degradation and inflammatory activity in the AngII AAA murine model, which could then be associated with AAA rupture risk (Brangsch et al., 2019). Dysfunctional ECM remodelling has further been investigated using a gadolinium-based contrast agent specific to tropoelastin, the soluble precursor to elastin, which was then shown to correlate with accumulated tropoelastin in human aneurysmal tissue (Lavin et al., 2019). MRI has also been used to quantitatively analyse aortic motion and curvature, as well as changes in aortic size following an intervention in mice with AAA (Turner et al., 2008, Goergen et al., 2011). MRI has also successfully been used perioperatively to guide EVAR in a swine model of AAA, raising the possibility of its role in the clinic during EVAR in patients

who are not suitable to undergo CTA (Raman et al., 2005). Despite its limitations associated with long scan durations and high costs, as a sensitive technique that confers excellent soft tissue contrast, MRI for AAA is a growing field of research.

1.4.4 CT

CT uses X-rays to generate three-dimensional images with or without contrast agents for target enhancement. Although CT is typically used as a supplement to functional imaging techniques, such as PET and SPECT, Wang *et al.* recently demonstrated that utilising gold nanoparticles as contrast agents with micro-CT can help predict elastin damage and rupture pressure in the AngII AAA mouse model (Wang et al., 2019). A CT-based method that targets phagocytosis to image vessel wall inflammation in the same model has also been developed (Toczek et al., 2018).

1.4.5 Single-photon emission computed tomography

Single-photon emission computed tomography (SPECT) is a modality that involves the detection of emitted gamma photons following the injection of radiotracers such as ^{99m}Tc , ^{123}I , and ^{111}In . Golestani *et al.* used SPECT with RP805, a [^{99m}Tc]-labelled tracer that targets matrix metalloproteinases (MMPs), to demonstrate that MMP-targeted SPECT may indicate aortic wall inflammation and help predict expansion or rupture in AAA (Golestani et al., 2015). Toczek *et al.* also used SPECT, but with a novel pan-MMP tracer called RYM1, to successfully demonstrate specific detection of MMP and inflammatory activity in AAA (Toczek et al., 2017). As a lower-cost option compared to PET, the application of SPECT to investigate AAA is promising, particularly as its spatial resolution is superior to that of preclinical PET (approximately 0.25 mm vs. 1 mm). The main obstacle lies in the translation of SPECT to the clinic, as clinical SPECT scanners have poorer resolutions than those of clinical PET scanners. SPECT is closely related to PET, which is the central focus of this thesis, thus warranting a more focussed separate discussion in the following section.

1.5 PET

Molecular imaging utilises biologically specific tracer molecules to target, characterise, and quantify cellular and subcellular pathways and processes (Fernandez-Friera et al., 2014, Golestani et al., 2016). PET is a molecular imaging modality that relies on radioactive tracers to generate three-dimensional images of functional processes within the body. The working

principle of PET involves the simultaneous detection of two gamma-ray photons emitted in opposite directions after the annihilation between an electron and tracer-emitted positron. Reconstructed images based on the localisation of pairs of photons then reveal the distribution of injected radioactive tracer throughout the body, effectively producing a three-dimensional functional map that is biologically specific to the injected tracer. These reconstructions may incorporate corrections that have been made for attenuation, scatter, dead time, and random photon coincidences, which further improve the spatial resolution of images (Ramaswamy et al., 2013, Tarkin et al., 2016).

1.5.1 Data analysis

Quantitative measurements are a defining feature of nuclear medicine techniques such as PET, allowing for the ability to precisely characterise physiological parameters of interest to inform the diagnosis, staging, and monitoring of various diseases. To provide anatomical context to supplement quantitative data, stand-alone PET imaging systems are often coupled with CT or MRI to compensate for the limited spatial resolution of PET; the integration of a function-dominant modality (PET) with readily available structure-dominant modalities (CT, MRI) improves the quantitative analysis of biological functions (Golestani et al., 2016).

PET/CT can counter some of the caveats associated with USS and, more importantly, supplement the information acquired from USS. Unlike USS, PET is operator-independent, as it relies on an automated scanner and a radiotracer, the activity distribution of which is independent of patient factors such as obesity; this feature makes PET an objective technique. Large patients, as long as they fit within the scanner, can undergo PET scans with minimal effects of tissue depth on the resultant PET signal. One concern involving PET is the possible inter-analytical variability depending on how the region of interest (ROI) is defined. There is ongoing research to standardise ROI definitions and analytical methods, and a significant advantage of PET is that data can be reviewed and corrected post-acquisition using analytic methods to correct for temporal and spatial resolution, something that USS does not yet offer. Meanwhile, standardising the human error that contributes to operator-dependent variability in USS is difficult (Veronesi et al., 2015, Comelli et al., 2018).

PET image analysis often relies on the standardised uptake value (SUV) metric, a widely used radioactivity quantifier that takes the injected activity

and body weight of the subject into account. SUVs are calculated using the following equation (Equation 1.2):

$$SUV = \frac{\text{Radioactivity concentration in a region of interest } \left(\frac{kBq}{mL}\right)}{\frac{\text{Injected activity (kBq)}}{\text{Body weight (g)}}}$$

Equation 1.2 Standardised uptake value

The resultant value is unitless (g/mL, where g and mL are equivalent), representing radiotracer accumulation in a given ROI. SUV thresholds are commonly used in clinical practice as a basis for disease classification and criterion for diagnoses, particularly in the cancer field; for example, regions of radioactive glucose uptake (further described in section 1.5.2) may indicate where a tumour is located and how aggressive and metabolically active the cancer might be (Kinahan and Fletcher, 2010, Nakajima et al., 2012, Hofman and Hicks, 2016). Use of the SUV to aid diagnosis is controversial based on the notions that (a) relative image appearance may suffice for diagnostic purposes and (b) calculated SUVs exhibit high variability due to non-standardised methods of image acquisition, reconstruction, and analysis. However, the SUV may be better used as a trend marker, especially in conservative surveillance, wherein clinicians might evaluate trends in SUV change to decide how to advance with treatment options in AAA; it may be useful to determine whether a ‘watch-and-wait’ strategy should be adopted to avoid performing invasive procedures that may not be necessary for AAA management (Gambhir, 2002, Boellaard et al., 2004, Kinahan and Fletcher, 2010).

Despite the widespread use of the SUV, its quantification may be largely affected by a number of physiological (e.g. body weight and composition, mode of radiotracer administration, time between radiotracer administration) and physical (e.g. scanner calibration, reconstruction parameters, ROI definition) factors. A variation of 10–25% in repeated SUV measurements can be expected in the same patients due to instrument-related and analytical factors (Fahey et al., 2010, Kinahan and Fletcher, 2010). The most common methods of calculating the SUV are based on the average or maximum SUV of all voxels within a predefined ROI (SUV_{mean} and SUV_{max} , respectively). Although the SUV_{mean} shows less sensitivity to image noise, it is subject to intra- and inter-observer variability, as it is highly dependent on the voxels that are included in the final calculation. Meanwhile, the SUV_{max} is largely independent of the ROI definition, as it reflects the single ‘hottest’ voxel value; however, it may be adversely affected by image noise (Massaro

et al., 2009, Vanderhoek et al., 2013). In an effort to reduce the variability in SUVs, other methods of calculating the SUV have been explored, wherein the average SUV in a group of voxels surrounding the 'hottest' voxel value is determined. This is achieved by applying specific threshold values to calculate the SUV_{mean} for voxels within predefined ROIs that are equal to or greater than the 'hottest' voxels. This approach may maintain the reproducibility of the SUV_{max} with improved statistics to reduce noise (Nakamoto et al., 2002, Krak et al., 2005, Velasquez et al., 2009). Averaging the 10 'hottest' voxels has been shown to reduce the variability in the SUV_{max} by a factor of 2.7 (Burger et al., 2012). In similar studies, different threshold values have been investigated, ranging from 40% to 90% of the highest values, which evidently raises the need for a standardised percentage threshold that can be applied consistently to provide uniform SUV results (Boellaard, 2009, Wahl et al., 2009).

In addition to the quantitative threshold, the morphology of the ROI also contributes to SUV quantification. Manually drawing the ROI to precisely delineate the area of tracer uptake is the most intuitive and simple segmentation method. However, this method is time-consuming and highly subjective, leading to variability in the results (Velasquez et al., 2009, Vorwerk et al., 2009). Alternatively, implementing fixed-size ROIs permits semi-automatic delineation of areas of tracer uptake, hence requiring less time than that required for manual delineation (Nakamoto et al., 2002, Benz et al., 2008, Vanderhoek et al., 2013). Different sizes and shapes of fixed-size ROIs have been explored, including square, cylindrical, and spherical regions with side lengths ranging from 7 to 15 mm (Nahmias and Wahl, 2008, Weber et al., 2015). Moreover, advanced automatic image segmentation methods that utilise properties of image reconstruction algorithms, such as edge detection, region growing, and fuzzy locally adaptive Bayesian methods, are under continuous development (Day et al., 2009, Hatt et al., 2010); this domain has evolved to what is now called 'radiomics'. Studies of the effects of different thresholds on SUV quantification have largely used data from the oncology field; however, the implications of the results are also useful for cardiovascular and other medical fields.

Another metric that is commonly implemented in PET image analysis is the target-to-background ratio (TBR). The TBR takes the SUV a step further, in dividing the target lesion's SUV with the venous blood pool SUV, as follows (Chen and Dilsizian, 2015) (Equation 1.3):

$$TBR = \frac{SUV_{target}}{SUV_{background}}$$

Equation 1.3 Target-to-background ratio

Doing so corrects the SUV for blood uptake of the tracer, enabling researchers and clinicians to differentiate between radiotracer uptake in a target lesion versus radioactivity due to radiotracer that has not been taken up into cells and has instead remained in the blood supply circulating around the target lesion. Nonetheless, similar to the use of the SUV, the use of the TBR is also controversial. The TBR depends on how the blood pool activity is measured, reflecting the denominator in the ratio. This measure could be acquired from the superior vena cava, IVC, right atrium, or jugular vein, a source that varies across different studies. Furthermore, the blood pool activity may vary because of biological (e.g. differential renal clearance) or analytical (e.g. differential ROI definitions or low spatial resolution) reasons (Chen and Dilsizian, 2015). Regarding this, Huet *et al.* implemented a mathematical model that summed vascular wall activity and blood activity with adjustments based on weighting factors considering activity spill-out. They suggested that differences in the TBR result from notable differences in vascular wall activity and in estimated blood pool activity, rendering the TBR less reproducible than the SUV (Huet *et al.*, 2015). Improvements in spatial resolution and application of partial volume correction may enhance the precision and accuracy of methods of PET analysis in the future (Tsoumpas *et al.*, 2016).

1.5.2 PET radiotracers

The most common radioactive tracer used in PET imaging is [¹⁸F]FDG, an analogue of glucose. Uptake of [¹⁸F]FDG occurs in cells that metabolise glucose, after which it is phosphorylated by hexokinase into [¹⁸F]FDG-6-phosphate. At this stage, it is then metabolically trapped, as it does not harbour the 2' hydroxyl group that is essential to proceed with glycolytic reactions (Figure 1.3). Therefore, the intracellular distribution of [¹⁸F]FDG is associated with the degree of metabolic activity and inflammation in regions of uptake (Tarkin *et al.*, 2016). [¹⁸F]FDG uptake on PET has been demonstrated to be correlated with macrophage density in plaques, cardiovascular risk factors, the Framingham Risk Score, and various inflammatory and glycolysis-related biomarkers, such as glucose transporter (GLUT)-1, GLUT-3, and total lesion glycolysis (Zhao *et al.*, 2002, Tarkin *et al.*, 2014, Suzuki *et al.*, 2018). A downside to the advantage of [¹⁸F]FDG

having the capacity to highlight all regions of active glucose metabolism is that, as a result, it is difficult to differentiate disease-specific activity. Moreover, the uptake of [^{18}F]FDG can be influenced by conditions of disease microenvironments, such as hypoxia or increased myocardial muscle activity, or the efficiency with which the microcirculation distributes the radiotracer (Wykrzykowska et al., 2009, Folco et al., 2011, Taqueti et al., 2014). To help overcome these and similar limitations, novel radioactive tracers are continually under development to elucidate different pathobiological mechanisms in different diseases.

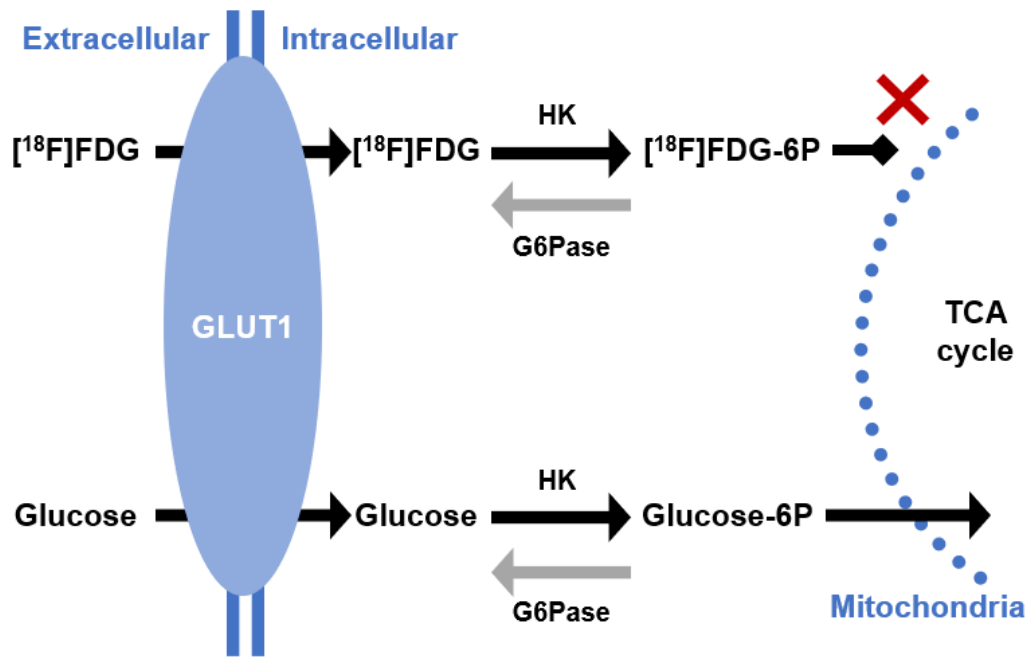


Figure 1.3 Schematic of the metabolic pathway of glucose and its analogue $[^{18}\text{F}]\text{FDG}$. $[^{18}\text{F}]\text{FDG}$, $[^{18}\text{F}]\text{fluorodeoxyglucose}$; $[^{18}\text{F}]\text{-FDG-6P}$, $[^{18}\text{F}]\text{fluorodeoxyglucose-6-phosphate}$; GLUT1, glucose transporter-1; HK, hexokinase; G6Pase, glucose-6-phosphatase; Glucose-6P, glucose-6-phosphate; TCA, tricarboxylic acid.

Primary research studies of AAA involving PET imaging that have been conducted in the last decade are presented in Table 1.2. There has been an extensive focus on markers of inflammatory activity, evidenced by the overwhelming predominance of [¹⁸F]FDG PET studies. Both preclinical and clinical studies of gold-standard [¹⁸F]FDG PET to assess glucose metabolism and inflammation in AAA have yielded varying results, with both increased and variable [¹⁸F]FDG uptake being demonstrated (Sakalihan et al., 2002, Kotze et al., 2011, English et al., 2015, Huang et al., 2016, Nie et al., 2018, English et al., 2020). Some studies have shown that [¹⁸F]FDG PET may be useful to predict AAA expansion and/or progression (Reeps et al., 2008, Courtois et al., 2013, Nchimi et al., 2014), whilst other studies have contradicted this (Kotze et al., 2011, Barwick et al., 2014). For example, Reeps *et al.* showed that increased aortic uptake of [¹⁸F]FDG in patients was associated with a higher density of inflammatory markers, which may contribute to aortic expansion, whilst patients showing [¹⁸F]FDG uptake in AAA revealed no correlation with aortic expansion 12 months later in a study by Kotze *et al.* (Reeps et al., 2008, Kotze et al., 2011). Moreover, Nchimi *et al.* demonstrated that [¹⁸F]FDG uptake correlated positively with wall stress and strength in AAA, whereas Barwick *et al.* found no significant difference in aortic uptake of [¹⁸F]FDG between patients with infra-renal AAA and patients without AAA (Barwick et al., 2014, Nchimi et al., 2014). Based on a study involving [¹⁸F]FDG PET and contrast-enhanced MRI, Kuzniar *et al.* further demonstrated that the hotspots of [¹⁸F]FDG uptake and late gadolinium enhancement rarely coincide in AAA, although both are associated with aneurysm growth, raising questions about the distribution of cellular activity in AAA (Kuzniar et al., 2019). Collectively, these findings lend to a complicated story of glucose metabolism in AAA.

Other PET radiotracers are also promising in the context of AAA. The Sodium Fluoride Imaging of AAA (SoFIA³) trial has shown that uptake of [¹⁸F]-labelled sodium fluoride (NaF), which reflects regions of microcalcification, in patients with asymptomatic AAA predicts AAA progression and rupture, providing proof-of-concept data for the feasibility of a non-[¹⁸F]FDG PET radiotracer for AAA stratification (Forsythe et al., 2018). A key point coming out of this study is that aneurysm size is not necessarily a predictor of rupture; AAA growth can be non-linear and influenced by biomechanical processes that may not exhibit a detectable pattern. The SoFIA³ trial demonstrated that [¹⁸F]NaF uptake is a positive predictor of aneurysm growth and clinical outcomes, which are independent but supplementary to classic clinical parameters such as aneurysm diameter

(Forsythe et al., 2018). That being said, the findings of this trial must be considered in light of the confounding issue of spill-in contamination from the nearby bone into the aneurysm; thus, background correction techniques can provide more robust quantitative assessments of AAA (Akerlele et al., 2019).

Alternative tracers that may prove to be useful include markers of other characteristics of AAA development, such as angiogenesis (Shi et al., 2015) and integrins (Kitagawa et al., 2013, Tegler et al., 2014).

[¹⁸F]fluoromethylcholine, which is commonly implemented for staging prostate cancer, may also be useful to incidentally detect AAA in patients with prostate cancer (Ferda et al., 2019). In this way, PET will undoubtedly remain an attractive modality to advance our understanding of AAA pathophysiology, whilst novel molecular tracer agents are introduced and hybrid multimodality systems are improved. As PET is readily accessible and already being used in the clinic, continued research using PET has practical applications that are feasible for clinical translation.

Table 1.2 Studies using PET imaging to investigate AAA published in the most recent decade. The following Boolean operators were used as search terminology: (AAA OR abdominal aortic aneurysm*) AND (PET OR positron emission tomography). Only original research articles were included (i.e. reviews, case reports, conference proceedings, etc. were excluded).

Reference	Radiotracer	Target (Species)	Key Conclusions
(Barwick et al., 2014)	[¹⁸ F]FDG	Glucose metabolism (humans)	Metabolic activity levels may not correlate with aortic size and may not differ between aneurysms vs. controls.
(Courtois et al., 2013)	[¹⁸ F]FDG	Correlation between inflammation and histological analysis (humans)	[¹⁸ F]FDG uptake in the aneurysmal wall may be associated with an active inflammatory process involving proliferating leukocytes and increased circulating C-reactive protein.
(Courtois et al., 2018)	[¹⁸ F]FDG	Circulating miRNAs (humans)	Specific miRNAs are significantly correlated with [¹⁸ F]FDG uptake in the aneurysmal wall and may be directly involved in AAA instability.
(Courtois et al., 2019)	[¹⁸ F]FDG	Prediction of complications after EVAR (humans)	Aortic [¹⁸ F]FDG uptake may be a predictor of post-EVAR complications.
(English et al., 2014)	[¹⁸ F]FDG and [¹¹ C]PBR28	Aortic wall inflammation (rats)	AAA wall inflammation can be detected using [¹⁸ F]FDG and [¹¹ C]PBR28.
(English et al., 2015)	[¹⁸ F]FDG	Rupture prediction (rats)	Increased pre-rupture glucose uptake may be associated with increased inflammation in the ruptured AAA wall.

(English et al., 2020)	[⁶⁴ Cu]DOTA-ECL1i	Expression of chemokine receptor 2 (rats)	Chemokine receptor 2 may predict AAA rupture.
(Ferda et al., 2019)	[¹⁸ F]FCH	Incidental AAA detection in patients with prostate cancer (humans)	[¹⁸ F]FCH PET/CT may be an effective approach for secondary prevention and stratification of AAA in patients with prostate cancer.
(Forsythe et al., 2018)	[¹⁸ F]NaF	AAA growth and clinical outcomes (humans)	[¹⁸ F]NaF uptake may help identify advanced AAA and may be correlated with aneurysm growth and clinical AAA events that differ from established risk factors.
(Huang et al., 2016)	[¹⁸ F]FDG	Structural stress (humans)	Increased [¹⁸ F]FDG is associated with high mechanical stress of thick intraluminal thrombus in AAA.
(Kitagawa et al., 2013)	[¹⁸ F]FPPRGD ₂	$\alpha_v\beta_3$ expression (mice)	[¹⁸ F]FPPRGD ₂ uptake in AAA may correlate with vascular inflammation and neoangiogenesis.
(Kotze et al., 2009)	[¹⁸ F]FDG	Metabolic activity (humans)	There may be increased metabolic activity mediated by GLUTs in the AAA wall.
(Kotze et al., 2011)	[¹⁸ F]FDG	Future aneurysm expansion (humans)	AAA with lower metabolic activity may be more likely to expand.
(Kotze et al., 2014)	[¹⁸ F]FDG	Correlation between CT texture analysis data and metabolism (humans)	CT textural data may reflect AAA metabolism measured by [¹⁸ F]FDG PET.

(Kuzniar et al., 2019)	[¹⁸ F]FDG	Inflammation (humans)	[¹⁸ F]FDG PET/MRI may be used to assess inflammation in asymptomatic AAA, although the hotspots of [¹⁸ F]FDG uptake and late gadolinium enhancement are not always aligned.
(Lee et al., 2018)	[¹⁸ F]FDG	Decision to perform intervention (humans)	[¹⁸ F]FDG uptake may be related to the clinical conditions of patients with AAA who require intervention.
(Maier et al., 2012)	[¹⁸ F]FDG	Correlation between metabolic activity and non-linear finite element analysis (humans)	Greater [¹⁸ F]FDG activity may be associated with increased mechanical stress in the AAA wall.
(Marini et al., 2012)	[¹⁸ F]FDG	Correlation between [¹⁸ F]FDG uptake and asymptomatic non-inflammatory AAA (humans)	Low [¹⁸ F]FDG uptake in asymptomatic AAA reflects the loss of tissue structure and reduced cell density.
(McBride et al., 2016)	[¹⁸ F]FDG	Vascular inflammation (humans)	[¹⁸ F]FDG PET/CT may indicate macrophage glycolytic activity in AAA.
(Menezes et al., 2009)	[¹⁸ F]FDG	Ideal imaging time after [¹⁸ F]FDG injection (humans)	There may be no advantage in terms of image analysis in imaging 3 h vs. 1 h after [¹⁸ F]FDG injection.
(Molacek et al., 2019)	[¹⁸ F]FDG	AAA progression (humans)	[¹⁸ F]FDG PET/CT or PET/MRI does not correlate with disease symptoms, AAA progression, or dissection.
(Morbelli et al., 2014)	[¹⁸ F]FDG	Relationship between inflammation and risk factors (humans)	Vascular inflammation plays a role at all stages of AAA, which may involve the local result of systemic inflammation.

(Morel et al., 2015)	[¹⁸ F]FDG	Metabolic changes (humans)	Metabolic changes in AAA may follow a cyclic pattern, similar to that observed with changes in maximal aortic diameter.
(Murakami et al., 2014)	[¹⁸ F]FDG	Infection (humans)	[¹⁸ F]FDG PET is useful to diagnose infected AAA.
(Nahrendorf et al., 2011)	[¹⁸ F]CLIO	Macrophages (mice)	[¹⁸ F]CLIO may be used to quantify macrophage content in AAA.
(Nchimi et al., 2014)	[¹⁸ F]FDG	Biomechanical properties (humans)	Increased [¹⁸ F]FDG uptake is correlated with AAA location, wall stress, and patient risk factors.
(Nchimi et al., 2016)	[¹⁸ F]FDG	Intraluminal thrombus occurrence in AAA (rats)	Increased [¹⁸ F]FDG uptake and growth may be associated with intraluminal thrombus occurrence in AAA.
(Nie et al., 2018)	[¹⁸ F]FDG	AAA progression (rabbits)	Inflammation plays a key role early in AAA development.
(Palombo et al., 2012)	[¹⁸ F]FDG	Asymptomatic aneurysmal uptake (humans)	[¹⁸ F]FDG uptake may be rare in patients with AAA of diameter approaching the surgical threshold.
(Reeps et al., 2013)	[¹⁸ F]FDG	Correlation between glucose metabolism and partial volume correction (humans)	Partial volume correction may be necessary to quantitatively stratify patients for AAA repair.

(Sarda-Mantel et al., 2012)	[¹⁸ F]FDG, [¹⁸ F]FCH, [¹⁸ F]DPA714	Correlation between aortic wall inflammation and histopathological analysis (rats)	[¹⁸ F]FDG may have higher sensitivity than that of [¹⁸ F]FCH and [¹⁸ F]DPA714 in detecting activated leukocytes in the aneurysmal wall.
(Shi et al., 2015)	[⁶⁴ Cu]NOTA-TRC105-Fab	Angiogenesis (mice)	[⁶⁴ Cu]NOTA-TRC105-Fab uptake indicates regions of increased angiogenesis in AAA, based on CD105 expression.
(Tegler et al., 2012)	[¹⁸ F]FDG	Inflammation (humans)	[¹⁸ F]FDG PET cannot be used to detect chronic inflammation in asymptomatic aneurysms.
(Tegler et al., 2013)	[¹¹ C]PK11195 and [¹¹ C]-d-deprenyl	Inflammation (humans)	Inflammation in AAA cannot be detected using [¹¹ C]PK11195 and [¹¹ C]-d-deprenyl.
(Tegler et al., 2014)	[¹⁸ F]-fluciclatide	$\alpha_v\beta_3$ expression (humans)	$\alpha_v\beta_3$ integrin expression in AAA may be visualised using [¹⁸ F]fluciclatide
(Truijers et al., 2009)	[¹⁸ F]FDG	Aneurysm wall pathology (humans)	[¹⁸ F]FDG PET/CT may be useful in detecting concomitant malignancies in patients with AAA.
(Tsuruda et al., 2016)	[¹⁸ F]FDG	Aortic wall inflammation (humans)	Active aortic wall inflammation may contribute to AAA progression and rupture.
(Xu et al., 2010)	[¹⁸ F]FDG	Wall stress and metabolic activity (humans)	High AAA wall stress and accelerated metabolism may be associated.

AAA, abdominal aortic aneurysm; CD105, cluster of differentiation-105; CT, computed tomography; EVAR, endovascular aneurysm repair; [¹⁸F]CLIO, [¹⁸F]dextran-coated iron oxide; [¹⁸F]FCH, [¹⁸F]fluoromethylcholine; [¹⁸F]DPA714, [¹⁸F]N,N-diethyl-2-[4-(2-fluoroethoxy)phenyl]-5,7-dimethylpyrazolo[1,5-a]pyrimidine-3-acetamide; [¹⁸F]FDG, [¹⁸F]fluorodeoxyglucose; [¹⁸F]NaF, [¹⁸]sodium fluoride; GLUT, glucose transporter; miRNA, microRNA; MRI, magnetic resonance imaging; PET, positron emission tomography

1.5.3 [¹⁸F]FLT and thymidine

A key idea underlying this thesis, as described in section 1.3.5, is that AAA formation involves cell proliferation, which may be a feasible target for [¹⁸F]FLT PET. [¹⁸F]FLT is an example of a radioactive PET tracer that is useful to elucidate a non-glucose activity mechanism: cell proliferation. [¹⁸F]FLT has a similar structure to that of thymidine, with the exception of the fluorine atom that replaces the hydroxyl group at the 3' position; this precise positioning prevents [¹⁸F]FLT from proceeding along the complete mechanistic pathway of thymidine. Once [¹⁸F]FLT is actively transported from the blood into cells, it acts as a substrate for thymidine kinase (TK)-1, a cytosolic enzyme with peak expression during the synthesis phase of the cell cycle and very low expression in resting cells (He et al., 2004). At this stage, it is phosphorylated and metabolically trapped within the cell, such that it is restricted from incorporating into DNA (Figure 1.4).

Few researchers have attempted kinetic analysis for [¹⁸F]FLT quantification in PET imaging of non-neural regions. However, a mathematical model similar to that for [¹⁸F]FDG has been established, which consists of (i) an extracellular blood pool compartment shared by [¹⁸F]FLT and thymidine; (ii) an exchangeable tissue compartment, from which [¹⁸F]FLT and thymidine exchange freely between the blood pool or continue to be metabolised intracellularly; and (iii) a compartment of phosphorylated (and thus trapped) [¹⁸F]FLT nucleotides. Four rate constants are used to define the kinetic transfer rates between these two compartments and blood. The transfer from blood into tissue is represented by K_1 , with k_2 representing the return of non-phosphorylated [¹⁸F]FLT from tissue. The phosphorylation of [¹⁸F]FLT is conveyed through k_3 , which is the rate-limiting step of [¹⁸F]FLT retention in tissue (Shields et al., 2002, Muzi et al., 2006). These phosphorylated products then show negligible dephosphorylation back to the extracellular compartment, represented by k_4 , as [¹⁸F]FLT is not a substrate for thymidine phosphorylase (Grierson et al., 2004).

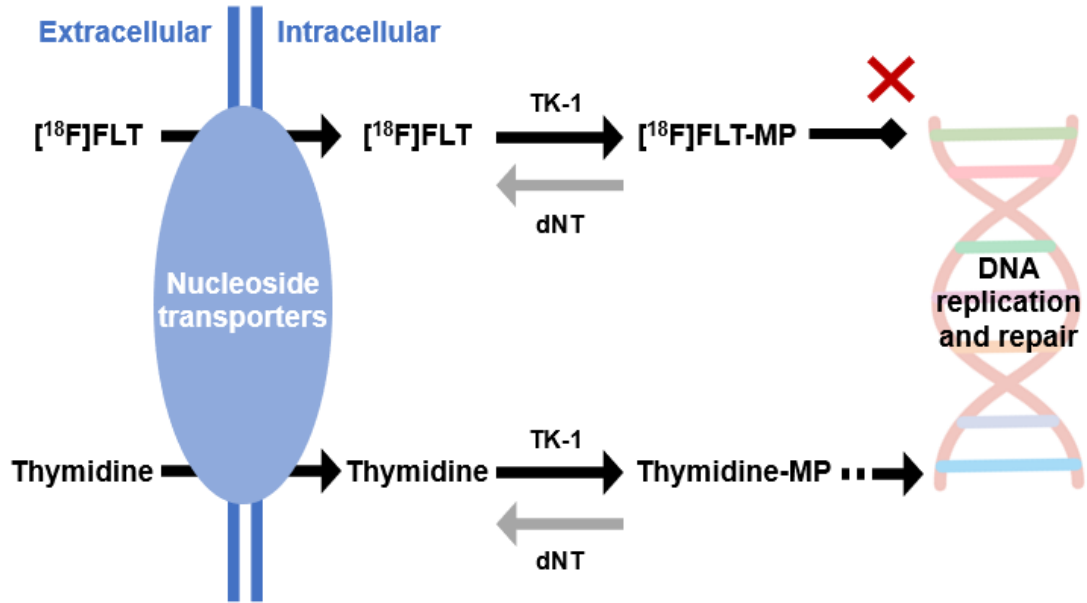


Figure 1.4 Schematic of the metabolic pathway of thymidine and its analogue $[^{18}\text{F}]\text{FLT}$. TK-1, thymidine kinase-1; dNT, deoxyribonucleotidase; DNA, deoxyribonucleic acid; $[^{18}\text{F}]\text{FLT}$, $[^{18}\text{F}]\text{fluorothymidine}$; $[^{18}\text{F}]\text{-FLT-MP}$, $[^{18}\text{F}]\text{fluorothymidine-monophosphate}$; Thymidine-MP, thymidine-monophosphate.

Based on the notion that TK-1 activity is directly associated with the concentration of [^{18}F]FLT in cells, [^{18}F]FLT signal and uptake are reflective of proliferative activity. Phosphorylated [^{18}F]FLT is unable to escape from cells and has been demonstrated to act as a substrate for TK-1 and not for mitochondrial TK-2, the latter being cell cycle-independent, making [^{18}F]FLT a tracer that exhibits high specificity for its biological target (i.e. proliferative cells) (Hannigan et al., 1993, Toyohara et al., 2002). Furthermore, the compartmental model of [^{18}F]FLT indicates that the metabolic flux parameter, K_{FLT} , which is a product of the rate constants, is strongly correlated with the Ki67 proliferative index as well as TK-1 expression (Muzi et al., 2005, Brockenbrough et al., 2011).

The utility of [^{18}F]FLT in cancer imaging has been extensively demonstrated because its biological target is one of the key hallmarks of cancer (Shields et al., 1998, Salskov et al., 2007, Yue et al., 2010, Hanahan and Weinberg, 2011, Viertl et al., 2011). Furthermore, Ye et al. demonstrated that [^{18}F]FLT PET could be used to visualise proliferating macrophages, hematopoietic stem cells, and progenitor cells in preclinical and clinical models of atherosclerosis (Ye et al., 2015). Their findings highlight the promise of [^{18}F]FLT PET for non-cancer applications; however, its usefulness for other cardiovascular applications is unclear.

1.6 Research hypotheses, aims, and objectives

The hypothesis to be tested in this thesis is that there is an active period of cell proliferation in AAA that can be detected using [^{18}F]FLT PET/CT and modulated in response to anti-proliferative drugs. To test this hypothesis, the aim of this thesis was to determine the feasibility of [^{18}F]FLT PET/CT to visualise and quantify cell proliferation in the AngII AAA murine model. The key objectives of this study were to

- (i) investigate if there is significant [^{18}F]FLT uptake in the aneurysms of the AngII and PPE AAA mouse models;
- (ii) evaluate the expression of key proteins involved in the thymidine proliferative pathway;
- (iii) investigate a variety of image quantification metrics by assessing the effects of different ROI definitions; and
- (iii) determine if [^{18}F]FLT PET/CT can be used to assess a therapeutic response in the AngII AAA model.

Chapter 2 Methods

This chapter provides an overview of the methods implemented to conduct the experiments presented in this thesis. The rationale for each method chosen is also described.

2.1 Animal models

All animal work was conducted in accordance with the UK Home Office, Animals (Scientific Procedures) Act 1986 under Project Licence P606320FB. Male Jax™ ApoE^{-/-} mice (B6.129P2-Apoetm1Unc/J; Charles River, UK) underwent surgery at 14 weeks of age. Male C57BL6/J mice (Charles River, UK) were used at 8 weeks of age for baseline biodistribution studies. Male mice were chosen for the overall study as AAA predominantly occurs in male patients (Bloomer et al., 2012). All animals were part of the Jackson Laboratories Genetic Stability Programme to limit cumulative genetic drift. Mice were maintained at 21°C with a 12-hour light / dark cycle and 50–70% humidity in GM500 individually ventilated cages (Techniplast, Italy) with a maximum of 5 animals per cage and fed a standard RM1 chow pellet diet (Special Diet Services) and triple-filtered water via Hydropac pouches *ad libitum*. All mice were provided with a housing dome and two chew sticks as environmental enrichment. All mice were checked daily by an animal technician.

The traditional murine AAA models were generated as described below. All surgical procedures were performed under isoflurane anaesthesia via inhalation (to allow for tight control of anaesthetic depth with rapid recovery) in a purpose-built murine operating facility under sterile surgical conditions using an OPMI Pico operating microscope (Zeiss) in accordance with the guiding principles of the laboratory animal science association (www.lasa.co.uk) by Dr Marc Bailey. Mice were maintained at 37°C during surgery and recovery using a heated operating table and recovery platform. Wounds were closed using continuous Vicryl (Ethicon) sutures, 6-0 for the peritoneum and 4-0 for the skin. All animals received suitable buprenorphine analgesia via intraperitoneal injection (100 µL of 0.1 mg/mL solution with additional 50-µL injections as needed). Mice were identified by ear notching.

The AngII AAA model was the main model used for the experiments presented in this thesis because of (i) the favourable location of the AAA distant from the bladder, which would impart partial volume effects, and (ii) its surgical ease, as these mice needed to undergo surgery at the University

of Hull, where the surgical facilities were limited. For this model, 14-week-old male ApoE^{-/-} mice (Jackson Laboratories) received human AngII (Sigma A9525) infusions at 750 ng/kg-min via Alzet[®] 1002 (14 days) or 1004 (28 days) osmotic mini-pumps that were implanted subcutaneously by posterior neck incision under recovery isoflurane anaesthesia, as described previously (Bridges et al., 2017). Matched male ApoE^{-/-} mice infused with a saline solution were used as controls for this model.

For the PPE model, 12-week-old male C57BL6/J mice were subjected to laparotomy, and the abdominal aorta was exposed by blunt dissection. PPE (10 µL, Sigma E1250) was applied to the adventitia of the infra-renal aorta for 5 min. For the CaCl₂ model, the approach was identical to that of the PPE model, but CaCl₂ (0.5 M) was applied to the adventitia of the infra-renal aorta for 14 min on disassociated cotton bud tips. Sham-operated matched male C57BL6/J mice were used as controls for both the PPE and CaCl₂ models; these animals underwent identical laparotomy and aortic exposure, but saline washout only.

For all mice used for experiments at the University of Hull, the presence of AAA was determined based on visual inspection at post-imaging necropsy (i.e. the presence or lack of AAA) because of the limited resources available at this site; moreover, it was difficult to grade the severity of the AAA without access to a microscope. For all mice used for experiments at the University of Leeds, the presence of AAA was determined using USS, which also provided measurements of size.

2.2 Histological staining

For the initial experiment investigating cell proliferation in murine models of AAA, AAA was first induced in mice by three methods: AngII infusion to ApoE^{-/-} mice or peri-adventitial application of CaCl₂ or PPE to the aorta in C57BL6/J mice, as described in section 2.1. In each case, AAA tissues were compared with equivalent tissues from appropriate and matched sham control animals. The aortic tissues were harvested at 28 days post-induction of AngII and CaCl₂ AAA and at 14 days post-induction of PPE AAA (per the standard time points of the models) and used for 3,3'-diaminobenzidine staining for proliferative cells using an antibody raised against the cell proliferation marker Ki67. The Ki67 index is defined by the proportion of cells in a specified ROI with positive immunohistochemical staining and has been demonstrated to be particularly useful in cancer research to monitor the proliferative rate of tumour cells (Scholzen and Gerdes, 2000). Ki67 protein

expression peaks in cells throughout the active G1, S, G2, and M cell cycle phases, with drastically reduced expression in resting cells (i.e. G0) (Miller et al., 2018). Therefore, Ki67 was chosen for the initial experiments to explore the detectability of cell proliferation in murine AAA models.

To perform Ki67 staining, the mice were first terminally exsanguinated via the IVC. Murine aortae were each fixed *in situ* by perfuse fixation with 10 mL of phosphate-buffered saline followed by 5 mL of 4% paraformaldehyde in terminally anaesthetised animals via cardiac puncture with an outflow tract through the severed pulmonary arteries. Aortae were then fixed at 4°C for 48 hours before they were embedded in Cellwax (Cellpath Ltd., UK) using the Leica EG1150H embedding station. Four- μ m thickness sections were cut onto Plus Frost slides (Solmedia, UK) using a Leica RM2235 microtome, and the slides were dried overnight at 37°C. Proliferating cells were stained with rabbit anti-mouse Ki67 antibody (ab15580, Abcam; 1:750 dilution) for 1 hour and Menapath Polymer HRP secondary antibody (Menarini Diagnostics Ltd., Winnersh, UK) for 30 minutes. The specificity of the antibody was first confirmed in positive control (spleen) tissue with and without primary antibody. Following a final wash, all sections were treated with Menapath diaminobenzidine peroxidase for 5 minutes and counterstained with Mayer's Haematoxylin for 2 minutes, dehydrated, cleared in xylene, and mounted in dibutyl phthalate xylene. The slides were then imaged using the Aperio® AT2 (Leica Biosystems, Wetzlar, Germany) digital pathology slide scanner with $\times 20$ maximal magnification. Images were stored on the secure Leeds Institute of Cancer and Pathology digital pathology server and accessed remotely using Aperio® Image Scope software (Leica Biosystems). All quantitative analyses were performed using ImageJ 1.51k software (Schneider et al., 2012). For quantification of the Ki67 staining, the proportions of Ki67-positive nuclei were determined in three 50- μ m² ROIs and averaged for each animal. Finally, aortae from control models were compared against aortae from the three different aneurysm models.

2.3 *In vivo* USS

To evaluate aortic volumes and diameters, *in vivo* USS was performed in two cohorts: (i) the animals used for Ki67 analysis and (ii) those that were subsequently used for [¹⁸F]FLT gamma counting analysis. USS was performed using the Vevo2100 high-resolution (30 μ m), high-frequency preclinical μ USS system (Visualsonics, FUJIFILM VisualSonics, Inc., Toronto, ON, Canada) with an MS-550D transducer at a 40-MHz frequency on a heated platform maintaining a core body temperature of 35°C to 37°C,

monitored via a rectal probe. Recovery anaesthesia was induced in the mice at 5% isoflurane and maintained at 2%. Prior to imaging, the abdomen area was shaved and hair removed using depilatory cream. Imaging was performed using Aquasonic® clear gel (Parker Labs). Transverse imaging was acquired using a motor along an 11.96-mm ROI from the right renal artery in the cranial direction with 157 frames at 0.076-mm intervals gated for respiration with electrocardiographic triggering 50 ms after the *r*-wave. Images were reconstructed and measured using Vevo Lab v1.7.0 (VisualSonics, FUJIFILM VisualSonics, Inc., Toronto, ON, Canada) to generate three-dimensional lumen volume measurements. For the co-registration analysis, bony landmarks on CT and USS images were aligned and displayed using ImageJ 1.51k (Schneider et al., 2012).

2.4 *In vivo* [¹⁸F]FLT PET/CT

[¹⁸F]FLT was prepared from [¹⁸F]fluoride produced by a radiochemist at the University of Hull using an on-site 7.5-MeV ABT Biomarker Generator cyclotron and purified using an in-house developed microfluidic electrochemical cell for electrode trapping, through which irradiated target water (0.5 mL, [¹⁸O]H₂O) containing ca. 1 GBq of [¹⁸F]fluoride was pumped at 0.2 mL/min whilst applying a 20 V potential, and the cell was flushed with 2 mL of MeCN at 1 mL/min with no potential applied. Subsequently, 0.4 mL of a solution containing KHCO₃ (30 mM) and K222 (37 mM) in MeCN was pumped through the cell at 40°C at 0.1 mL/min. Ten mg of fluorothymidine precursor 3'-N-Boc-5'-dimethoxytrityl-3'-O-nosyl-thymidine was added to the released solution to perform a radio-labeling reaction at 100°C for 10 min. After the fluorination, the unreacted [¹⁸F]fluoride was trapped on the neutral alumina cartridge (light) and reaction mixture treated for 5 min at room temperature with an equivalent volume of 2 N HCl solution. The mixture was then neutralised with a stoichiometric amount of 8 N NaOH solution and purified by semi-preparative high-performance liquid chromatography (HPLC) on an ACE 5 C18 10×250 5A column eluted with 35% acetonitrile in water (both 0.1% trifluoroacetic acid) (flow rate=4.7 mL/min, R_t=12 min). The HPLC fraction containing partially protected product was diluted 2–3-fold with water and passed over an HBL Oasis C18 cartridge. Trapped product was eluted with 0.5 mL of ethanol and 3 mL of diethyl ether and dried at 60°C under an inert gas stream. The heat applied for drying generated the fully de-protected [¹⁸F]FLT (confirmed by analytical HPLC with a cold [¹⁹F]FLT standard), which was re-dissolved in 10% ethanol/PBS solution, filtered through a 0.22-µm filter for sterility, and delivered for animal

administration. Tracer preparation started with 1.0–1.3 GBq of cyclotron-produced [^{18}F]fluoride and yielded 40 ± 8 MBq (n.d.c.) [^{18}F]FLT intravenous-injectable formulation in 136 ± 15 min ($n=5$) (RCY (decay-corrected)= $8\pm 2\%$).

Prior to imaging for the AngII AAA study, mice were induced with 5% isoflurane/oxygen (v/v) anaesthesia before maintenance at 2% at 1 L/min. Mice were cannulated in the tail vein using a bespoke catheter before being placed into an imaging cell where temperature and respiration were monitored (Minerve, France). [^{18}F]FLT was injected with the following means \pm standard deviations (SDs) of activity in 200 μL of 0.9% saline solution (Aqupharm No1, Animalcare Ltd., York, UK) through the pre-cannulated lateral tail vein at the beginning of a 90-minute dynamic imaging sequence: 7.27 ± 2.89 MBq (0.20 ± 0.08 mCi) (14-day scans; $n=12$) and 10.08 ± 1.77 MBq (0.27 ± 0.05 mCi) (28-day scans; $n=7$). Images were acquired using the Super Argus (Sedecal) small-animal PET/CT scanner installed at the University of Hull, with animals placed prone and the field-of-view centred on the abdominal aorta. Mice were maintained at 1% anaesthesia during scanning, with temperature and respiration monitored throughout. Following the 90-minute dynamic PET scan, a CT image was acquired for anatomic co-registration (40 kV, 140 μA , 360 projections, 8 shots). PET images were histogrammed into 15 2-second, 2 15-second, 4 60-second, 1 300-second, and 8 600-second frames and reconstructed using the 3D ordered subsets expectation maximisation algorithm with 2 iterations and 16 subsets with attenuation correction (as standard protocol at the University of Hull), yielding voxel dimensions of $0.39 \times 0.39 \times 0.78$ mm³.

Prior to imaging for the PPE model and imatinib studies, mice were induced with 5% isoflurane/oxygen (v/v) anaesthesia before maintenance at 2% at 1 L/min. [^{18}F]FLT was injected at mean \pm SD doses of 9.3 ± 0.7 MBq and 9.4 ± 0.1 MBq in 100 μL of 0.9% saline solution (Aqupharm No1, Animalcare Ltd., York, UK), respectively. After 80 and 90 min to allow for biodistribution of the radiotracer, respectively, images were acquired using the Albira Si (Bruker) small-animal PET/SPECT/CT scanner at the University of Leeds, with animals placed prone and the field-of-view centred on the abdominal aorta. Mice were maintained at 1% anaesthesia during scanning, with temperature and respiration monitored throughout (Bruker). Following the 20-min static and 90-min dynamic PET scans, respectively, a CT image was acquired for anatomic co-registration. PET/CT images were reconstructed using the maximum likelihood estimation maximisation algorithm (25 iterations), yielding voxel dimensions of 0.5 mm³.

A cohort of animals received imatinib via oral gavage on days 14–15 following mini-pump implantation. Matched controls received tap water, the solvent for imatinib.

The imaging protocols implemented in the present study were based not only on the standard protocols at the University of Hull, but also on a number of well-established notions, as follows. In a study that involved toxicological evaluation of [^{18}F]FLT in patients, blood-derived TACs showed a significant peak in activity within 5 min, followed by a gradual decrease to 110 min after radiotracer injection (Turcotte et al., 2007). Another study further showed a gradual decrease in the blood biodistribution of [^{18}F]FLT in patients with cancer (Cysouw et al., 2017). Moreover, [^{18}F]FLT uptake in proliferative lesions has been found to progressively increase over time to 80–100 min after radiotracer injection until eventual renal clearance (Lovinfosse et al., 2019). Evaluation of the compartmental model of [^{18}F]FLT kinetics, which describes the radiotracer's uptake and retention over 120 min, has revealed that restricting PET data acquisition to 60 min leads to a loss in the accuracy of ROI-specific information. This study also revealed that curves corresponding to k_3 , which reflects [^{18}F]FLT retention in tissues, are fairly stable between 90 and 120 min, with data acquisition beyond 90 min adding minimal value (Muzi et al., 2005). High repeatability of SUV quantification has also been demonstrated to occur when PET imaging is initiated at least 60 min after radiotracer administration (Lodge et al., 2017). Keeping with these findings, dynamic PET imaging protocols commonly include short timeframes that progress to increasingly longer timeframes by the end of a 90–120-min scan (Ukon et al., 2016). For these reasons, each dynamic scan was 90 min in duration, and short timeframes were implemented at the beginning of each dynamic scan in the present study to capture the peak activity of and any interesting fluctuations in the radiotracer immediately post-injection.

2.4.1 PET/CT image analysis

Animals with failed or paravenous radiotracer injection were excluded from the analyses. Three-dimensional isocontour ROIs incorporating the supra-renal abdominal aortic area (between the renal arteries and diaphragm) were manually drawn on the reconstructed images using AMIDE v1.0.4 software (Loening and Gambhir, 2003). The aortic ROI was constructed between the kidneys and anterior to the anterior border of the vertebral column based on the CT images including the most prominent PET signal in the 80- to 90-minute timeframe. For saline controls, the aortic ROI was

constructed between the kidneys, superior to the bladder, and anterior to the anterior border of the vertebral column based on the CT images. These ROIs had dimensions of 1.08 mm³ and contained 15 voxels. Incorporating mouse weights and injected radioactivity doses, the output statistics revealed the SUV_{max} and SUV_{mean} across all frames. These values were used to generate time–activity curves (TACs) for ROIs in the abdominal aorta, spleen, kidneys, and urinary bladder. The SUV_{max} was the metric of choice for quantification of the aortic ROI to avoid partial volume effects of the adjacent kidneys and bladder, where high [¹⁸F]FLT signals were observed consistently.

2.4.2 Generation of different ROI definitions for SUV analyses

For the experiments conducted to assess the effect of different ROI definitions on the resulting SUVs, analyses were conducted based on two types of ROI definitions: (i) shape (manually drawn vs. fixed-size ROIs) and (ii) voxel threshold (the proportion of voxels included in the final SUV calculation).

To address (i), the ellipsoid ROI-drawing tool was used to draw 4-mm ellipsoid ROIs in the abdominal aortic regions on images from both saline control and AngII AAA mice; these were the fixed-size ROIs. The size of the fixed-size ROI was chosen based on the maximum observed aneurysmal diameter of the aortae (approx. 3 mm). Therefore, the fixed-size ROIs were sufficiently large to contain the aneurysmal uptake without a deliberate attempt to align precisely with its contours, whilst also avoiding the inclusion of adjacent organs, such as the kidneys and urinary bladder. Manually drawn ROIs were generated using the 3D isocontour ROI-drawing tool to include as much of the abdominal aortic uptake as possible without including edges that may be subject to partial volume effects. For saline control images (i.e. the images that did not reveal abdominal aortic uptake of [¹⁸F]FLT), the aortic ROI was constructed between the kidneys, superior to the bladder, and anterior to the anterior border of the vertebral column based on the CT images, a similar approach to that described in section 2.4.1. To test the efficiency of each segmentation method, the time spent drawing each ROI was recorded.

To address (ii), the following values were then determined for all fixed-size and manually drawn ROIs: SUV_{mean}, SUV₄₀, SUV₅₀, SUV₇₀, and SUV₉₀, and SUV_{max}. The calculations for SUV₄₀, SUV₅₀, SUV₇₀, and SUV₉₀ included voxels that were equal to or greater than 40%, 50%, 70%, and 90% of the

highest value voxels, respectively, as defined in the AMIDE software manual (Leoning, 2014). For clinical relevance, the threshold values were chosen based on those implemented in previous studies (Dutour et al., 2009, Kahraman et al., 2011).

2.5 *Ex vivo* [¹⁸F]FLT gamma counting

Animals were anaesthetised with 5% isoflurane with an oxygen flow rate of 2 L/min. [¹⁸F]FLT in 100 µL of 0.9% saline solution (Aqupharm No1, Animalcare Ltd., York, UK) was injected into the tail vein at the following doses (mean ± SD): C57BL6/J study, 6.07 ± 2.57 MBq (0.16 ± 0.07 mCi); AngII AAA study, 0.25 ± 0.32 MBq (0.01 ± 0.01 mCi). A significant difference in the injection doses is noted here. For the C57BL6/J study, the mice underwent *in vivo* PET imaging prior to their organs being used for *ex vivo* gamma counting; the PET imaging necessitated a sufficiently high radiotracer dose for the signals to be detected on the resultant images. For the AngII AAA study, the mice did not undergo prior *in vivo* PET imaging; thus, the injected dose was reduced to allow more animals to be included in a single experiment with a single delivery of [¹⁸F]FLT. This was possible owing to the high sensitivity of the Hidex gamma counter; furthermore, the reduced dose helped avoid oversaturation of the gamma ray detectors. Animals were recovered for 90 minutes and subsequently humanely culled by cervical dislocation under Schedule 1 of the UK (Scientific Procedures) Act 1986. Samples (blood, plasma, heart, spleen, kidneys, small and large intestines, supra-renal abdominal aorta, bone, and tail) were collected, weighed, and measured for radioactivity using the Hidex gamma counter. Importantly, blood was removed from the aortic lumen before it was placed in the gamma counter. All *ex vivo* biodistribution data were decay-corrected, and radioactivity counts were expressed as the percentage of injected dose per gram of tissue (%ID/g). The following equation was used for decay corrections (Multi-Agency Radiological Laboratory Analytical Protocols, 2004) (Equation 2.1):

$$\frac{\%ID}{g} = \frac{\left(\frac{C_G - C_B}{\left(\frac{1 - e^{-\lambda \Delta t_c}}{\lambda \Delta t_c} \right) \times e^{-\lambda \Delta t_i}} \right)}{M_S} \times 100$$

Equation 2.1 Normalised percentage of injected dose per gram of sample (%ID/g). C_G , counting rate of sample (cps); C_B , counting rate of blank/background (cps); λ , decay constant; Δt_c , total counting time (s), Δt_i , time from injection to start of counting (s); A_i , injected activity (MBq); M_s , mass of sample (g)

2.6 *Ex vivo* [^{18}F]FLT autoradiography

Following a 90-minute delay for biodistribution (corresponding to the peak radiotracer uptake observed on *in vivo* PET images) and gamma counting, spleen, control aorta, and 14-day AngII AAA whole-organ samples were placed on a phosphor screen (PerkinElmer) covered with clear cellophane wrap. After overnight exposure, the imaging plates were scanned using the Cyclone Plus imager (PerkinElmer) at a resolution of 300 DPI. Images were processed using OptiQuant software (PerkinElmer).

2.7 Western blotting

Aortic tissue (supra-renal abdominal aortic segment only) was harvested under terminal isoflurane anaesthesia, snap-frozen in liquid nitrogen after phosphate-buffered saline perfusion, and stored at -80°C until use. Proteins were extracted using cell extraction buffer (FNN0011, Invitrogen) supplemented with Protease Inhibitor Cocktail (P8340, Sigma). The DC Protein assay kit (5000112, Bio-Rad) was used to quantify isolated proteins. The average yield was more than 3 mg of protein per aorta. Western blotting was performed for TK-1, a key enzyme expressed during DNA synthesis and the substrate for [^{18}F]FLT, and the specific carriers responsible for the transport of both [^{18}F]FLT and thymidine across the cell membrane: equilibrative nucleoside transporter (ENT)-1 and -2 and concentrative nucleoside transporter (CNT)-1 and -3. Each protein's expression was compared to the expression of β -actin, a housekeeping protein expressed in all cells that is commonly used for data normalisation and as a loading control; this ensures that each well of the agarose gel contains consistent amounts of protein to be tested. For each protein, blots were conducted as per the manufacturer's suggestions using 100 μg of protein per well. To create the running samples, β -mercaptoethanol (a reducing agent added to reduce disulphide bonds to irreversibly denature RNases) was added to laemmli sample buffer at a ratio of 1:4, and 3 parts of the target protein sample were then diluted into 1 part of this mixture. Antibodies and dilutions used were anti-TK-1, 1:500 (GTX113281; GeneTex, CA, USA); ENT-1, 1:1000 (ab135756); ENT-2, 1:1000 (ab181192); CNT-1, 1:500 (ab192438); CNT-3, 1:500 (ab223085); and β -actin, 1:1000 (Ab8226; all Abcam,

Cambridge, UK). Proteins were detected using SuperSignal West Femto Maximum Sensitivity enhanced chemiluminescent substrate (ThermoFisher Scientific, Loughborough, UK). ImageJ 1.51k software was used to quantify the optical intensity of the bands relative to that of corresponding β -actin bands (Schneider et al., 2012).

2.8 Statistical analyses

All statistical analyses were performed using Origin 2017 software (OriginLab Corporation, Northampton, MA, USA). All graphs show the mean \pm the standard error of the mean (SEM) unless otherwise stated. There are two types of statistical tests: parametric and non-parametric. Parametric tests are typically used when the data to be analysed are normally distributed (i.e. the mean is a more accurate representation of the centre of the data) and sample sizes are large. Meanwhile, non-parametric tests are typically used when the data to be analysed are 'distribution-free' (i.e. the median more accurately represents the centre of the data) and when sample sizes are small. The Shapiro–Wilk test revealed that the data populations were normally distributed, unless indicated otherwise in the subsequent chapter; thus, parametric statistical tests were conducted to analyse all data. However, given the small sample sizes, non-parametric tests may be an appropriate alternative for statistical analysis, the results of which are presented in Appendix B. Histology, USS, and some gamma counting results were analysed using two-sampled *t* tests with Welch's correction. Welch's correction was implemented rather than Student's *t* test as the former tends to be more reliable when sample sizes and variances are unequal (Glen, 2015). PET/CT, western blotting, and some gamma counting results were analysed using one-way analysis of variance with *post hoc* Bonferroni–Holm correction. Funding limitations generally restrict the number of animals that can be used; thus, it is important to implement a statistical test with maximum statistical power. Bonferroni–Holm correction is a uniformly more robust correction method than the Bonferroni method, as the former controls for the probability of type I error adjustments and the false discovery rate (Aickin and Gensler, 1996). The threshold for statistical significance was set at $p < 0.05$.

Chapter 3

Results

This chapter describes the outcomes of a series of experiments performed to answer critical questions about AAA-associated cell proliferation. Central to this thesis, PET/CT was undertaken with the aim of assessing the feasibility of using [¹⁸F]FLT to visualise and quantify cell proliferation in the AngII AAA model. This was followed up with Western blotting to directly test for biochemical markers of [¹⁸F]FLT activity, including the substrate and transporters of [¹⁸F]FLT. An attempt was also made to explore [¹⁸F]FLT PET/CT in a second model of AAA, and the findings of a pilot proof-of-concept therapeutic study are also described in this chapter. The overall experimental flow of all batches of ApoE^{-/-} mice is illustrated in Figure 3.1. These ApoE^{-/-} mice were used to obtain the results presented in sections 3.1, 3.3, 3.4, 3.5, and 3.7.

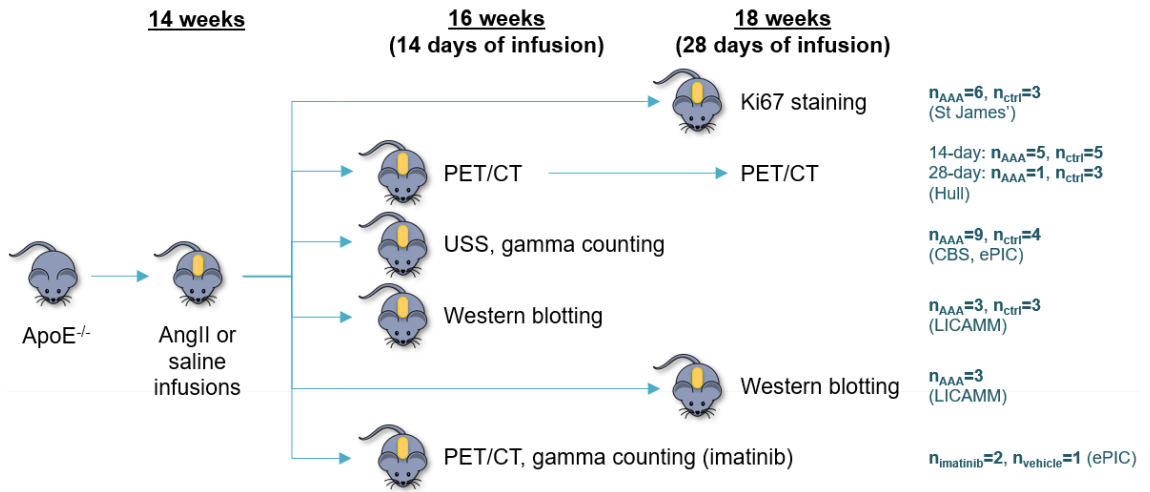


Figure 3.1 Different cohorts of ApoE^{-/-} mice were used for different experiments. The age (weeks) of the mice at each stage is presented across the top of the figure.

3.1 Cell proliferation is detectable in murine AAA models

AAA was first induced in mice by three methods: AngII infusion in ApoE^{-/-} mice or CaCl₂ or PPE application to the aorta in C57BL6/J mice (as described in section 2.1). The aortic tissues were harvested at 28 days post-induction of AAA for the AngII and CaCl₂ models and 14 days post-induction of AAA for the PPE model (per the standard time points of the models). The tissues were then used for immunohistochemical staining for proliferative cells using an antibody raised against the cell proliferation marker Ki67, as described in section 2.2. Histological staining results from mouse aortic samples were analysed for the average proportion of Ki67-positive cells in three randomly selected regions containing proliferative cells (i.e. within the aortic wall), which was reflective of the proliferative activity. Aortae from control animals were compared against aortae from the three different aneurysm models. The abdominal aortic tissue from all three AAA models showed greater Ki67 staining compared to the control aortic tissue (Figure 3.2).

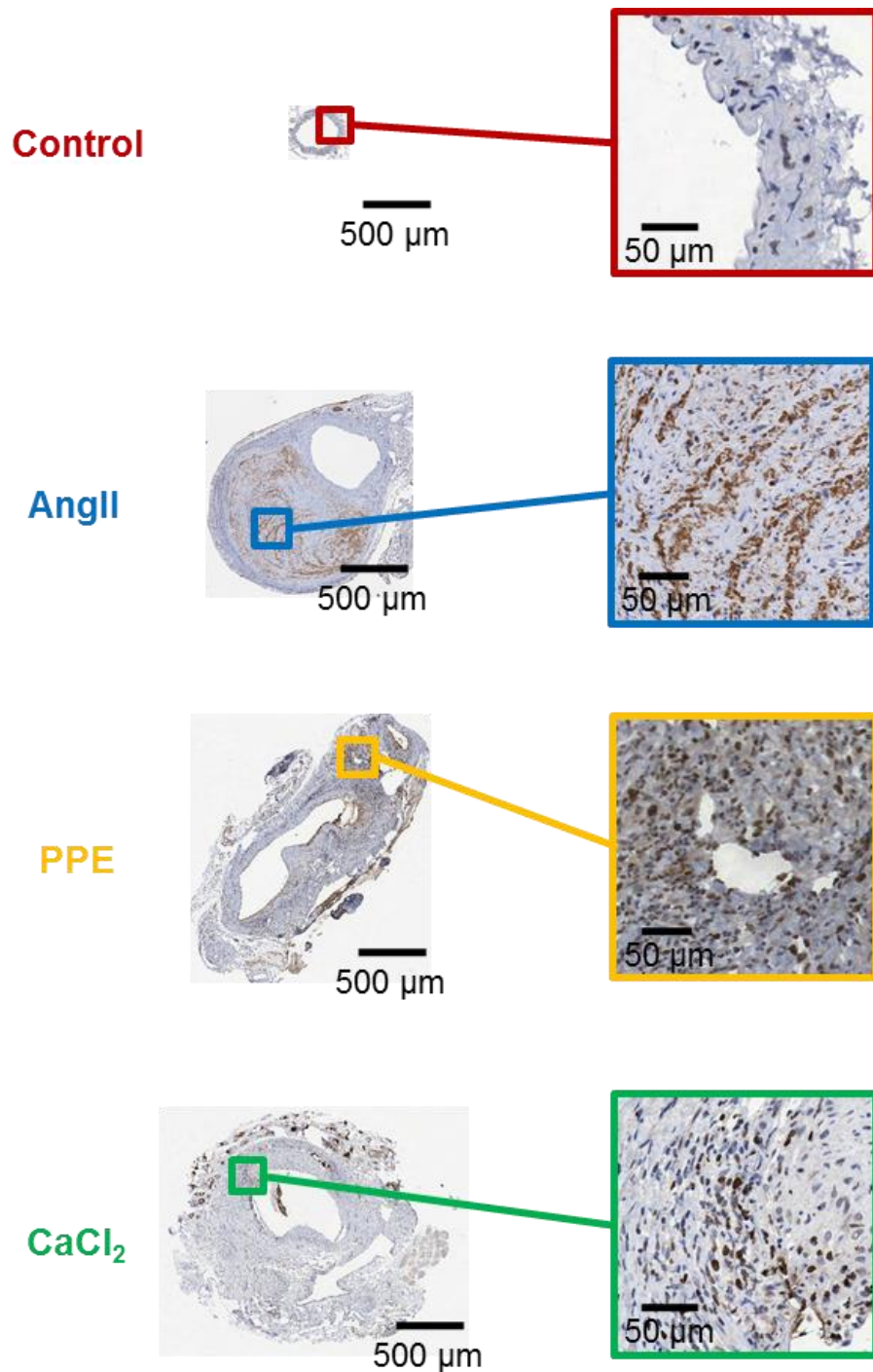


Figure 3.2 Aneurysm tissues show greater Ki67 staining than control aortic tissue. Representative histological images of Ki67-stained aortic tissue from the three AAA models: AngII, angiotensin II (blue); PPE, porcine pancreatic elastase (yellow); and CaCl₂, calcium chloride (green). A single example control aorta is shown in red. Ki67 positivity is indicated by the brown colour, and a blue haematoxylin counterstain has been applied to aid visualisation.

On quantification, the proportions of Ki67-positive nuclei (mean±SEM) for the PPE-, AngII-, and CaCl₂-induced AAA and saline control aortic tissues were 81.4±1.1, 78.5±2.2, 68.7±1.0, and 0.11±0.01, respectively. Tissue from all the AAA models revealed a significant increase in the proportion of Ki67-positive nuclei in the aortic wall compared to that in the saline controls (all $p < 0.001$) (Figure 3.3). The greatest proportions of Ki67-positive nuclei were observed in the PPE and AngII AAA models (both with significantly greater proportions compared to that in the CaCl₂ model, $p < 0.001$), whilst almost no proliferating cells were observed in the control aortic tissue. Overall, these data support the idea that cell proliferation occurs in the three major murine models of AAA. As the Ki67 staining was most pronounced in the AngII and PPE models, these were prioritised for use in the rest of the thesis.

3.2 AngII AAA volume correlates with the proportion of Ki67-positive nuclei

In vivo USS imaging was performed in the AngII AAA animals eventually used for the Ki67 analysis. Evaluation by 3D USS revealed significant increases in aortic diameter and volume following 14-day AngII infusion compared to those in saline-infused controls. The aortic diameters (mean±SEM) were 1.39±0.06 mm and 1.10±0.03 mm ($p < 0.001$) and aortic volumes (mean±SEM) were 15.34±0.80 mm³ and 11.16±0.73 mm³ ($p < 0.01$) in the 14-day AngII AAA model ($n=9$) and saline controls ($n=4$), respectively (Figure 3.4). The proportion of Ki67-positive nuclei showed a positive correlation with aortic volume ($p < 0.05$, Pearson's $r=0.85$) (Figure 3.5). The results of the non-parametric statistical tests for these figures are presented in Appendix B.

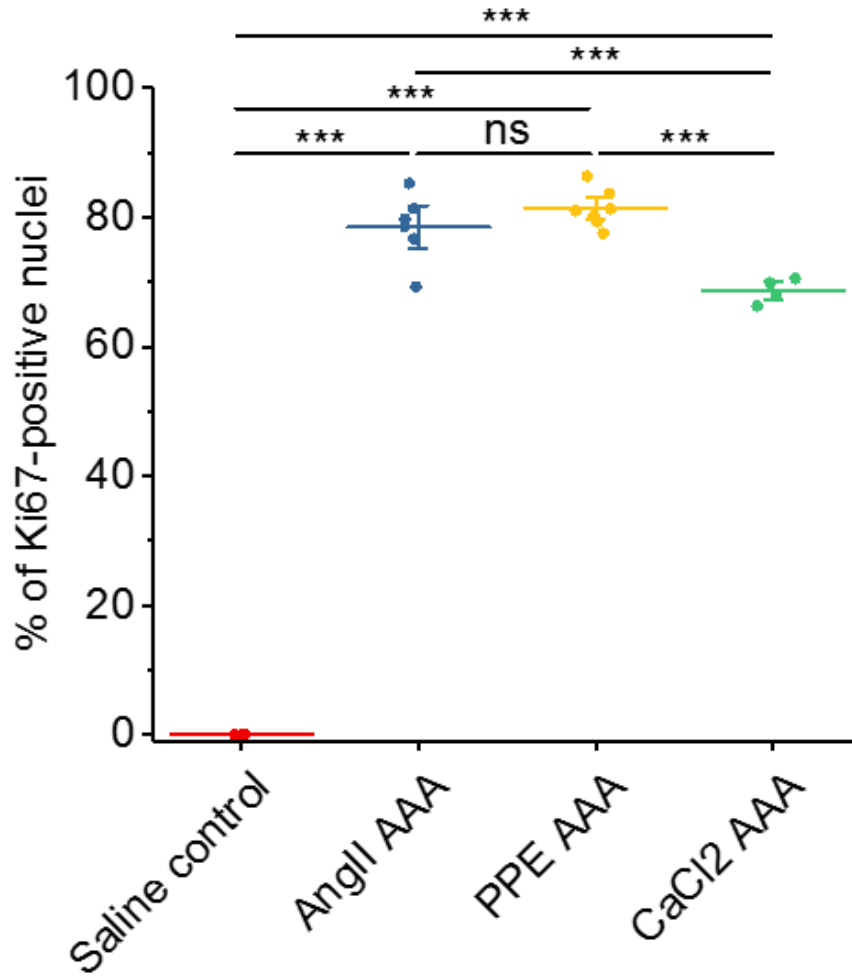
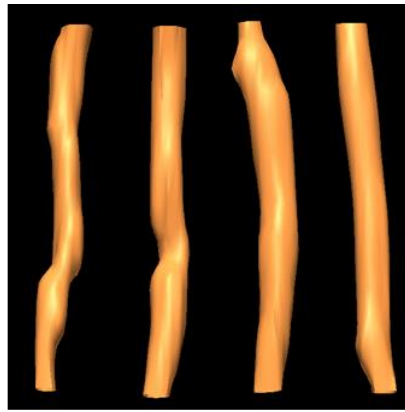
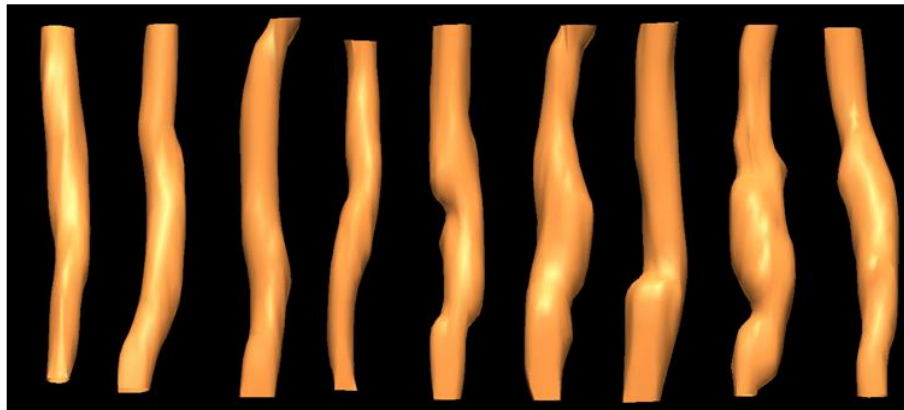


Figure 3.3 PPE and AngII AAA tissue reveal the greatest proportions of Ki67-positive nuclei. Proportion of Ki67-positive nuclei in saline controls ($n=3$) and in the AngII ($n=6$), PPE ($n=7$), and CaCl₂ ($n=4$) AAA models. *** $p<0.001$, ns: not significant on one-way ANOVA with post-hoc Bonferroni-Holm correction.



14-day Saline Control ($n=4$)



14-day AngII AAA ($n=9$)

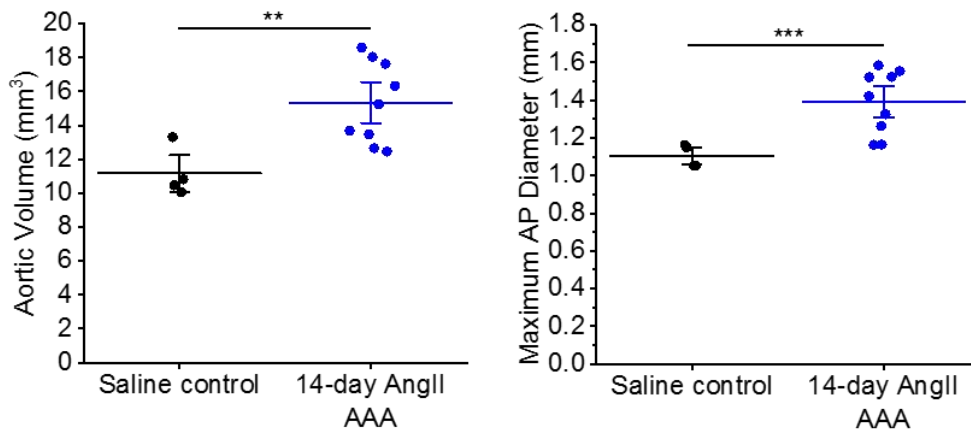


Figure 3.4 Aortic volumes and diameters are larger in the AngII AAA model than in saline controls. Three-dimensional USS aortic reconstructions, volumes, and diameters in 14-day AngII AAA ($n=9$) vs. saline control aortae ($n=4$). ** $p < 0.01$, *** $p < 0.001$ on two-sample t test.

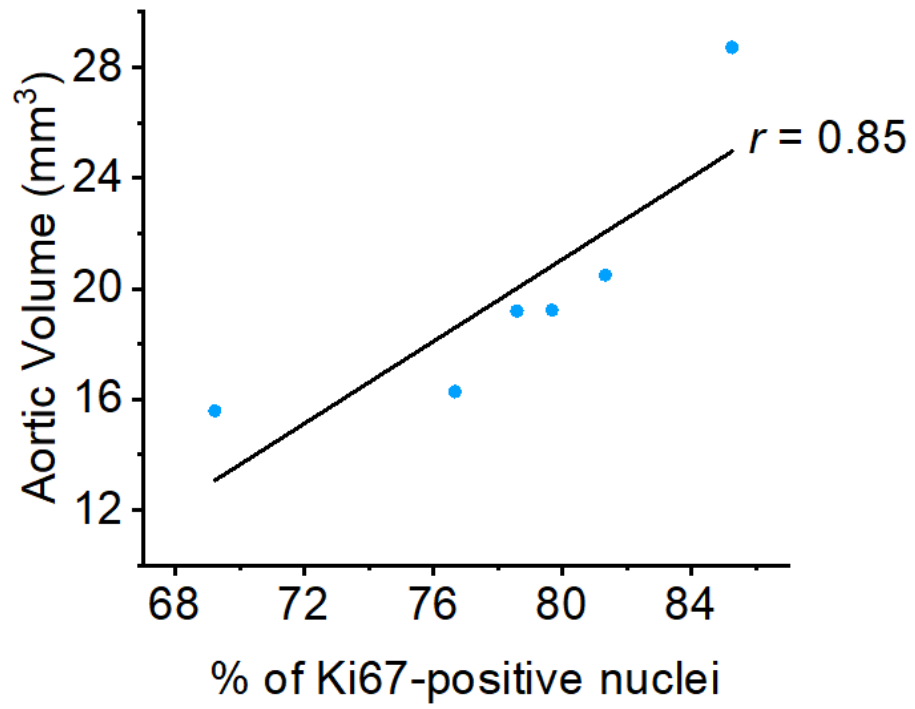


Figure 3.5 AngII AAA volume and the proportion of Ki67-positive nuclei are positively correlated. AngII AAA ($n=6$; blue). Pearson's $r=0.85$, $p<0.05$.

3.3 Cell proliferation can be visualised and quantified using [¹⁸F]FLT PET/CT in the AngII AAA model

Although the PPE and AngII models showed no significant difference in the proportion of Ki67-positive nuclei, the AngII model was chosen to implement for further experiments described in this thesis for two main reasons: (i) the surgery for AngII AAA is much simpler than that for PPE AAA and the experiments were performed at the University of Hull, where only basic surgical facilities were available; and (ii) AngII AAA consistently develops in the suprarenal region of the abdominal aorta, whereas PPE AAA develops in the infra-renal portion (Daugherty and Cassis, 2004). As [¹⁸F]-based PET radiotracers are excreted via the bladder, the signal in AngII AAA was anticipated to be further away from the signal due to bladder excretion than the signal in PPE AAA would be; hence, the AngII AAA was predicted to be easier to visualise and analyse.

3.3.1 Animal survival decreased over the course of the experiment

Twenty-two male ApoE^{-/-} mice were enrolled in the saline vs. AngII PET/CT experiment performed at the University of Hull. Fourteen mice died at various time points during the experiment, as outlined in Figure 3.6. Images were only excluded from the subsequent SUV analysis in cases wherein the radiotracer injection was suboptimal, based on (i) judgment by the individual administering the injection and (ii) a lack of radiotracer signal in the inferior vena cava within the first 15 seconds of the scan. Meanwhile, Figure 3.7 presents Kaplan–Meier curves illustrating the proportion of surviving animals over the course of the experiment. All mice were harvested by terminal anaesthesia following the 28-day PET scan. There was a greater proportion of surviving AngII AAA mice than surviving saline controls (Kaplan–Meier survival log rank $p < 0.01$); all mice were then sacrificed in week 18.

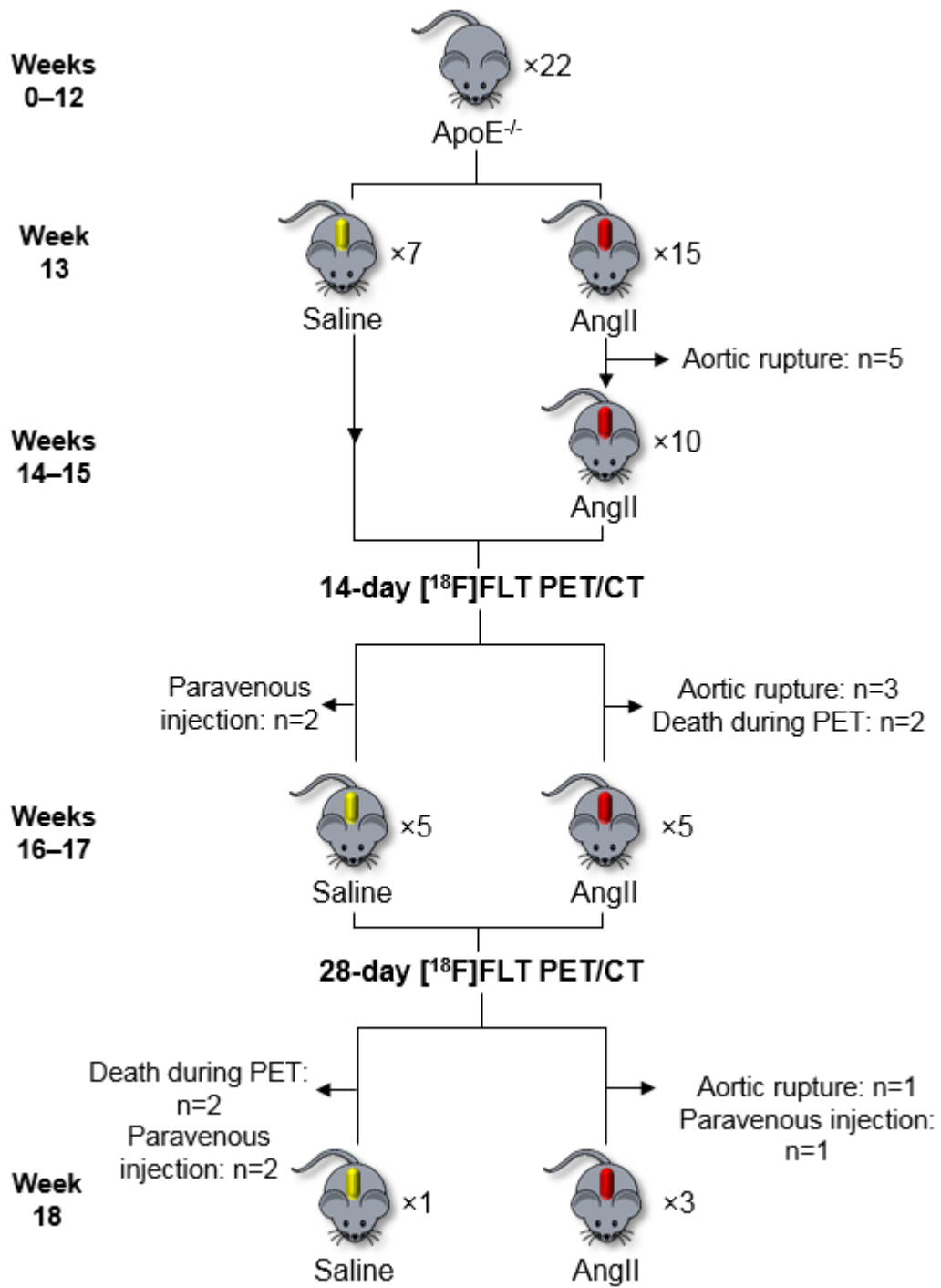


Figure 3.6 Number of surviving animals decreased from 13 to 18 weeks of age. Flow of surviving animals that produced images for analysis through the experiment.

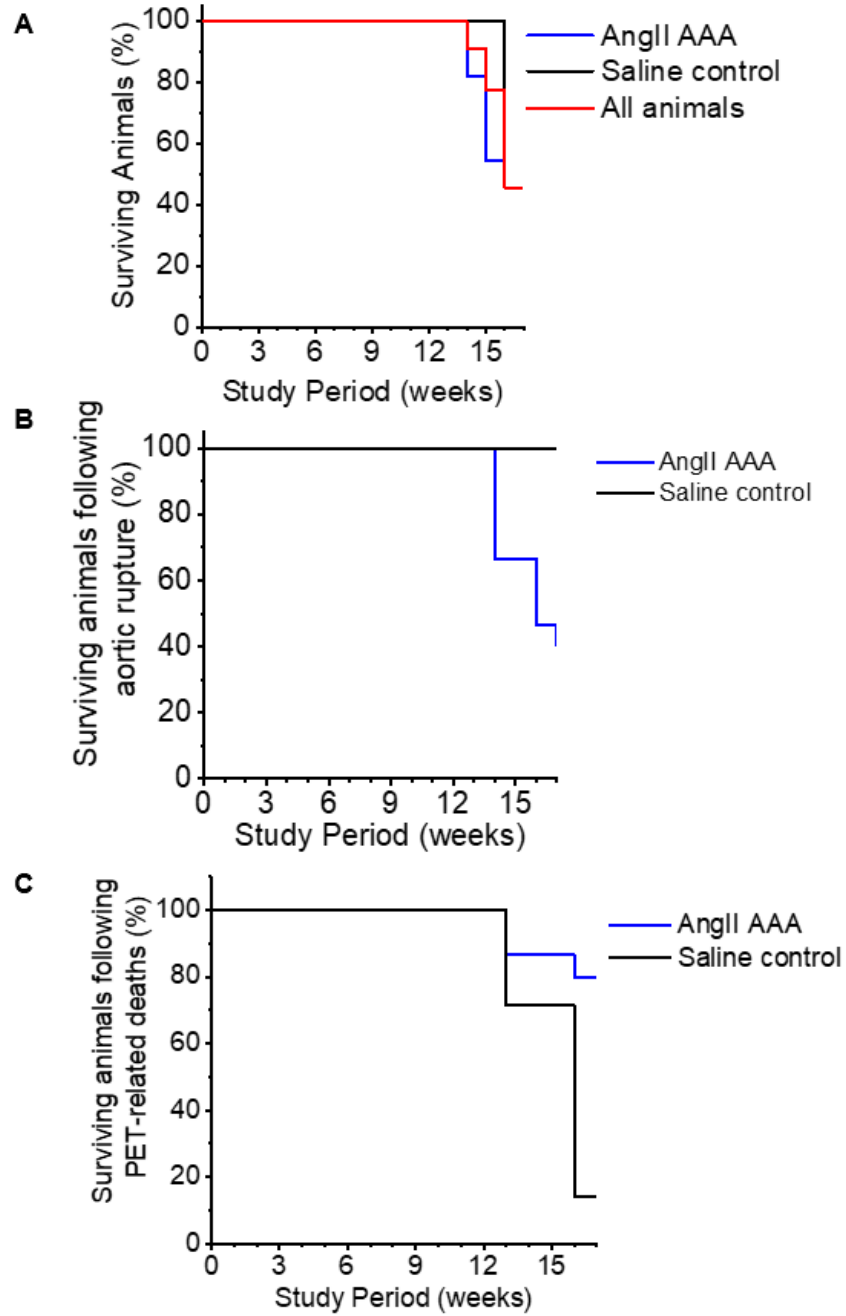


Figure 3.7 Number of surviving animals decreased from 13 to 18 weeks of the study period. Kaplan–Meier survival curves illustrate the proportions of surviving animals due to (A) all causes of death, (B) aortic rupture, and (C) PET-related deaths. All mice were sacrificed after the final PET/CT scan in week 18.

3.3.2 [¹⁸F]FDG uptake differs between saline controls and AngII AAA mice

[¹⁸F]FDG is the most well-established radiotracer used in the clinic, particularly in the field of oncology, and is normally the first radiotracer to be considered for diagnostic imaging. Therefore, [¹⁸F]FDG was used for the initial experiment, the first preclinical PET study in collaboration with and performed at the University of Hull PET Imaging Centre. Starting with [¹⁸F]FDG allowed us to become familiar with and resolve any difficulties associated with the imaging protocol without any issues being attributed to [¹⁸F]FLT, a more novel radiotracer.

For this initial experiment, ApoE^{-/-} mice were divided into two treatment groups: saline or AngII infusions for 28 days (saline controls and AngII AAA mice, respectively). Dynamic PET/CT was performed on day 28 following implantation of the osmotic mini-pumps in the ApoE^{-/-} mice. Radiotracer uptake was assessed in the IVC, myocardium, paraspinal region, and abdominal aorta. [¹⁸F]FDG uptake in the IVC was visualised within the first 15 s of each scan, reflecting the bolus radiotracer injection. This early signal confirmed successful intravenous radiotracer delivery and uptake after administration (Figure 3.8).

[¹⁸F]FDG uptake was visualised in the myocardium of all mice, reflecting the typical basal myocardial energetics and confirming the radiotracer's expected biodistribution. The myocardial [¹⁸F]FDG signal in the AngII AAA model was noticeably greater (Figure 3.9). Three-dimensional isocontour ROIs were manually drawn on the acquired images to extract SUV_{max} information over time, revealing the following values for myocardial ROIs (mean±SEM SUV_{max} 80–90 min post-radiotracer injection, consistent with all other SUV calculations): 1.91±0.00 (healthy controls, *n*=3); 5.06±0.20 (28-day AngII AAA, *n*=4) vs. 1.92±0.02 (28-day saline control, *n*=6) (two-sample *t* test, *p*<0.001) (Figure 3.10). Myocardial uptake of [¹⁸F]FDG in the 28-day AngII AAA model was greater than that in 28-day saline controls, as AngII infusion is also a model system for heart failure (Figure 3.10).

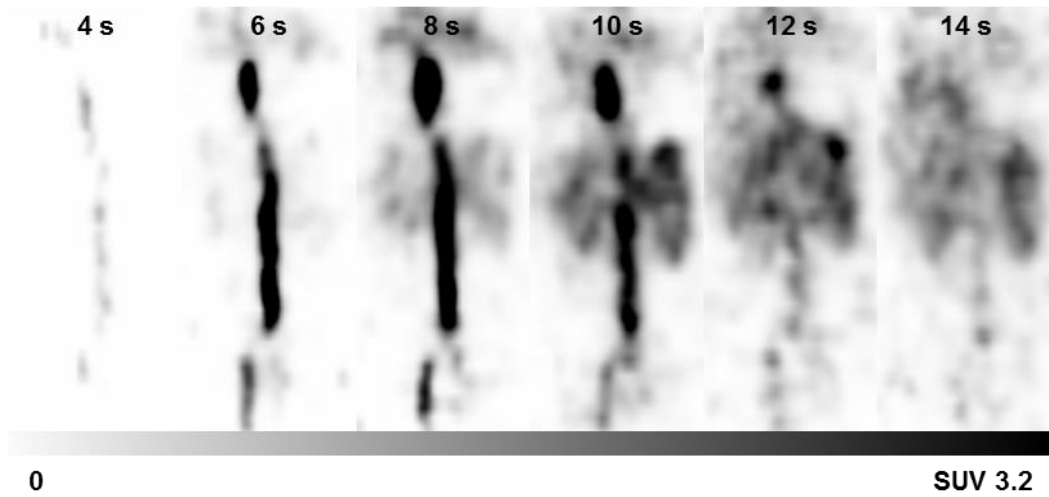


Figure 3.8 $[^{18}\text{F}]$ FDG uptake was visualised in the IVC at the beginning of each scan. Representative coronal-view PET images of dynamic IVC uptake of $[^{18}\text{F}]$ FDG from 4 to 14 s post-radiotracer injection. Colour scale bar indicates SUV thresholding to aid visualisation.

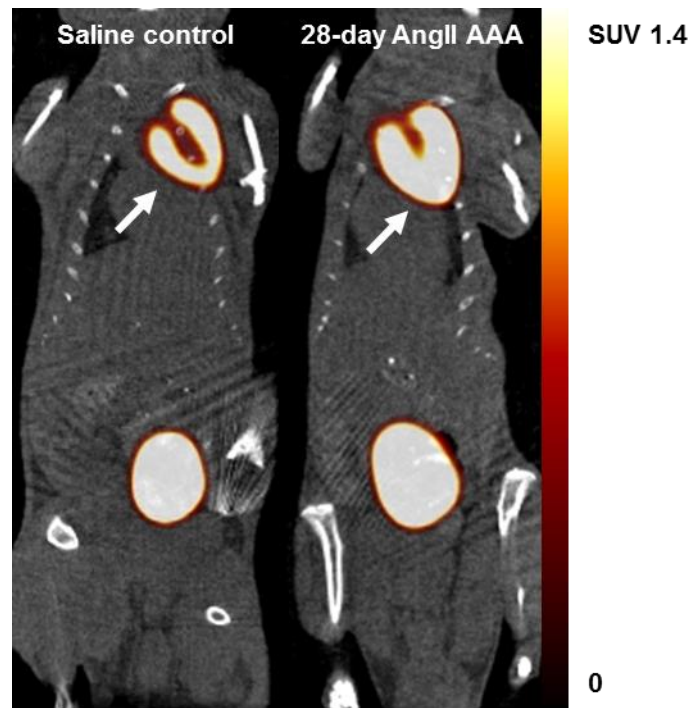


Figure 3.9 [^{18}F]FDG uptake was visualised in the myocardium of all mice. Representative coronal-view PET/CT image of static myocardial uptake 80–90 min post-radiotracer injection. Arrows indicate the myocardium. Colour scale bar indicates SUV thresholding to aid visualisation.

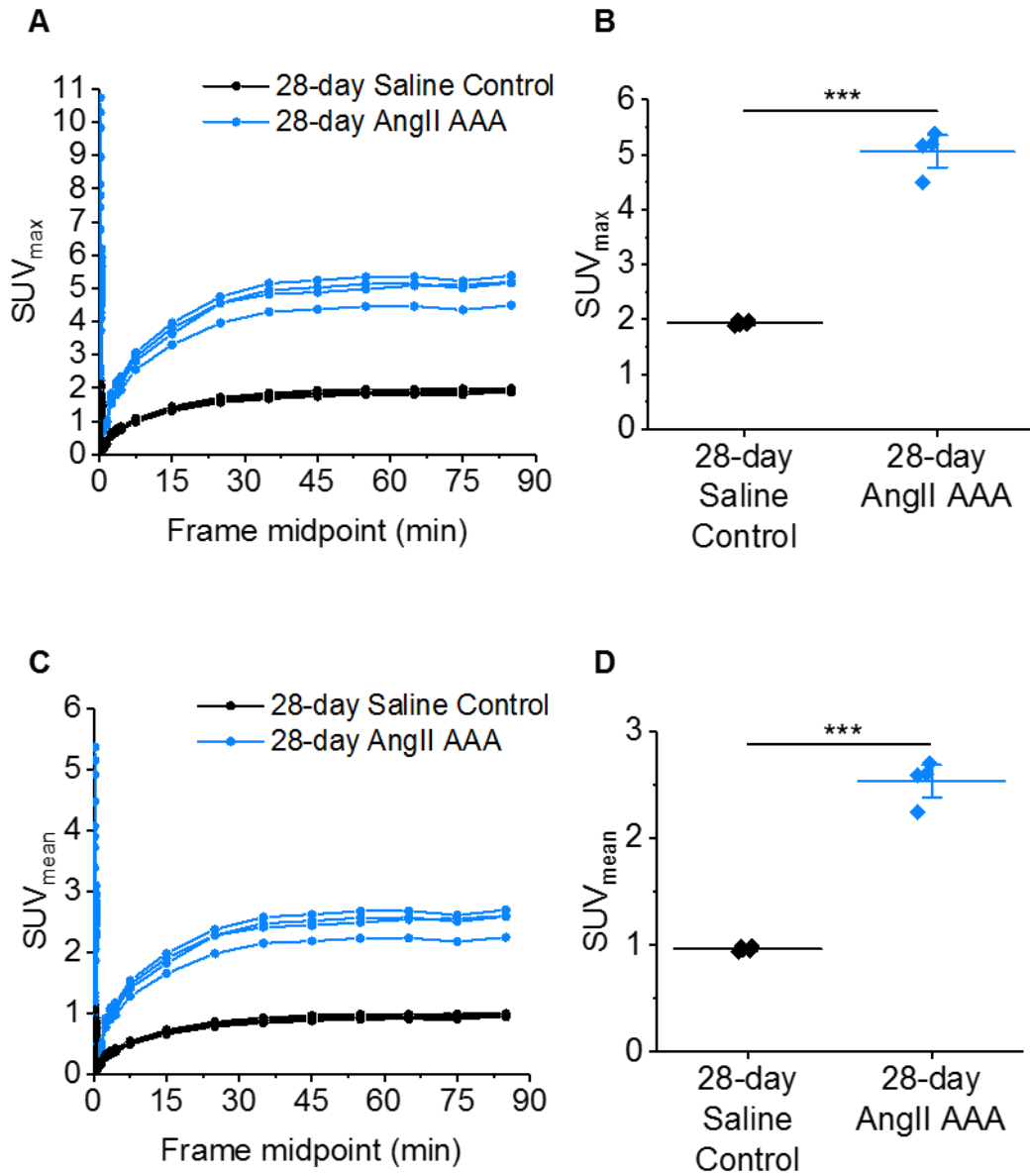


Figure 3.10 $[^{18}\text{F}]\text{FDG}$ uptake in the myocardium increased from 0 to 90 min post- $[^{18}\text{F}]\text{FDG}$ injection. (A) Time-activity curves of SUV_{max} and (B) absolute values of SUV_{max} . (C) Time-activity curves of SUV_{mean} and (D) absolute values of SUV_{mean} . SUV_{max} and SUV_{mean} in (B) and (D) represent 28-day $[^{18}\text{F}]\text{FDG}$ uptake in myocardial ROIs 80–90 min post-radiotracer injection of $[^{18}\text{F}]\text{FDG}$ in 28-day saline controls ($n=6$) and the 28-day AngII AAA model ($n=4$).

Uptake of [¹⁸F]FDG was also visualised in the paraspinal region in several mice. This was likely in response to standard animal handling practices and resultant stress induced in the animals (Fueger et al., 2006) (Figure 3.11).

[¹⁸F]FDG uptake in the abdominal aortic region in the 28-day AngII AAA model was variable, with only two mice showing clear uptake in AAA (Figure 3.12). The TACs indicated that the radiotracer distributed to the abdominal aortic region at later time points of the scan in the mice that exhibited AAA uptake (Figure 3.13). Thus, 3D isocontour ROIs were drawn on images from the final time frame, which revealed the following values (mean±SEM 80–90 min post-radiotracer injection): SUV_{mean}, 28-day saline controls (*n*=6) 0.07±0.004 vs. 28-day AngII AAA (*n*=4) 0.17±0.06 (two-sample *t* test, *p*=0.06); SUV_{max}, 28-day saline controls (*n*=6) 0.09±0.01 vs. 28-day AngII AAA (*n*=4) 0.24±0.08 (two-sample *t* test, *p*<0.05). A significant difference was noted in [¹⁸F]FDG abdominal aortic SUV_{max} between saline controls and 28-day AngII AAA mice (Figure 3.13).

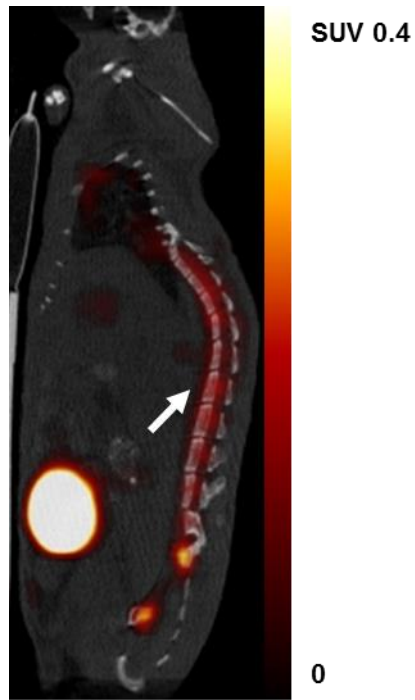


Figure 3.11 [^{18}F]FDG uptake was visualised in the paraspinal region of most mice. Representative sagittal-view PET/CT image of static paraspinal uptake 80–90 min post-radiotracer injection. Arrow indicates the paraspinal region. Colour scale bar indicates SUV thresholding to aid visualisation.

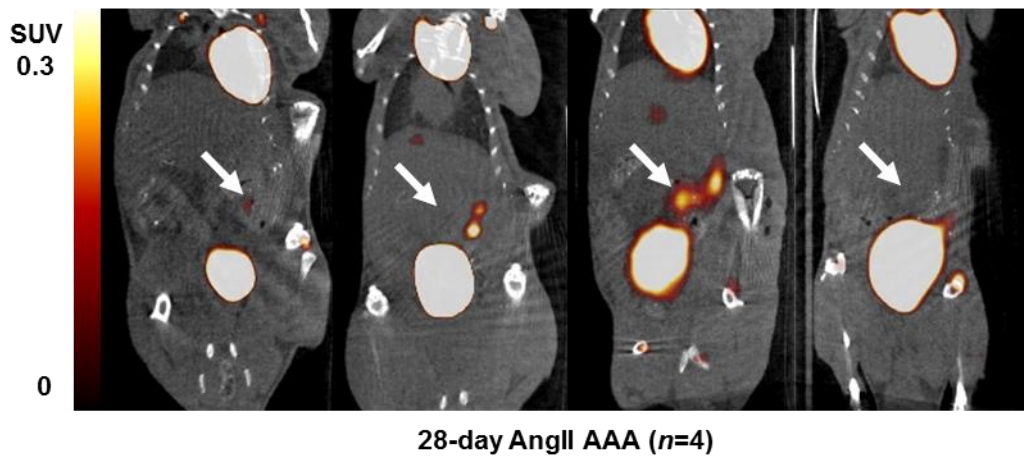
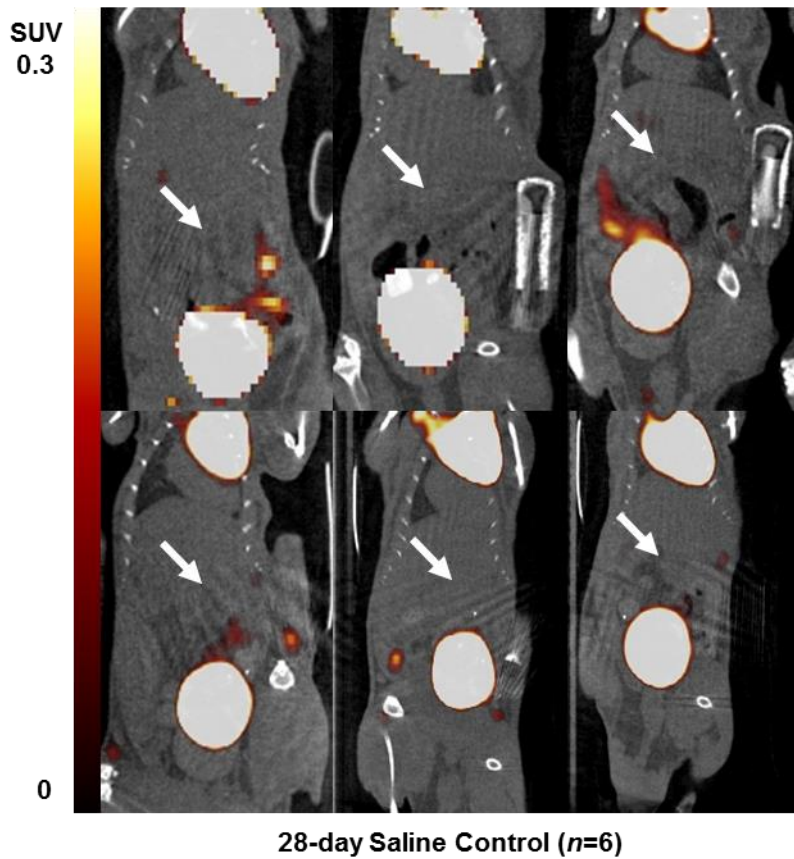


Figure 3.12 [^{18}F]FDG uptake in the abdominal aorta was greater but variable in the 28-day AngII AAA model than in 28-day saline controls. Coronal-view PET/CT images of static 28-day abdominal aortic uptake of [^{18}F]FDG 80–90 min post-radiotracer injection in all animals. Arrows indicate the abdominal aorta. Colour scale bars indicate SUV thresholding to aid visualisation.

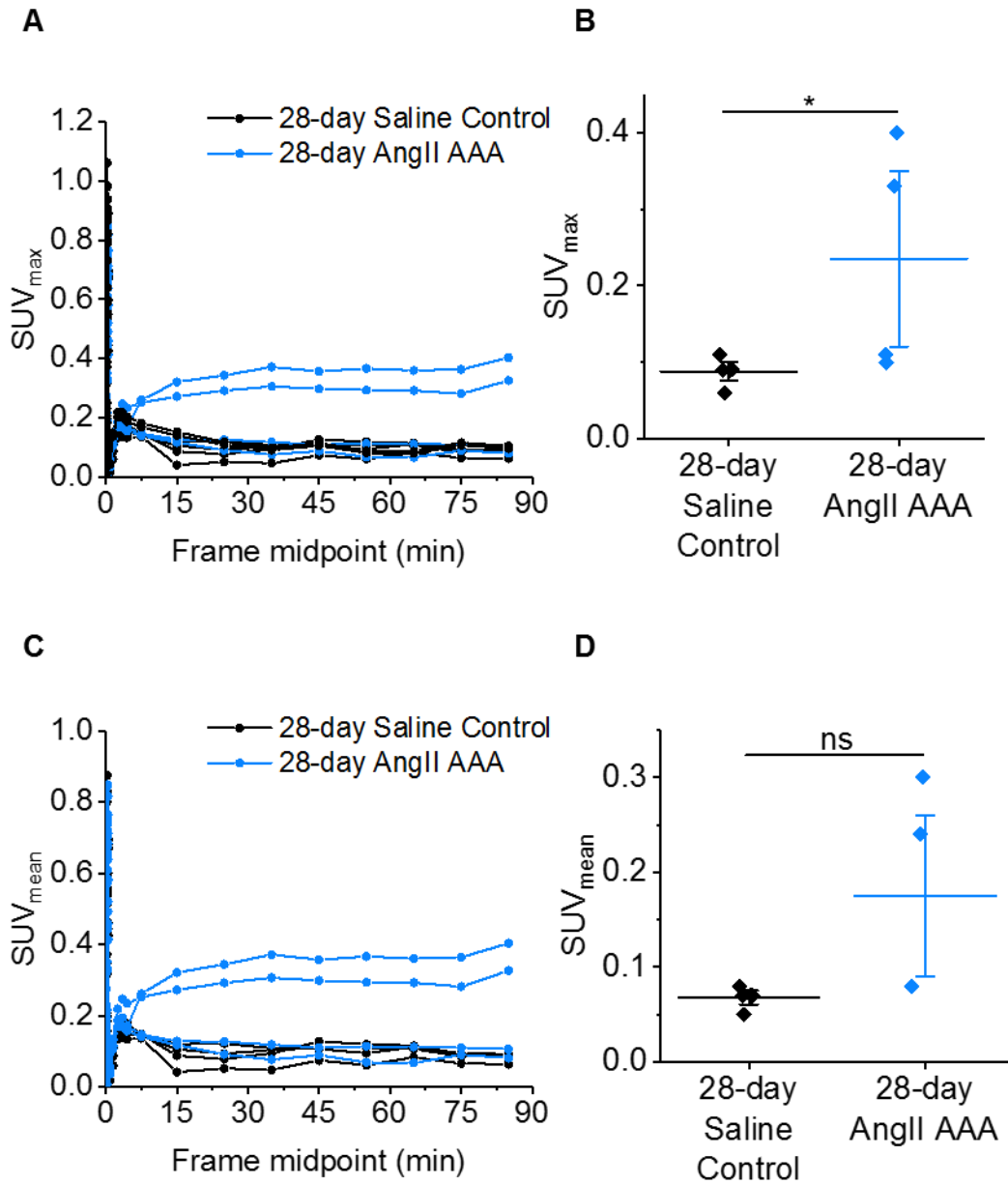


Figure 3.13 [¹⁸F]FDG uptake in the abdominal aorta was variable in the 28-day AngII AAA model than in saline controls. (A) Time-activity curves of SUV_{max} and (B) absolute values of SUV_{max}. (C) Time-activity curves of SUV_{mean} and (D) absolute values of SUV_{mean}. SUV_{max} and SUV_{mean} in (B) and (D) represent 28-day [¹⁸F]FDG uptake in abdominal aortic ROIs 80–90 min post-radiotracer injection in 28-day saline controls (*n*=6) and the 28-day AngII AAA model (*n*=4).

3.3.3 [¹⁸F]FLT localises to expected regions of cell proliferation in control mice

To establish reference data, healthy control mice were used to assess aortic [¹⁸F]FLT uptake and validate the biodistribution of [¹⁸F]FLT for the overall study. First, 90-min dynamic PET/CT revealed [¹⁸F]FLT uptake in the IVC within the first 15 s of each scan, reflecting the bolus radiotracer injection. This early signal confirmed successful intravenous radiotracer delivery and uptake after administration (Figure 3.14).

[¹⁸F]FLT uptake was then visualised in the spleen of all mice, reflecting the role of the spleen as a reservoir of proliferative cells and confirming the radiotracer's expected biodistribution (Figure 3.15). Three-dimensional isocontour ROIs were manually drawn on the acquired images to extract SUV_{max} information over time, revealing a mean±SEM SUV_{max} 80–90 min post-radiotracer injection of 0.47±0.03 (*n*=3) in the spleen (Figure 3.16). These results were further confirmed by greater *ex vivo* uptake of [¹⁸F]FLT uptake in the spleen relative to the heart by gamma counting (mean±SEM: 186.99±9.99 vs. 86.82±17.18 %ID/g, *p*<0.001), whilst the aorta exhibited comparable uptake to the heart (mean±SEM: 76.23±24.98 vs. 86.82±17.18 %ID/g, *p*=0.69), as expected (Figure 3.17). Hepatic uptake of [¹⁸F]FLT was noted in some animals, but this was less consistently observed across all the animals than splenic uptake. Moreover, the low signal in the bone marrow was difficult to detect as a distinct region that could be easily delineated for further ROI analyses without significantly increasing the SUV threshold on the image visualisation software (AMIDE), which resulted in saturated signal across the image and reduced visibility of other ROIs. The heart and spleen were therefore used as negative and positive control organs, respectively, for all experiments involving [¹⁸F]FLT thereafter.

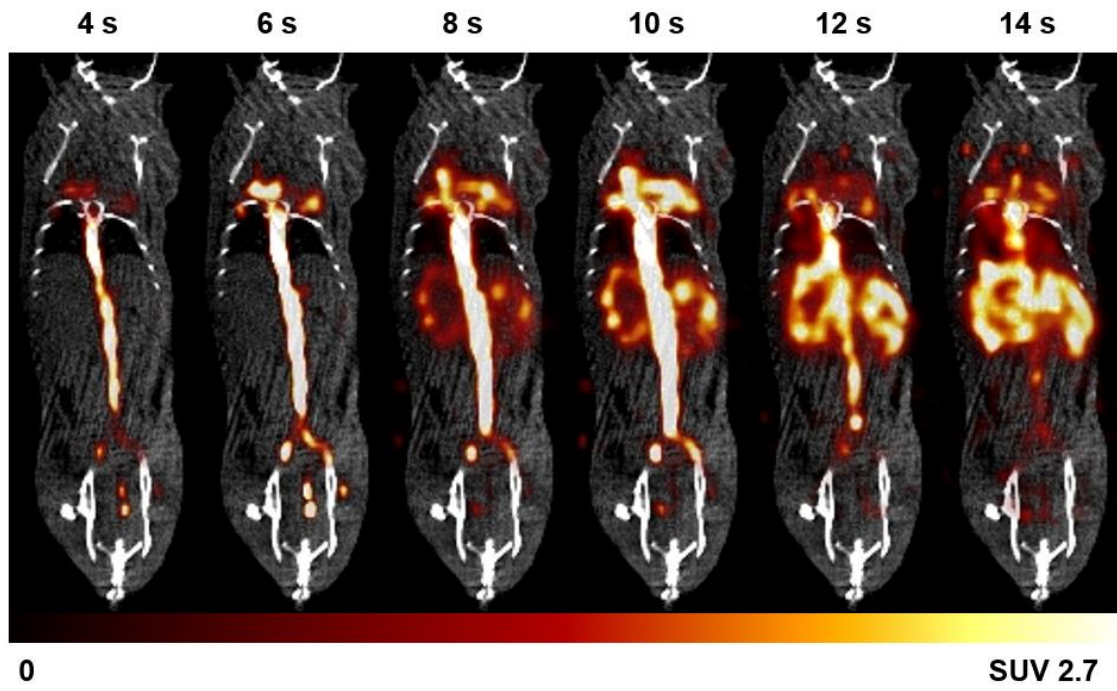


Figure 3.14 $[^{18}\text{F}]\text{FLT}$ uptake was visualised in the IVC at the beginning of each PET scan. Representative coronal-view PET images of dynamic IVC uptake of $[^{18}\text{F}]\text{FLT}$ from 4 to 14 s post-radiotracer injection. Colour scale bar indicates SUV thresholding to aid visualisation.

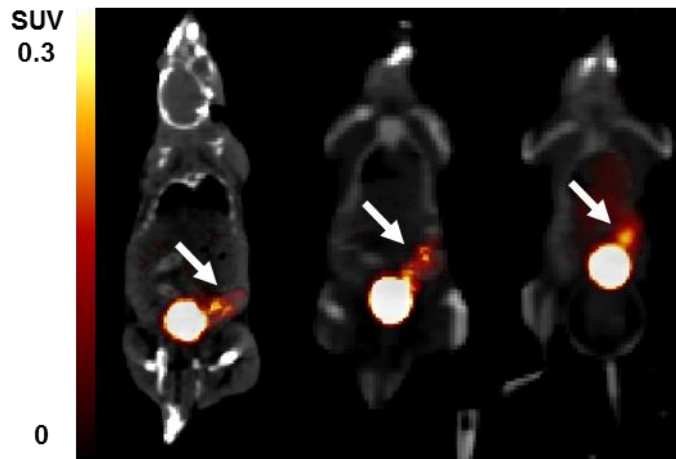


Figure 3.15 $[^{18}\text{F}]\text{FLT}$ uptake was visualised in the spleen of all healthy controls. Coronal-view PET/CT images of static splenic uptake of $[^{18}\text{F}]\text{FLT}$ 80–90 min post-radiotracer injection. Arrows indicate the spleen. Colour scale bar indicates SUV thresholding to aid visualisation.

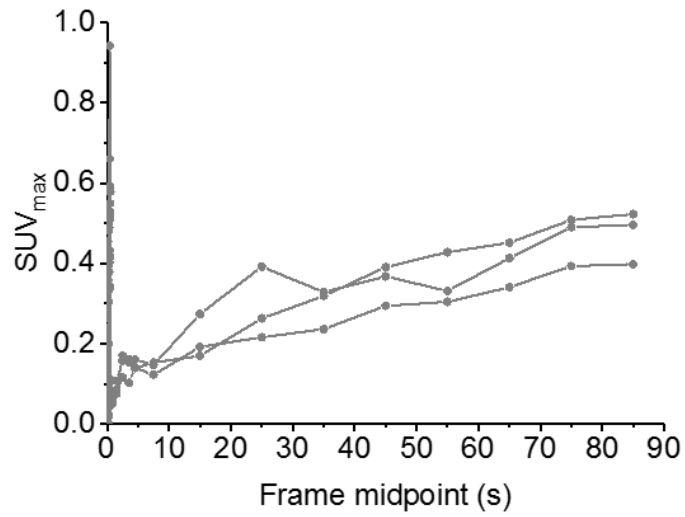


Figure 3.16 [¹⁸F]FLT uptake in the spleen increased from 0 to 90 min post-[¹⁸F]FLT injection. Time-activity curves representing splenic uptake of [¹⁸F]FLT in healthy control mice (*n*=3).

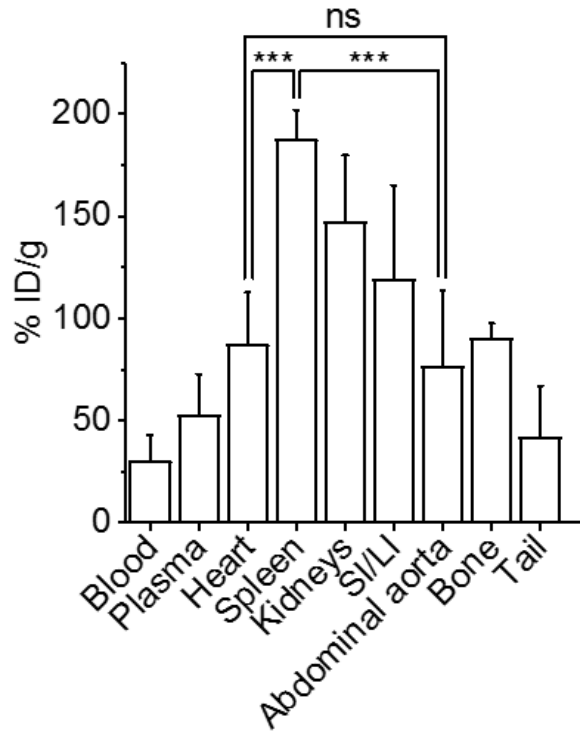


Figure 3.17 *Ex vivo* [¹⁸F]FLT uptake in the spleen was greater than that in the heart and abdominal aorta in healthy control mice. Decay-corrected *ex vivo* [¹⁸F]FLT counts per mass units (*n*=3). *** *p*<0.001 on one-way ANOVA with post-hoc Bonferroni–Holm correction.

3.3.4 [¹⁸F]FLT uptake is observed in regions of cell proliferation in the AngII model of AAA

For the AngII AAA experiments, dynamic PET/CT was performed on days 14 and 28 following implantation of the osmotic mini-pumps. [¹⁸F]FLT uptake in the IVC was visualised within the first 15 s of each scan, reflecting the bolus radiotracer injection. Observation of this peak was facilitated by the short 2-s timeframes, which effectively revealed the early fluctuations in activity. The appearance of this signal at such an early time point of the scan confirmed successful intravenous radiotracer delivery and uptake after administration in the saline controls and AngII AAA mice (Figure 3.18).

[¹⁸F]FLT uptake was consistently visualised in the spleen of all mice, as expected based on the baseline [¹⁸F]FLT experiment in healthy control mice (Figure 3.19). Three-dimensional isocontour ROIs were manually drawn on the acquired images to extract SUV_{max} information over time, revealing the following values for splenic ROIs (mean±SEM SUV_{max} 80–90 min post-radiotracer injection): 0.52±0.01 (14-day AngII AAA, *n*=5) vs. 0.52±0.00 (14-day saline control, *n*=5) (two-sample *t* test, *p*=0.48); 0.37±0.07 (28-day AngII AAA, *n*=3) vs. 0.52 (28-day saline control, *n*=1) (Figure 3.20). Splenic uptake confirmed that [¹⁸F]FLT distributed to expected regions, as the spleen exhibits high basal proliferative activity. Interestingly, splenic uptake in the 28-day AngII AAA model was variable.

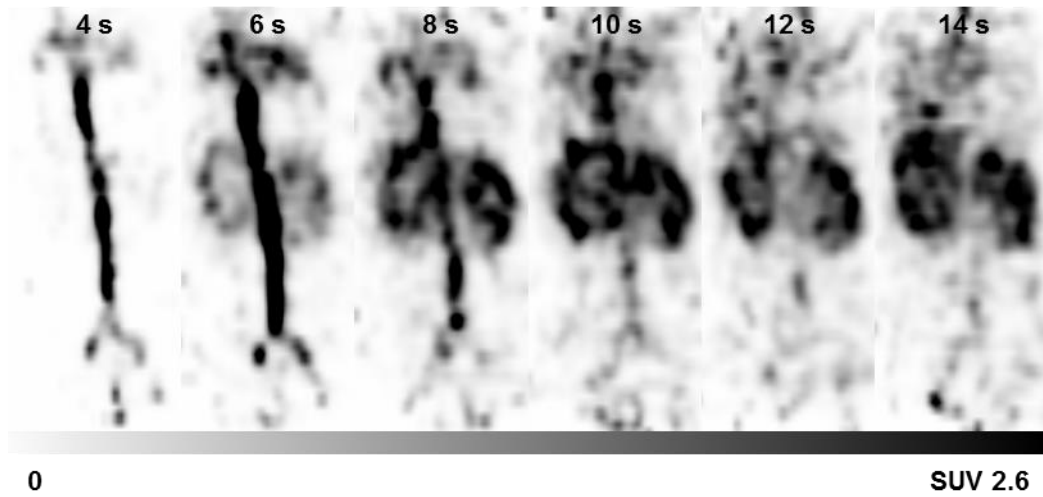


Figure 3.18 $[^{18}\text{F}]\text{FLT}$ uptake was visualised in the IVC at the beginning of each PET scan. Representative coronal-view PET images of dynamic IVC uptake of $[^{18}\text{F}]\text{FLT}$ from 4 to 14 s post-radiotracer injection. Colour scale bar indicates SUV thresholding to aid visualisation.



Figure 3.19 [^{18}F]FLT uptake was visualised in the spleen of all mice. Representative coronal-view PET/CT image of static splenic uptake of [^{18}F]FLT 80–90 min post-radiotracer injection. Arrow indicates the spleen. Colour scale bar indicates SUV thresholding to aid visualisation.

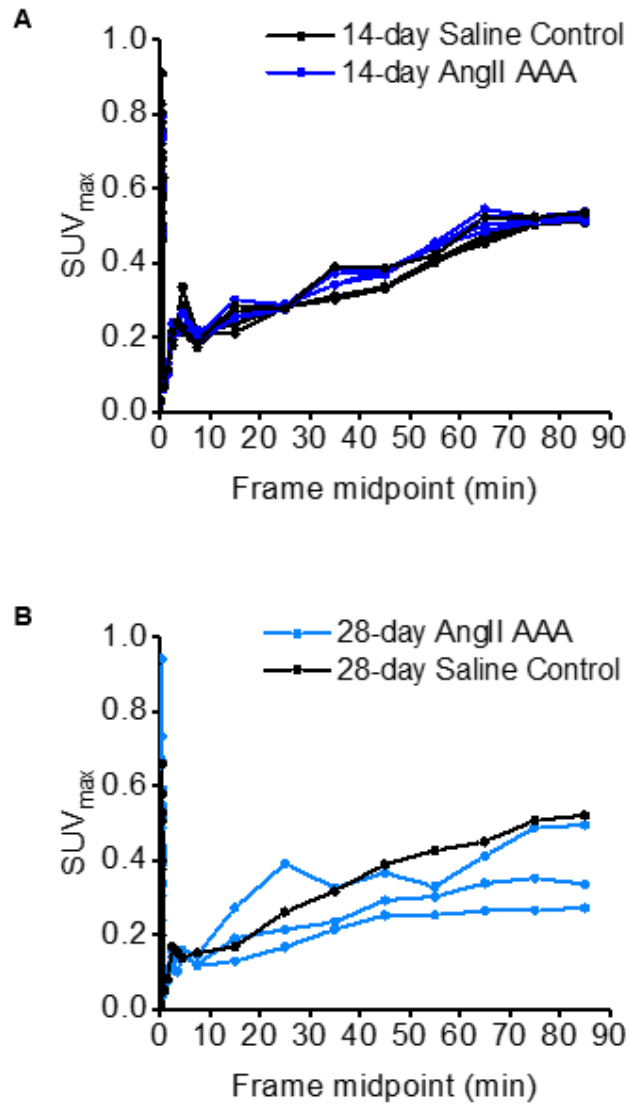


Figure 3.20 $[^{18}\text{F}]\text{FLT}$ uptake in the spleen increased from 0 to 90 min post- $[^{18}\text{F}]\text{FLT}$ injection. Time-activity curves representing splenic uptake of $[^{18}\text{F}]\text{FLT}$ in (A) 14-day saline controls ($n=5$) and the 14-day AngII AAA model ($n=5$) and (B) 28-day saline control ($n=1$) and the 28-day AngII AAA model ($n=3$).

3.3.5 [¹⁸F]FLT uptake is observed in AngII AAA

The dynamic PET data revealed that [¹⁸F]FLT distributed to the abdominal aortic region in the AngII AAA model in the later time points of the scan (Figure 3.21). Static PET/CT images revealed that [¹⁸F]FLT uptake in the 14-day AngII AAA model in the final timeframe (80–90 min post-injection of [¹⁸F]FLT) was consistently enhanced compared to that in the saline controls (Figure 3.22).

Three-dimensional isocontour ROIs were manually drawn between the renal arteries and diaphragm to incorporate the suprarenal abdominal aortic area in the final timeframe using AMIDE v1.0.4 software. The abdominal aortic ROI was constructed between the kidneys and anterior to the anterior border of the vertebral column based on the CT images, including the most prominent PET signal in the 80–90-min timeframe. Efforts were made to avoid including the edges of the region of [¹⁸F]FLT uptake to minimise partial volume effects due to signal spill-over from adjacent organs, notably the bladder. For saline controls, the aortic ROI was constructed between the kidneys, superior to the bladder, and anterior to the anterior border of the vertebral column based on the CT images; these ROIs had dimensions of 1.08 mm³ and contained 15 voxels (Figure 3.23).

Incorporating mouse weights and injected radioactivity doses, output statistics revealed the SUV_{max} and SUV_{mean} across all timeframes. These values were used to generate TACs for ROIs in the abdominal aorta. The late uptake of [¹⁸F]FLT in the 14-day AngII AAA model was also reflected in these corresponding TACs (Figure 3.24). As the [¹⁸F]FLT signal was the most prominent in the final timeframe, the SUVs were extracted from the final timeframe for analysis. The following values were obtained from the data of the 14-day scan (mean±SEM 80–90 min post-radiotracer injection): SUV_{max}, 0.010±0.002 (14-day saline controls, *n*=5) vs. 0.33±0.02 (14-day AngII AAA, *n*=5) (two-sample *t* test, *p*<0.001); SUV_{mean}, 0.004±0.002 (14-day saline controls, *n*=5) vs. 0.25±0.02 (14-day AngII AAA, *n*=5) (two-sample *t* test, *p*<0.001) (Figure 3.24). The Shapiro–Wilk test revealed that the data of the 14-day saline control group were not normally distributed. The results of the non-parametric statistical test are presented in Appendix B.

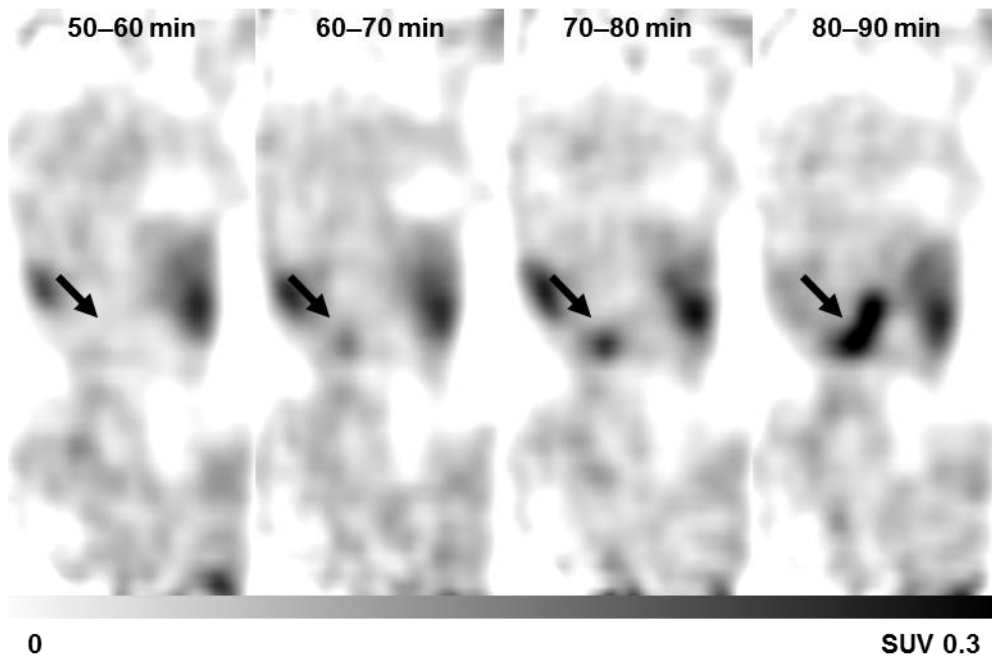


Figure 3.21 [^{18}F]FLT uptake in the abdominal aorta was visualised late in the 90-min scan. Representative coronal-view PET images of dynamic AAA uptake of [^{18}F]FLT from 50 to 90 min post-radiotracer injection. Colour scale bar indicates SUV thresholding to aid visualisation. Arrows indicate the AAA.

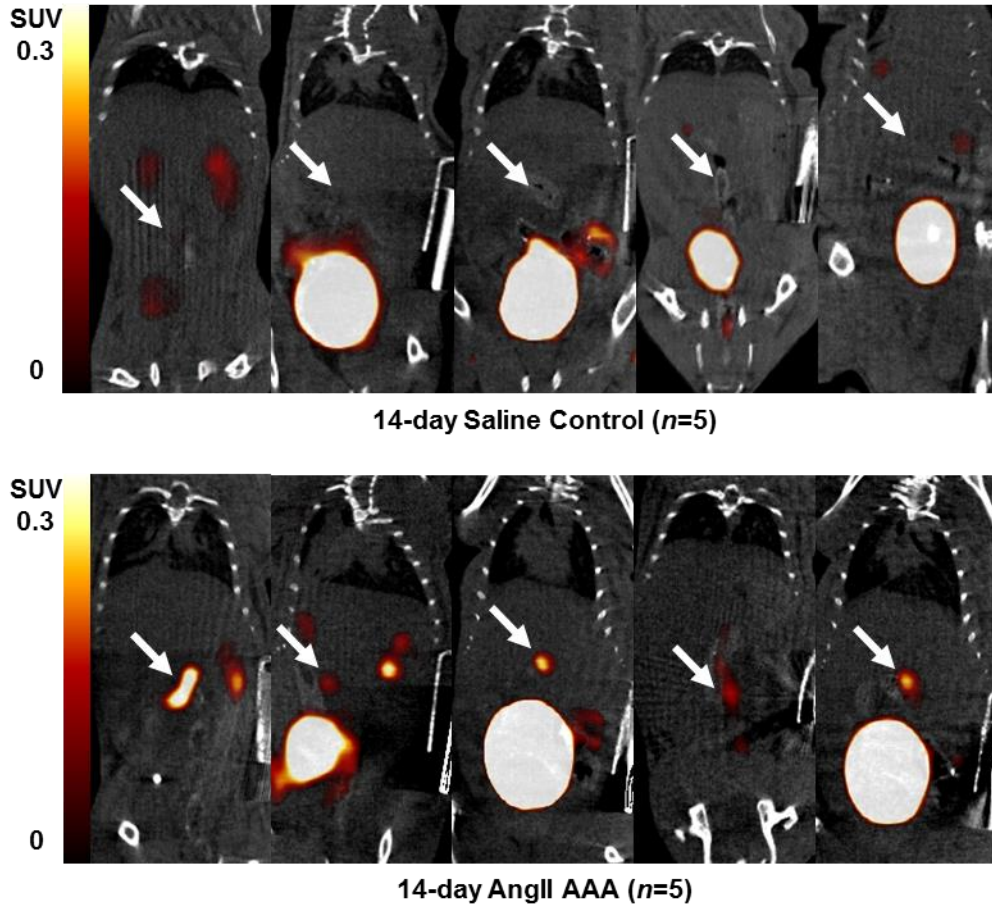


Figure 3.22 [^{18}F]FLT uptake in the abdominal aorta was greater in the 14-day AngII AAA model than in saline controls. Coronal-view PET/CT images of static 14-day abdominal aortic uptake of [^{18}F]FLT 80–90 min post-radiotracer injection in 14-day saline controls ($n=5$) and the 14-day AngII AAA model ($n=5$). Arrows indicate the abdominal aorta. Colour scale bars indicate SUV thresholding to aid visualisation.

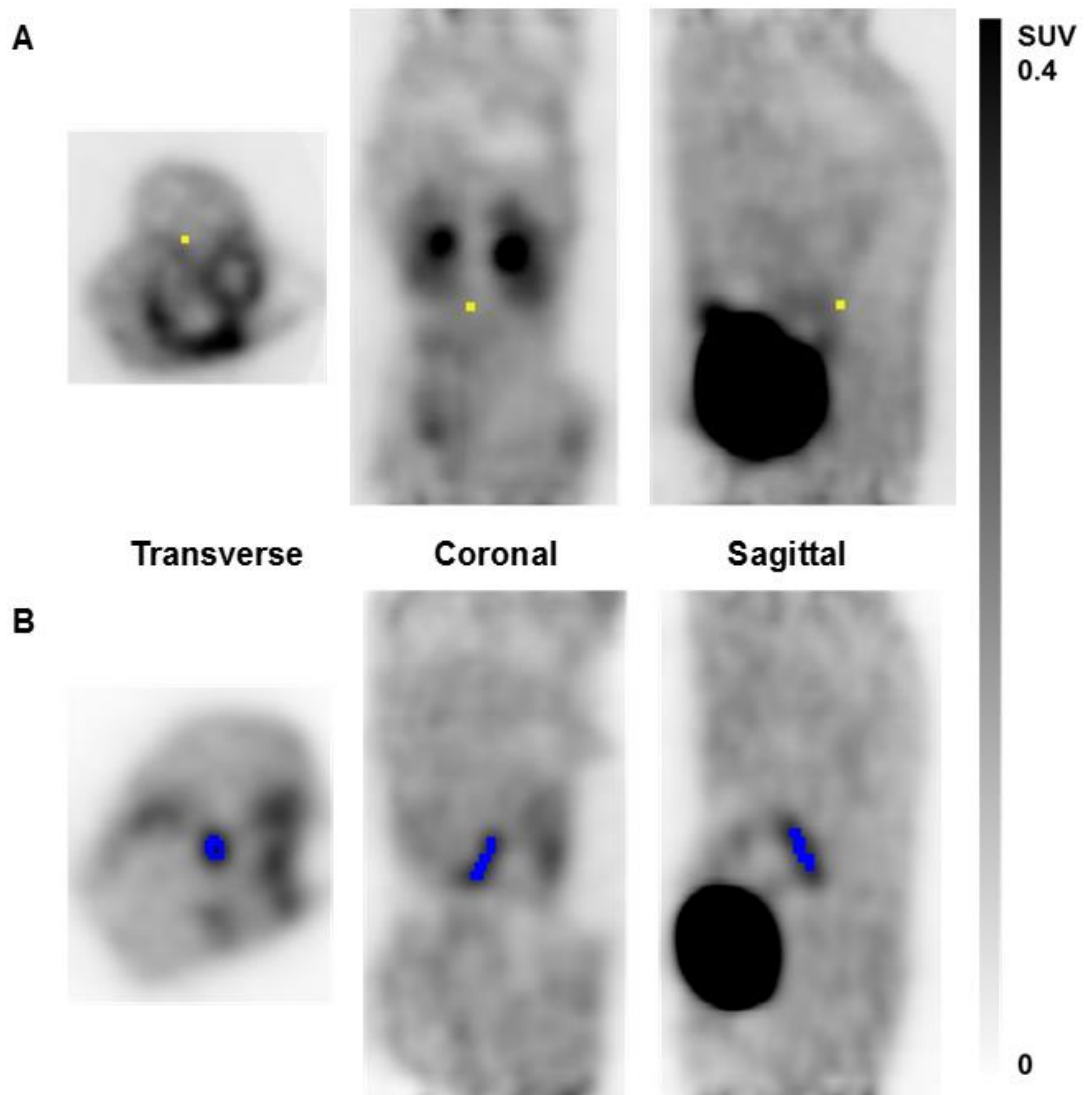


Figure 3.23 Abdominal aortic ROIs for SUV analysis were constructed avoiding adjacent organs. Representative transverse-, coronal-, and sagittal-view static PET images and corresponding abdominal aortic ROI generation in (A) saline controls (yellow) and (B) 14-day AngII AAA mice (blue).

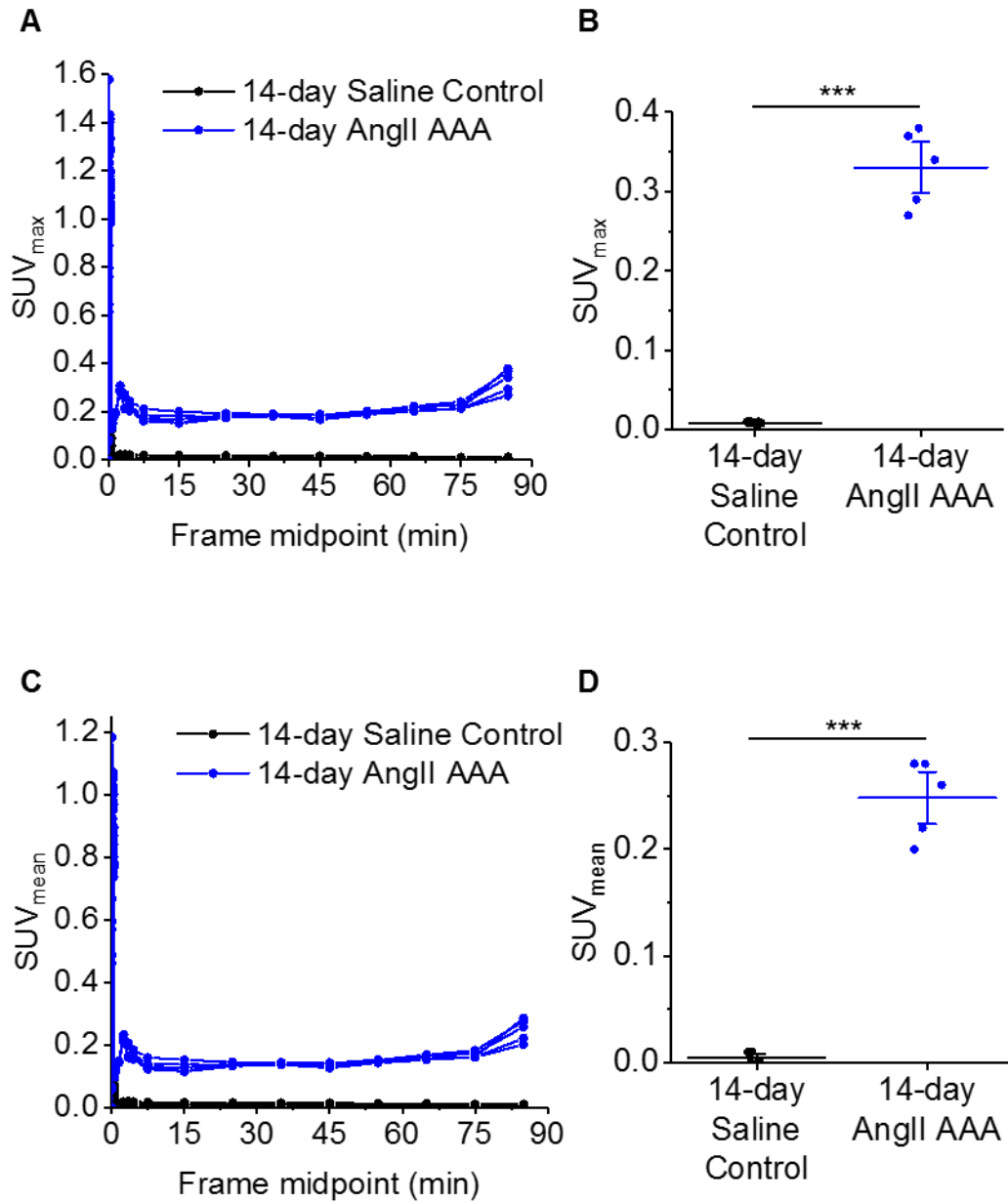
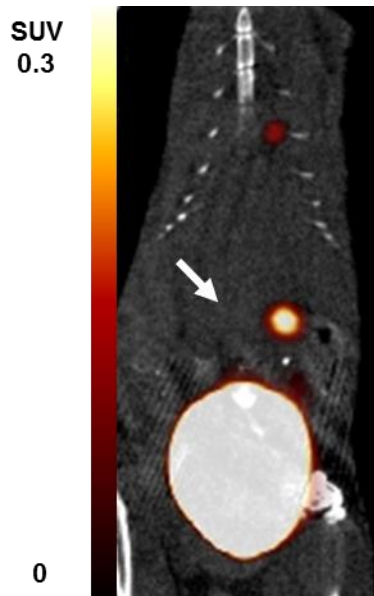
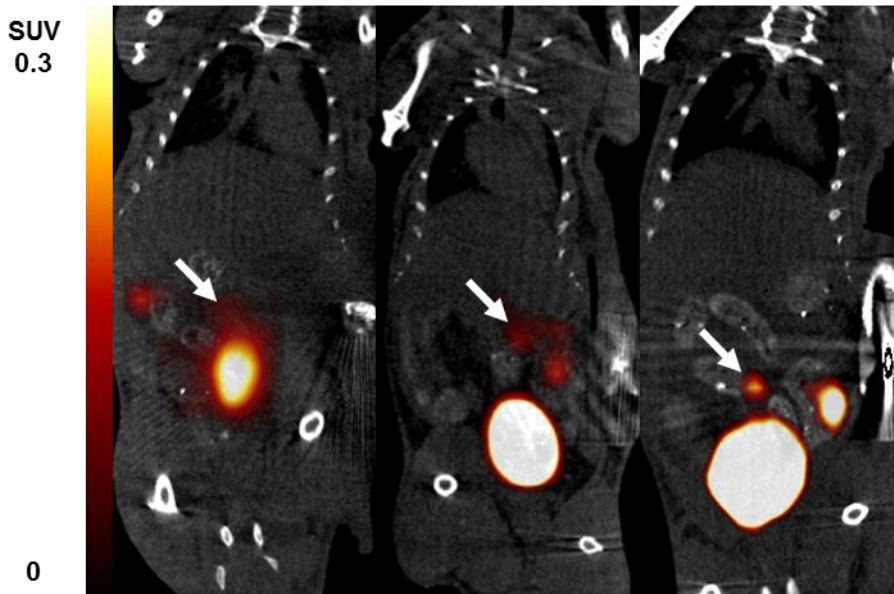


Figure 3.24 [¹⁸F]FLT uptake in the abdominal aorta was consistently greater in the 14-day AngII AAA model than in saline controls. (A) Time-activity curves of SUV_{max} and (B) absolute values of SUV_{max}. (C) Time-activity curves of SUV_{mean} and (D) absolute values of SUV_{mean}. SUV_{max} and SUV_{mean} in (B) and (D) represent 14-day [¹⁸F]FLT uptake in abdominal aortic ROIs 80–90 min post-radiotracer injection in 14-day saline controls (*n*=5) and the 14-day AngII AAA model (*n*=5). *** *p*<0.001 on two-sample *t* test.

Of all mice with AngII AAA, [¹⁸F]FLT scans could be conducted at both the 14- and 28-day stages in only 3 mice, allowing for a comparison between early- and late-stage AngII AAA uptake of [¹⁸F]FLT. Data from the other animals were not available due to episodes of aneurysm rupture or unsuccessful radiotracer injection. All acquired static images of [¹⁸F]FLT uptake in the abdominal aortic regions of saline controls and 28-day AngII AAA mice in the 80–90-min timeframe are presented in Figure 3.25. The TACs for abdominal aortic ROIs following the 28-day PET/CT scans revealed greater [¹⁸F]FLT uptake in the 28-day AngII AAA model than in the 28-day saline control (Figure 3.26). Similar to the analysis of the 14-day scan data, the SUVs were extracted from the final timeframe for analysis. Compared to [¹⁸F]FLT uptake in 14-day AngII AAA, reduced uptake was noted in 28-day AngII AAA ($n=3$) with a mean \pm SEM (80–90 min post-radiotracer injection) SUV_{max} of 0.15 \pm 0.01 and SUV_{mean} of 0.13 \pm 0.02. The single 28-day saline control mouse from which suitable data were retrieved presented with an SUV_{max} of 0.03 and SUV_{mean} of 0.02, which were similar to the results of the 14-day saline controls (Figure 3.26); however, these data were not used for further analysis as they were insufficient for tests of statistical rigour.



28-day Saline Control (*n*=1)



28-day AngII AAA (*n*=3)

Figure 3.25 [¹⁸F]FLT uptake in the abdominal aorta was greater in the 28-day AngII AAA model than in the saline control. Coronal-view PET/CT images of static 28-day abdominal aortic uptake of [¹⁸F]FLT 80–90 min post-radiotracer injection in 28-day saline controls (*n*=1) and the 28-day AngII AAA model (*n*=3). Arrows indicate the abdominal aorta. Colour scale bars indicate SUV thresholding to aid visualisation.

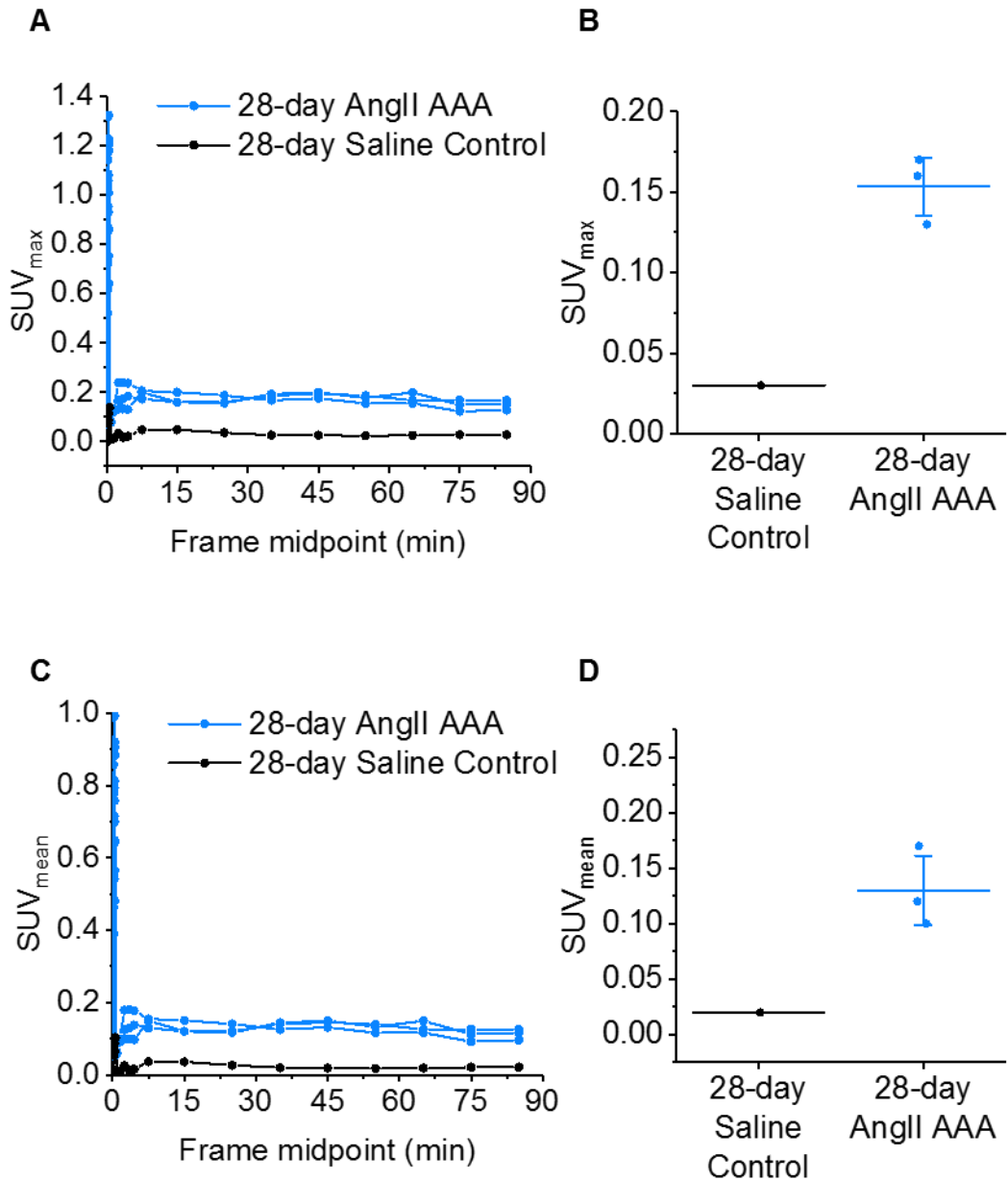


Figure 3.26 ^{18}F FLT uptake in the abdominal aorta was consistently greater in the 28-day AngII AAA model than in the saline control. (A) Time-activity curves of SUV_{max} and (B) absolute values of SUV_{max} . (C) Time-activity curves of SUV_{mean} and (D) absolute values of SUV_{mean} . SUV_{max} and SUV_{mean} in (B) and (D) represent 28-day ^{18}F FLT uptake in abdominal aortic ROIs 80–90 min post-radiotracer injection in 28-day saline controls ($n=1$) and the 28-day AngII AAA model ($n=3$).

3.3.6 Different ROI definitions may affect resultant SUVs

Amide, the image visualisation and analysis software used for the PET/CT analysis in this study, includes parameters related to the ROI that can be modified by the user. A pilot investigation was conducted to determine whether changing these parameters in the software would influence the PET image analysis results. Fixed-size and manually drawn ROIs were generated and SUV_{mean} , SUV_{40} , SUV_{50} , SUV_{70} , SUV_{90} , and SUV_{max} were determined, as described in section 2.4.2. The mean \pm SEM SUV_{mean} , SUV_{40} , SUV_{50} , SUV_{70} , SUV_{90} , and SUV_{max} for both fixed-size and manually drawn abdominal aortic ROIs on all images are presented in Figure 3.27. In all images, the fixed-size and manually drawn abdominal aortic ROIs revealed the following mean \pm SEM values, respectively: SUV_{mean} , 0.14 ± 0.01 and 0.16 ± 0.02 ; SUV_{40} , 0.14 ± 0.01 and 0.16 ± 0.02 ; SUV_{50} , 0.14 ± 0.02 and 0.16 ± 0.02 ; SUV_{70} , 0.16 ± 0.02 and 0.16 ± 0.02 ; SUV_{90} , 0.19 ± 0.02 and 0.17 ± 0.02 ; and SUV_{max} , 0.20 ± 0.02 and 0.18 ± 0.03 . Following a Shapiro–Wilk test that confirmed that the data were normally distributed (all $p < 0.05$), paired t tests were conducted for all fixed-size and manually drawn ROI pairs of SUV thresholds, which revealed significant differences at all SUV thresholds ($p < 0.01$) except at SUV_{70} ($p = 0.73$). This indicated that the SUVs were correlated between fixed-size and manually drawn ROIs only when a 70% threshold was applied to the voxels included in the given ROI.

The average times spent delineating the abdominal aortic regions were 0.49 ± 0.67 min and 1.54 ± 0.54 min when implementing the fixed-size and manually drawn approaches, respectively; thus, fixed-size ROIs are less time-consuming to generate, a finding that is likely important when tasked with analysing large datasets containing many images.

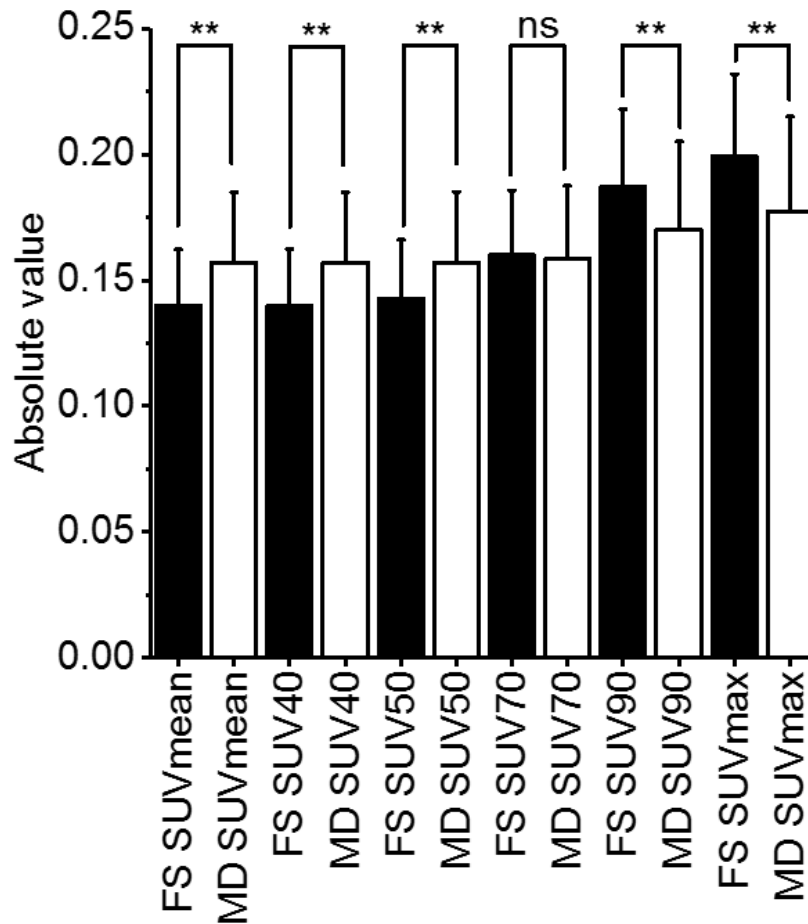


Figure 3.27 SUV₇₀ corresponding to both fixed-size and manually drawn aortic ROIs exhibited no significant differences. The SUV_{mean}, SUV₄₀, SUV₅₀, SUV₉₀, and SUV_{max} were significantly different between fixed-size and manually drawn aortic ROIs. ** $p < 0.01$, ns: not significant on paired t test. FS, fixed-size; MD, manually drawn

3.3.7 [¹⁸F]FLT uptake in the AngII AAA model may be localised to the aortic wall

Using ImageJ 1.51k software, USS and PET/CT images were manually co-registered. For the co-registration analysis, bony landmarks on CT and USS were aligned, which revealed [¹⁸F]FLT PET signal in the aortic wall in the AngII AAA model (Figure 3.28).



Figure 3.28 [¹⁸F]FLT uptake in the AngII AAA model may occur in the aortic wall. Representative transverse-view ultrasound, [¹⁸F]FLT PET/CT, and fused ultrasound–PET/CT images. Short arrow, aortic lumen; long arrow, remodelling aortic wall.

3.4 *Ex vivo* [¹⁸F]FLT uptake is greater in AngII AAA than in saline control aortae

As described previously in section 3.3.3, the baseline [¹⁸F]FLT biodistribution study demonstrated high uptake in the spleen and low uptake in the aorta and heart; the aorta exhibited comparable uptake to the heart, whilst the spleen exhibited greater uptake relative to the heart. Therefore, the heart and spleen were used as negative and positive control reference tissues, respectively, going forward. To confirm the tissue-specific origin of the [¹⁸F]FLT signal observed on PET/CT in the abdominal aortic ROI, *ex vivo* gamma counting was performed using whole organs from 14-day AngII AAA mice and saline controls. Uptake in the aorta and spleen were then normalised to uptake in the heart to control for mouse-to-mouse variability. [¹⁸F]FLT counts in the abdominal aorta relative to the heart in the 14-day AngII-infused mice ($n=9$) were significantly increased compared to those in saline controls ($n=4$) (mean \pm SEM: 3.30 ± 1.01 vs. 0.37 ± 0.14 %ID/g, $p<0.05$) (Figure 3.29). The Shapiro–Wilk test revealed that the data of the 14-day AngII AAA group were not normally distributed. The results of the non-parametric statistical test are presented in Appendix B.

Moreover, a pilot attempt was made to perform *ex vivo* autoradiography of [¹⁸F]FLT uptake in whole-organ samples. Although the number of samples was small, greater [¹⁸F]FLT uptake in the aneurysmal aorta compared to that in the control aorta was observed, as expected based on the *ex vivo* biodistribution results.

3.4.1 Aortic [¹⁸F]FLT uptake is correlated with aortic volume

A significantly positive correlation was noted between [¹⁸F]FLT uptake on *ex vivo* gamma counting and aortic volume on *in vivo* USS ($p<0.05$, Pearson's $r=0.67$) (Figure 3.30).

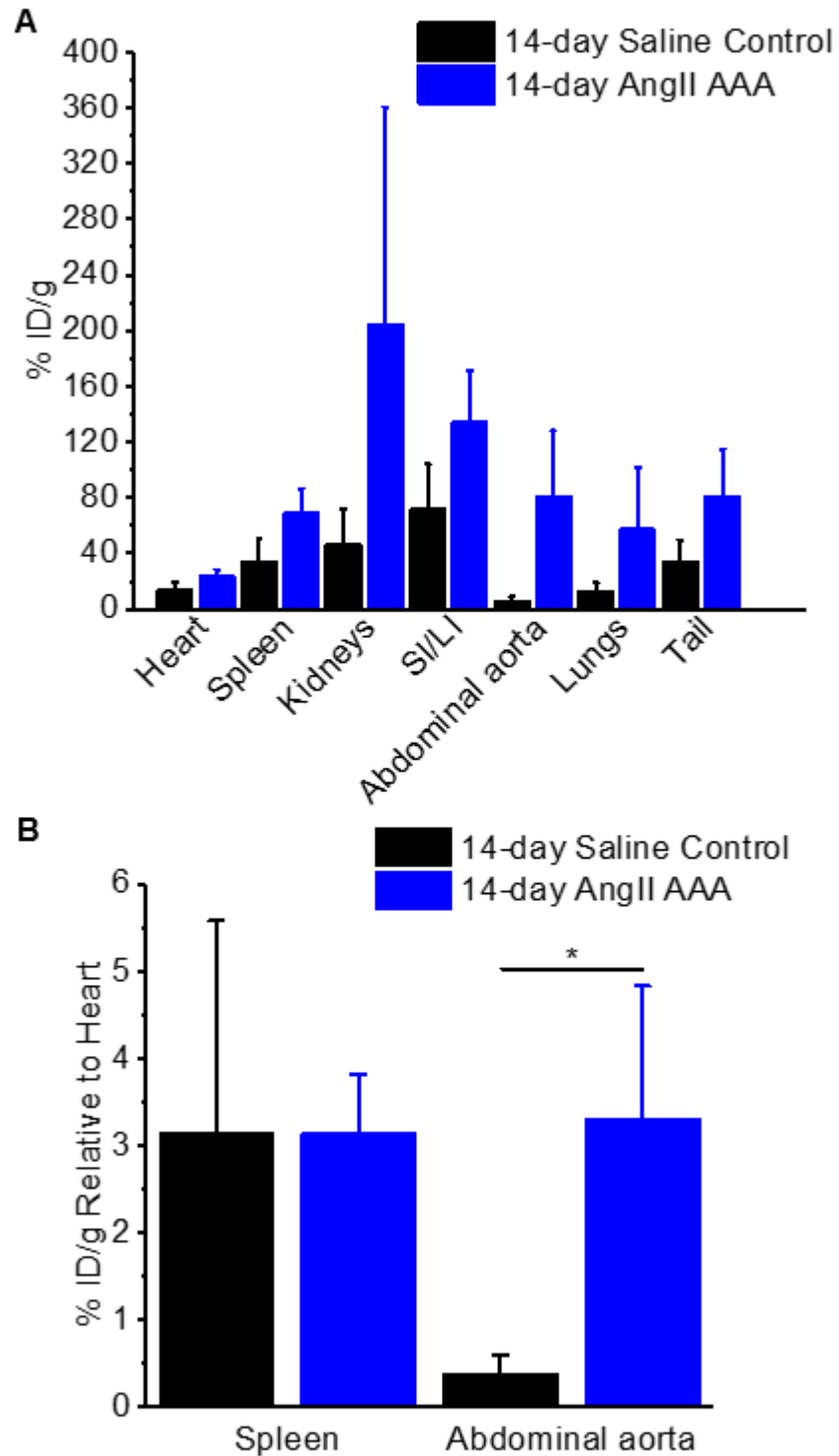


Figure 3.29 *Ex vivo* [¹⁸F]FLT uptake in the abdominal aorta was greater in the 14-day AngII AAA model than in 14-day saline controls. Decay-corrected *ex vivo* [¹⁸F]FLT counts per mass units. (A) All organs. (B) Uptake in the spleen and abdominal aorta normalised to uptake in the heart in the 14-day AngII AAA model (*n*=9) and 14-day saline controls (*n*=4). * *p*<0.05 on two-sampled *t* test with Welch's correction.

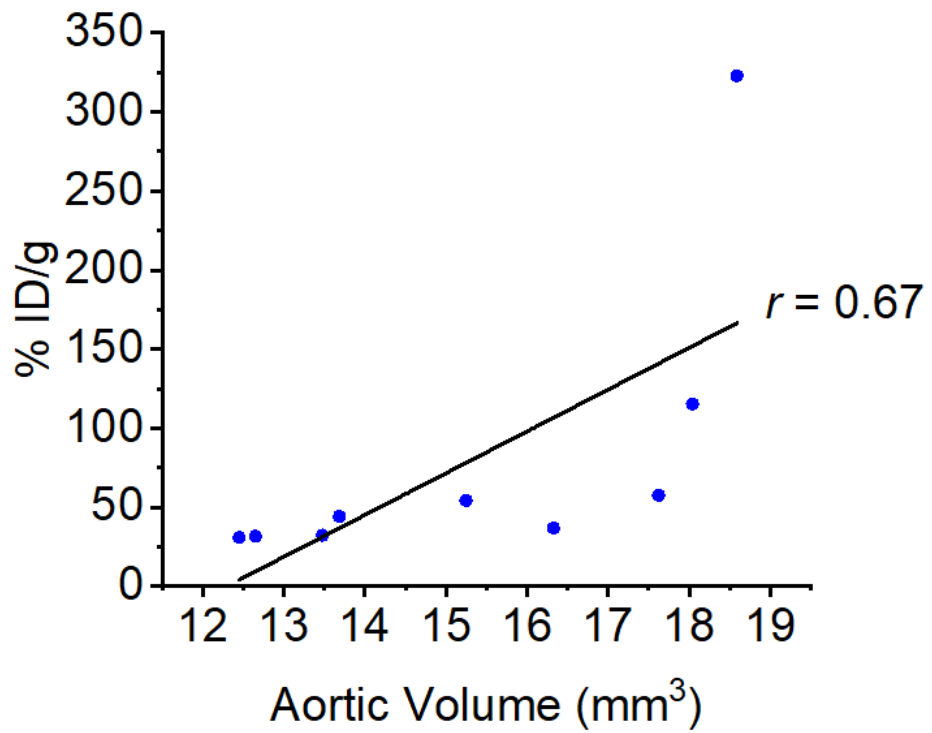


Figure 3.30 Aortic volume is positively correlated with [¹⁸F]FLT uptake. Correlation between aortic volume and ex vivo [¹⁸F]FLT counts in AngII AAA (blue, *n*=9). Pearson's *r*=0.67, *p*<0.05.

3.5 Expression of key molecules involved in [¹⁸F]FLT metabolism are upregulated in the AngII AAA model

The [¹⁸F]FLT PET/CT data presented in section 3.3 suggest increased abdominal aortic proliferative activity in the 14-day AngII AAA model compared to that in control animals, which diminishes at the 28-day time point. To further investigate the change in [¹⁸F]FLT signal observed between 14- and 28-day AngII AAA, an independent cohort of mice was divided into 4 groups, and aortae were harvested: baseline group ($n=3$), containing ApoE^{-/-} mice; saline control group ($n=3$), containing ApoE^{-/-} mice that received saline infusions for 14 days; 14-day AngII AAA group ($n=3$), containing ApoE^{-/-} mice that received AngII infusions for 14 days; and 28-day AngII AAA ($n=3$), containing ApoE^{-/-} mice that received AngII infusions for 28 days. This was followed by western blotting for (i) TK-1, the key substrate of [¹⁸F]FLT, and (ii) the nucleoside transporters that carry [¹⁸F]FLT into the cell: ENT-1, ENT-2, CNT-1, and CNT-3. The response of these proteins to AngII-induced AAA is unknown.

3.5.1 Expression of the substrate of [¹⁸F]FLT is increased in the AngII AAA model

Consistent with [¹⁸F]FLT uptake observed using PET/CT, the TK-1 band intensity was increased after 14-day AngII infusion compared to that after saline control and 28-day AngII infusion (mean \pm SD TK-1: β -actin band intensities: 2.45 \pm 0.24, 0.34 \pm 0.02, and 1.07 \pm 0.07, respectively; all $p<0.001$) (Figure 3.31). The results of the non-parametric statistical test are presented in Appendix B.

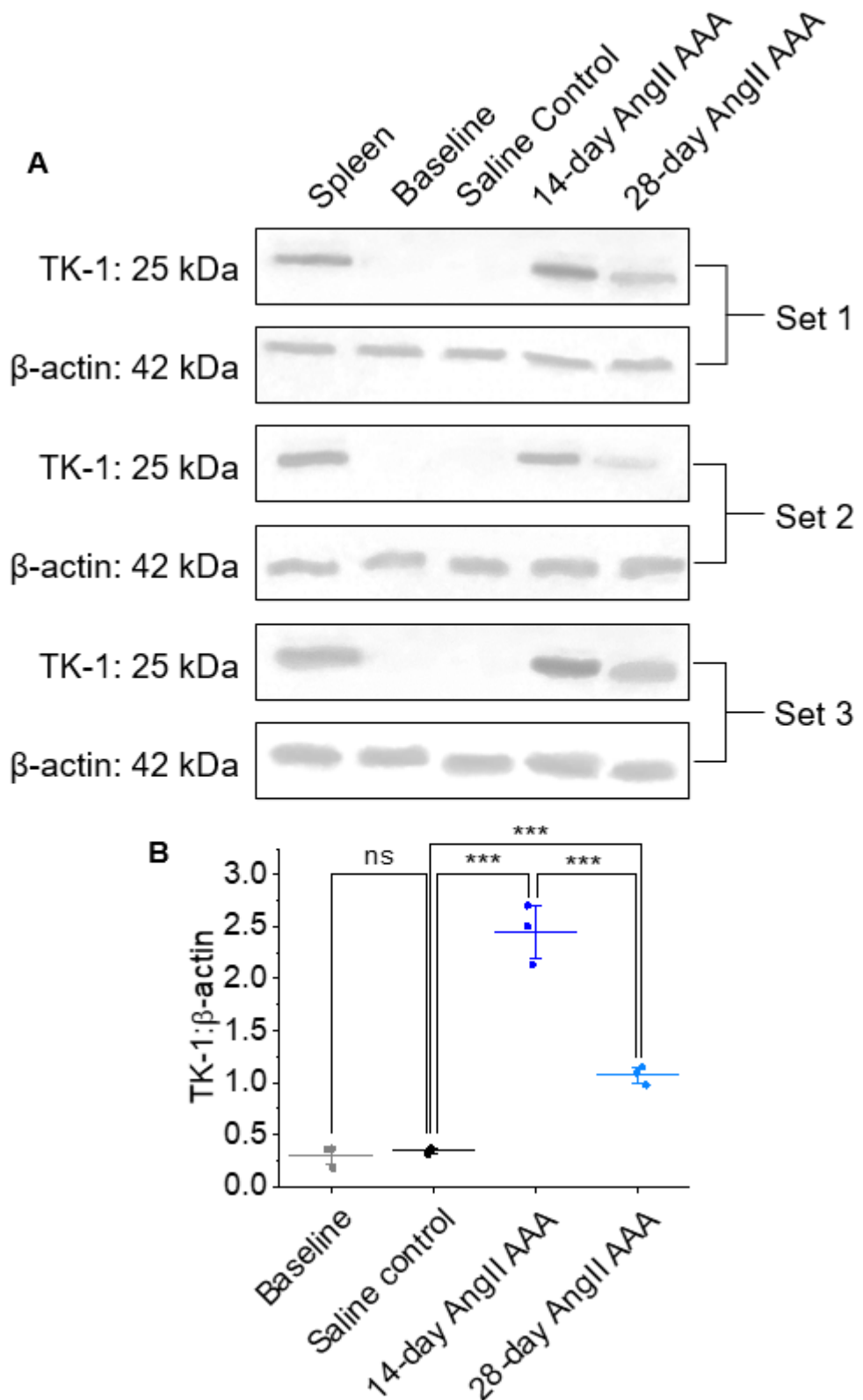


Figure 3.31 TK-1 expression was the greatest in 14-day AngII AAA. (A) Representative TK-1 western blots. (B) Quantitative analysis. TK-1 band intensity was normalised to β -actin band intensity. *** $p < 0.001$, ns: not significant on one-way analysis of variance with post-hoc Bonferroni-Holm correction.

3.5.2 Expression of [¹⁸F]FLT transporters is increased in the AngII AAA model

The ENT-1 band intensity was increased after 14-day AngII infusion compared to that after saline control and 28-day AngII infusion (mean±SD ENT-1:β-actin band intensities: 2.74±0.09, 0.10±0.06, and 1.45±0.11, respectively; all $p<0.001$) (Figure 3.32). The Shapiro–Wilk test revealed that the data of the saline control group were not normally distributed. The intensity of the ENT-2 band was also increased after 14-day AngII infusion compared to that after saline control and 28-day AngII infusion (mean±SD ENT-2:β-actin band intensities: 2.66±0.13, 0.29±0.00, and 1.68±0.04, respectively; all $p<0.001$) (Figure 3.33). Keeping with a similar pattern, the CNT-1 band intensity was increased following 14-day AngII infusion compared to that following saline control and 28-day AngII infusion (mean±SD CNT-1:β-actin band intensities: 4.06±0.45, 0.24±0.02, and 1.53±0.09, respectively; all $p<0.001$) (Figure 3.34). Finally, the intensity of the CNT-3 band was increased after 14-day AngII infusion compared to that after saline control and 28-day AngII infusion (mean±SD CNT-3:β-actin band intensities: 3.69±0.70, 0.40±0.21, and 2.03±0.44, respectively; all $p<0.001$) (Figure 3.35). Overall, the key proteins tested that play a role in [¹⁸F]FLT metabolism were upregulated in 14-day AngII AAA tissue compared to 28-day AngII AAA and saline control tissue. For reference, all the tested proteins were found to be expressed in tissue from a saline control spleen, which was expected as the spleen contains proliferative cells. The differences in protein expression were insignificant between baseline and saline control aortae for all the tested proteins. The results of all non-parametric statistical tests corresponding to these findings are presented in Appendix B.

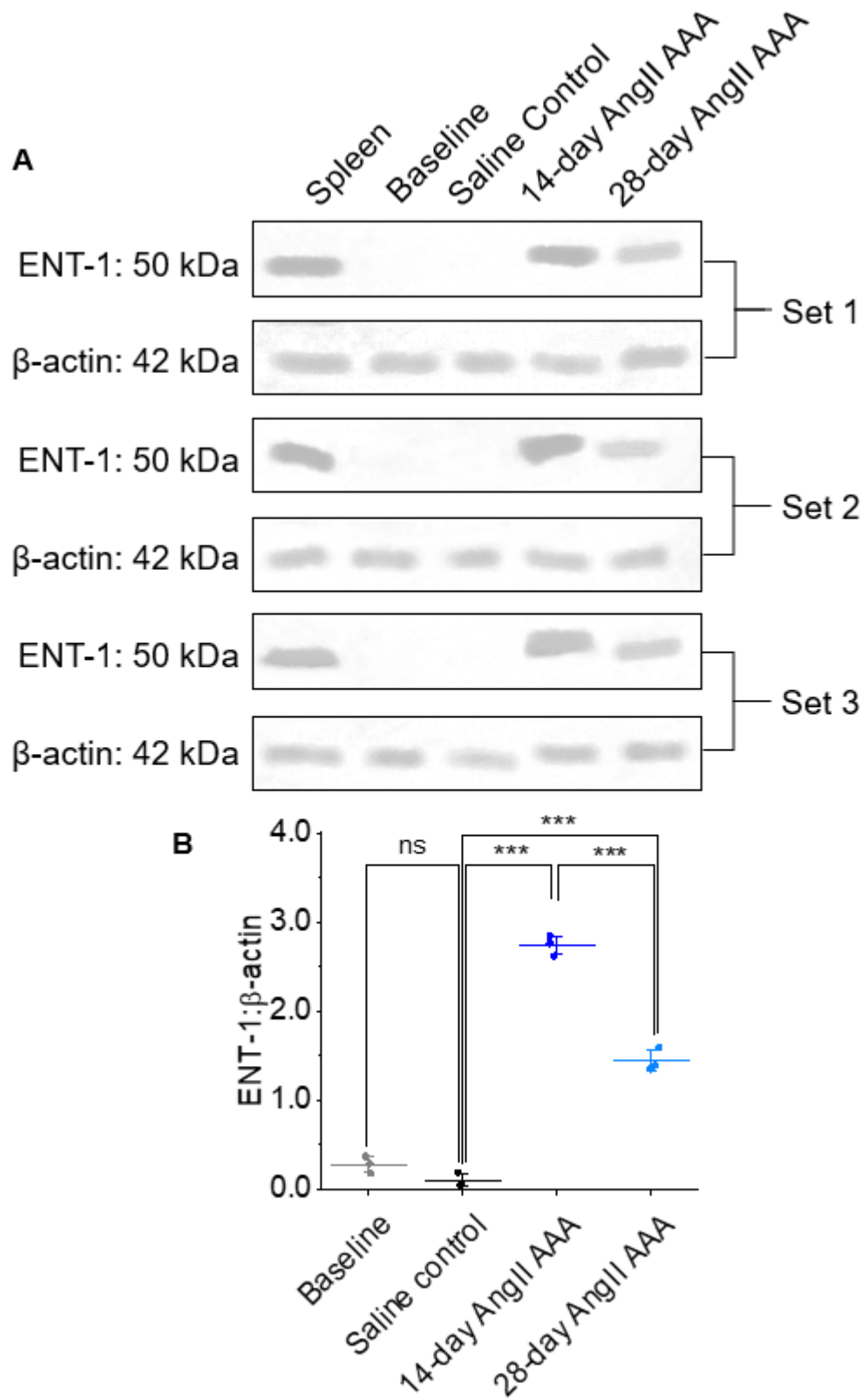


Figure 3.32 ENT-1 expression was the greatest in 14-day AngII AAA. (A) Representative ENT-1 western blots. (B) Quantitative analysis. ENT-1 band intensity was normalised to β -actin band intensity. *** $p < 0.001$, ns: not significant on one-way analysis of variance with post-hoc Bonferroni-Holm correction.

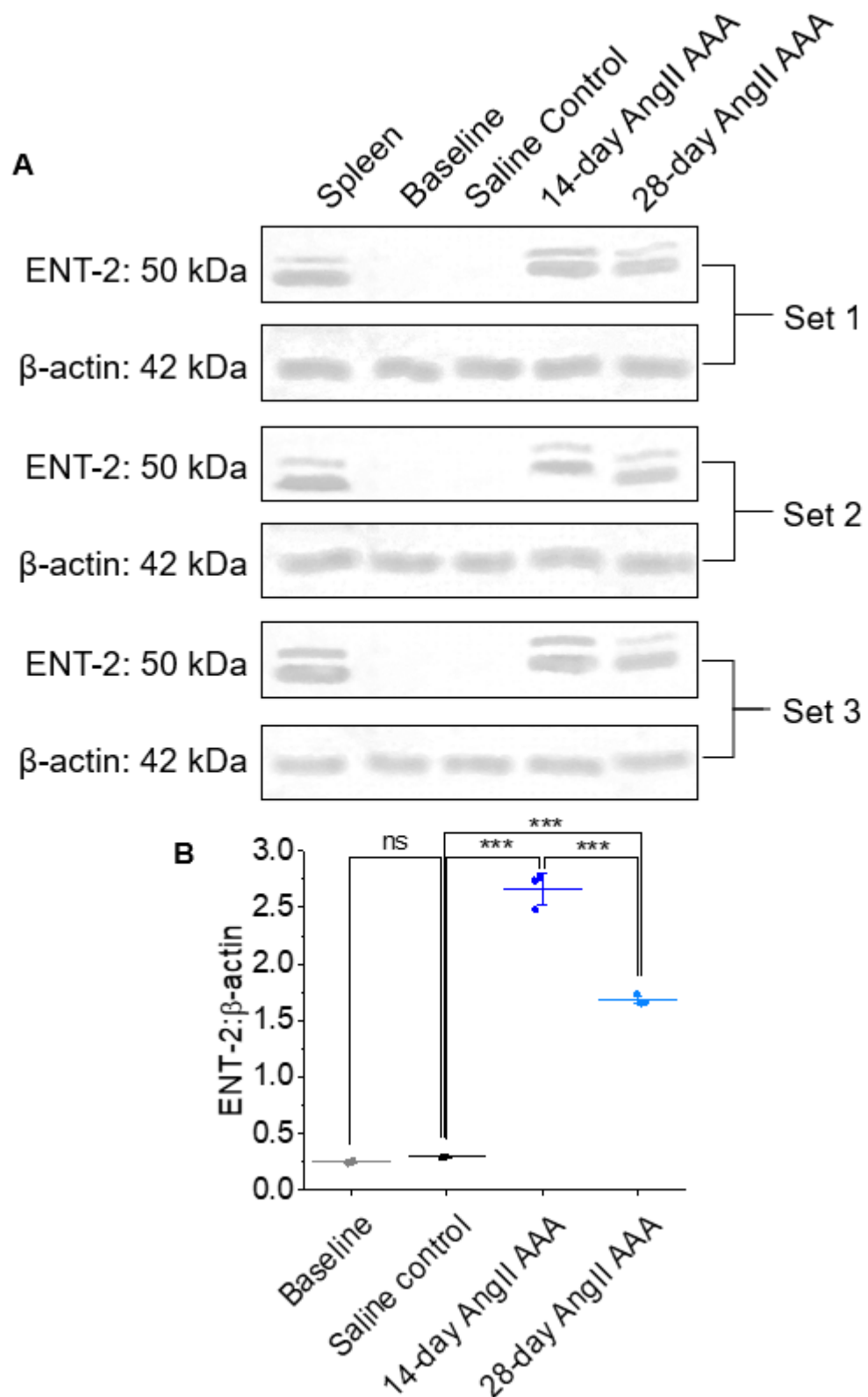


Figure 3.33 ENT-2 expression was the greatest in 14-day AngII AAA. (A) Representative ENT-2 western blots. (B) Quantitative analysis. ENT-2 band intensity was normalised to β -actin band intensity. *** $p < 0.001$, ns: not significant on one-way analysis of variance with post-hoc Bonferroni-Holm correction.

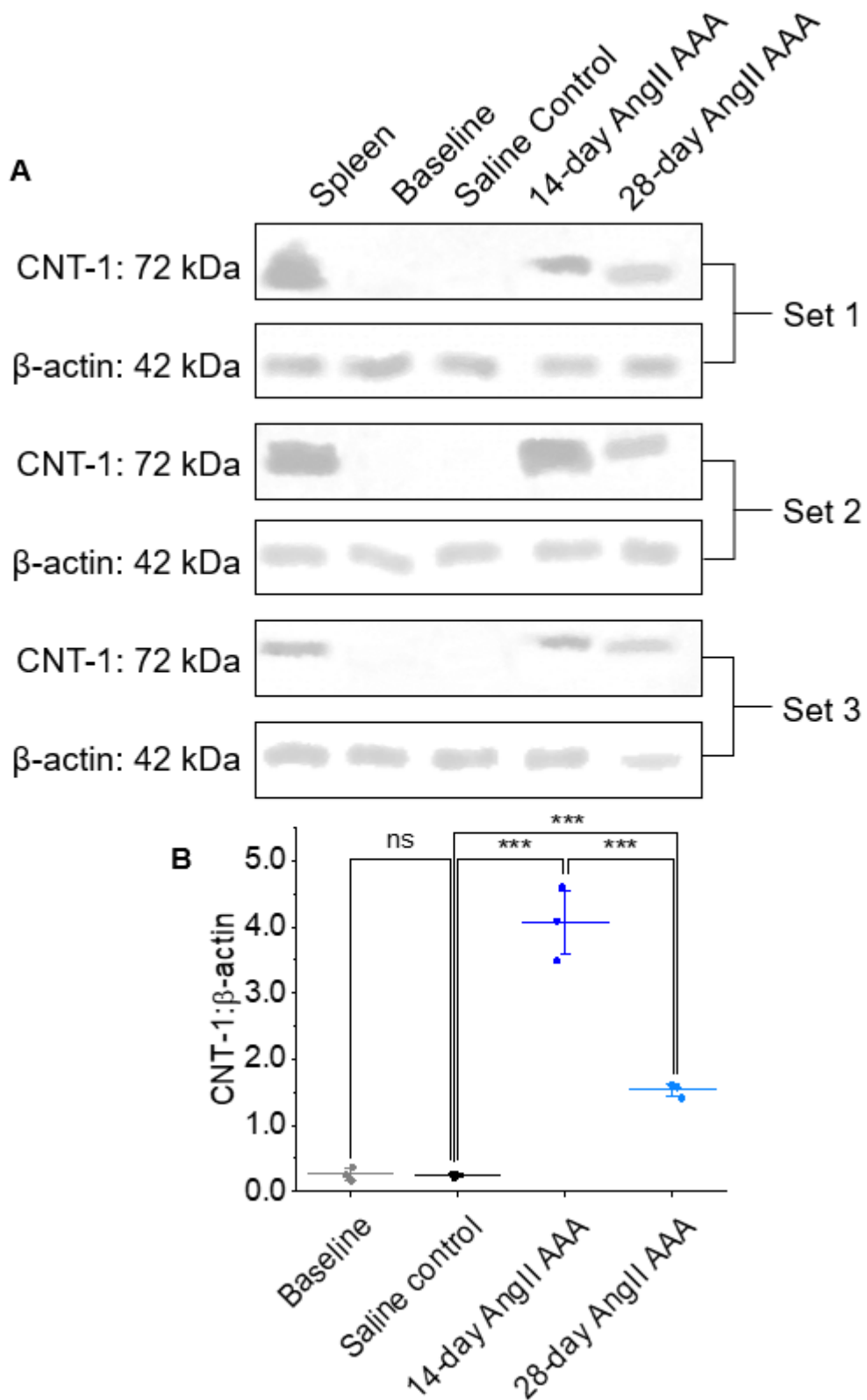


Figure 3.34 CNT-1 expression was the greatest in 14-day AngII AAA. (A) Representative CNT-1 western blots. (B) Quantitative analysis. CNT-1 band intensity was normalised to β -actin band intensity. *** $p < 0.001$, ns: not significant on one-way analysis of variance with post-hoc Bonferroni-Holm correction.

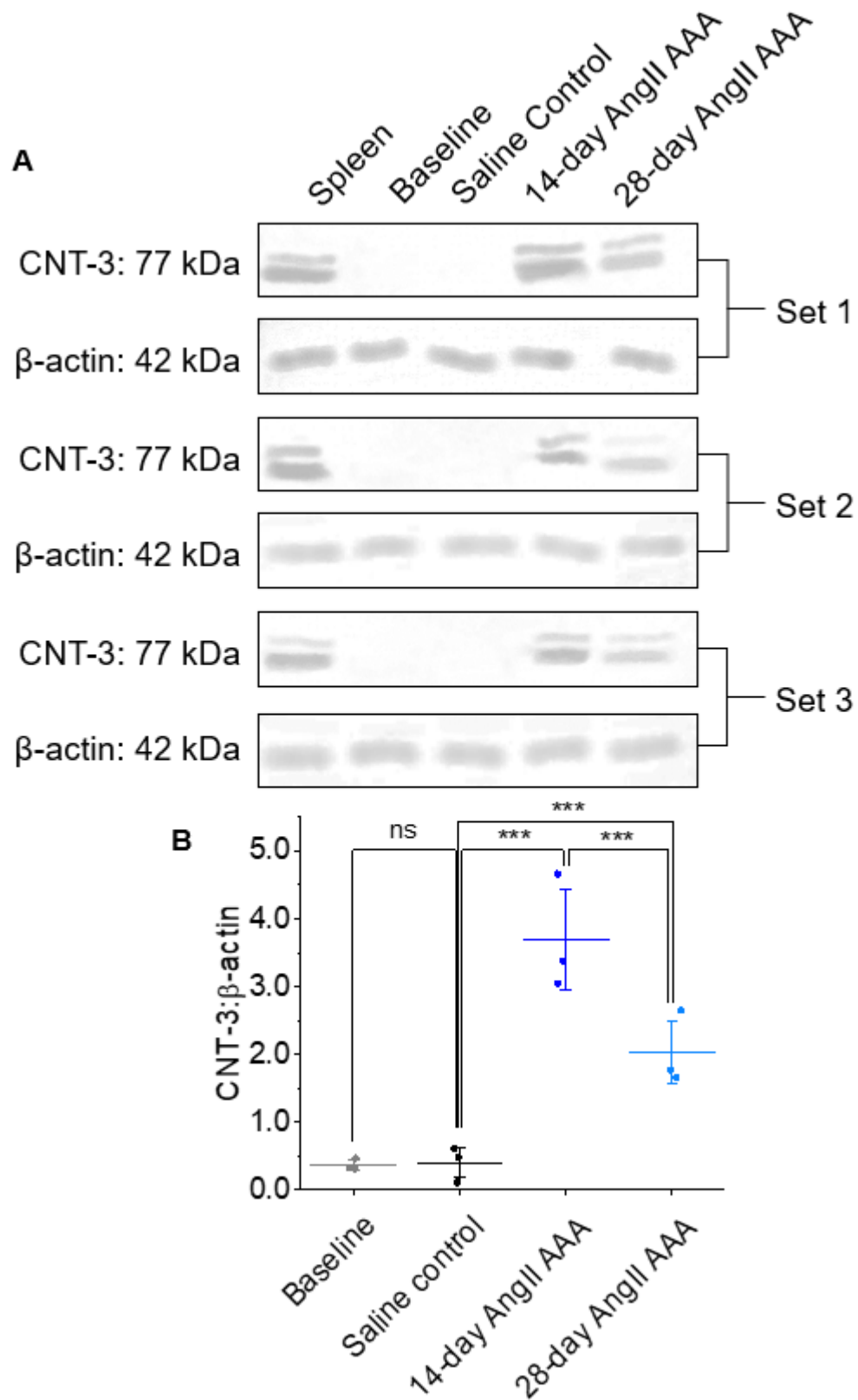


Figure 3.35 CNT-3 expression was the greatest in 14-day AngII AAA. (A) Representative CNT-3 western blots. (B) Quantitative analysis. CNT-3 band intensity was normalised to β -actin band intensity. *** $p < 0.001$, ns: not significant on one-way analysis of variance with post-hoc Bonferroni-Holm correction.

3.6 Cell proliferation is difficult to visualise and quantify using [¹⁸F]FLT PET/CT in the PPE AAA model

The PPE model of AAA is a well-established non-progressive disease model that is less likely to rupture than the AngII infusion model (Senemaud et al., 2017). As one of the commonly studied murine models of AAA and the model that showed the greatest proportion of Ki67-positive nuclei (reported in section 3.1), aortic volumes and [¹⁸F]FLT uptake were explored in the PPE AAA model to investigate if the findings from the AngII model could be replicated in a second model.

3.6.1 Aortic volumes and diameters in the PPE AAA model are larger than those in sham controls

Evaluation by 3D USS revealed the expected significant increases in aortic diameter ($p<0.05$) and volume ($p<0.05$) 14 days post-PPE application compared to baseline and sham-operated controls. The aortic diameters were 1.66 ± 0.53 mm (mean \pm SEM) and 0.52 mm and aortic volumes were 18.72 ± 5.47 mm³ (mean \pm SEM) and 2.70 mm³ in the 14-day PPE model ($n=3$) and 14-day sham control ($n=1$), respectively (Figure 3.36).

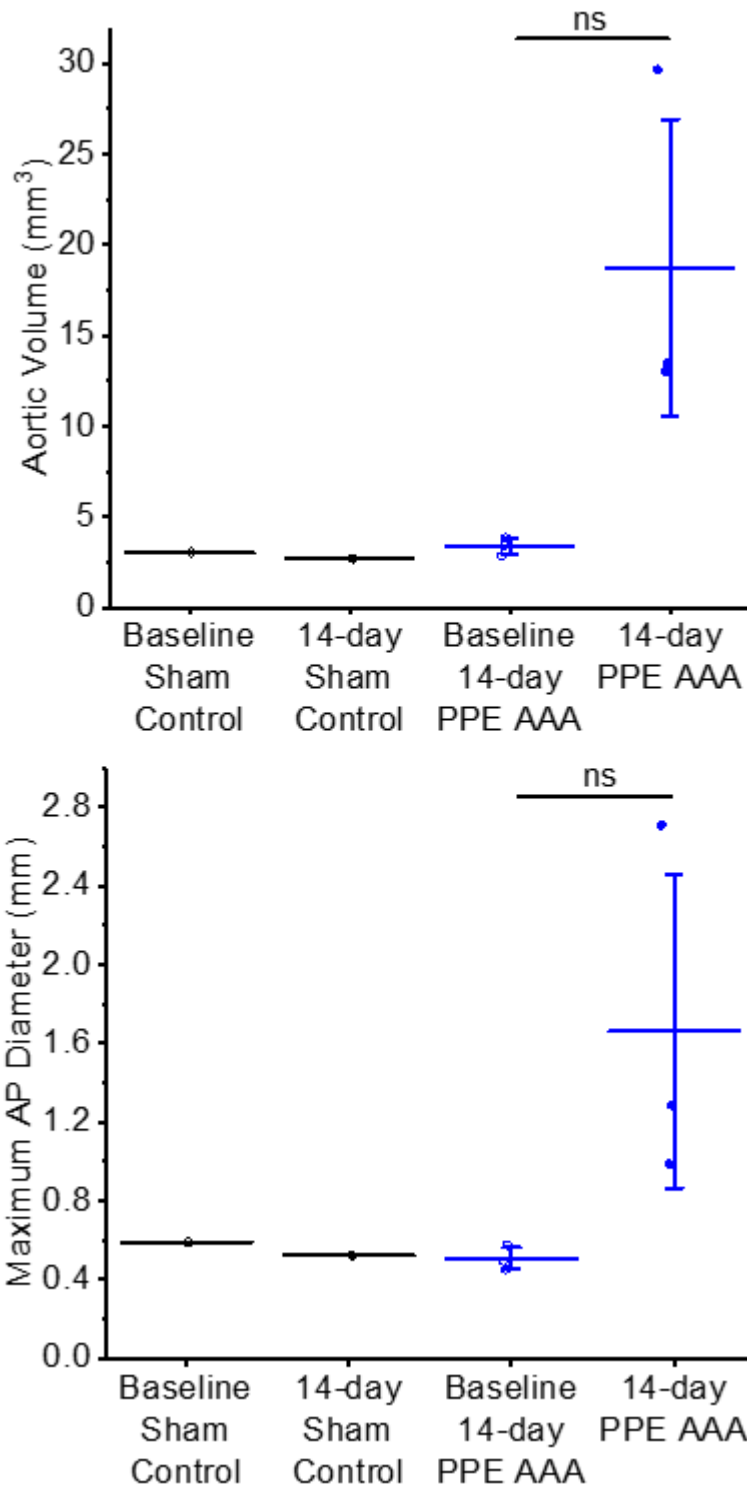


Figure 3.36 Aortic volume and AP diameters were greater in the 14-day PPE AAA model than in sham controls. Aortic volumes and AP diameters based on 3D USS of 14-day PPE AAA ($n=3$) vs. 14-day sham control aortae ($n=1$). ns: not significant on two-sample t test.

3.6.2 *In vivo* [¹⁸F]FLT uptake is variable in the PPE AAA model

Static PET/CT images revealed that [¹⁸F]FLT uptake in the 14-day PPE AAA model 80–95 min post-injection of [¹⁸F]FLT was variable and noisy due to uptake in regions surrounding the abdominal aorta, such as areas of the bowel, leading to inconclusive evidence of [¹⁸F]FLT uptake in PPE AAA (Figure 3.37). Additionally, multiple hotspots of diffuse radiotracer uptake were noted on the PET images of the abdominal region, making it difficult to confidently delineate the abdominal aorta. This background uptake was not observed in the AngII AAA model, leading to the suspicion that these hotspots in the abdominal and bowel areas resulted from the method of PPE application. For this method, the mice are laparotomised, and 10 µL of PPE is applied to the abdominal aorta using a syringe. The [¹⁸F]FLT signal may relate to post-surgical changes in the abdomen involving the formation of adhesions, which can occur following any laparotomy.

3.6.3 *Ex vivo* [¹⁸F]FLT uptake in PPE AAA is similar to that in sham control aortae

Ex vivo gamma counting was then performed, as per section 2.5. The experiment revealed no significant difference in [¹⁸F]FLT counts in the abdominal aorta relative to the heart between the 14-day PPE AAA and 14-day sham control (Figure 3.38). These results suggested that there was no significant uptake in the AAA.

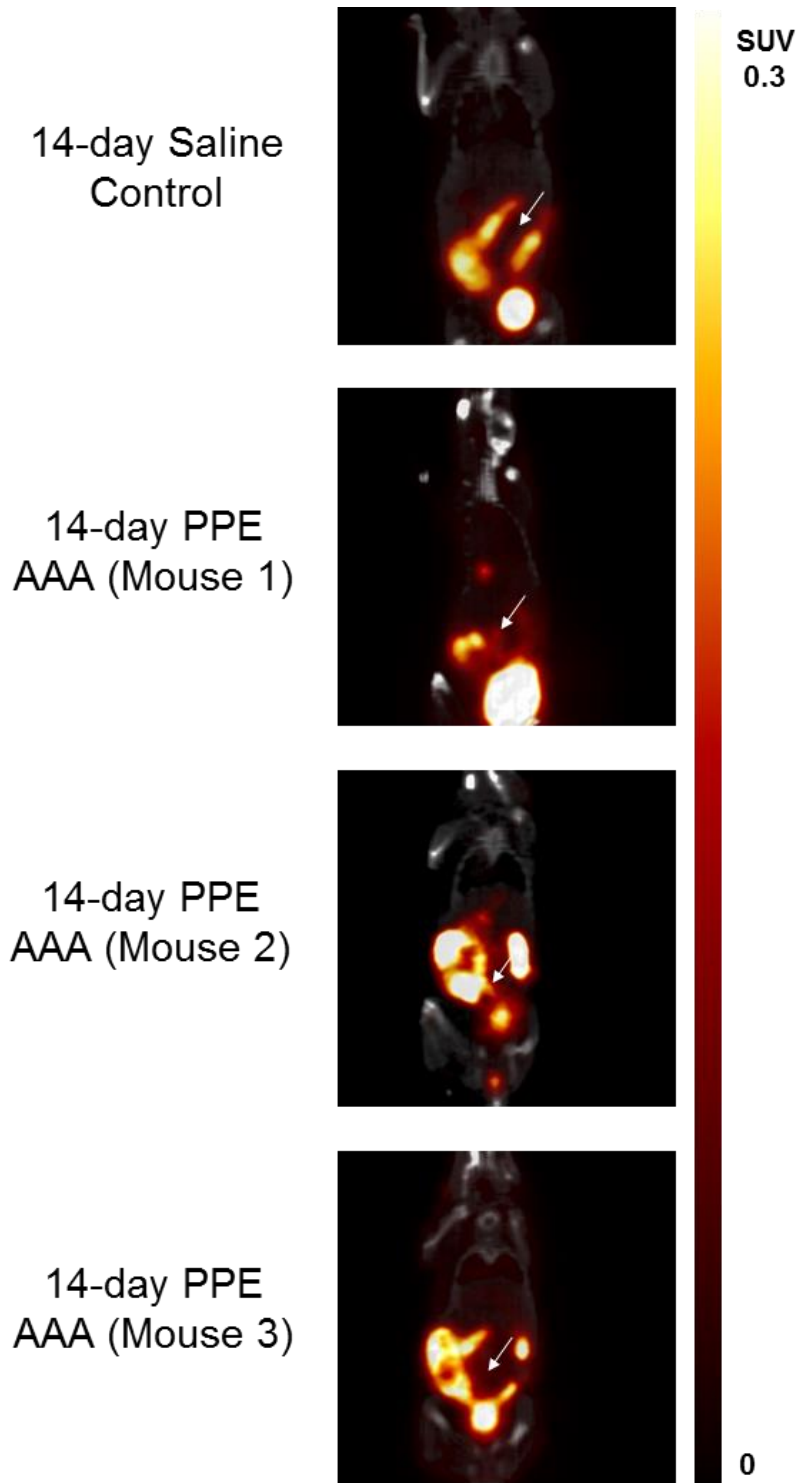


Figure 3.37 [^{18}F]FLT uptake in the abdominal aorta was difficult to visualise in the 14-day PPE AAA model. Coronal-view PET/CT images of static 14-day abdominal aortic uptake of [^{18}F]FLT 80–95 min post-radiotracer injection in all animals. Arrows indicate the abdominal aortic region. Colour scale bars indicate SUV thresholding to aid visualisation.

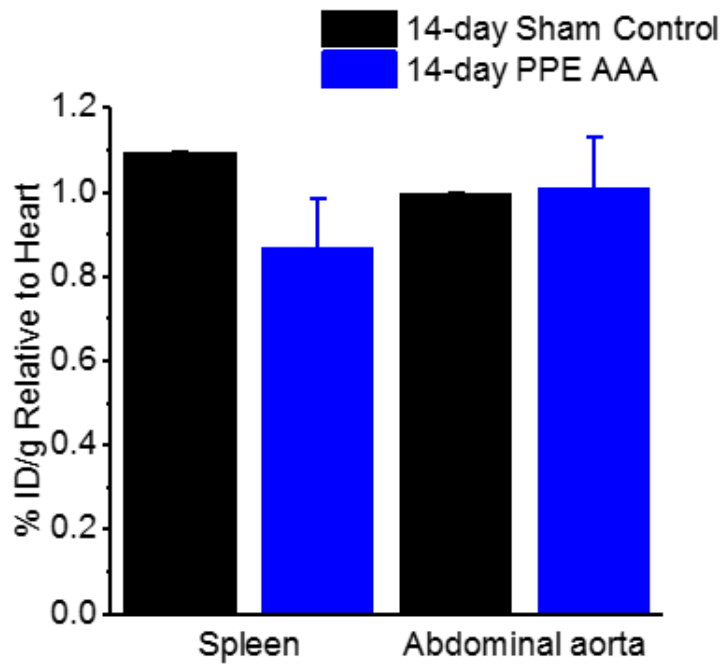
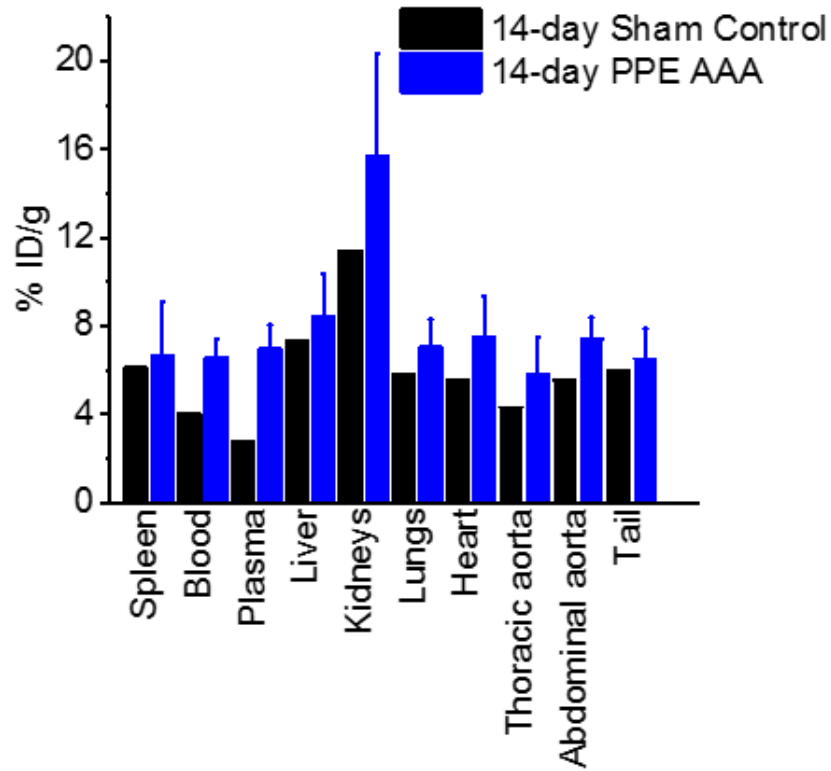


Figure 3.38 *Ex vivo* [^{18}F]FLT uptake in the abdominal aorta was similar in PPE AAA and sham control aortae. Decay-corrected *ex vivo* [^{18}F]FLT counts per mass units (A) All organs. (B) Uptake in the spleen and abdominal aorta normalised to uptake in the heart in PPE AAA ($n=3$) and sham control ($n=1$) aortae.

3.7 [¹⁸F]FLT PET/CT might be useful to assess a therapeutic response in the AngII AAA model

Finally, [¹⁸F]FLT PET/CT was used in a proof-of-concept exploratory experiment to determine if the response to an anti-proliferative tyrosine kinase inhibitor commonly used as a cancer therapeutic (imatinib) could be detected in the AngII AAA model. Considering the high rupture rate of the AngII AAA model and economic feasibility, 15 mice received AngII infusions. Aortic rupture occurred in 5 mice within 12 days of AngII treatment. Three-dimensional USS after 12-day AngII infusion revealed that aneurysms developed in all surviving mice; 6 of the 10 mice presented with aneurysms that were neither dissecting nor ectatic, which were categorised as 'high priority' for PET/CT imaging. The remaining 4 mice with smaller aneurysms were categorised as 'low priority' for PET/CT imaging.

Pre-treatment [¹⁸F]FLT PET/CT was performed on day 13 of AngII infusion, during which 2 of the high-priority mice and 2 of the low-priority mice died following [¹⁸F]FLT injection. The PET/CT data acquired from 3 of the 4 mice that survived to produce follow-up data revealed notable [¹⁸F]FLT uptake in the AAA region. Three-dimensional isocontour ROIs revealed a mean±SEM ($n=3$) SUV_{max} of 0.19 ± 0.01 and SUV_{mean} of 0.18 ± 0.01 . All mice were then administered 3 doses of imatinib or tap water (as the vehicle treatment) via oral gavage before undergoing follow-up PET/CT on day 15 of AngII infusion. Post-imatinib PET data revealed a mean±SEM ($n=2$) SUV_{max} of 0.02 ± 0.0 and SUV_{mean} of 0.02 ± 0.0 ; these were significantly decreased compared to the pre-treatment values ($p<0.001$ and $p<0.001$, respectively). [¹⁸F]FLT uptake in AAA decreased after 3 doses of imatinib, reflecting an anti-proliferative response that was detectable in the early stage of AAA progression using PET/CT.

Meanwhile, matched tap water treatment resulted in no significant change in [¹⁸F]FLT uptake, lending support to the imatinib data ($n=1$: SUV_{max} of 0.23 and SUV_{mean} of 0.21, respectively, compared to pre-treatment) (Figure 3.39).

Ex vivo gamma counting was then performed. [¹⁸F]FLT counts in the abdominal aorta relative to the heart in the AngII AAA mice that received imatinib were decreased compared to that in the AngII AAA mouse that received vehicle treatment (mean±SEM: 23.89 ± 8.57 vs. 51.55 %ID/g) (Figure 3.40).

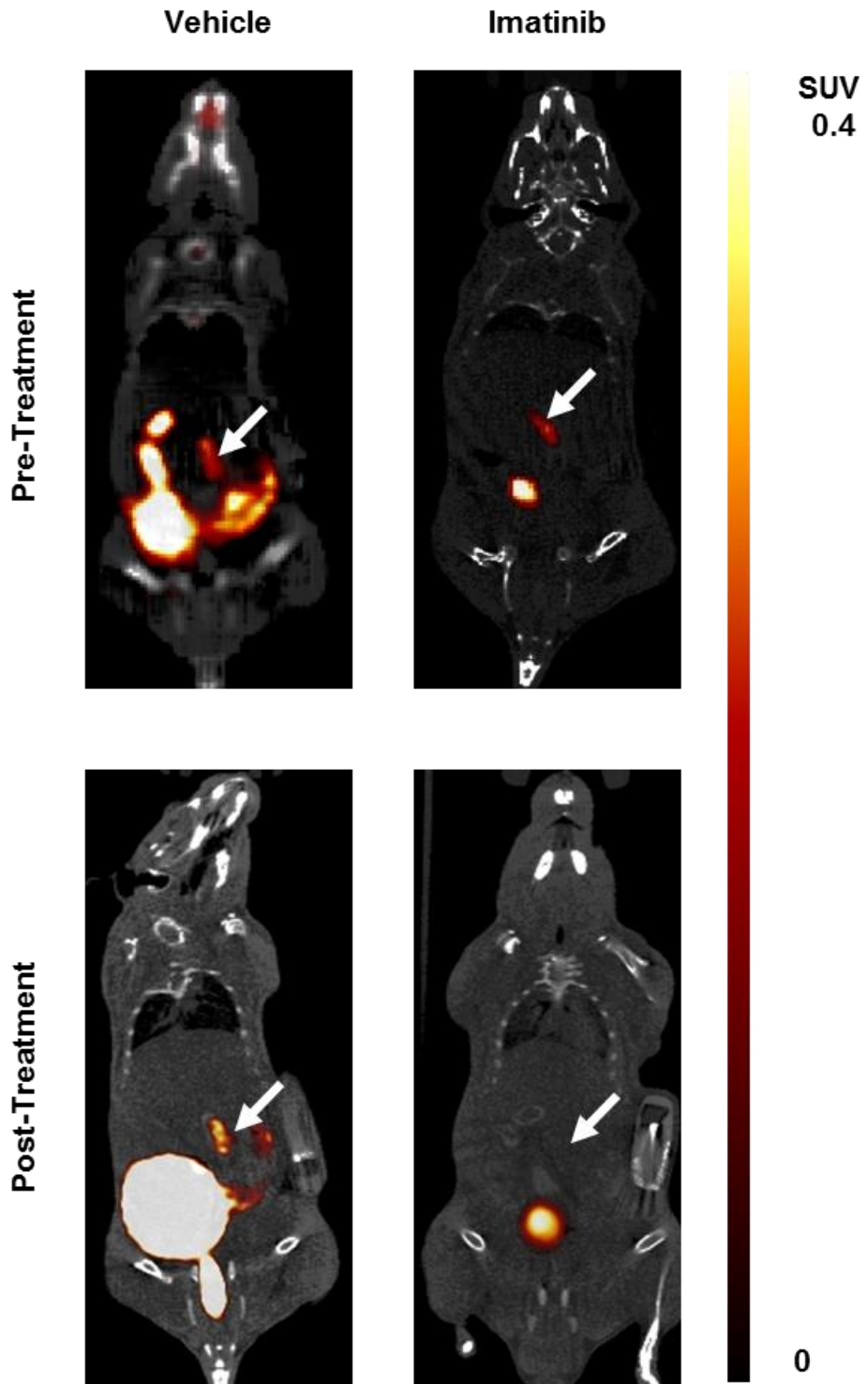


Figure 3.39 [^{18}F]FLT uptake in AngII AAA decreased following imatinib treatment. Coronal-view PET/CT images of static abdominal aortic uptake of [^{18}F]FLT 80–100 min post-radiotracer injection pre- and post-treatment with imatinib or vehicle (tap water). Arrows indicate the abdominal aorta. Colour scale bars indicate SUV thresholding to aid visualisation.

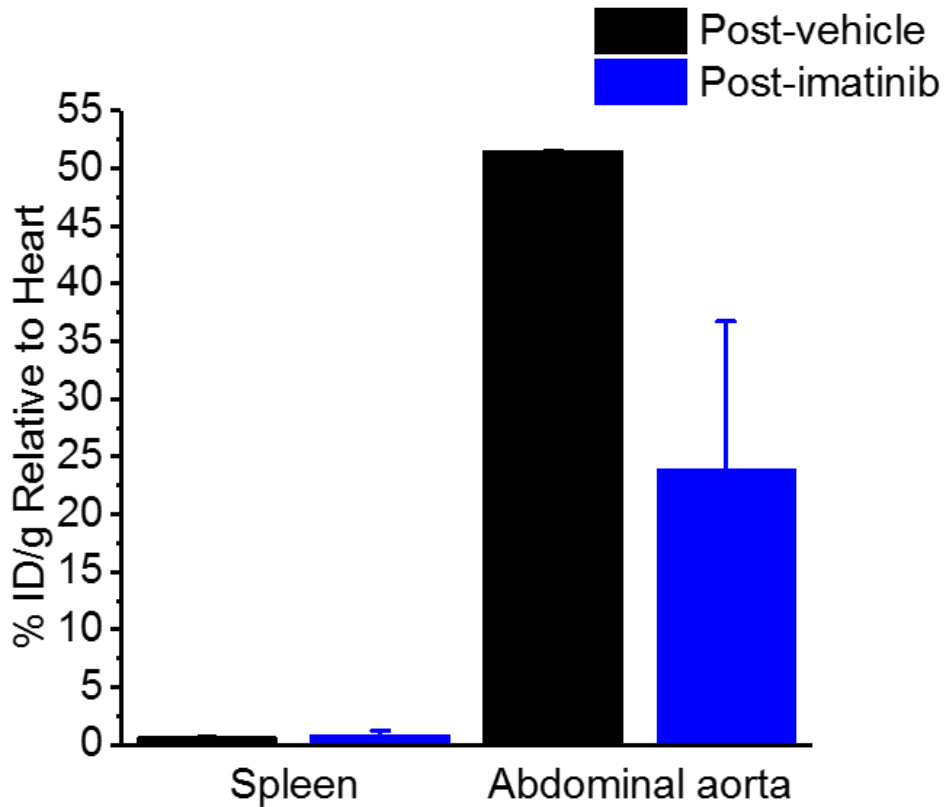


Figure 3.40 *Ex vivo* $[^{18}\text{F}]\text{FLT}$ uptake in AngII AAA was reduced following imatinib treatment than that following vehicle treatment. *Ex vivo* $[^{18}\text{F}]\text{FLT}$ uptake in the spleen and abdominal aorta normalised to uptake in the heart following vehicle ($n=1$) and imatinib ($n=2$) treatment.

3.8 Summary and conclusions

This chapter presented critical experiments conducted to explore if [^{18}F]FLT uptake could be observed in experimental murine models of AAA. The proportion of Ki67-positive nuclei was shown to be the greatest in the PPE and AngII AAA models and is correlated with aortic volume in the AngII AAA model. Uptake of [^{18}F]FDG was investigated in saline controls and the AngII AAA model, revealing variable aneurysmal uptake. Myocardial [^{18}F]FDG uptake was observed in all animals, with significantly greater uptake in AngII AAA mice. Furthermore, the uptake of [^{18}F]FLT was explored in healthy controls to establish control data and validate the use of [^{18}F]FLT as a cell proliferation marker in a non-disease control model. Finally, and most importantly, [^{18}F]FLT PET/CT appears to be a feasible modality to visualise and quantify cell proliferation in the AngII AAA model. This was further validated by *ex vivo* [^{18}F]FLT uptake in AAA, which was correlated with aortic volume 14 days post-induction of AAA. The expression levels of TK-1, the substrate of [^{18}F]FLT, and the transporters that carry [^{18}F]FLT into cells are also increased in the 14-day AngII AAA model, mirroring the *in vivo* [^{18}F]FLT PET data. The [^{18}F]FLT results in the AngII model could not be positively replicated in the PPE model. An exploratory study demonstrated that [^{18}F]FLT PET/CT may be used to visualise a decrease in the proliferative signal in the AngII AAA model following 3 doses of imatinib; however, these results must be interpreted with caution owing to the small sample sizes.

Chapter 4 Discussion

The main objective of this thesis was to assess the feasibility of using [^{18}F]FLT PET/CT to visualise and quantify cell proliferation in the AngII AAA mouse model. In 14-day AngII-induced AAA compared to 28-day AngII-induced AAA and saline-infused controls, the [^{18}F]FLT PET signal was found to be significantly increased, along with greater [^{18}F]FLT counts in excised aortic tissue, which correlate with aortic volume. The expression of the [^{18}F]FLT substrate TK-1 and [^{18}F]FLT transporters ENT-1, ENT-2, CNT-1, and CNT-3 are also increased in 14-day AngII AAA than in 28-day AngII AAA and saline controls. These findings collectively suggest an early period of cell proliferation in the AngII AAA murine model, which is detectable using PET/CT. Some key findings are discussed in this chapter, including the evidence of cell proliferation and an early active growth phase, the correlation between aortic volume and cell proliferation, and features of PET/CT image analysis that may be improved to generate even more robust results. These key aspects are further discussed in the context of clinical applications to highlight the long-term translatability of the findings of this thesis. This chapter concludes with a discussion of areas for future research and a brief summary.

It is well known that the AngII AAA mouse model exhibits a number of features that pose a challenge to the type of experiments described in this thesis, wherein large numbers of subjects are required to optimally utilise both the expensive bespoke radiotracer production and time on the PET/CT scanner: (i) the AngII model has a high rate of mortality due to aneurysm rupture, with most deaths occurring within the first 7 days following mini-pump implantation (Cao et al., 2010); (ii) a proportion of animals will not respond to AngII infusion to form an aneurysm (i.e. non-responders); and (iii) tail vein injection for radiotracer delivery in the AngII model was more challenging than in wildtype C57BL6/J mice, and some animals needed to be excluded because of failure of radiotracer delivery via the fragile and poorly accessible tail vein. To overcome (i–iii), the sample sizes at the start of the experiments were overestimated to take account of estimated losses due to aortic rupture, non-response, and technical problems. However, to achieve this, ApoE^{-/-} mice had to be bought from commercial suppliers, as sufficient numbers could not be guaranteed from the University's internal breeding programme. During the project, the main supplier discontinued breeding in the UK, and the animals had to be imported from the EU, posing

a significant economic challenge. Therefore, the sample sizes in this study were relatively small.

4.1 Histological evidence of cell proliferation in AAA

The first finding in the present study was evidence of a significantly increased proportion of cells with Ki67-positive nuclei in the suprarenal abdominal aortic wall from AngII-infused ApoE^{-/-} mice compared to those from saline-infused controls with a relative difference of approx. 200%, which was positively correlated with aortic volume. This result indicated that cell proliferation is indeed upregulated in the AngII AAA model. This is an important finding to justify the use of an expensive tool like [¹⁸F]FLT PET/CT later in the study to test its feasibility in visualising and quantifying the observed cell proliferation. Ki67 staining is a well-established method to identify proliferative cells, and [¹⁸F]FLT is a marker of cell proliferation; in line with this, the correlation between [¹⁸F]FLT uptake and Ki67 positivity has been demonstrated in several tumour models (Grierson and Shields, 2000, Salskov et al., 2007). Ki67 is an extensively utilised marker for cell proliferation in laboratory and clinical studies, and its utility has been demonstrated in detecting proliferative activity in numerous cell types in various diseases. In the present study, significantly greater proportions of Ki67-positive nuclei were observed in tissues from three different AAA murine models than that from saline control tissue. This is in line with reports of increased Ki67 positivity in patients with AAA, reflecting VSMCs, endothelial cells, and macrophages based on combined staining for anti- α -smooth muscle actin, cluster of differentiation (CD)-31, and CD68, respectively (Cafueri et al., 2012, Ryer et al., 2015). In terms of other non-aneurysmal diseases, positive Ki67 expression is observed in systemic lupus erythematosus in association with disease activity (Hudspeth et al., 2019), and positive Ki67 staining has also been noted in human and ApoE^{-/-} murine atherosclerotic lesions, wherein the proliferating cells are suggested to be rich in macrophages and inflammatory cell infiltrates in the active growth phase of lesion development, eventually leading to localised apoptosis; however, the exact cell types contributing to the disease process remain mostly uncharacterised, similar to that in AAA (Lhoták et al., 2016). The heightened Ki67 positivity observed in the present study is also similar to that observed in human prostate carcinoma (Keshgegian et al., 1998, Claudio et al., 2002), follicular thyroid tumours (Mu et al., 2018), severe cervical cancer lesions (Silva et al., 2017), and breast cancer (Qiu et al.,

2019). Therefore, the positive Ki67 data in the AngII AAA mouse samples suggest that there is indeed a proliferative phase in the AngII AAA model.

4.2 Expression of key players in the [¹⁸F]FLT mechanistic pathway

In line with the Ki67 data, the level of TK-1 expression was significantly increased in 14-day AngII AAA tissue than in saline control tissue with a relative difference of approximately 151%, followed by a decrease to a 78% relative difference in 28-day AngII AAA tissues, supporting the notion that cell proliferation is an event that occurs during the progressive phase of AAA in this model. [¹⁸F]FLT is a substrate for cytoplasmic TK-1, which has been demonstrated as a proliferation biomarker in leukaemia, Hodgkin's and non-Hodgkin's lymphoma, lung carcinoma, and breast cancer, amongst other cancers (Zhou et al., 2013). Furthermore, studies of TK-1 expression in cancer have revealed its associations with tumour stage, histological grade, metastasis, size, and distant and local recurrence (He et al., 2000, Mao et al., 2002, He et al., 2006, Aufderklamm et al., 2012, Nisman et al., 2013). The (i) overexpression of TK-1 and (ii) its correlation with the Ki67 proliferation index have also been demonstrated in various cancers (Mao et al., 2005, Chen et al., 2013, Bagegni et al., 2017).

In addition to TK-1, the expression levels of the equilibrative and concentrative transporters ENT-1, ENT-2, CNT-1, and CNT-3 were found to be significantly increased in 14-day AngII AAA tissue compared to those in saline control tissues with relative differences of 160–185%, followed by a decrease to 45–90% relative differences in 28-day AngII AAA tissues. These transporters contribute to nucleoside homeostasis, and as they are responsible for the cellular uptake of some nucleoside-based drugs, they may be valuable in nucleoside-derived therapy (Molina-Arcas et al., 2009, Jiraskova et al., 2018). These nucleoside transporters are also reported to influence [¹⁸F]FLT uptake; Paproski *et al.* previously characterised [¹⁸F]FLT transport by these transporters in cancer cell lines and demonstrated that they contribute to [¹⁸F]FLT uptake, with ENT-1 showing the most significant expression (Paproski et al., 2008, Paproski et al., 2010). There is an established association between [¹⁸F]FLT uptake and proliferation- or thymidine-associated marker expression in various cancers, some of which include Ki67 expression in breast cancer, CD8 and Ki67 expression in metastatic prostate cancer, Ki67 and TK-1 expression in lung cancer, and proliferating cell nuclear antigen and TK-1 expression in fibrosarcoma; these

associations are interesting to draw parallels with correlations amongst [¹⁸F]FLT uptake and the expression of TK-1, ENT-1, ENT-2, CNT-1, and CNT-3 observed in AAA (Barthel et al., 2003, Brockenbrough et al., 2011, Woolf et al., 2014, Scarpelli et al., 2019). Furthermore, concomitant malignancies have been reported in up to 14% of AAA cases, of which most involve colorectal cancer (Jibawi et al., 2011). Although it might be ambitious to propose that cancers and AAA involve similar proliferative mechanisms, further studies are warranted to determine whether significant commonalities exist between their pathogeneses. Considering our current understanding of [¹⁸F]FLT in cancer progression and proliferation, the findings of these proteins being upregulated and expressed in AngII AAA tissue support the notion of proliferation occurring at an early stage of AAA development.

4.3 [¹⁸F]FLT uptake in the AngII AAA model

Given the significantly high proportion of Ki67-positive nuclei at the end of the period of AngII infusion (28 days post-implantation of the mini-pump), [¹⁸F]FLT PET/CT was planned to be performed on day 28. As this experiment was complex and expensive, the decision was made to perform an additional scan at a second time point (i.e. day 14) to identify if there was a change in radiotracer uptake over time in the AngII AAA disease course. In this study, the uptake of [¹⁸F]FLT in AAA was successfully demonstrated for the first time. Interestingly, the uptake significantly decreased by a relative difference of 55% between days 14 and 28 of the model, suggesting that there may be a decrease in proliferative activity in the late stage of AAA. Furthermore, the alignment of [¹⁸F]FLT results with Ki67 staining data and supporting evidence from Western blotting for key players in the [¹⁸F]FLT mechanistic pathway support the PET/CT observations and raise the potential of using [¹⁸F]FLT as a tool to observe proliferative activity in *in vivo* model systems or indeed in humans.

As described in section 1.3.5, AAA formation and progression rely on multiple contributing factors. These include changes in the mechanical properties of the vessel wall, such as wall stress and elasticity; inflammatory cell infiltration of the aortic wall; increased autoimmunity; enhanced oxidative stress; vascular remodelling; degradation of the ECM; and microcalcification. This multifactorial nature corresponds to many cells contributing to the AAA pathophysiology, such as lymphocytes, mast cells, macrophages, ECM proteins, VSMCs, and endothelial cells, amongst others (Wang et al., 2014, Kuivaniemi et al., 2015, Sun et al., 2018). Reports of the precise cell types that may contribute to the early-stage proliferative signal are largely

inconclusive, owing to the wide variety of implicated cell types and difficulties in accurately identifying them *in vivo* using antibody staining. Although the experiments presented in this thesis do not concretely prove that the proliferative signal originates from VSMCs, the findings are in line with reports of VSMC apoptosis, medial wall thinning, and degeneration in late-stage AAA, which are critical for aortic dilatation and rupture (Lopez-Candales et al., 1997, Henderson et al., 1999, Ailawadi et al., 2009, Riches et al., 2013, Salmon et al., 2013, Clement et al., 2019, Quintana and Taylor, 2019). These events are associated with VSMC phenotypic switching early in AAA development. The reduced density of VSMCs in late-stage AAA is suggested to be the result of apoptosis, evidenced by the observation of apoptotic VSMCs in the medial layer of AAA in humans (Rowe et al., 2000, Kuivaniemi et al., 2015). When the rate of VSMC apoptosis exceeds the rate of VSMC proliferation, the number of SMC layers in the aortic wall decreases, eventually leading to rupture. When VSMC proliferation is promoted via anti-inflammatory treatment with interleukin-10, the degradation of SMCs is inhibited, leading to a delay in the development of AAA in rabbits (Zhu et al., 2019). Aneurysm growth is also inhibited in ApoE^{-/-} mice following treatment with the xanthine derivative KMUP-3, which inhibits AAA phenotypic switching and apoptosis (Lai et al., 2020). Moreover, studies have demonstrated VSMC proliferation and the role of dedifferentiated medial VSMCs in neo-intimal development following vascular injury (Herring et al., 2014, Roostalu et al., 2018). These findings propose an important role for VSMCs in AAA development; however, further experiments are warranted to determine the precise contributions of other cell types and regardless of the implicated cell types, it is suggested that the pathobiology differs between early- and late-stage AAA.

The overall findings of an increase in proliferation-associated biomarkers at 14 days followed by a decrease at 28 days point to an active period of cell proliferation early in the AngII-infused AAA disease course that then leads to replicative senescence and reduced proliferative activity late in the disease course. 'Replicative senescence' was first described in the context of human fibroblasts in culture and reflects the process that limits the proliferative activity of cells, as cells have a finite life span in which division occurs (Campisi, 1997). Cell senescence has been reported in patients with AAA and patients manifesting risk factors of AAA (Liao et al., 2000, Gacchina et al., 2011), and senescence can also progress to apoptosis (Thompson et al., 1997). In addition, accelerated replicative senescence comprises a distinct phenotype of VSMCs in human AAA compared to that of VSMCs in the non-

aneurysmal inferior mesenteric artery, indicating that senescence may play a role in the VSMC reduction that is specifically observed in AAA (Liao et al., 2000, Riches et al., 2018). Furthermore, this late-stage VSMC reduction may reflect the increased accumulation of ECM degradative proteins, the production of which is stimulated by VSMCs, as well as endothelial cells, adventitial fibroblasts, and inflammatory cells that are adherent to the ECM. In AAA, the amount of proteins that confer aortic wall integrity, such as collagen and elastin, is reduced compared to that in normal aortae (Lin et al., 2018, Quintana and Taylor, 2019). An imbalance between proteolytic enzymes, such as MMPs, and their inhibitors contributes to this reduction; correspondingly, various MMPs have been shown to be produced by VSMCs, and a marked increase in MMP expression has then been shown to be associated with a reduction in VSMCs with AAA disease progression (Knox et al., 1997, Mao et al., 1999, Kadoglou and Liapis, 2004, Fanjul-Fernández et al., 2010, Courtois et al., 2013, Lin et al., 2018, Quintana and Taylor, 2019). This imbalance leads to a disruption in the equilibrium between ECM synthesis and degradation, which then influences the course of expansion and rupture of AAA. For example, slow-growing aneurysms may reflect ECM synthesis mechanisms counterbalancing the ECM degradation mechanisms. Acceleration of aneurysm growth and rupture in the AAA disease course may result from this equilibrium shifting towards degradation. Therefore, it is encouraging that the data presented in this thesis suggest a period of decreased proliferative activity late in the AAA disease course, which may suggest that VSMCs may partially contribute to the proliferative signal being detected.

Ex vivo gamma counting of whole organs, which provided definitive evidence of the [¹⁸F]FLT hotspots noted on the PET/CT images, revealed 160% greater [¹⁸F]FLT uptake in 14-day AngII AAA compared to saline control aortae. All the counted organs also demonstrated greater uptake of [¹⁸F]FLT compared to that in the saline control organs (Figure 3.29). This observation may be explained by the effects of AngII on widespread cell proliferation in the AngII-infused model of AAA. As introduced in section 1.4.1.1, AngII mediates growth processes and has been shown to induce the activity of other vasoactive factors, such as endothelin, which further confer growth-altering effects in cells of the kidneys, lungs, and intestines, among other organs (Johnson et al., 1992, Wolf and Wenzel, 2004, Slice et al., 2005, Wang et al., 2015). Regardless of the effects of AngII in other organs, it is encouraging and convincing to observe such a significant increase in proliferative activity as measured by [¹⁸F]FLT uptake in the aneurysmal aorta

of the classical AngII-infused model of AAA. In addition to the abdominal aorta, the spleen may be another interesting region for analysis. As expected, [¹⁸F]FLT uptake was observed in the spleen of all animals. Significant differences in splenic SUVs were not observed between saline control and 14-day AngII AAA mice. However, in 28-day AngII AAA mice, the splenic SUVs showed a 33% relative difference and a slightly greater SEM. Further investigation of this splenic uptake in a greater number of 28-day AngII AAA mice is warranted to better understand if long-term AAA disease is associated with changes in proliferative activity in the spleen. The spleen is a major repository of proliferative cells, as monocytes differentiate into dendritic cells and macrophages in tissue healing and repair processes (Drutman et al., 2012); thus, [¹⁸F]FLT uptake in the spleen is expected. Splenic uptake of [¹⁸F]FLT was also noted by Ye *et al.* in atherosclerotic mice, although with a difference in splenic SUVs between wildtype and ApoE^{-/-} mice (Ye et al., 2015). Furthermore, in male patients with AAA, maximal aortic diameter and spleen volume exhibit a strong positive correlation (Li et al., 2017); however, more data are needed to suggest that spleen enlargement may play a role as an indicator of AAA progression and rupture. The variations in splenic SUVs observed in this study are in line with these previous findings, indicating that further research on the association between splenic activity and AAA progression is warranted.

Finally, a positive correlation was observed between *ex vivo* [¹⁸F]FLT uptake and aortic volume at 14 days. Given the limitations of this study, there was no evidence to suggest that aortic volume remains positively correlated specifically with [¹⁸F]FLT uptake in later stages of AAA development, while other mechanisms may contribute to changes in aortic volume with further AAA progression. Nonetheless, this result is important in the context of early-stage AAA management post-USS screening, as [¹⁸F]FLT uptake may provide an additional dimension of information about AAA progression: proliferative activity in relation to early aortic volume changes. The utility of this additional dimension has considerable potential in risk assessment; for example, a small but highly active AAA may warrant treatment, whereas an indolent large AAA may not. Similar to the way in which SUV thresholds of [¹⁸F]FDG uptake are currently implemented in the cancer field to classify tumour grade/aggressiveness and guide patient intervention, there may thus be a role for [¹⁸F]FLT uptake thresholds in AAA management. Following from the previous example, a patient exhibiting greater aneurysmal [¹⁸F]FLT uptake (and thus harbouring early-stage AAA) might benefit more from an anti-proliferative drug therapy, compared to a patient exhibiting lower

[¹⁸F]FLT uptake (and thus harbouring late-stage AAA) who would benefit from surgical repair. Therapy for AAA currently involves patient health optimisation and surgical intervention. An added layer of information may pave the way for trialling medical therapies as opposed to implementing surgery-only options based on physical aneurysm characteristics. However, to confirm the correlation between [¹⁸F]FLT uptake in the abdominal aorta and AAA severity, further longitudinal preclinical investigations of aneurysmal [¹⁸F]FLT uptake and its associations with aortic size at baseline, 14 days, and 28 days in the AngII AAA model are needed, a key limiting aspect in the current study due to the high rates of mortality, non-response to AngII, and failure of intravenous radiotracer administration, as well as the significantly high costs of the AngII AAA mouse model. Using the same cohort of mice from study initiation (i.e. day of mini-pump implantation) to completion (i.e. day 28 of AngII infusion) would yield robust results, although large numbers of animals would be needed to mitigate the aforementioned challenges. In terms of clinical research, a large-scale analysis of patient data to precisely determine the relationship between aortic sizes based on USS screening and [¹⁸F]FLT uptake on PET would facilitate a clearer understanding of whether [¹⁸F]FLT SUVs might be used as informative indicators of size and/or AAA stage.

4.4 PET image analysis

It is worth noting here that the abdominal aorta and spleen are located in close proximity to the urinary bladder and kidneys; the two latter organs readily take up [¹⁸F]FLT (as all [¹⁸F]-based radiotracers are renally excreted), which consequently raises the possibility of partial volume effects due to signal spill-over into the aortic ROI. Moreover, the combination of the PET scanner's spatial resolution (1.55 mm) (Sanchez et al., 2013) and diameter of the aneurysmal aorta (1.5–3 mm) made it difficult to definitively study [¹⁸F]FLT uptake within specific regions of the aortic wall. Nonetheless, to validate that the PET/CT signal was indeed originating from the aortic wall, *ex vivo* [¹⁸F]FLT gamma counting of whole aortae was performed following PET scanning, and the [¹⁸F]FLT PET/CT and 3D USS datasets were manually co-registered. To mitigate the risk of introducing significant partial volume effects in the image analysis results, SUV_{max} was the parameter of choice when reporting PET data in presentations or publications, for example. The SUV_{max} is prone to being affected by image noise, whilst SUV_{mean} has high inter-observer variability (Büyükdereli et al., 2016); therefore, applying a percentage threshold of the maximum voxel values

within preselected ROIs is an approach that may help exclude regions of low radiotracer uptake. Determining optimal quantification metrics to assess PET images of AAA is an ongoing effort (Akerlele et al., 2020).

A pilot investigation of the effects of applying different SUV thresholds and ROI definitions on the resultant SUVs in the present study revealed that the SUV_{mean} , SUV_{40} , SUV_{50} , SUV_{90} , and SUV_{max} of abdominal aortic uptake of [^{18}F]FLT in both saline controls and AngII AAA mice were significantly different between fixed-size and manually drawn ROIs; meanwhile, the SUV_{70} was not significantly different between the two types of ROIs. A potential explanation of these findings may lie in the presumption that applying a 70% SUV threshold may be an optimal balance between the SUV_{max} , which is predominantly affected by noise, and SUV_{mean} , which is predominantly affected by partial volume effects in a given ROI. Furthermore, these findings are in line with supporting evidence to suggest that applying threshold values of 70–75% may yield consistent quantitative outcomes of lesion uptake throughout a longitudinal study period, regardless of changes in lesion morphology (Krak et al., 2005). However, conversely, other studies have found that thresholding values of 40–43% may be adequate to segment lesions (Ford et al., 2006, Sher et al., 2016), implicating the need for further studies to achieve conclusive results of optimal thresholds. In the present study, the resultant SUVs corresponding to the manually drawn ROIs showed less variability compared to those corresponding to the fixed-size ROIs, which may have been attributed to the fact that the manually drawn ROIs were generated uniquely to each dataset that i) avoided the edges of the region of uptake to minimise partial volume effects, ii) were in accordance with the morphology of the aneurysms, and iii) could be adapted to individual differences in the anatomy. On the other hand, the fixed-size ROIs did not account for these factors, as they were simply sized according to the maximum aortic diameter acquired in the study model without individual considerations of ROI edges, leading to more variable resultant SUVs, because of the included voxels being independent of the lesion size and shape. In addition, implementing fixed-size ROIs was significantly more time-efficient and a more objective approach than manually drawing ROIs. As a result, future research on ROI definitions will need to resolve the issues that manually drawn ROIs are currently able to overcome.

The overall findings are likely to have clinical implications when analysing large datasets and images containing regions of low uptake; in these cases,

it may be more beneficial to determine the SUV_{70} for consistency between different approaches of ROI generation. Delineating lesions using fixed-size ROIs is a simple, relatively quick, semi-automatic approach that is correlated with less sensitivity to partial volume effects. Meanwhile, a potential problem associated with using the fixed-size method in the context of AAA is the variability in the size and shape of aneurysms across different patients, reflected in the variability in radiotracer uptake, in turn leading to differences in the proportion of an aneurysm contained within a fixed-size ROI. This may particularly cause difficulties in longitudinal studies, wherein the size and shape of aneurysms are likely to alter over time. Although studies have been conducted to determine the size of a fixed-size ROI that would result in the least deviation from the actual radioactivity concentration (Nahmias and Wahl, 2008, Weber et al., 2015), these issues are minimised when implementing manually drawn ROIs.

4.5 Anti-proliferative treatment for AAA

Currently, no targeted pharmacological treatments for AAA are used in clinical practice; EVAR and OAR remain the mainstay of current interventions. The evidence of a period of active cell proliferation in the AngII AAA model is encouraging to test the effectiveness of anti-proliferative therapies in targeting AAA, which was the original motivation for investigating cell proliferation in the present study. Imatinib, also known as Gleevec[®], is a tyrosine kinase inhibitor that is suggested to play a role in the inhibition of T lymphocyte proliferation and mast cell activation, both of which contribute to AAA development (Juurikivi et al., 2005, Seggewiss et al., 2005, Shimizu et al., 2006, Sun et al., 2007). Imatinib has also been demonstrated to inhibit endothelial cell population growth, platelet-derived growth factor (PDGF) receptor activation, and the proliferation and migration of VSMCs, which are key players in AAA formation (Vrekoussis et al., 2006, Hacker et al., 2007, Ballinger et al., 2010). Based on these findings, imatinib as a treatment for AAA was tested by Vorkapic *et al.* using the AngII AAA murine model and human samples of AAA tissue. They demonstrated that imatinib attenuates AAA development by inhibiting the recruitment of T lymphocytes and mast cells and SMC-mediated processes (Vorkapic et al., 2016). Drawing inspiration from this study but with a focus on early changes in cell proliferation post-treatment, the present pilot study demonstrated increased abdominal aortic [¹⁸F]FLT uptake in the AngII AAA model at 14 days, which was then shown to decrease by 89% following only 3 doses of imatinib. An important limitation in the present results was the small sample

size; the high rate of deaths immediately after radiotracer injection and unusually high bone uptake in this cohort led to the suspicion that the radiotracer stock might have been supplied from an unstable batch, resulting in unintended interactions once injected. Anti-proliferative treatments, such as imatinib, might be a promising therapeutic option for early-stage AAA, although further preclinical studies with larger numbers are needed to justify and validate this. The fundamental aim of treating AAA is to prevent aortic rupture and its corresponding high rate of mortality. Given that the only treatments currently offered (EVAR and OAR) are plagued with considerable postoperative complications, such as the need for re-repair, occurrence of endoleaks, and postoperative morbidity and mortality, there is a precedence for identifying less invasive means to treat AAA. In this context, a prevailing issue with the prospect of imatinib as a treatment option for patients with AAA is the reduced ability to detect AAA in patients during the early, proliferative growth stage of the disease. Furthermore, as a chemotherapeutic agent, imatinib is likely to confer toxic effects on non-aneurysmal proliferative cells, such as cells of the spleen and bone marrow, and also lead to adverse side effects, such as gastrointestinal disruption and hair loss. Nevertheless, the present findings provide further validation of the increased [^{18}F]FLT signal observed at the 14-day time point in this model and demonstrate that [^{18}F]FLT PET/CT can be used to detect changes in cell proliferation that are induced by short-term anti-proliferative treatment. Regardless of whether imatinib becomes a treatment option for AAA, it may be beneficial to adopt oncologic clinical approaches, such as using [^{18}F]FLT PET/CT as a tool to stratify patients in the pursuit of personalised medicine and to evaluate the response to a less toxic equivalent of chemotherapy.

It is important to recognise that proliferation in AAA may not be solely detrimental, and thus, the use of anti-proliferative agents may not be a 'one-off' treatment option. As outlined in sections 1.3.5 and 4.3, accumulating evidence suggests that there is an active proliferative phase early in the AAA disease course. Halting this activity via anti-proliferative agents may indeed slow down or delay AAA progression. However, when also considering other factors contributing to aortic wall stress, if the aortic wall integrity has already been compromised, then it may be beneficial to leave proliferation unhindered in an attempt to stabilise the aortic wall and prevent further degradation. Thus, anti-proliferative therapy could ideally be determined on a patient-to-patient basis, according to AAA progression and aortic wall stability in those who show abdominal aortic [^{18}F]FLT uptake on PET imaging. With insignificant aortic expansion and low wall stress, anti-

proliferative therapy may not be as effective because the proliferative activity may protect the wall from further degradation. However, in cases of rapid aortic expansion and increased wall stress, patients may benefit from anti-proliferative therapy to inhibit further wall weakening and degradation leading to rupture. In this way, with an imminent need for pharmacological treatment options for AAA, patient-specific therapy decisions incorporating different biomarkers hold significant potential.

4.6 Future directions

AAA remains a significant cause of mortality in adults as a result of aortic rupture. USS provides information regarding anatomical changes in AAA size and shape; however, there remain gaps in our knowledge of the molecular changes that precede physical manifestation of the disease and in our ability to visualise these pathological mechanisms at the molecular level. A better understanding of these functional changes in early-stage AAA may help stratify patients based on rupture risk early in the disease course and guide appropriate treatment selection. Despite the large number of AAA studies conducted, our knowledge of AAA pathobiology is incomplete, and there remains a lack of concrete data to translate preclinical findings to clinical practice. Although several risk factors and potential contributors to the disease process have been identified, these are not yet sufficiently predictive when applied to individual patients.

As we move forward, a shift away from aortic diameter as the main indicator of AAA repair is perhaps required. There is a need to investigate the feasibility of alternative markers of AAA rupture that may be more reliable, such as circulating biomarkers, MRI findings, and haemodynamic parameters. In this context, the pathophysiology of AAA in humans remains partially clear and represents an ever-growing area in cardiovascular research. This is largely due to the fact that studies of AAA in humans are predominantly limited to using late-stage aortic tissue obtained during surgery, owing to the asymptomatic presentation of early-stage AAA. A wide array of imaging techniques have been and are currently being explored for applications in AAA diagnosis and management. Anatomical modalities have reigned over the past few decades in both preclinical and clinical imaging of AAA. Meanwhile, functional imaging is gaining increasing importance for AAA, and several new functional imaging studies of AAA are anticipated in forthcoming years. Non-invasive molecular imaging of AAA is significantly promising for clinical translation, particularly in facilitating patient risk stratification. It is important to note that anatomical and molecular imaging

techniques are not competitive; rather, they are complementary in their usefulness for AAA management. Thus, non-invasive imaging modalities such as PET offer a means to detect and evaluate components of potentially contributing pathways in patients to better understand the development of AAA beyond morphological features. The overall findings of the present study open up several avenues for further research to elucidate the pathobiology of AAA beyond the scope of this thesis.

4.6.1 Considerations of the AngII AAA mouse model

Aortic tissues cannot be obtained from patients at early stages of the AAA disease course; this creates an evident need for appropriate laboratory models to study early-stage mechanisms. The evidence of heightened cell proliferation in the 14-day AngII AAA mouse model is encouraging to investigate changes in the proliferative activity at more time points in the disease course using [¹⁸F]FLT PET/CT. With less stringent economic restrictions, it would be ideal to image mice of this model at serial time points, i.e. weekly, to track even slight fluctuations in cell proliferation until the aneurysm ruptures. Moreover, the cellular composition of early-stage AAA remains largely unclear owing to the lack of access to early-stage human tissue. Histological staining of early-stage AAA tissues from mice could be performed using markers such as alpha-smooth muscle actin to identify SMCs, FLK1 to identify endothelial cells, collagen, and macrophage markers (e.g., CD45, CD68). The use of mice also facilitates genetic studies, wherein the effects of knocking out or overexpressing a gene can be investigated; some candidate genes to study in the setting of early-stage AAA to further elucidate the cellular composition include those specific for SMCs, such as SM22 α ; MMPs; collagen, such as COL3A1; or elastin, such as ELN (Lin et al., 2018, Quintana and Taylor, 2019).

Although it is clear that preclinical models are invaluable in the progression to clinical studies, whether animal models of AAA accurately represent human AAA remains a point of discussion. With the widespread use of rodent models of AAA, several pathophysiological characteristics of human AAA are mimicked, such as ECM degradation, SMC loss, inflammation, calcification, and neovascularisation (Daugherty and Cassis, 2004). However, when translating the findings of this study to clinical practice, it is important to consider that a notable difference between AAA in humans and AAA in the AngII mouse model is the localisation of the disease in the infra-renal and suprarenal regions of the abdominal aorta, respectively. The suprarenal localisation of AAA is consistently observed in the AngII AAA

murine model (Cao et al., 2010, Rateri et al., 2011, Lu et al., 2015). Meanwhile, regional differences in collagen and elastin content are proposed to contribute to the infra-renal localisation of AAA in humans (Halloran et al., 1995). These points highlight the importance of considering the distinguishing characteristics of different models and species when tailoring AAA investigations to a specific aim. However, because of the lack of data regarding AAA formation in humans due to research being limited to late-stage tissues from patients with confirmed AAA, it remains difficult to assess the comparability of molecular mechanisms between animal models and humans.

Whilst the findings of this study are encouraging, it is important to acknowledge that cell proliferation in patients with AAA likely occurs at a much slower rate than that observed in mouse models of 14-day AngII-induced AAA. This is based on the reported mean rate of AAA growth amongst patients included in the UK Small Aneurysm Trial: 2.6 mm/year (Brady et al., 2004). Another study of AAA growth rates in the Chinese population found that the mean growth rates are 2.8 mm/year in patients with small AAA (aortic diameters 30–49 mm) and 7.5 mm/year in patients with large AAA (aortic diameters ≥ 50 mm) (Huang et al., 2019). The typical spatial resolutions of clinical PET scanners (4 mm) may be insufficient to detect slight changes in [^{18}F]FLT uptake based on slow changes in cell proliferation, like that reported in small AAA (Khalil et al., 2011). Therefore, [^{18}F]FLT PET/CT shows greater potential in stratifying patients, guiding therapeutic trials, and aiding the prediction of AAA-targeted drug response after AAA has been diagnosed, rather than in initial disease detection.

4.6.2 Future studies of calcification

Identifying key pathways in the pathogenesis of AAA warrants the application of additional radiotracers to visualise and quantify other contributing factors. The role of calcification in AAA formation is one active area of research. Calcification, which entails calcium phosphate crystal deposition in the medial vessel wall layer, contributes to mechanical stiffening of the vessel wall and decreased vascular compliance (Wu et al., 2013). Through these structural changes, calcification has been demonstrated to contribute to AAA rupture risk and is increased in patients who exhibit AAA symptoms (Buijs et al., 2013, O'Leary et al., 2015, Chowdhury et al., 2018, Forsythe et al., 2018). Furthermore, apoptosis—as reported in late-stage AAA—involves the production of apoptotic bodies, which play a role in promoting calcification in AAA (Proudfoot et al., 2000).

CT is a useful tool to generate images with detailed anatomical information, particularly of hard tissues such as bone. Thus, calcification is an ideal target for CT imaging of AAA, as evidenced by the use of calcium scoring in the clinic to indicate the narrowing or blockage of coronary arteries due to plaque build-up, which in turn helps assess the severity of coronary artery disease. A retrospective study of patients with TAA or AAA who underwent CT-based calcium scoring revealed that macrocalcification is correlated with greater cardiac and all-cause mortality (Chowdhury et al., 2018). Furthermore, vascular calcification is enhanced in symptomatic AAA and augments AAA rupture risk (Buijs et al., 2013, O'Leary et al., 2015). The most convincing evidence of calcification in AAA is reflected in the SoFIA³ trial, the findings of which suggest that [¹⁸F]NaF PET/CT is an effective tool to identify AAA disease activity in patients, based on the localisation of the radiotracer in regions of microcalcification, which in turn, is a susceptibility marker of aneurysm expansion and rupture early after AAA formation (Forsythe et al., 2018). These findings collectively suggest that calcification can be used as a prognostic marker in patients with AAA to help stratify high-risk patients for risk-reducing interventions. It is then also worth considering the addition of a vascular contrast-enhanced CT or CTA scan, which would yield more detailed anatomical information than plain CT alone, following [¹⁸F]FLT PET/CT. This combination would offer insight into two key molecular processes that contribute to the AAA disease course (i.e. cell proliferation and calcification), thus conferring a more comprehensive assessment of patient prognosis. Additionally, it would be beneficial to perform [¹⁸F]NaF PET/CT of mice with AAA to acquire data that could serve as the preclinical version of the SoFIA³ trial. Preclinical data of [¹⁸F]NaF uptake in AAA have not yet been published, but a study using animal models would be useful to further elucidate the timing of microcalcification in AAA formation and progression.

4.6.3 Prospective studies based on genetic pathways

[¹⁸F]FDG, [¹⁸F]NaF, and [¹⁸F]FLT are some commonly used radiotracers in the clinic for various diseases, largely due to their ease of access and availability. In addition to the array of radiotracers used to investigate AAA as outlined in Table 1.2, there is scope for the development and testing of radiotracers related to pathways of genes identified to play a role in AAA formation and progression. For example, the Arg95 genetic variant of factor XIII-B is associated with an increased risk of AAA (Macrae et al., 2014), suggesting the role of platelets and coagulation factors in AAA

pathogenesis, which represent an important field of study. Radiotracers that are selective for coagulation factors may prove to be useful in elucidating AAA pathogenesis, much like the radiotracer [¹⁸F]ENC2015, which is specific for factor XIIIa and has been used to investigate arterial thrombi in rats (Andrews et al., 2019). The rs6511720 single-nucleotide polymorphism in the low-density lipoprotein receptor gene has also been shown to be a risk factor of AAA, implicating the correlation between AAA and cholesterol homeostasis (Bradley et al., 2013); thus, cholesterol-targeted radiotracers may be informative in the context of AAA. Furthermore, a meta-genome-wide association study by Jones *et al.* confirmed the roles of several risk loci in the following genes that seem to exhibit specificity for AAA than for other cardiovascular diseases: *BCAR3*, *SORT1*, *NOTCH2*, *TDRD10*, *UBE2W*, *CDKN2B-AS1/ANRIL*, *LRP1*, *NAB2*, *FGF9*, and *PLTP* (Jones et al., 2017). The specificities of these genes are promising for the development of radiotracers that specially target AAA-associated gene transcription. For example, *BCAR3* is known to play a role in the development of anti-oestrogen resistance in oestrogen receptor (ER)-positive breast cancer (Wallez et al., 2014). The radiotracer 16a-[¹⁸F]-fluoro-17b-estradiol ([¹⁸F]FES) has recently been demonstrated to be an effective PET radiotracer to detect ER-positive breast cancer (Liu et al., 2019); thus, based on the genetic link, [¹⁸F]FES may also have PET imaging applications in patients with AAA harbouring upregulated *BCAR3* expression. Moreover, determining the correlation between the expression of these susceptibility genes and [¹⁸F]FLT uptake in AAA may be informative. For example, *CDKN2B-AS1/ANRIL* is a tumour suppressor that is also consistently associated with cardiovascular diseases and has been shown to influence cell proliferation, senescence, and apoptosis via epigenetic mechanisms (Congrains et al., 2013). A patient that exhibits both upregulated *CDKN2B-AS1/ANRIL* expression and increased [¹⁸F]FLT uptake may have a high-risk AAA that would benefit from immediate therapeutic intervention as opposed to a patient with only one of these risk factors.

4.6.4 Potential studies related to angiogenic and immune mechanisms in AAA

Angiogenesis is another mechanistic area that provides a basis for PET imaging targets. AAA is associated with a marked angiogenic response and enhanced medial neovascularisation (Thompson et al., 1996, Choke et al., 2006). Various pro-angiogenic factors have been implicated in the formation and progression of AAA. In particular, vascular endothelial growth factor

(VEGF) has been shown to promote AngII-induced AAA formation in ApoE^{-/-} mice (Kobayashi et al., 2002). A VEGF-specific PET radiotracer, ⁸⁹Zr-ranibizumab, has been investigated in human xenograft tumour models and shown to correlate with VEGF status and angiogenesis (Nagengast et al., 2011). In addition, ⁶⁴Cu-DOTA-VEGF₁₂₁ has been demonstrated to reveal VEGF receptor levels in small-animal tumour models (Chen et al., 2009). Another pro-angiogenic factor that has been reported to contribute to AAA is PDGF, the receptors of which are strongly expressed in VSMCs in AAA, and reducing PDGF receptor activation via imatinib has been shown to attenuate AAA formation (Kanazawa et al., 2005, Vorkapic et al., 2016). Meanwhile, the tracer ¹¹¹In-DOTA-Z09591 has been demonstrated to accumulate in regions with increased levels of PDGF receptor expression (Tolmachev et al., 2014). Radiotracers specific for the microRNA-195 family may also be useful to study AAA development, as microRNA-195, which modulates angiogenesis, has been demonstrated to regulate the aortic ECM in murine AAA (Zampetaki et al., 2014). Exploring the usefulness of angiogenesis-specific tracers that have been validated in other disease models in visualising sites of angiogenesis in AAA models may be interesting avenues in preclinical research.

Immune cells, such as lymphocytes, cytokines, and antigen-presenting cells are observed in AAA (Kuivaniemi et al., 2008); however, no dedicated PET studies have been conducted previously to specifically investigate these cell types in AAA. The spleen plays a key role in immunologic functions, being a site of immune cell subsets (Lewis et al., 2019). Thus, the variations in splenic uptake of [¹⁸F]FLT demonstrated in this study may correspond to the distinct varying roles of immune cells at different stages of the AAA disease course. The radiotracer ⁶⁴Cu-DOTA-ipilimumab has been investigated in models of non-small cell lung cancer (Ehlerding et al., 2017). This tracer targets cytotoxic T lymphocyte-associated protein 4, the levels of which are reported to be increased in AAA (Sakthivel et al., 2007), thus making it a potential biomarker for AAA. Additionally, ⁶⁸Ga-pentixafor has been studied in atherosclerotic plaques to image the cytokine receptor CXCR4, which may also be informative in AAA (Hyafil et al., 2017). Immune mechanisms thus remain an active area of AAA research.

4.6.5 Clinical translation

It is well established that PET can be used to evaluate treatment response, in addition to its uses in disease management. Its ability to provide detailed longitudinal information at the molecular level makes it ideal to stratify

patients according to disease risk. In the context of AAA, [¹⁸F]FLT PET may be useful as a management indicator in high-risk patients who have not yet developed AAA. For example, if a patient exhibits many risk factors (such as a man aged 65 years or older with heavy smoking habits and a familial history of AAA) but does not yet physically manifest AAA, then [¹⁸F]FLT PET may be used as a tool to determine if there is evidence of abnormal cell proliferation based on the radiotracer's uptake in the aortic region. Cases of positive [¹⁸F]FLT uptake suggest a role for prophylactic interventions, such as early placement of anti-proliferative drug-eluting aortic stents.

Additionally, [¹⁸F]FLT may be utilised as a predictor of prognosis in patients who are already diagnosed with AAA. For example, if a patient with USS-established AAA does not reveal [¹⁸F]FLT uptake on PET, then he/she may be stratified to a more advanced disease stage, possibly requiring surgical intervention. Conversely, if a patient with established AAA reveals [¹⁸F]FLT uptake on PET, then he/she may be stratified with an earlier disease stage, requiring a less surgically intensive intervention. In this way, [¹⁸F]FLT PET may then play a more significant role in personalised medicine to aid disease risk stratification as opposed to population-level screening.

The clinical translation of radionuclide-based tracers is crucial to maximally benefit patients with AAA. PET imaging is immensely useful in comparison to USS and optical imaging methods; however, much of the preclinical PET research on AAA never proceeds to the clinic. This is largely due to hurdles such as the overwhelming cost of introduction in the clinic, a lack of understanding between preclinical scientists and clinicians, and long-standing regulations. Cooperative partnerships amongst researchers, clinicians, and pharmaceutical chemists are imperative to identify and verify novel imaging markers and more clinically applicable preclinical models, as well as to generate and test tracers, followed by smooth transition for application to patient management. Ultimately, the optimal imaging marker will reveal key aspects of AAA formation in humans, be used for patient risk stratification, and help assess treatment efficacy in novel clinical trials.

4.7 Conclusion

Overall, in this thesis, [¹⁸F]FLT PET/CT was demonstrated to be a feasible modality to visualise and quantify cell proliferation in a classical preclinical model of AAA, the AngII AAA murine model. This method shows great potential as a clinical risk stratification biomarker and in monitoring pharmacological treatment response in patients with AAA. Future studies of PET image analysis would benefit all clinical fields by establishing

quantitative metrics that could yield reliable and consistent results across varying ROI definitions. Prospective studies of PET in the context of AAA would benefit from focussing on the development of PET radiotracers that target alternative molecular pathways involved in the development of AAA disease before its physical manifestation. Until then, 65 years on, two issues remain unresolved: Einstein's unified field theory and how best to manage early-stage AAA.

References

- Aickin, M. and Gensler, H. 1996. Adjusting for multiple testing when reporting research results: the Bonferroni vs Holm methods. *Am J Public Health* **86**(5), 726-728.
- Ailawadi, G., Moehle, C.W., Pei, H., Walton, S.P., Yang, Z., Kron, I.L., Lau, C.L. and Owens, G.K. 2009. Smooth muscle phenotypic modulation is an early event in aortic aneurysms. *J Thorac Cardiovasc Surg* **138**(6), 1392-1399.
- Akerele, M., Mushari, N., Forsythe, R., Syed, M., Karakatsanis, N., Newby, D., Dweck, M. and Tsoumpas, C. 2020. Assessment of different quantification metrics of [18F]-NaF PET/CT images of patients with abdominal aortic aneurysm. *J Nucl Cardiol*.
- Akerele, M.I., Karakatsanis, N.A., Forsythe, R.O., Dweck, M.R., Syed, M., Aykroyd, R.G., Sourbron, S., Newby, D.E. and Tsoumpas, C. 2019. Iterative reconstruction incorporating background correction improves quantification of [18F]-NaF PET/CT images of patients with abdominal aortic aneurysm. *J Nucl Cardiol*.
- Andrews, J.P.M., Portal, C., Walton, T., Macaskill, M.G., Hadoke, P.W.F., Alcaide Corral, C., Lucatelli, C., Wilson, S., Wilson, I., MacNaught, G., Dweck, M.R., Newby, D.E. and Tavares, A.A.S. 2019. Non-invasive in vivo imaging of acute thrombosis: development of a novel factor XIIIa radiotracer. *Eur Heart J Cardiovasc Imaging*.
- Anidjar, S., Salzmann, J.L., Gentric, D., Lagneau, P., Camilleri, J.P. and Michel, J.B. 1990. Elastase-induced experimental aneurysms in rats. *Circulation* **82**(3), 973-981.
- Ashton, H.A., Buxton, M.J., Day, N.E., Kim, L.G., Marteau, T.M., Scott, R.A., Thompson, S.G. and Walker, N.M. 2002. The Multicentre Aneurysm Screening Study (MASS) into the effect of abdominal aortic aneurysm screening on mortality in men: a randomised controlled trial. *Lancet* **360**(9345), 1531-1539.
- Aufderklamm, S., Todenhofer, T., Gakis, G., Kruck, S., Hennenlotter, J., Stenzl, A. and Schwentner, C. 2012. Thymidine kinase and cancer monitoring. *Cancer Lett* **316**(1), 6-10.
- Azuma, J., Maegdefessel, L., Kitagawa, T., Dalman, R.L., McConnell, M.V. and Tsao, P.S. 2011. Assessment of elastase-induced murine abdominal aortic aneurysms: comparison of ultrasound imaging with in situ video microscopy. *J Biomed Biotechnol* **2011**, 252141.
- Bagegni, N., Thomas, S., Liu, N., Luo, J., Hoog, J., Northfelt, D.W., Goetz, M.P., Forero, A., Bergqvist, M., Karen, J., Neumüller, M., Suh, E.M., Guo, Z., Vij, K., Sanati, S., Ellis, M. and Ma, C.X. 2017. Serum thymidine kinase 1 activity as a pharmacodynamic marker of cyclin-dependent kinase 4/6 inhibition in patients with early-stage breast cancer receiving neoadjuvant palbociclib. *Breast Cancer Res* **19**(1), 123.

- Bakris, G.L. and Re, R.N. 1993. Endothelin modulates angiotensin II-induced mitogenesis of human mesangial cells. *Am J Physiol* **264**(6 Pt 2), F937-F942.
- Ballinger, M.L., Osman, N., Hashimura, K., de Haan, J.B., Jandeleit-Dahm, K., Allen, T., Tannock, L.R., Rutledge, J.C. and Little, P.J. 2010. Imatinib inhibits vascular smooth muscle proteoglycan synthesis and reduces LDL binding in vitro and aortic lipid deposition in vivo. *J Cell Mol Med* **14**(6B), 1408-1418.
- Barisione, C., Charnigo, R., Howatt, D.A., Moorlegghen, J.J., Rateri, D.L. and Daugherty, A. 2006. Rapid dilation of the abdominal aorta during infusion of angiotensin II detected by noninvasive high-frequency ultrasonography. *J Vasc Surg* **44**(2), 372-376.
- Barthel, H., Cleij, M.C., Collingridge, D.R., Hutchinson, O.C., Osman, S., He, Q., Luthra, S.K., Brady, F., Price, P.M. and Aboagye, E.O. 2003. 3'-deoxy-3'-[¹⁸F]fluorothymidine as a new marker for monitoring tumor response to antiproliferative therapy in vivo with positron emission tomography. *Cancer Res* **63**(13), 3791-3798.
- Barwick, T.D., Lyons, O.T., Mikhaeel, N.G., Waltham, M. and O'Doherty, M.J. 2014. 18F-FDG PET-CT uptake is a feature of both normal diameter and aneurysmal aortic wall and is not related to aneurysm size. *Eur J Nucl Med Mol Imaging* **41**(12), 2310-2318.
- Bazeli, R., Coutard, M., Duport, B.D., Lancelot, E., Corot, C., Laissy, J.P., Letourneur, D., Michel, J.B. and Serfaty, J.M. 2010. In vivo evaluation of a new magnetic resonance imaging contrast agent (P947) to target matrix metalloproteinases in expanding experimental abdominal aortic aneurysms. *Invest Radiol* **45**(10), 662-668.
- Benz, M.R., Evilevitch, V., Allen-Auerbach, M.S., Eilber, F.C., Phelps, M.E., Czernin, J. and Weber, W.A. 2008. Treatment monitoring by 18F-FDG PET/CT in patients with sarcomas: interobserver variability of quantitative parameters in treatment-induced changes in histopathologically responding and nonresponding tumors. *J Nucl Med* **49**(7), 1038-1046.
- Bhamidipati, C.M., Mehta, G.S., Lu, G., Moehle, C.W., Barbery, C., DiMusto, P.D., Laser, A., Kron, I.L., Upchurch, G.R., Jr. and Ailawadi, G. 2012. Development of a novel murine model of aortic aneurysms using peri-adventitial elastase. *Surgery* **152**(2), 238-246.
- Blanchard, J.F., Armenian, H.K. and Friesen, P.P. 2000. Risk factors for abdominal aortic aneurysm: results of a case-control study. *Am J Epidemiol* **151**(6), 575-583.
- Bloomer, L.D., Bown, M.J. and Tomaszewski, M. 2012. Sexual dimorphism of abdominal aortic aneurysms: a striking example of "male disadvantage" in cardiovascular disease. *Atherosclerosis* **225**(1), 22-28.
- Boellaard, R. 2009. Standards for PET image acquisition and quantitative data analysis. *J Nucl Med* **50 Suppl 1**, 11s-20s.

- Boellaard, R., Krak, N.C., Hoekstra, O.S. and Lammertsma, A.A. 2004. Effects of noise, image resolution, and ROI definition on the accuracy of standard uptake values: a simulation study. *J Nucl Med* **45**(9), 1519-1527.
- Botnar, R.M., Brangsch, J., Reimann, C., Janssen, C.H.P., Razavi, R., Hamm, B. and Makowski, M.R. 2018. In vivo molecular characterization of abdominal aortic aneurysms using fibrin-specific magnetic resonance imaging. *J Am Heart Assoc* **7**(11).
- Bradley, D.T., Hughes, A.E., Badger, S.A., Jones, G.T., Harrison, S.C., Wright, B.J., Bumpstead, S., Baas, A.F., Gretarsdottir, S., Burnand, K., Child, A.H., Clough, R.E., Cockerill, G., Hafez, H., Scott, D.J., Ariens, R.A., Johnson, A., Sohrabi, S., Smith, A., Thompson, M.M., van Bockxmeer, F.M., Waltham, M., Matthiasson, S.E., Thorleifsson, G., Thorsteinsdottir, U., Blankensteijn, J.D., Teijink, J.A., Wijmenga, C., de Graaf, J., Kiemeny, L.A., Wild, J.B., Edkins, S., Gwilliam, R., Hunt, S.E., Potter, S., Lindholt, J.S., Golledge, J., Norman, P.E., van Rij, A., Powell, J.T., Eriksson, P., Stefansson, K., Thompson, J.R., Humphries, S.E., Sayers, R.D., Deloukas, P., Samani, N.J. and Bown, M.J. 2013. A variant in LDLR is associated with abdominal aortic aneurysm. *Circ Cardiovasc Genet* **6**(5), 498-504.
- Brady, A.R., Thompson, S.G., Fowkes, F.G., Greenhalgh, R.M. and Powell, J.T. 2004. Abdominal aortic aneurysm expansion: risk factors and time intervals for surveillance. *Circulation* **110**(1), 16-21.
- Brangsch, J., Reimann, C., Colletini, F., Buchert, R., Botnar, R.M. and Makowski, M.R. 2017. Molecular imaging of abdominal aortic aneurysms. *Trends Mol Med* **23**(2), 150-164.
- Brangsch, J., Reimann, C., Kaufmann, J.O., Adams, L.C., Onthank, D.C., Thone-Reineke, C., Robinson, S.P., Buchholz, R., Karst, U., Botnar, R.M., Hamm, B. and Makowski, M.R. 2019. Concurrent molecular magnetic resonance imaging of inflammatory activity and extracellular matrix degradation for the prediction of aneurysm rupture. *Circ Cardiovasc Imaging* **12**(3), e008707.
- Bridge, K., Revill, C., Macrae, F., Bailey, M., Yuldasheva, N., Wheatcroft, S., Butlin, R., Foster, R., Scott, D.J., Gils, A. and Ariens, R. 2017. Inhibition of plasmin-mediated TAFI activation may affect development but not progression of abdominal aortic aneurysms. *PLoS One* **12**(5), e0177117.
- Brockenbrough, J.S., Souquet, T., Morihara, J.K., Stern, J.E., Hawes, S.E., Rasey, J.S., Leblond, A., Wiens, L.W., Feng, Q., Grierson, J. and Vesselle, H. 2011. Tumor 3'-deoxy-3'-(¹⁸F)-fluorothymidine ((¹⁸F)-FLT) uptake by PET correlates with thymidine kinase 1 expression: static and kinetic analysis of (¹⁸F)-FLT PET studies in lung tumors. *J Nucl Med* **52**(8), 1181-1188.
- Brown, L.C. and Powell, J.T. 1999. Risk factors for aneurysm rupture in patients kept under ultrasound surveillance. UK Small Aneurysm Trial Participants. *Ann Surg* **230**(3), 289-296; discussion 296-287.

Buijs, R.V., Willems, T.P., Tio, R.A., Boersma, H.H., Tielliu, I.F., Slart, R.H. and Zeebregts, C.J. 2013. Calcification as a risk factor for rupture of abdominal aortic aneurysm. *Eur J Vasc Endovasc Surg* **46**(5), 542-548.

Burger, I.A., Huser, D.M., Burger, C., von Schulthess, G.K. and Buck, A. 2012. Repeatability of FDG quantification in tumor imaging: averaged SUVs are superior to SUVmax. *Nucl Med Biol* **39**(5), 666-670.

Büyükdere, G., Güler, M. and Şeydaoğlu, G. 2016. Interobserver and intraobserver variability among measurements of FDG PET/CT parameters in pulmonary tumors. *Balk Med J* **33**(3), 308-315.

Cafueri, G., Parodi, F., Pistorio, A., Bertolotto, M., Ventura, F., Gambini, C., Bianco, P., Dallegri, F., Pistoia, V., Pezzolo, A. and Palombo, D. 2012. Endothelial and smooth muscle cells from abdominal aortic aneurysm have increased oxidative stress and telomere attrition. *PloS One* **7**(4), e35312-e35312.

Campisi, J. 1997. The biology of replicative senescence. *Eur J Cancer* **33**(5), 703-709.

Cao, R., St. Amand, T., Ford, M., Piomelli, U. and Funk, C. 2010. The murine angiotensin II-induced abdominal aortic aneurysm model: Rupture risk and inflammatory progression patterns. *Front Pharmacol* **1**(9).

Chasman, D.I. and Lawler, P.R. 2017. Understanding AAA pathobiology: A GWAS leads the way. *Circ Res* **120**(2), 259-261.

Chen, G., He, C., Li, L., Lin, A., Zheng, X., He, E. and Skog, S. 2013. Nuclear TK1 expression is an independent prognostic factor for survival in pre-malignant and malignant lesions of the cervix. *BMC Cancer* **13**(1), 249.

Chen, K., Cai, W., Li, Z.B., Wang, H. and Chen, X. 2009. Quantitative PET imaging of VEGF receptor expression. *Mol Imaging Biol* **11**(1), 15-22.

Chen, W. and Dilsizian, V. 2015. PET assessment of vascular inflammation and atherosclerotic plaques: SUV or TBR? *J Nucl Med* **56**(4), 503-504.

Chiou, A.C., Chiu, B. and Pearce, W.H. 2001. Murine aortic aneurysm produced by periarterial application of calcium chloride. *J Surg Res* **99**(2), 371-376.

Choke, E., Thompson, M.M., Dawson, J., Wilson, W.R., Sayed, S., Loftus, I.M. and Cockerill, G.W. 2006. Abdominal aortic aneurysm rupture is associated with increased medial neovascularization and overexpression of proangiogenic cytokines. *Arterioscler Thromb Vasc Biol* **26**(9), 2077-2082.

Chowdhury, M.M., Zielinski, L.P., Sun, J.J., Lambracos, S., Boyle, J.R., Harrison, S.C., Rudd, J.H.F. and Coughlin, P.A. 2018. Editor's Choice - Calcification of thoracic and abdominal aneurysms is associated with mortality and morbidity. *Eur J Vasc Endovasc Surg* **55**(1), 101-108.

Chuen, J. and Theivendran, M. 2018. AAA An update. *Aust Fam Physician* **47**, 252-256.

Claudio, P.P., Zamparelli, A., Garcia, F.U., Claudio, L., Ammirati, G., Farina, A., Bovicelli, A., Russo, G., Giordano, G.G., McGinnis, D.E., Giordano, A. and Cardi, G. 2002. Expression of cell-cycle-regulated proteins pRb2/p130, p107, p27(kip1), p53, mdm-2, and Ki-67 (MIB-1) in prostatic gland adenocarcinoma. *Clin Cancer Res* **8**(6), 1808-1815.

Clement, M., Chappell, J., Raffort, J., Lareyre, F., Vandestienne, M., Taylor, A.L., Finigan, A., Harrison, J., Bennett, M.R., Bruneval, P., Taleb, S., Jorgensen, H.F. and Mallat, Z. 2019. Vascular smooth muscle cell plasticity and autophagy in dissecting aortic aneurysms. *Arterioscler Thromb Vasc Biol* **39**(6), 1149-1159.

Comelli, A., Stefano, A., Russo, G., Sabini, M.G., Ippolito, M., Bignardi, S., Petrucci, G. and Yezzi, A. 2018. A smart and operator independent system to delineate tumours in positron emission tomography scans. *Comput Biol Med* **102**, 1-15.

Congrains, A., Kamide, K., Ohishi, M. and Rakugi, H. 2013. ANRIL: molecular mechanisms and implications in human health. *Int J Mol Sci* **14**(1), 1278-1292.

Conlisk, N., Forsythe, R.O., Hollis, L., Doyle, B.J., McBride, O.M.B., Robson, J.M.J., Wang, C., Gray, C.D., Semple, S.I.K., MacGillivray, T., van Beek, E.J.R., Newby, D.E. and Hoskins, P.R. 2017. Exploring the biological and mechanical properties of abdominal aortic aneurysms using USPIO MRI and peak tissue stress: A combined clinical and finite element study. *J Cardiovasc Transl Res* **10**(5), 489-498.

Courtois, A., Makrygiannis, G., El Hachemi, M., Hultgren, R., Allaire, E., Namur, G., Hustinx, R., Defraigne, J.O. and Sakalihasan, N. 2019. Positron emission tomography/computed tomography predicts and detects complications after endovascular repair of abdominal aortic aneurysms. *J Endovasc Ther* **26**(4), 520-528.

Courtois, A., Nusgens, B., Garbacki, N., Hustinx, R., Gomez, P., Defraigne, J.O., Colige, A.C. and Sakalihasan, N. 2018. Circulating microRNAs signature correlates with positive [(18)F]fluorodeoxyglucose-positron emission tomography in patients with abdominal aortic aneurysm. *J Vasc Surg* **67**(2), 585-595.e583.

Courtois, A., Nusgens, B.V., Hustinx, R., Namur, G., Gomez, P., Somja, J., Defraigne, J.O., Delvenne, P., Michel, J.B., Colige, A.C. and Sakalihasan, N. 2013. 18F-FDG uptake assessed by PET/CT in abdominal aortic aneurysms is associated with cellular and molecular alterations prefacing wall deterioration and rupture. *J Nucl Med* **54**(10), 1740-1747.

Cysouw, M.C.F., Kramer, G.M., Frings, V., De Langen, A.J., Wondergem, M.J., Kenny, L.M., Aboagye, E.O., Kobe, C., Wolf, J., Hoekstra, O.S. and Boellaard, R. 2017. Baseline and longitudinal variability of normal tissue uptake values of [18F]-fluorothymidine-PET images. *Nucl Med Biol* **51**, 18-24.

Daugherty, A. and Cassis, L.A. 2004. Mouse models of abdominal aortic aneurysms. *Arterioscler Thromb Vasc Biol* **24**(3), 429-434.

Daugherty, A., Manning, M.W. and Cassis, L.A. 2000. Angiotensin II promotes atherosclerotic lesions and aneurysms in apolipoprotein E-deficient mice. *J Clin Invest* **105**(11), 1605-1612.

Davies, M.J. 1998. Aortic aneurysm formation: lessons from human studies and experimental models. *Circulation* **98**(3), 193-195.

Davis, M., Harris, M. and Earnshaw, J.J. 2013. Implementation of the National Health Service abdominal aortic aneurysm screening program in England. *J Vasc Surg* **57**(5), 1440-1445.

Day, E., Betler, J., Parda, D., Reitz, B., Kirichenko, A., Mohammadi, S. and Miften, M. 2009. A region growing method for tumor volume segmentation on PET images for rectal and anal cancer patients. *Med Phys* **36**(10), 4349-4358.

Deng, G.G., Martin-McNulty, B., Sukovich, D.A., Freay, A., Halks-Miller, M., Thinnes, T., Loskutoff, D.J., Carmeliet, P., Dole, W.P. and Wang, Y.X. 2003. Urokinase-type plasminogen activator plays a critical role in angiotensin II-induced abdominal aortic aneurysm. *Circ Res* **92**(5), 510-517.

Didangelos, A., Yin, X., Mandal, K., Saje, A., Smith, A., Xu, Q., Jahangiri, M. and Mayr, M. 2011. Extracellular matrix composition and remodeling in human abdominal aortic aneurysms: a proteomics approach. *Mol Cell Proteomics* **10**(8), M111.008128-M008111.008128.

Dobrucki, L.W. and Sinusas, A.J. 2020. Targeted imaging of abdominal aortic aneurysm: Biology over structure. *Circ Cardiovasc Imaging* **13**(3), e010495.

Doyle, B.J., Callanan, A., Burke, P.E., Grace, P.A., Walsh, M.T., Vorp, D.A. and McGloughlin, T.M. 2009. Vessel asymmetry as an additional diagnostic tool in the assessment of abdominal aortic aneurysms. *J Vasc Surg* **49**(2), 443-454.

Drutman, S.B., Kendall, J.C. and Trombetta, E.S. 2012. Inflammatory spleen monocytes can upregulate CD11c expression without converting into dendritic cells. *J Immunol* **188**(8), 3603-3610.

Dutour, A., Decouvelaere, A.V., Monteil, J., Duclos, M.E., Roualdes, O., Rousseau, R. and Marec-Berard, P. 2009. 18F-FDG PET SUVmax correlates with osteosarcoma histologic response to neoadjuvant chemotherapy: preclinical evaluation in an orthotopic rat model. *J Nucl Med* **50**(9), 1533-1540.

Ehlerding, E.B., England, C.G., Majewski, R.L., Valdovinos, H.F., Jiang, D., Liu, G., McNeel, D.G., Nickles, R.J. and Cai, W. 2017. ImmunoPET imaging of CTLA-4 expression in mouse models of non-small cell lung cancer. *Mol Pharm* **14**(5), 1782-1789.

Elefteriades, J.A. and Pomianowski, P. 2013. Practical genetics of thoracic aortic aneurysm. *Prog Cardiovasc Dis* **56**(1), 57-67.

English, S.J., Diaz, J.A., Shao, X., Gordon, D., Bevard, M., Su, G., Henke, P.K., Rogers, V.E., Upchurch, G.R. and Piert, M. 2014. Utility of (18) F-FDG and (11)C-PBR28 microPET for the assessment of rat aortic aneurysm inflammation. *EJNMMI Res* **4**(1), 20.

- English, S.J., Piert, M.R., Diaz, J.A., Gordon, D., Ghosh, A., D'Alecy, L.G., Whitesall, S.E., Sharma, A.K., DeRoo, E.P., Watt, T., Su, G., Henke, P.K., Eliason, J.L., Ailawadi, G. and Upchurch, G.R. 2015. Increased (18)F-FDG uptake is predictive of rupture in a novel rat abdominal aortic aneurysm rupture model. *Ann Surg* **261**(2), 395-404.
- English, S.J., Sastriques, S.E., Detering, L., Sultan, D., Luehmann, H., Arif, B., Heo, G.S., Zhang, X., Laforest, R., Zheng, J., Lin, C.Y., Gropler, R.J. and Liu, Y. 2020. CCR2 positron emission tomography for the assessment of abdominal aortic aneurysm inflammation and rupture prediction. *Circ Cardiovasc Imaging* **13**(3), e009889.
- Fahey, F.H., Kinahan, P.E., Doot, R.K., Kocak, M., Thurston, H. and Poussaint, T.Y. 2010. Variability in PET quantitation within a multicenter consortium. *Med Phys* **37**(7), 3660-3666.
- Fanjul-Fernández, M., Folgueras, A.R., Cabrera, S. and López-Otín, C. 2010. Matrix metalloproteinases: Evolution, gene regulation and functional analysis in mouse models. *Biochim Biophys Acta* **1803**(1), 3-19.
- Favreau, J.T., Nguyen, B.T., Gao, I., Yu, P., Tao, M., Schneiderman, J., Gaudette, G.R. and Ozaki, C.K. 2012. Murine ultrasound imaging for circumferential strain analyses in the angiotensin II abdominal aortic aneurysm model. *J Vasc Surg* **56**(2), 462-469.
- Ferda, J., Baxa, J., Ferdova, E., Kucera, R., Topolcan, O. and Molacek, J. 2019. Abdominal aortic aneurysm in prostate cancer patients: the "road map" from incidental detection to advanced predictive, preventive, and personalized approach utilizing common follow-up for both pathologies. *EPMA J* **10**(4), 415-423.
- Fernandez-Friera, L., Ibanez, B. and Fuster, V. 2014. Imaging subclinical atherosclerosis: is it ready for prime time? A review. *J Cardiovasc Transl Res* **7**(7), 623-634.
- Filardo, G., Powell, J.T., Martinez, M.A. and Ballard, D.J. 2015. Surgery for small asymptomatic abdominal aortic aneurysms. *Cochrane DB Syst Rev*(2), Cd001835.
- Fillinger, M.F., Marra, S.P., Raghavan, M.L. and Kennedy, F.E. 2003. Prediction of rupture risk in abdominal aortic aneurysm during observation: wall stress versus diameter. *J Vasc Surg* **37**(4), 724-732.
- Folco, E.J., Sheikine, Y., Rocha, V.Z., Christen, T., Shvartz, E., Sukhova, G.K., Di Carli, M.F. and Libby, P. 2011. Hypoxia but not inflammation augments glucose uptake in human macrophages: Implications for imaging atherosclerosis with 18Fluorine-labeled 2-deoxy-D-glucose positron emission tomography. *J Am Coll Cardiol* **58**(6), 603-614.
- Ford, E.C., Kinahan, P.E., Hanlon, L., Alessio, A., Rajendran, J., Schwartz, D.L. and Phillips, M. 2006. Tumor delineation using PET in head and neck cancers: threshold contouring and lesion volumes. *Med Phys* **33**(11), 4280-4288.

- Forsythe, R.O., Dweck, M.R., McBride, O.M.B., Vesey, A.T., Semple, S.I., Shah, A.S.V., Adamson, P.D., Wallace, W.A., Kaczynski, J., Ho, W., van Beek, E.J.R., Gray, C.D., Fletcher, A., Lucatelli, C., Marin, A., Burns, P., Tambyraja, A., Chalmers, R.T.A., Weir, G., Mitchard, N., Tavares, A., Robson, J.M.J. and Newby, D.E. 2018. (18)F-sodium fluoride uptake in abdominal aortic aneurysms: The SoFIA(3) study. *J Am Coll Cardiol* **71**(5), 513-523.
- Freestone, T., Turner, R.J., Higman, D.J., Lever, M.J. and Powell, J.T. 1997. Influence of hypercholesterolemia and adventitial inflammation on the development of aortic aneurysm in rabbits. *Arterioscler Thromb Vasc Biol* **17**(1), 10-17.
- Fueger, B.J., Czernin, J., Hildebrandt, I., Tran, C., Halpern, B.S., Stout, D., Phelps, M.E. and Weber, W.A. 2006. Impact of animal handling on the results of 18F-FDG PET studies in mice. *J Nucl Med* **47**(6), 999-1006.
- Gacchina, C., Brothers, T. and Ramamurthi, A. 2011. Evaluating smooth muscle cells from CaCl₂-induced rat aortal expansions as a surrogate culture model for study of elastogenic induction of human aneurysmal cells. *Tissue Eng Part A* **17**(15-16), 1945-1958.
- Gambhir, S.S. 2002. Molecular imaging of cancer with positron emission tomography. *Nat Rev Cancer* **2**(9), 683-693.
- Gandhi, R., Cawthorne, C., Craggs, L.J.L., Wright, J.D., Domarkas, J., He, P., Koch-Paszkowski, J., Shires, M., Scarsbrook, A.F., Archibald, S.J., Tsoumpas, C. and Bailey, M.A. 2019. Cell proliferation detected using [(18)F]FLT PET/CT as an early marker of abdominal aortic aneurysm. *J Nucl Cardiol*.
- Gandhi, R. and Tsoumpas, C. 2019. Preclinical imaging biomarkers for postischaemic neurovascular remodelling. *Contrast Media Mol Imaging* **2019**, 3128529-3128529.
- Gertz, S.D., Kurgan, A. and Eisenberg, D. 1988. Aneurysm of the rabbit common carotid artery induced by periarterial application of calcium chloride in vivo. *J Clin Invest* **81**(3), 649-656.
- Gill, G.N., III, C.R. and Simonian, M.H. 1977. Angiotensin stimulation of bovine adrenocortical cell growth. *Proc Natl Acad Sci* **74**(12), 5569.
- Glen, S. 2015. *Welch's Test for Unequal Variances*. [Online] Statistics How To. Available from: <https://www.statisticshowto.datasciencecentral.com/welchs-test-for-unequal-variances/>
- Glover, M.J., Kim, L.G., Sweeting, M.J., Thompson, S.G. and Buxton, M.J. 2014. Cost-effectiveness of the National Health Service abdominal aortic aneurysm screening programme in England. *Br J Surg* **101**(8), 976-982.
- Goergen, C.J., Azuma, J., Barr, K.N., Magdefessel, L., Kallop, D.Y., Gogineni, A., Grewall, A., Weimer, R.M., Connolly, A.J., Dalman, R.L., Taylor, C.A., Tsao, P.S. and Greve, J.M. 2011. Influences of aortic motion and curvature on vessel expansion in murine experimental aneurysms. *Arterioscler Thromb Vasc Biol* **31**(2), 270-279.

- Goldberg, A., Pakkiri, P., Dai, E., Lucas, A. and Fenster, A. 2007. Measurements of aneurysm morphology determined by 3-d micro-ultrasound imaging as potential quantitative biomarkers in a mouse aneurysm model. *Ultrasound Med Biol* **33**(10), 1552-1560.
- Golestani, R., Jung, J.J. and Sadeghi, M.M. 2016. Molecular imaging of angiogenesis and vascular remodeling in cardiovascular pathology. *J Clin Med* **5**(6).
- Golestani, R., Razavian, M., Nie, L., Zhang, J., Jung, J.J., Ye, Y., de Roo, M., Hilgerink, K., Liu, C., Robinson, S.P. and Sadeghi, M.M. 2015. Imaging vessel wall biology to predict outcome in abdominal aortic aneurysm. *Circ Cardiovasc Imaging* **8**(1).
- Greenhalgh, R.M. 2004. Comparison of endovascular aneurysm repair with open repair in patients with abdominal aortic aneurysm (EVAR trial 1), 30-day operative mortality results: randomised controlled trial. *Lancet* **364**(9437), 843-848.
- Grierson, J.R., Schwartz, J.L., Muzi, M., Jordan, R. and Krohn, K.A. 2004. Metabolism of 3'-deoxy-3'-[F-18]fluorothymidine in proliferating A549 cells: Validations for positron emission tomography. *Nucl Med Biol* **31**(7), 829-837.
- Grierson, J.R. and Shields, A.F. 2000. Radiosynthesis of 3'-deoxy-3'-[(18)F]fluorothymidine: [(18)F]FLT for imaging of cellular proliferation in vivo. *Nucl Med Biol* **27**(2), 143-156.
- Guirguis-Blake, J.M., Beil, T.L., Senger, C.A. and Whitlock, E.P. 2014. Ultrasonography screening for abdominal aortic aneurysms: a systematic evidence review for the U.S. Preventive Services Task Force. *Ann Intern Med* **160**(5), 321-329.
- Guo, D.C., Pannu, H., Tran-Fadulu, V., Papke, C.L., Yu, R.K., Avidan, N., Bourgeois, S., Estrera, A.L., Safi, H.J., Sparks, E., Amor, D., Ades, L., McConnell, V., Willoughby, C.E., Abuelo, D., Willing, M., Lewis, R.A., Kim, D.H., Scherer, S., Tung, P.P., Ahn, C., Buja, L.M., Raman, C.S., Shete, S.S. and Milewicz, D.M. 2007. Mutations in smooth muscle alpha-actin (ACTA2) lead to thoracic aortic aneurysms and dissections. *Nat Genet* **39**(12), 1488-1493.
- Guo, D.C., Papke, C.L., He, R. and Milewicz, D.M. 2006. Pathogenesis of thoracic and abdominal aortic aneurysms. *Ann N Y Acad Sci* **1085**, 339-352.
- Hacker, T.A., Griffin, M.O., Guttormsen, B., Stoker, S. and Wolff, M.R. 2007. Platelet-derived growth factor receptor antagonist STI571 (imatinib mesylate) inhibits human vascular smooth muscle proliferation and migration in vitro but not in vivo. *J Invasive Cardiol* **19**(6), 269-274.
- Hall, A.J., Busse, E.F., McCarville, D.J. and Burgess, J.J. 2000. Aortic wall tension as a predictive factor for abdominal aortic aneurysm rupture: improving the selection of patients for abdominal aortic aneurysm repair. *Ann Vasc Surg* **14**(2), 152-157.

- Halloran, B.G., Davis, V.A., McManus, B.M., Lynch, T.G. and Baxter, B.T. 1995. Localization of aortic disease is associated with intrinsic differences in aortic structure. *J Surg Res* **59**(1), 17-22.
- Hanahan, D. and Weinberg, R.A. 2011. Hallmarks of cancer: the next generation. *Cell* **144**(5), 646-674.
- Hannigan, B.M., Barnett, Y.A., Armstrong, D.B.A., McKelvey-Martin, V.J. and McKenna, P.G. 1993. Thymidine kinases: The enzymes and their clinical usefulness. *Cancer Biother* **8**(3), 189-197.
- Harris, C., Croce, B. and Cao, C. 2016. Thoracic aortic aneurysm. *Ann Cardiothorac Surg* **5**(4), 407-407.
- Hatakeyama, T., Shigematsu, H. and Muto, T. 2001. Risk factors for rupture of abdominal aortic aneurysm based on three-dimensional study. *J Vasc Surg* **33**(3), 453-461.
- Hatt, M., Cheze le Rest, C., Descourt, P., Dekker, A., De Ruyscher, D., Oellers, M., Lambin, P., Pradier, O. and Visvikis, D. 2010. Accurate automatic delineation of heterogeneous functional volumes in positron emission tomography for oncology applications. *Int J Radiat Oncol Biol Phys* **77**(1), 301-308.
- He, Q., Fornander, T., Johansson, H., Johansson, U., Hu, G.Z., Rutqvist, L.E. and Skog, S. 2006. Thymidine kinase 1 in serum predicts increased risk of distant or loco-regional recurrence following surgery in patients with early breast cancer. *Anticancer Res* **26**(6c), 4753-4759.
- He, Q., Mao, Y., Wu, J., Decker, C., Merza, M., Wang, N., Eriksson, S., Castro, J. and Skog, S. 2004. Cytosolic thymidine kinase is a specific histopathologic tumour marker for breast carcinomas. *Int J Oncol* **25**(4), 945-953.
- He, Q., Zou, L., Zhang, P.A., Lui, J.X., Skog, S. and Fornander, T. 2000. The clinical significance of thymidine kinase 1 measurement in serum of breast cancer patients using anti-TK1 antibody. *Int J Biol Markers* **15**(2), 139-146.
- Henderson, E.L., Geng, Y.J., Sukhova, G.K., Whittemore, A.D., Knox, J. and Libby, P. 1999. Death of smooth muscle cells and expression of mediators of apoptosis by T lymphocytes in human abdominal aortic aneurysms. *Circulation* **99**(1), 96-104.
- Herring, B.P., Hoggatt, A.M., Burlak, C. and Offermanns, S. 2014. Previously differentiated medial vascular smooth muscle cells contribute to neointima formation following vascular injury. *Vasc Cell* **6**, 21.
- Hofman, M.S. and Hicks, R.J. 2016. How we read oncologic FDG PET/CT. *Cancer Imaging* **16**(1), 35-35.
- Honda, T., Hamada, M., Matsumoto, Y., Matsuoka, H. and Hiwada, K. 1999. Diagnosis of thrombus and blood flow in aortic aneurysm using tagging cine magnetic resonance imaging. *Int J Angiol* **8**(1), 57-61.

Huang, T., Liu, S., Huang, J., Xu, B., Bai, Y. and Wang, W. 2019. Meta-analysis of the growth rates of abdominal aortic aneurysm in the Chinese population. *BMC Cardiovasc Disor* **19**(1), 204.

Huang, Y., Teng, Z., Elkhawad, M., Tarkin, J.M., Joshi, N., Boyle, J.R., Buscombe, J.R., Fryer, T.D., Zhang, Y., Park, A.Y., Wilkinson, I.B., Newby, D.E., Gillard, J.H. and Rudd, J.H.F. 2016. High structural stress and presence of intraluminal thrombus predict abdominal aortic aneurysm 18F-FDG uptake: Insights from biomechanics. *Circ Cardiovasc Imaging* **9**(11), e004656.

Hudspeth, K., Wang, S., Wang, J., Rahman, S., Smith, M.A., Casey, K.A., Manna, Z., Sanjuan, M., Kolbeck, R., Hasni, S., Ettinger, R. and Siegel, R.M. 2019. Natural killer cell expression of Ki67 is associated with elevated serum IL-15, disease activity and nephritis in systemic lupus erythematosus. *Clin Exp Immunol* **196**(2), 226-236.

Huet, P., Burg, S., Le Guludec, D., Hyafil, F. and Buvat, I. 2015. Variability and uncertainty of 18F-FDG PET imaging protocols for assessing inflammation in atherosclerosis: suggestions for improvement. *J Nucl Med* **56**(4), 552-559.

Hyafil, F., Pelisek, J., Laitinen, I., Schottelius, M., Mohring, M., Doring, Y., van der Vorst, E.P., Kallmayer, M., Steiger, K., Poschenrieder, A., Notni, J., Fischer, J., Baumgartner, C., Rischpler, C., Nekolla, S.G., Weber, C., Eckstein, H.H., Wester, H.J. and Schwaiger, M. 2017. Imaging the cytokine receptor CXCR4 in atherosclerotic plaques with the radiotracer (68)Ga-pentixafor for PET. *J Nucl Med* **58**(3), 499-506.

Janus, J., Kanber, B., Mahbuba, W., Beynon, C., Ramnarine, K.V., Lambert, D.G., Samani, N.J., Stringer, E.J. and Kelly, M.E. 2018. A preclinical ultrasound method for the assessment of vascular disease progression in murine models. *Ultrasound* **27**(2), 85-93.

Jayalath, R.W., Mangan, S.H. and Golledge, J. 2005. Aortic calcification. *Eur J Vasc Endovasc Surg* **30**(5), 476-488.

Jibawi, A., Ahmed, I., El-Sakka, K. and Yusuf, S.W. 2011. Management of concomitant cancer and abdominal aortic aneurysm. *Cardiol Res Pract* **2011**.

Jiraskova, L., Cervený, L., Karbanova, S., Ptackova, Z. and Staud, F. 2018. Expression of concentrative nucleoside transporters (SLC28A) in the human placenta: Effects of gestation age and prototype differentiation-affecting agents. *Mol Pharm* **15**(7), 2732-2741.

Johansson, M., Hansson, A. and Brodersen, J. 2015. Estimating overdiagnosis in screening for abdominal aortic aneurysm: could a change in smoking habits and lowered aortic diameter tip the balance of screening towards harm? *Br Med J* **350**, h825.

Johnson, R.J., Alpers, C.E., Yoshimura, A., Lombardi, D., Pritzl, P., Floege, J. and Schwartz, S.M. 1992. Renal injury from angiotensin II-mediated hypertension. *Hypertension* **19**(5), 464-474.

Jones, G.T., Tromp, G., Kuivaniemi, H., Gretarsdottir, S., Baas, A.F., Giusti, B., Strauss, E., Van't Hof, F.N., Webb, T.R., Erdman, R., Ritchie, M.D., Elmore,

J.R., Verma, A., Pendergrass, S., Kullo, I.J., Ye, Z., Peissig, P.L., Gottesman, O., Verma, S.S., Malinowski, J., Rasmussen-Torvik, L.J., Borthwick, K.M., Smelser, D.T., Crosslin, D.R., de Andrade, M., Ryer, E.J., McCarty, C.A., Bottinger, E.P., Pacheco, J.A., Crawford, D.C., Carrell, D.S., Gerhard, G.S., Franklin, D.P., Carey, D.J., Phillips, V.L., Williams, M.J., Wei, W., Blair, R., Hill, A.A., Vasudevan, T.M., Lewis, D.R., Thomson, I.A., Krysa, J., Hill, G.B., Roake, J., Merriman, T.R., Oszkinis, G., Galora, S., Saracini, C., Abbate, R., Pulli, R., Pratesi, C., Saratzis, A., Verissimo, A.R., Bumpstead, S., Badger, S.A., Clough, R.E., Cockerill, G., Hafez, H., Scott, D.J., Futers, T.S., Romaine, S.P., Bridge, K., Griffin, K.J., Bailey, M.A., Smith, A., Thompson, M.M., van Bockxmeer, F.M., Matthiasson, S.E., Thorleifsson, G., Thorsteinsdottir, U., Blankensteijn, J.D., Teijink, J.A., Wijmenga, C., de Graaf, J., Kiemeny, L.A., Lindholt, J.S., Hughes, A., Bradley, D.T., Stirrups, K., Golledge, J., Norman, P.E., Powell, J.T., Humphries, S.E., Hamby, S.E., Goodall, A.H., Nelson, C.P., Sakalihasan, N., Courtois, A., Ferrell, R.E., Eriksson, P., Folkersen, L., Franco-Cereceda, A., Eicher, J.D., Johnson, A.D., Betsholtz, C., Ruusalepp, A., Franzen, O., Schadt, E.E., Bjorkegren, J.L., Lipovich, L., Drolet, A.M., Verhoeven, E.L., Zeebregts, C.J., Geelkerken, R.H., van Sambeek, M.R., van Sterkenburg, S.M., de Vries, J.P., Stefansson, K., Thompson, J.R., de Bakker, P.I., Deloukas, P., Sayers, R.D., Harrison, S.C., van Rij, A.M., Samani, N.J. and Bown, M.J. 2017. Meta-analysis of genome-wide association studies for abdominal aortic aneurysm identifies four new disease-specific risk loci. *Circ Res* **120**(2), 341-353.

Juurikivi, A., Sandler, C., Lindstedt, K.A., Kovanen, P.T., Juutilainen, T., Leskinen, M.J., Mäki, T. and Eklund, K.K. 2005. Inhibition of c-kit tyrosine kinase by imatinib mesylate induces apoptosis in mast cells in rheumatoid synovia: a potential approach to the treatment of arthritis. *Ann Rheum Dis* **64**(8), 1126.

Kadoglou, N.P. and Liapis, C.D. 2004. Matrix metalloproteinases: contribution to pathogenesis, diagnosis, surveillance and treatment of abdominal aortic aneurysms. *Curr Med Res Opin* **20**(4), 419-432.

Kahraman, D., Scheffler, M., Zander, T., Nogova, L., Lammertsma, A.A., Boellaard, R., Neumaier, B., Ullrich, R.T., Holstein, A., Dietlein, M., Wolf, J. and Kobe, C. 2011. Quantitative analysis of response to treatment with erlotinib in advanced non-small cell lung cancer using 18F-FDG and 3'-deoxy-3'-18F-fluorothymidine PET. *J Nucl Med* **52**(12), 1871-1877.

Kamenskiy, A., Poulson, W., Sim, S., Reilly, A., Luo, J. and MacTaggart, J. 2018. Prevalence of calcification in human femoropopliteal arteries and its association with demographics, risk factors, and arterial stiffness. *Arterioscler Thromb Vasc Biol* **38**(4), e48-e57.

Kanazawa, S., Miyake, T., Kakinuma, T., Tanemoto, K., Tsunoda, T. and Kikuchi, K. 2005. The expression of platelet-derived growth factor and connective tissue growth factor in different types of abdominal aortic aneurysms. *J Cardiovasc Surg* **46**(3), 271-278.

Kapustin, A.N. and Shanahan, C.M. 2016. Emerging roles for vascular smooth muscle cell exosomes in calcification and coagulation. *J Physiol* **594**(11), 2905-2914.

- Karthikesalingam, A., Vidal-Diez, A., Holt, P.J., Loftus, I.M., Schermerhorn, M.L., Soden, P.A., Landon, B.E. and Thompson, M.M. 2016. Thresholds for abdominal aortic aneurysm repair in England and the United States. *N Engl J Med* **375**(21), 2051-2059.
- Keedy, A. 2006. An overview of intracranial aneurysms. *McGill J Med* **9**(2), 141-146.
- Kent, K.C. 2014. Abdominal aortic aneurysms. *N Engl J Med* **371**(22), 2101-2108.
- Keshgegian, A.A., Johnston, E. and Cnaan, A. 1998. Bcl-2 oncoprotein positivity and high MIB-1 (Ki-67) proliferative rate are independent predictive markers for recurrence in prostate carcinoma. *Am J Clin Pathol* **110**(4), 443-449.
- Khalil, M.M., Tremoleda, J.L., Bayomy, T.B. and Gsell, W. 2011. Molecular SPECT imaging: An overview. *Int J Mol Imaging* **2011**, 796025.
- Kim, S., Zingler, M., Harrison, J.K., Scott, E.W., Cogle, C.R., Luo, D. and Raizada, M.K. 2016. Angiotensin II regulation of proliferation, differentiation, and engraftment of hematopoietic stem cells. *Hypertension* **67**(3), 574-584.
- Kinahan, P.E. and Fletcher, J.W. 2010. Positron emission tomography-computed tomography standardized uptake values in clinical practice and assessing response to therapy. *Semin Ultrasound CT MR* **31**(6), 496-505.
- Kitagawa, T., Kosuge, H., Chang, E., James, M.L., Yamamoto, T., Shen, B., Chin, F.T., Gambhir, S.S., Dalman, R.L. and McConnell, M.V. 2013. Integrin-targeted molecular imaging of experimental abdominal aortic aneurysms by (18)F-labeled Arg-Gly-Asp positron-emission tomography. *Circ Cardiovasc Imaging* **6**(6), 950-956.
- Knox, J.B., Sukhova, G.K., Whittemore, A.D. and Libby, P. 1997. Evidence for altered balance between matrix metalloproteinases and their inhibitors in human aortic diseases. *Circulation* **95**(1), 205-212.
- Kobayashi, M., Matsubara, J., Matsushita, M., Nishikimi, N., Sakurai, T. and Nimura, Y. 2002. Expression of angiogenesis and angiogenic factors in human aortic vascular disease. *J Surg Res* **106**(2), 239-245.
- Kontopodis, N., Galanakis, N., Antoniou, S.A., Tsetis, D., Ioannou, C.V., Veith, F.J., Powell, J.T. and Antoniou, G.A. 2020. Meta-analysis and meta-regression analysis of outcomes of endovascular and open repair for ruptured abdominal aortic aneurysm. *Eur J Vasc Endovasc Surg* **59**(3), 399-410.
- Kornezos, I., Chatziioannou, A., Kokkonouzis, I., Nebotakis, P., Moschouris, H., Yiarmenitis, S., Mourikis, D. and Matsaidonis, D. 2010. Findings and limitations of focused ultrasound as a possible screening test in stable adult patients with blunt abdominal trauma: a Greek study. *Eur Radiol* **20**(1), 234-238.
- Kotze, C.W., Groves, A.M., Menezes, L.J., Harvey, R., Endozo, R., Kayani, I.A., Ell, P.J. and Yusuf, S.W. 2011. What is the relationship between (1)(8)F-FDG

aortic aneurysm uptake on PET/CT and future growth rate? *Eur J Nucl Med Mol Imaging* **38**(8), 1493-1499.

Kotze, C.W., Menezes, L.J., Endozo, R., Groves, A.M., Ell, P.J. and Yusuf, S.W. 2009. Increased metabolic activity in abdominal aortic aneurysm detected by 18F-fluorodeoxyglucose (18F-FDG) positron emission tomography/computed tomography (PET/CT). *Eur J Vasc Endovasc Surg* **38**(1), 93-99.

Kotze, C.W., Rudd, J.H., Ganeshan, B., Menezes, L.J., Brookes, J., Agu, O., Yusuf, S.W. and Groves, A.M. 2014. CT signal heterogeneity of abdominal aortic aneurysm as a possible predictive biomarker for expansion. *Atherosclerosis* **233**(2), 510-517.

Krak, N.C., Boellaard, R., Hoekstra, O.S., Twisk, J.W., Hoekstra, C.J. and Lammertsma, A.A. 2005. Effects of ROI definition and reconstruction method on quantitative outcome and applicability in a response monitoring trial. *Eur J Nucl Med Mol Imaging* **32**(3), 294-301.

Kuivaniemi, H., Platsoucas, C.D. and Tilson, M.D., 3rd. 2008. Aortic aneurysms: an immune disease with a strong genetic component. *Circulation* **117**(2), 242-252.

Kuivaniemi, H., Ryer, E.J., Elmore, J.R. and Tromp, G. 2015. Understanding the pathogenesis of abdominal aortic aneurysms. *Expert Rev Cardiovasc Ther* **13**(9), 975-987.

Kumar, Y., Hooda, K., Li, S., Goyal, P., Gupta, N. and Adeb, M. 2017. Abdominal aortic aneurysm: pictorial review of common appearances and complications. *Ann Transl Med* **5**(12), 256-256.

Kuzniar, M., Tegler, G., Wanhainen, A., Ahlstrom, H., Mani, K. and Hansen, T. 2019. Feasibility of assessing inflammation in asymptomatic abdominal aortic aneurysms with integrated 18F-fluorodeoxyglucose positron emission tomography/magnetic resonance imaging. *Eur J Vasc Endovasc Surg*.

Kyriakou, F., Dempster, W. and Nash, D. 2020. Analysing the cross-section of the abdominal aortic aneurysm neck and its effects on stent deployment. *Sci Rep* **10**(1), 4673.

Lai, C.H., Chang, C.W., Lee, F.T., Kuo, C.H., Hsu, J.H., Liu, C.P., Wu, H.L. and Yeh, J.L. 2020. Targeting vascular smooth muscle cell dysfunction with xanthine derivative KMUP-3 inhibits abdominal aortic aneurysm in mice. *Atherosclerosis* **297**, 16-24.

Lavin, B., Lacerda, S., Andia, M.E., Lorrio, S., Bakewell, R., Smith, A., Rashid, I., Botnar, R.M. and Phinikaridou, A. 2019. Tropoelastin: an in vivo imaging marker of dysfunctional matrix turnover during abdominal aortic dilation. *Cardiovasc Res* **116**(5), 995-1005.

Layne, M.D., Endege, W.O., Jain, M.K., Yet, S.F., Hsieh, C.M., Chin, M.T., Perrella, M.A., Blann, M.A., Haber, E. and Lee, M.E. 1998. Aortic carboxypeptidase-like protein, a novel protein with discoidin and carboxypeptidase-like domains, is up-regulated during vascular smooth muscle cell differentiation. *J Biol Chem* **273**(25), 15654-15660.

Lee, H., Paeng, J.C., Kim, K.H., Cheon, G.J., Lee, D.S., Chung, J.-K. and Kang, K.W. 2018. Correlation of FDG PET/CT findings with long-term growth and clinical course of abdominal aortic aneurysm. *Nucl Med Mol Imaging* **52**(1), 46-52.

Leoning, A. 2014. *The AMIDE User's Manual V0.3.1*. [Online] Available from: <http://amide.sourceforge.net/>

Lewis, S.M., Williams, A. and Eisenbarth, S.C. 2019. Structure and function of the immune system in the spleen. *Sci Immunol* **4**(33), eaau6085.

Lhoták, Š., Gyulay, G., Cutz, J.-C., Al-Hashimi, A., Trigatti, B.L., Richards, C.D., Igdoura, S.A., Steinberg, G.R., Bramson, J., Ask, K. and Austin, R.C. 2016. Characterization of proliferating lesion-resident cells during all stages of atherosclerotic growth. *J Am Heart Assoc* **5**(8), e003945.

Li, F.-D., Kang, R., Nie, H., Wang, X.-M. and Zheng, Y.-H. 2017. An association of spleen volume and aortic diameter in patients and in mice with abdominal aortic aneurysm. *BMC Surg* **17**(1), 134-134.

Liao, S., Curci, J.A., Kelley, B.J., Sicard, G.A. and Thompson, R.W. 2000. Accelerated replicative senescence of medial smooth muscle cells derived from abdominal aortic aneurysms compared to the adjacent inferior mesenteric artery. *J Surg Res* **92**(1), 85-95.

Lin, C.-J., Lin, C.-Y. and Stitzel, N.O. 2018. Genetics of the extracellular matrix in aortic aneurysmal diseases. *Matrix Biol* **71-72**, 128-143.

Liu, C., Gong, C., Liu, S., Zhang, Y., Zhang, Y., Xu, X., Yuan, H., Wang, B. and Yang, Z. 2019. (18)F-FES PET/CT influences the staging and management of patients with newly diagnosed estrogen receptor-positive breast cancer: A retrospective comparative study with (18)F-FDG PET/CT. *Oncologist*.

Liu, D., Fan, Z., Li, Y., Zhang, N., Sun, Z., An, J., Stalder, A.F., Greiser, A. and Liu, J. 2018. Quantitative study of abdominal blood flow patterns in patients with aortic dissection by 4-dimensional flow MRI. *Sci Rep* **8**(1), 9111.

Lodge, M.A., Holdhoff, M., Leal, J.P., Bag, A.K., Nabors, L.B., Mintz, A., Lesser, G.J., Mankoff, D.A., Desai, A.S., Mountz, J.M., Lieberman, F.S., Fisher, J.D., Desideri, S., Ye, X., Grossman, S.A., Schiff, D. and Wahl, R.L. 2017. Repeatability of (18)F-FLT PET in a Multicenter Study of Patients with High-Grade Glioma. *J Nucl Med* **58**(3), 393-398.

Loening, A.M. and Gambhir, S.S. 2003. AMIDE: A free software tool for multimodality medical image analysis. *Mol Imaging* **2**(3), 15353500200303133.

Lopez-Candales, A., Holmes, D.R., Liao, S., Scott, M.J., Wickline, S.A. and Thompson, R.W. 1997. Decreased vascular smooth muscle cell density in medial degeneration of human abdominal aortic aneurysms. *Am J Pathol* **150**(3), 993-1007.

Lovinfosse, P., Rousseau, C., Pierga, J.-Y., Bouchet, F., Cochet, A., Alberini, J.-L., Girault, S., Vera, P., Olivier, P., Uwer, L., Cachin, F., Scarwell, B., Lemonnier, J., Fourme, E., Mesleard, C., Martin, A.-L., Lacœuille, F. and

- Couturier, O.-F. 2019. Dual time point [18F]FLT-PET for differentiating proliferating tissues vs non-proliferating tissues. *EJNMMI Res* **9**(1), 109.
- Lu, H., Howatt, D.A., Balakrishnan, A., Moorleghen, J.J., Rateri, D.L., Cassis, L.A. and Daugherty, A. 2015. Subcutaneous angiotensin II infusion using osmotic pumps induces aortic aneurysms in mice. *J Vis Exp*(103).
- Macrae, F.L., Evans, H.L., Bridge, K.I., Johnson, A., Scott, D.J.A. and Ariens, R.A.S. 2014. Common FXIII and fibrinogen polymorphisms in abdominal aortic aneurysms. *PLoS One* **9**(11), e112407-e112407.
- MacSweeney, S.T., Powell, J.T. and Greenhalgh, R.M. 1994. Pathogenesis of abdominal aortic aneurysm. *Br J Surg* **81**(7), 935-941.
- Maier, A., Essler, M., Gee, M.W., Eckstein, H.H., Wall, W.A. and Reeps, C. 2012. Correlation of biomechanics to tissue reaction in aortic aneurysms assessed by finite elements and [18F]-fluorodeoxyglucose-PET/CT. *Int J Numer Method Biomed Eng* **28**(4), 456-471.
- Maier, A., Gee, M.W., Reeps, C., Eckstein, H.H. and Wall, W.A. 2010. Impact of calcifications on patient-specific wall stress analysis of abdominal aortic aneurysms. *Biomech Model Mechan* **9**(5), 511-521.
- Manning, M.W., Cassis, L.A. and Daugherty, A. 2003. Differential effects of doxycycline, a broad-spectrum matrix metalloproteinase inhibitor, on angiotensin II-induced atherosclerosis and abdominal aortic aneurysms. *Arterioscler Thromb Vasc Biol* **23**(3), 483-488.
- Mao, D., Lee, J.K., VanVickle, S.J. and Thompson, R.W. 1999. Expression of collagenase-3 (MMP-13) in human abdominal aortic aneurysms and vascular smooth muscle cells in culture. *Biochem Biophys Res Comm* **261**(3), 904-910.
- Mao, Y., Wu, J., Skog, S., Eriksson, S., Zhao, Y., Zhou, J. and He, Q. 2005. Expression of cell proliferating genes in patients with non-small cell lung cancer by immunohistochemistry and cDNA profiling. *Oncol Rep* **13**(5), 837-846.
- Mao, Y., Wu, J., Wang, N., He, L., Wu, C., He, Q. and Skog, S. 2002. A comparative study: immunohistochemical detection of cytosolic thymidine kinase and proliferating cell nuclear antigen in breast cancer. *Cancer Invest* **20**(7-8), 922-931.
- Marini, C., Morbelli, S., Armonino, R., Spinella, G., Riondato, M., Massollo, M., Sarocchi, F., Pane, B., Augeri, C., Abete, L., Ghigliotti, G., Palmieri, D., Fiz, F., Cittadini, G., Fulcheri, E., Palombo, D. and Sambucetti, G. 2012. Direct relationship between cell density and FDG uptake in asymptomatic aortic aneurysm close to surgical threshold: an in vivo and in vitro study. *Eur J Nucl Med Mol Imaging* **39**(1), 91-101.
- Martin-McNulty, B., Vincelette, J., Vergona, R., Sullivan, M.E. and Wang, Y.X. 2005. Noninvasive measurement of abdominal aortic aneurysms in intact mice by a high-frequency ultrasound imaging system. *Ultrasound Med Biol* **31**(6), 745-749.

- Massaro, A., Cittadin, S., Milan, E., Tamiso, L., Pavan, L., Secchiero, C., Rampin, L., Grassetto, G., Marzola, C.M. and Rubello, D. 2009. Reliability of SUVmax vs. SUVmean in FDG PET/CT. *J Nucl Med* **50**(2), 2121.
- McBride, O.M.B., Joshi, N.V., Robson, J.M.J., MacGillivray, T.J., Gray, C.D., Fletcher, A.M., Dweck, M.R., van Beek, E.J.R., Rudd, J.H.F., Newby, D.E. and Semple, S.I. 2016. Positron emission tomography and magnetic resonance imaging of cellular inflammation in patients with abdominal aortic aneurysms. *Eur J Vasc Endovasc Surg* **51**(4), 518-526.
- McGloughlin, T.M. and Doyle, B.J. 2010. New approaches to abdominal aortic aneurysm rupture risk assessment: engineering insights with clinical gain. *Arterioscler Thromb Vasc Biol* **30**(9), 1687-1694.
- Menezes, L.J., Kotze, C.W., Hutton, B.F., Endozo, R., Dickson, J.C., Cullum, I., Yusuf, S.W., Ell, P.J. and Groves, A.M. 2009. Vascular inflammation imaging with 18F-FDG PET/CT: When to image? *J Nucl Med* **50**(6), 854-857.
- Metaxa, E., Iordanov, I., Maravelakis, E. and Papaharilaou, Y. 2017. A novel approach for local abdominal aortic aneurysm growth quantification. *Med Biol Eng Comput* **55**(8), 1277-1286.
- Michel, J.B., Jondeau, G. and Milewicz, D.M. 2018. From genetics to response to injury: vascular smooth muscle cells in aneurysms and dissections of the ascending aorta. *Cardiovasc Res* **114**(4), 578-589.
- Miller, I., Min, M., Yang, C., Tian, C., Gookin, S., Carter, D. and Spencer, S.L. 2018. Ki67 is a graded rather than a binary marker of proliferation versus quiescence. *Cell Rep* **24**(5), 1105-1112.e1105.
- Molacek, J., Baxa, J., Opatrny, V., Treska, V., Hollan, I. and Ferda, J. 2019. Benefits of hybrid methods (PET/CT, PET MRI) in the diagnosis of abdominal aortic pathology. *Rozhl Chir* **98**(11), 450-456.
- Molina-Arcas, M., Casado, F.J. and Pastor-Anglada, M. 2009. Nucleoside transporter proteins. *Curr Vasc Pharmacol* **7**(4), 426-434.
- Mora, C., Marcus, C., Barbe, C., Ecartot, F. and Long, A. 2014. Measurement of maximum diameter of native abdominal aortic aneurysm by angio-CT: Reproducibility is better with the semi-automated method. *Eur J Vasc Endovasc Surg* **47**(2), 139-150.
- Morbelli, S., Ghigliotti, G., Spinella, G., Marini, C., Bossert, I., Cimmino, M., Pane, B., Rousas, N., Cittadini, G., Massollo, M., Camellino, D., Riondato, M., Palombo, D., Barisione, C. and Sambuceti, G. 2014. Systemic vascular inflammation in abdominal aortic aneurysm patients: a contrast-enhanced PET/CT study. *Q J Nucl Med Mol Imaging* **58**(3), 299-309.
- Morel, O., Mandry, D., Micard, E., Kauffmann, C., Lamiral, Z., Verger, A., Chevalier-Mathias, E., Mathias, J., Karcher, G., Meneroux, B., Rossignol, P. and Marie, P.Y. 2015. Evidence of cyclic changes in the metabolism of abdominal aortic aneurysms during growth phases: (1)(8)F-FDG PET sequential observational study. *J Nucl Med* **56**(7), 1030-1035.

Moxon, J.V., Parr, A., Emeto, T.I., Walker, P., Norman, P.E. and Golledge, J. 2010. Diagnosis and monitoring of abdominal aortic aneurysm: current status and future prospects. *Curr Probl Cardiol* **35**(10), 512-548.

Mu, N., Juhlin, C.C., Tani, E., Sofiadis, A., Reihner, E., Zedenius, J., Larsson, C. and Nilsson, I.L. 2018. High Ki-67 index in fine needle aspiration cytology of follicular thyroid tumors is associated with increased risk of carcinoma. *Endocrine* **61**(2), 293-302.

Multi-Agency Radiological Laboratory Analytical Protocols. 2004. *Chapter 16: Data acquisition, reduction, and reporting for nuclear-counting instrumentation*. United States Environmental Protection Agency. 1-45.

Murakami, M., Morikage, N., Samura, M., Yamashita, O., Suehiro, K. and Hamano, K. 2014. Fluorine-18-fluorodeoxyglucose positron emission tomography-computed tomography for diagnosis of infected aortic aneurysms. *Ann Vasc Surg* **28**(3), 575-578.

Muzi, M., Mankoff, D.A., Grierson, J.R., Wells, J.M., Vesselle, H. and Krohn, K.A. 2005. Kinetic modeling of 3'-deoxy-3'-fluorothymidine in somatic tumors: mathematical studies. *J Nucl Med* **46**(2), 371-380.

Muzi, M., Spence, A.M., O'Sullivan, F., Mankoff, D.A., Wells, J.M., Grierson, J.R., Link, J.M. and Krohn, K.A. 2006. Kinetic analysis of 3'-deoxy-3'-18F-fluorothymidine in patients with gliomas. *J Nucl Med* **47**(10), 1612-1621.

Muzi, M., Vesselle, H., Grierson, J.R., Mankoff, D.A., Schmidt, R.A., Peterson, L., Wells, J.M. and Krohn, K.A. 2005. Kinetic analysis of 3'-deoxy-3'-fluorothymidine PET studies: validation studies in patients with lung cancer. *J Nucl Med* **46**(2), 274-282.

Nagengast, W.B., Lub-de Hooge, M.N., Oosting, S.F., den Dunnen, W.F., Warnders, F.J., Brouwers, A.H., de Jong, J.R., Price, P.M., Hollema, H., Hospers, G.A., Elsinga, P.H., Hesselink, J.W., Gietema, J.A. and de Vries, E.G. 2011. VEGF-PET imaging is a noninvasive biomarker showing differential changes in the tumor during sunitinib treatment. *Cancer Res* **71**(1), 143-153.

Nahmias, C. and Wahl, L.M. 2008. Reproducibility of standardized uptake value measurements determined by 18F-FDG PET in malignant tumors. *J Nucl Med* **49**(11), 1804-1808.

Nahrendorf, M., Keliher, E., Marinelli, B., Leuschner, F., Robbins, C.S., Gerszten, R.E., Pittet, M.J., Swirski, F.K. and Weissleder, R. 2011. Detection of macrophages in aortic aneurysms by nanoparticle positron emission tomography-computed tomography. *Arterioscler Thromb Vasc Biol* **31**(4), 750-757.

Nakajima, A., Nishiyama, K., Morimoto, M., Nakamura, S., Suzuki, O., Hashiguchi, H., Tanaka, K. and Yoshino, K. 2012. Defining PET standardized uptake value threshold for tumor delineation with metastatic lymph nodes in head and neck cancer. *Jpn J Clin Oncol* **42**(6), 491-497.

Nakamoto, Y., Zasadny, K.R., Minn, H. and Wahl, R.L. 2002. Reproducibility of common semi-quantitative parameters for evaluating lung cancer glucose

metabolism with positron emission tomography using 2-deoxy-2-[18F]fluoro-D-glucose. *Mol Imaging Biol* **4**(2), 171-178.

National Institute for Health and Clinical Excellence (2008). Overview - Endovascular stents for abdominal aortic aneurysms: 1-37.

National Institute for Health and Clinical Excellence (2018). Abdominal aortic aneurysm: diagnosis and management: 1-36.

National Institute for Health and Clinical Excellence (2020). Abdominal aortic aneurysm: diagnosis and management: 1-49.

Nchimi, A., Cheramy-Bien, J.P., Gasser, T.C., Namur, G., Gomez, P., Seidel, L., Albert, A., Defraigne, J.O., Labropoulos, N. and Sakalihasan, N. 2014. Multifactorial relationship between 18F-fluoro-deoxy-glucose positron emission tomography signaling and biomechanical properties in unruptured aortic aneurysms. *Circ Cardiovasc Imaging* **7**(1), 82-91.

Nchimi, A., Courtois, A., El Hachemi, M., Touat, Z., Drion, P., Withofs, N., Warnock, G., Bahri, M.A., Dogne, J.M., Cheramy-Bien, J.P., Schoysman, L., Joskin, J., Michel, J.B., Defraigne, J.O., Plenevaux, A. and Sakalihasan, N. 2016. Multimodality imaging assessment of the deleterious role of the intraluminal thrombus on the growth of abdominal aortic aneurysm in a rat model. *Eur Radiol* **26**(7), 2378-2386.

Nguyen, B.T., Mizrahi, B., Tao, M., Yu, P., Hao, S., Ozaki, C.K. and Schneiderman, J. 2011. Aging enhances abdominal aortic aneurysm formation and promotes aortic arch rupture in angiotensin II treated mice. *J Am Coll Surg* **213**(3), S154.

Nie, M.-X., Zhang, X.-H., Yan, Y.-F. and Zhao, Q.-M. 2018. Relationship between inflammation and progression of an abdominal aortic aneurysm in a rabbit model based on 18F-FDG PET/CT imaging. *Vascular* **26**(6), 571-580.

Nisman, B., Allweis, T., Kadouri, L., Mali, B., Hamburger, T., Baras, M., Gronowitz, S. and Peretz, T. 2013. Comparison of diagnostic and prognostic performance of two assays measuring thymidine kinase 1 activity in serum of breast cancer patients. *Clin Chem Lab Med* **51**(2), 439-447.

O'Leary, S.A., Mulvihill, J.J., Barrett, H.E., Kavanagh, E.G., Walsh, M.T., McGloughlin, T.M. and Doyle, B.J. 2015. Determining the influence of calcification on the failure properties of abdominal aortic aneurysm (AAA) tissue. *J Mech Behav Biomed Mater* **42**, 154-167.

Oliver-Williams, C., Sweeting, M.J., Jacomelli, J., Summers, L., Stevenson, A., Lees, T. and Earnshaw, J.J. 2019. Safety of men with small and medium abdominal aortic aneurysms under surveillance in the NAAASP. *Circulation* **139**(11), 1371-1380.

Owens, G.K., Kumar, M.S. and Wamhoff, B.R. 2004. Molecular regulation of vascular smooth muscle cell differentiation in development and disease. *Physiol Rev* **84**(3), 767-801.

- Palombo, D., Morbelli, S., Spinella, G., Pane, B., Marini, C., Rousas, N., Massollo, M., Cittadini, G., Camellino, D. and Sambuceti, G. 2012. A positron emission tomography/computed tomography (PET/CT) evaluation of asymptomatic abdominal aortic aneurysms: another point of view. *Ann Vasc Surg* **26**(4), 491-499.
- Pannu, H., Avidan, N., Tran-Fadulu, V. and Milewicz, D.M. 2006. Genetic basis of thoracic aortic aneurysms and dissections: potential relevance to abdominal aortic aneurysms. *Ann N Y Acad Sci* **1085**, 242-255.
- Paproski, R.J., Ng, A.M.L., Yao, S.Y.M., Graham, K., Young, J.D. and Cass, C.E. 2008. The role of human nucleoside transporters in uptake of 3'-deoxy-3'-fluorothymidine. *Mol Pharmacol* **74**(5), 1372.
- Paproski, R.J., Wuest, M., Jans, H.-S., Graham, K., Gati, W.P., McQuarrie, S., McEwan, A., Mercer, J., Young, J.D. and Cass, C.E. 2010. Biodistribution and uptake of 3'-deoxy-3'-fluorothymidine in ENT1-knockout mice and in an ENT1-knockdown tumor model. *J Nucl Med* **51**(9), 1447-1455.
- Patel, M.I., Ghosh, P., Melrose, J. and Appleberg, M. 1996. Smooth muscle cell migration and proliferation is enhanced in abdominal aortic aneurysms. *Aust N Z J Surg* **66**(5), 305-308.
- Patel, M.I., Melrose, J., Ghosh, P. and Appleberg, M. 1996. Increased synthesis of matrix metalloproteinases by aortic smooth muscle cells is implicated in the etiopathogenesis of abdominal aortic aneurysms. *J Vasc Surg* **24**(1), 82-92.
- Patel, R., Sweeting, M.J., Powell, J.T. and Greenhalgh, R.M. 2016. Endovascular versus open repair of abdominal aortic aneurysm in 15-years' follow-up of the UK endovascular aneurysm repair trial 1 (EVAR trial 1): a randomised controlled trial. *Lancet* **388**(10058), 2366-2374.
- Patelis, N., Moris, D., Schizas, D., Damaskos, C., Perrea, D., Bakoyiannis, C., Liakakos, T. and Georgopoulos, S. 2017. Animal models in the research of abdominal aortic aneurysms development. *Physiol Res* **66**(6), 899-915.
- Petsophonsakul, P., Furmanik, M., Forsythe, R., Dweck, M., Schurink, G.W., Natour, E., Reutelingsperger, C., Jacobs, M., Mees, B. and Schurgers, L. 2019. Role of vascular smooth muscle cell phenotypic switching and calcification in aortic aneurysm formation. *Arterioscler Thromb Vasc Biol* **39**(7), 1351-1368.
- Polzer, S., Gasser, T.C., Vlachovský, R., Kubíček, L., Lambert, L., Man, V., Novák, K., Slažanský, M., Burša, J. and Staffa, R. 2020. Biomechanical indices are more sensitive than diameter in predicting rupture of asymptomatic abdominal aortic aneurysms. *J Vasc Surg* **71**(2), 617-626.e616.
- Poulsen, J.L., Stubbe, J. and Lindholt, J.S. 2016. Animal models used to explore abdominal aortic aneurysms: A systematic review. *Eur J Vasc Endovasc Surg* **52**(4), 487-499.
- Powell, J.T., Greenhalgh, R.M., Ruckley, C.V. and Fowkes, F.G. 1996. The UK small aneurysm trial. *Ann N Y Acad Sci* **800**, 249-251.

Prinssen, M., Verhoeven, E.L., Buth, J., Cuypers, P.W., van Sambeek, M.R., Balm, R., Buskens, E., Grobbee, D.E. and Blankensteijn, J.D. 2004. A randomized trial comparing conventional and endovascular repair of abdominal aortic aneurysms. *N Engl J Med* **351**(16), 1607-1618.

Proudfoot, D., Skepper, J.N., Hegyi, L., Bennett, M.R., Shanahan, C.M. and Weissberg, P.L. 2000. Apoptosis regulates human vascular calcification in vitro: evidence for initiation of vascular calcification by apoptotic bodies. *Circ Res* **87**(11), 1055-1062.

Qiu, X., Wang, H., Wang, Z., Fu, Y. and Yin, J. 2019. Expression of PCNA, Ki-67 and COX-2 in breast cancer based on DCE-MRI image information. *J Infect Public Health*.

Quintana, R.A. and Taylor, W.R. 2019. Cellular mechanisms of aortic aneurysm formation. *Circ Res* **124**(4), 607-618.

Raman, V.K., Karmarkar, P.V., Guttman, M.A., Dick, A.J., Peters, D.C., Ozturk, C., Pessanha, B.S., Thompson, R.B., Raval, A.N., DeSilva, R., Aviles, R.J., Atalar, E., McVeigh, E.R. and Lederman, R.J. 2005. Real-time magnetic resonance-guided endovascular repair of experimental abdominal aortic aneurysm in swine. *J Am Coll Cardiol* **45**(12), 2069-2077.

Ramaswamy, A.K., Hamilton, M., 2nd, Joshi, R.V., Kline, B.P., Li, R., Wang, P. and Goergen, C.J. 2013. Molecular imaging of experimental abdominal aortic aneurysms. *Sci World J* **2013**, 973150.

Rateri, D.L., Howatt, D.A., Moorleghen, J.J., Charnigo, R., Cassis, L.A. and Daugherty, A. 2011. Prolonged infusion of angiotensin II in apoE(-/-) mice promotes macrophage recruitment with continued expansion of abdominal aortic aneurysm. *Am J Pathol* **179**(3), 1542-1548.

Reeps, C., Bundschuh, R.A., Pellisek, J., Herz, M., van Marwick, S., Schwaiger, M., Eckstein, H.H., Nekolla, S.G. and Essler, M. 2013. Quantitative assessment of glucose metabolism in the vessel wall of abdominal aortic aneurysms: correlation with histology and role of partial volume correction. *Int J Cardiovasc Imaging* **29**(2), 505-512.

Reeps, C., Essler, M., Pelisek, J., Seidl, S., Eckstein, H.H. and Krause, B.J. 2008. Increased 18F-fluorodeoxyglucose uptake in abdominal aortic aneurysms in positron emission/computed tomography is associated with inflammation, aortic wall instability, and acute symptoms. *J Vasc Surg* **48**(2), 417-423; discussion 424.

Reis, S.P., Majdalany, B.S., AbuRahma, A.F., Collins, J.D., Francois, C.J., Ganguli, S., Gornik, H.L., Kendi, A.T., Khaja, M.S., Norton, P.T., Sutphin, P.D., Rybicki, F.J. and Kalva, S.P. 2017. ACR appropriateness criteria((R)) pulsatile abdominal mass suspected abdominal aortic aneurysm. *J Am Coll Radiol* **14**(5s), S258-s265.

RESCAN Collaborators, Bown, M.J., Sweeting, M.J., Brown, L.C., Powell, J.T. and Thompson, S.G. 2013. Surveillance intervals for small abdominal aortic aneurysms: a meta-analysis. *JAMA* **309**(8), 806-813.

Riches, K., Angelini, T.G., Mudhar, G.S., Kaye, J., Clark, E., Bailey, M.A., Sohrabi, S., Korossis, S., Walker, P.G., Scott, D.J.A. and Porter, K.E. 2013. Exploring smooth muscle phenotype and function in a bioreactor model of abdominal aortic aneurysm. *J Transl Med* **11**, 208-208.

Riches, K., Clark, E., Helliwell, R.J., Angelini, T.G., Hemmings, K.E., Bailey, M.A., Bridge, K.I., Scott, D.J.A. and Porter, K.E. 2018. Progressive development of aberrant smooth muscle cell phenotype in abdominal aortic aneurysm disease. *J Vasc Res* **55**(1), 35-46.

Roostalu, U., Aldeiri, B., Albertini, A., Humphreys, N., Simonsen-Jackson, M., Wong, J.K.F. and Cossu, G. 2018. Distinct cellular mechanisms underlie smooth muscle turnover in vascular development and repair. *Circ Res* **122**(2), 267-281.

Rowe, V.L., Stevens, S.L., Reddick, T.T., Freeman, M.B., Donnell, R., Carroll, R.C. and Goldman, M.H. 2000. Vascular smooth muscle cell apoptosis in aneurysmal, occlusive, and normal human aortas. *J Vasc Surg* **31**(3), 567-576.

Ruddy, J.M., Jones, J.A., Spinale, F.G. and Ikonomidis, J.S. 2008. Regional heterogeneity within the aorta: relevance to aneurysm disease. *J Thorac Cardiovasc Surg* **136**(5), 1123-1130.

Ryer, E.J., Garvin, R.P., Schworer, C.M., Bernard-Eckroth, K.R., Tromp, G., Franklin, D.P., Elmore, J.R. and Kuivaniemi, H. 2015. Proinflammatory role of stem cells in abdominal aortic aneurysms. *J Vasc Surg* **62**(5), 1303-1311.e1304.

Sakalihasan, N., Michel, J.B., Katsargyris, A., Kuivaniemi, H., Defraigne, J.O., Nchimi, A., Powell, J.T., Yoshimura, K. and Hultgren, R. 2018. Abdominal aortic aneurysms. *Nat Rev Dis Primers* **4**(1), 34.

Sakalihasan, N., Van Damme, H., Gomez, P., Rigo, P., Lapiere, C.M., Nusgens, B. and Limet, R. 2002. Positron emission tomography (PET) evaluation of abdominal aortic aneurysm (AAA). *Eur J Vasc Endovasc Surg* **23**(5), 431-436.

Sakthivel, P., Shively, V., Kakoulidou, M., Pearce, W. and Lefvert, A.K. 2007. The soluble forms of CD28, CD86 and CTLA-4 constitute possible immunological markers in patients with abdominal aortic aneurysm. *J Intern Med* **261**(4), 399-407.

Salmon, M., Johnston, W.F., Woo, A., Pope, N.H., Su, G., Upchurch, G.R., Jr., Owens, G.K. and Ailawadi, G. 2013. KLF4 regulates abdominal aortic aneurysm morphology and deletion attenuates aneurysm formation. *Circulation* **128**(11 Suppl 1), S163-174.

Salskov, A., Tammisetti, V.S., Grierson, J. and Vesselle, H. 2007. FLT: measuring tumor cell proliferation in vivo with positron emission tomography and 3'-deoxy-3'-[18F]fluorothymidine. *Semin Nucl Med* **37**(6), 429-439.

Sanchez, F., Orero, A., Soriano, A., Correcher, C., Conde, P., Gonzalez, A., Hernandez, L., Moliner, L., Rodriguez-Alvarez, M.J., Vidal, L.F., Benlloch, J.M., Chapman, S.E. and Leevy, W.M. 2013. ALBIRA: a small animal PETSPECTCT imaging system. *Med Phys* **40**(5), 051906.

Sandford, R.M., Choke, E., Bown, M.J. and Sayers, R.D. 2014. What is the best option for elective repair of an abdominal aortic aneurysm in a young fit patient? *Eur J Vasc Endovasc Surg* **47**(1), 13-18.

Sarda-Mantel, L., Alsac, J.M., Boisgard, R., Hervatin, F., Montravers, F., Tavitian, B., Michel, J.B. and Le Guludec, D. 2012. Comparison of 18F-fluoro-deoxy-glucose, 18F-fluoro-methyl-choline, and 18F-DPA714 for positron-emission tomography imaging of leukocyte accumulation in the aortic wall of experimental abdominal aneurysms. *J Vasc Surg* **56**(3), 765-773.

Satta, J., Soini, Y., Pöllänen, R., Pääkkö, P. and Juvonen, T. 1997. Tenascin expression is associated with a chronic inflammatory process in abdominal aortic aneurysms. *J Vasc Surg* **26**(4), 670-675.

Scarpelli, M., Zahm, C., Perlman, S., McNeel, D.G., Jeraj, R. and Liu, G. 2019. FLT PET/CT imaging of metastatic prostate cancer patients treated with pTVG-HP DNA vaccine and pembrolizumab. *J Immunother Cancer* **7**(1), 23.

Schneider, C.A., Rasband, W.S. and Eliceiri, K.W. 2012. NIH Image to ImageJ: 25 years of image analysis. *Nat Methods* **9**(7), 671-675.

Scholzen, T. and Gerdes, J. 2000. The Ki-67 protein: from the known and the unknown. *J Cell Physiol* **182**(3), 311-322.

Schurgers, L.J., Akbulut, A.C., Kaczor, D.M., Halder, M., Koenen, R.R. and Kramann, R. 2018. Initiation and propagation of vascular calcification is regulated by a concert of platelet- and smooth muscle cell-derived extracellular vesicles. *Front Cardiovasc Med* **5**, 36.

Seggewiss, R., Loré, K., Greiner, E., Magnusson, M.K., Price, D.A., Douek, D.C., Dunbar, C.E. and Wiestner, A. 2005. Imatinib inhibits T-cell receptor-mediated T-cell proliferation and activation in a dose-dependent manner. *Blood* **105**(6), 2473.

Senemaud, J., Caligiuri, G., Etienne, H., Delbosc, S., Michel, J.B. and Coscas, R. 2017. Translational relevance and recent advances of animal models of abdominal aortic aneurysm. *Arterioscler Thromb Vasc Biol* **37**(3), 401-410.

Shanahan, C.M., Crouthamel, M.H., Kapustin, A. and Giachelli, C.M. 2011. Arterial calcification in chronic kidney disease: key roles for calcium and phosphate. *Circ Res* **109**(6), 697-711.

Sher, A., Lacoeyille, F., Fosse, P., Vervueren, L., Cahouet-Vannier, A., Dabli, D., Bouchet, F. and Couturier, O. 2016. For avid glucose tumors, the SUV peak is the most reliable parameter for [(18)F]FDG-PET/CT quantification, regardless of acquisition time. *EJNMMI Res* **6**(1), 21-21.

Shi, S., Orbay, H., Yang, Y., Graves, S.A., Nayak, T.R., Hong, H., Hernandez, R., Luo, H., Goel, S., Theuer, C.P., Nickles, R.J. and Cai, W. 2015. PET imaging of abdominal aortic aneurysm with 64Cu-labeled anti-CD105 antibody Fab fragment. *J Nucl Med* **56**(6), 927-932.

Shields, A.F., Grierson, J.R., Dohmen, B.M., Machulla, H.-J., Stayanoff, J.C., Lawhorn-Crews, J.M., Obradovich, J.E., Muzik, O. and Mangner, T.J. 1998.

- Imaging proliferation in vivo with [F-18] FLT and positron emission tomography. *Nat Med* **4**(11), 1334.
- Shields, A.F., Grierson, J.R., Muzik, O., Stayanoff, J.C., Lawhorn-Crews, J.M., Obradovich, J.E. and Mangner, T.J. 2002. Kinetics of 3'-deoxy-3'-[F-18]fluorothymidine uptake and retention in dogs. *Mol Imaging Biol* **4**(1), 83-89.
- Shimizu, K., Mitchell Richard, N. and Libby, P. 2006. Inflammation and cellular immune responses in abdominal aortic aneurysms. *Arterioscler Thromb Vasc Biol* **26**(5), 987-994.
- Silva, D.C., Goncalves, A.K., Cobucci, R.N., Mendonca, R.C., Lima, P.H. and Cavalcanti, G.J. 2017. Immunohistochemical expression of p16, Ki-67 and p53 in cervical lesions - A systematic review. *Pathol Res Pract* **213**(7), 723-729.
- Slice, L.W., Chiu, T. and Rozengurt, E. 2005. Angiotensin II and epidermal growth factor induce cyclooxygenase-2 expression in intestinal epithelial cells through small GTPases using distinct signaling pathways. *J Biol Chem* **280**(2), 1582-1593.
- Stenbaek, J., Kalin, B. and Swedenborg, J. 2000. Growth of thrombus may be a better predictor of rupture than diameter in patients with abdominal aortic aneurysms. *Eur J Vasc Endovasc Surg* **20**(5), 466-469.
- Sun, J., Deng, H., Zhou, Z., Xiong, X. and Gao, L. 2018. Endothelium as a potential target for treatment of abdominal aortic aneurysm. *Oxidative Med Cell Longev* **2018**, 12.
- Sun, J., Sukhova, G.K., Yang, M., Wolters, P.J., MacFarlane, L.A., Libby, P., Sun, C., Zhang, Y., Liu, J., Ennis, T.L., Knispel, R., Xiong, W., Thompson, R.W., Baxter, B.T. and Shi, G.-P. 2007. Mast cells modulate the pathogenesis of elastase-induced abdominal aortic aneurysms in mice. *J Clin Invest* **117**(11), 3359-3368.
- Suzuki, H., Tamaki, T., Nishio, M., Nakata, Y., Hanai, N., Nishikawa, D., Koide, Y. and Hasegawa, Y. 2018. Total lesion glycolysis on FDG-PET/CT before salvage surgery predicts survival in laryngeal or pharyngeal cancer. *Oncotarget* **9**(27), 19115-19122.
- Syed, M.B.J., Fletcher, A.J. and Dweck, M.R. 2019. Imaging cellular activity and proliferation in the aortic wall. *J Nucl Cardiol*.
- Taqueti, V.R., Di Carli, M.F., Jerosch-Herold, M., Sukhova, G.K., Murthy, V.L., Folco, E.J., Kwong, R.Y., Ozaki, C.K., Belkin, M., Nahrendorf, M., Weissleder, R. and Libby, P. 2014. Increased microvascularization and vessel permeability associate with active inflammation in human atheromata. *Circ Cardiovasc Imaging* **7**(6), 920-929.
- Tarkin, J.M., Dweck, M.R., Evans, N.R., Takx, R.A., Brown, A.J., Tawakol, A., Fayad, Z.A. and Rudd, J.H. 2016. Imaging atherosclerosis. *Circ Res* **118**(4), 750-769.
- Tarkin, J.M., Joshi, F.R. and Rudd, J.H.F. 2014. PET imaging of inflammation in atherosclerosis. *Nat Rev Cardiol* **11**, 443.

Tedjawirja, V.N. and de Waard, V. 2019. Which mouse model of abdominal aortic aneurysm deserves triple A status? *Eur J Vasc Endovasc Surg* **58**(5), 777-778.

Tegler, G., Ericson, K., Sorensen, J., Bjorck, M. and Wanhainen, A. 2012. Inflammation in the walls of asymptomatic abdominal aortic aneurysms is not associated with increased metabolic activity detectable by 18-fluorodeoxyglucose positron-emission tomography. *J Vasc Surg* **56**(3), 802-807.

Tegler, G., Estrada, S., Hall, H., Wanhainen, A., Bjorck, M., Sorensen, J. and Antoni, G. 2014. Autoradiography screening of potential positron emission tomography tracers for asymptomatic abdominal aortic aneurysms. *Ups J Med Sci* **119**(3), 229-235.

Tegler, G., Sorensen, J., Ericson, K., Bjorck, M. and Wanhainen, A. 2013. 4D-PET/CT with [(11)C]-PK11195 and [(11)C]-(D)-deprenyl does not identify the chronic inflammation in asymptomatic abdominal aortic aneurysms. *Eur J Vasc Endovasc Surg* **45**(4), 351-356.

Theocharis, A.D., Tsolakis, I., Hjerpe, A. and Karamanos, N.K. 2001. Human abdominal aortic aneurysm is characterized by decreased versican concentration and specific downregulation of versican isoform V(0). *Atherosclerosis* **154**(2), 367-376.

Thompson, M.M., Jones, L., Nasim, A., Sayers, R.D. and Bell, P.R. 1996. Angiogenesis in abdominal aortic aneurysms. *Eur J Vasc Endovasc Surg* **11**(4), 464-469.

Thompson, R.W., Geraghty, P.J. and Lee, J.K. 2002. Abdominal aortic aneurysms: basic mechanisms and clinical implications. *Curr Probl Surg* **39**(2), 110-230.

Thompson, R.W., Liao, S. and Curci, J.A. 1997. Vascular smooth muscle cell apoptosis in abdominal aortic aneurysms. *Coron Artery Dis* **8**(10), 623-631.

Thompson, S.G., Ashton, H.A., Gao, L., Buxton, M.J., Scott, R.A.P. and Group, o.b.o.t.M.A.S.S. 2012. Final follow-up of the Multicentre Aneurysm Screening Study (MASS) randomized trial of abdominal aortic aneurysm screening. *Br J Surg* **99**(12), 1649-1656.

Toczek, J., Gona, K., Han, J., Zhang, J., Jung, J.-J. and Sadeghi, M. 2018. Molecular imaging of phagocytic activity in abdominal aortic aneurysm. *J Nucl Med* **59**(1), 104.

Toczek, J., Meadows, J.L. and Sadeghi, M.M. 2016. Novel molecular imaging approaches to abdominal aortic aneurysm risk stratification. *Circ Cardiovasc Imaging* **9**(1), e003023-e003023.

Toczek, J., Ye, Y., Gona, K., Kim, H.Y., Han, J., Razavian, M., Golestani, R., Zhang, J., Wu, T.L., Jung, J.J. and Sadeghi, M.M. 2017. Preclinical evaluation of RYM1, a matrix metalloproteinase-targeted tracer for imaging aneurysm. *J Nucl Med* **58**(8), 1318-1323.

- Tolmachev, V., Varasteh, Z., Honarvar, H., Hosseinimehr, S.J., Eriksson, O., Jonasson, P., Frejd, F.Y., Abrahmsen, L. and Orlova, A. 2014. Imaging of platelet-derived growth factor receptor beta expression in glioblastoma xenografts using affibody molecule ^{111}In -DOTA-Z09591. *J Nucl Med* **55**(2), 294-300.
- Toyohara, J., Waki, A., Takamatsu, S., Yonekura, Y., Magata, Y. and Fujibayashi, Y. 2002. Basis of FLT as a cell proliferation marker: comparative uptake studies with ^3H thymidine and ^3H arabinothymidine, and cell-analysis in 22 asynchronously growing tumor cell lines. *Nucl Med Biol* **29**(3), 281-287.
- Trachet, B., Aslanidou, L., Piersigilli, A., Fraga-Silva, R.A., Sordet-Dessimoz, J., Villanueva-Perez, P., Stampanoni, M.F.M., Stergiopoulos, N. and Segers, P. 2017. Angiotensin II infusion into ApoE^{-/-} mice: a model for aortic dissection rather than abdominal aortic aneurysm? *Cardiovasc Res* **113**(10), 1230-1242.
- Truijers, M., Pol, J.A., Kurvers, H., Bredie, S., Oyen, W.J. and Blankensteijn, J.D. 2009. Incidental finding of malignancy in patients preoperatively evaluated for aneurysm wall pathology using PET/CT. *J Vasc Surg* **49**(5), 1313-1315.
- Tsoumpas, C., Visvikis, D. and Loudos, G. 2016. Innovations in small-animal PET/MR imaging instrumentation. *PET Clinics* **11**(2), 105-118.
- Tsuruda, T., Nagamachi, S., Nishimura, M., Nakamura, K. and Kitamura, K. 2016. Multiple ^{18}F -fluorodeoxyglucose positron emission tomography scans showing progression of abdominal aortic aneurysm: A case report. *Medicine (Baltimore)* **95**(19), e3650.
- Turcotte, E., Wiens, L.W., Grierson, J.R., Peterson, L.M., Wener, M.H. and Vesselle, H. 2007. Toxicology evaluation of radiotracer doses of 3'-deoxy-3'- ^{18}F fluorothymidine (^{18}F -FLT) for human PET imaging: Laboratory analysis of serial blood samples and comparison to previously investigated therapeutic FLT doses. *BMC Nucl Med* **7**, 3-3.
- Turner, G.H., Olzinski, A.R., Bernard, R.E., Aravindhan, K., Karr, H.W., Mirabile, R.C., Willette, R.N., Gough, P.J. and Jucker, B.M. 2008. In vivo serial assessment of aortic aneurysm formation in apolipoprotein E-deficient mice via MRI. *Circ Cardiovasc Imaging* **1**(3), 220-226.
- Ukon, N., Zhao, S., Yu, W., Shimizu, Y., Nishijima, K.-I., Kubo, N., Kitagawa, Y., Tamaki, N., Higashikawa, K., Yasui, H. and Kuge, Y. 2016. Dynamic PET evaluation of elevated FLT level after sorafenib treatment in mice bearing human renal cell carcinoma xenograft. *EJNMMI Res* **6**(1), 90-90.
- Ullery, B.W., Hallett, R.L. and Fleischmann, D. 2018. Epidemiology and contemporary management of abdominal aortic aneurysms. *Abdom Radiol* **43**(5), 1032-1043.
- van der Weyden, L., White, J.K., Adams, D.J. and Logan, D.W. 2011. The mouse genetics toolkit: revealing function and mechanism. *Genome Biology* **12**(6), 224.
- van Disseldorp, E.M.J., Petterson, N.J., van de Vosse, F.N., van Sambeek, M. and Lopata, R.G.P. 2019. Quantification of aortic stiffness and wall stress in

healthy volunteers and abdominal aortic aneurysm patients using time-resolved 3D ultrasound: a comparison study. *Eur Heart J Cardiovasc Imaging* **20**(2), 185-191.

Vande Geest, J.P., Di Martino, E.S., Bohra, A., Makaroun, M.S. and Vorp, D.A. 2006. A biomechanics-based rupture potential index for abdominal aortic aneurysm risk assessment: demonstrative application. *Ann N Y Acad Sci* **1085**, 11-21.

Vanderhoek, M., Perlman, S.B. and Jeraj, R. 2013. Impact of different standardized uptake value measures on PET-based quantification of treatment response. *J Nucl Med* **54**(8), 1188-1194.

Vega de Céniga, M., Gómez, R., Estallo, L., Rodríguez, L., Baquer, M. and Barba, A. 2006. Growth rate and associated factors in small abdominal aortic aneurysms. *Eur J Vasc Endovasc Surg* **31**(3), 231-236.

Velasquez, L.M., Boellaard, R., Kollia, G., Hayes, W., Hoekstra, O.S., Lammertsma, A.A. and Galbraith, S.M. 2009. Repeatability of 18F-FDG PET in a multicenter phase I study of patients with advanced gastrointestinal malignancies. *J Nucl Med* **50**(10), 1646-1654.

Veronesi, G., Travaini, L.L., Maisonneuve, P., Rampinelli, C., Bertolotti, R., Spaggiari, L., Bellomi, M. and Paganelli, G. 2015. Positron emission tomography in the diagnostic work-up of screening-detected lung nodules. *Eur Respir J* **45**(2), 501.

Viertl, D., Delaloye, A.B., Lanz, B., Poitry-Yamate, C., Gruetter, R., Mlynarik, V., Ametamey, S.M., Ross, T.L., Lehr, H.-A. and André, P.-A. 2011. Increase of [18 F] FLT tumor uptake in vivo mediated by FdUrd: toward improving cell proliferation positron emission tomography. *Mol Imaging Biol* **13**(2), 321-331.

Vorkapic, E., Dugic, E., Vikingsson, S., Roy, J., Mäyränpää, M.I., Eriksson, P. and Wågsäter, D. 2016. Imatinib treatment attenuates growth and inflammation of angiotensin II induced abdominal aortic aneurysm. *Atherosclerosis* **249**, 101-109.

Vorp, D.A. 2007. Biomechanics of abdominal aortic aneurysm. *J Biomech* **40**(9), 1887-1902.

Vorwerk, H., Beckmann, G., Bremer, M., Degen, M., Dietl, B., Fietkau, R., Gsanger, T., Hermann, R.M., Alfred Herrmann, M.K., Holler, U., van Kampen, M., Korber, W., Maier, B., Martin, T., Metz, M., Richter, R., Siekmeyer, B., Steder, M., Wagner, D., Hess, C.F., Weiss, E. and Christiansen, H. 2009. The delineation of target volumes for radiotherapy of lung cancer patients. *Radiother Oncol* **91**(3), 455-460.

Vrekoussis, T., Stathopoulos, E.N., De Giorgi, U., Kafousi, M., Pavlaki, K., Kalogeraki, A., Chrysos, E., Fiorentini, G. and Zoras, O. 2006. Modulation of vascular endothelium by imatinib: a study on the EA.hy 926 endothelial cell line. *J Chemother* **18**(1), 56-65.

- Wahl, R.L., Jacene, H., Kasamon, Y. and Lodge, M.A. 2009. From RECIST to PERCIST: Evolving considerations for PET response criteria in solid tumors. *J Nucl Med* **50 Suppl 1**, 122s-150s.
- Wallez, Y., Riedl, S.J. and Pasquale, E.B. 2014. Association of the breast cancer antiestrogen resistance protein 1 (BCAR1) and BCAR3 scaffolding proteins in cell signaling and antiestrogen resistance. *J Biol Chem* **289**(15), 10431-10444.
- Wang, J., Chen, L., Chen, B., Meliton, A., Liu, S.Q., Shi, Y., Liu, T., Deb, D.K., Solway, J. and Li, Y.C. 2015. Chronic activation of the renin-angiotensin system induces lung fibrosis. *Sci Rep* **5**, 15561.
- Wang, J., Lindholt, J.S., Sukhova, G.K., Shi, M.A., Xia, M., Chen, H., Xiang, M., He, A., Wang, Y., Xiong, N., Libby, P., Wang, J.A. and Shi, G.P. 2014. IgE actions on CD4+ T cells, mast cells, and macrophages participate in the pathogenesis of experimental abdominal aortic aneurysms. *EMBO Mol Med* **6**(7), 952-969.
- Wang, X., Lane, B.A., Eberth, J.F., Lessner, S.M. and Vyavahare, N.R. 2019. Gold nanoparticles that target degraded elastin improve imaging and rupture prediction in an AngII mediated mouse model of abdominal aortic aneurysm. *Theranostics* **9**(14), 4156-4167.
- Wang, Y., Krishna, S. and Golledge, J. 2013. The calcium chloride-induced rodent model of abdominal aortic aneurysm. *Atherosclerosis* **226**(1), 29-39.
- Weber, W.A., Gatsonis, C.A., Mozley, P.D., Hanna, L.G., Shields, A.F., Aberle, D.R., Govindan, R., Torigian, D.A., Karp, J.S., Yu, J.Q., Subramaniam, R.M., Halvorsen, R.A. and Siegel, B.A. 2015. Repeatability of 18F-FDG PET/CT in Advanced Non-Small Cell Lung Cancer: Prospective Assessment in 2 Multicenter Trials. *J Nucl Med* **56**(8), 1137-1143.
- Wicky, S., Fan, C.M., Geller, S.C., Greenfield, A., Santilli, J. and Waltman, A.C. 2003. MR angiography of endoleak with inconclusive concomitant CT angiography. *AJR Am J Roentgenol* **181**(3), 736-738.
- Wills, A., Thompson, M.M., Crowther, M., Sayers, R.D. and Bell, P.R. 1996. Pathogenesis of abdominal aortic aneurysms--cellular and biochemical mechanisms. *Eur J Vasc Endovasc Surg* **12**(4), 391-400.
- Wolf, G. and Wenzel, U.O. 2004. Angiotensin II and cell cycle regulation. *Hypertension* **43**(4), 693-698.
- Wolf, G., Ziyadeh, F.N., Zahner, G. and Stahl, R.A. 1996. Angiotensin II is mitogenic for cultured rat glomerular endothelial cells. *Hypertension* **27**(4), 897-905.
- Woolf, D.K., Beresford, M., Li, S.P., Dowsett, M., Sanghera, B., Wong, W.L., Sonoda, L., Detre, S., Amin, V., Ah-See, M.L., Miles, D. and Makris, A. 2014. Evaluation of FLT-PET-CT as an imaging biomarker of proliferation in primary breast cancer. *Br J Cancer* **110**(12), 2847-2854.

- Wu, M., Rementer, C. and Giachelli, C.M. 2013. Vascular calcification: an update on mechanisms and challenges in treatment. *Calcif Tissue Int* **93**(4), 365-373.
- Wykrzykowska, J., Lehman, S., Williams, G., Parker, J.A., Palmer, M.R., Varkey, S., Kolodny, G. and Laham, R. 2009. Imaging of inflamed and vulnerable plaque in coronary arteries with 18F-FDG PET/CT in patients with suppression of myocardial uptake using a low-carbohydrate, high-fat preparation. *J Nucl Med* **50**(4), 563-568.
- Xu, X.Y., Borghi, A., Nchimi, A., Leung, J., Gomez, P., Cheng, Z., Defraigne, J.O. and Sakalihasan, N. 2010. High levels of 18F-FDG uptake in aortic aneurysm wall are associated with high wall stress. *Eur J Vasc Endovasc Surg* **39**(3), 295-301.
- Yaghini, F.A., Song, C.Y., Lavrentyev, E.N., Ghafoor, H.U.B., Fang, X.R., Estes, A.M., Campbell, W.B. and Malik, K.U. 2010. Angiotensin II-induced vascular smooth muscle cell migration and growth are mediated by cytochrome P450 1B1-dependent superoxide generation. *Hypertension* **55**(6), 1461-1467.
- Yao, Y., Cheng, K. and Cheng, Z. 2020. Evaluation of a smart activatable MRI nanoprobe to target matrix metalloproteinases in the early-stages of abdominal aortic aneurysms. *Nanomedicine* **26**, 102177.
- Ye, Y.X., Calcagno, C., Binderup, T., Courties, G., Keliher, E.J., Wojtkiewicz, G.R., Iwamoto, Y., Tang, J., Perez-Medina, C., Mani, V., Ishino, S., Johnbeck, C.B., Knigge, U., Fayad, Z.A., Libby, P., Weissleder, R., Tawakol, A., Dubey, S., Belanger, A.P., Di Carli, M.F., Swirski, F.K., Kjaer, A., Mulder, W.J. and Nahrendorf, M. 2015. Imaging macrophage and hematopoietic progenitor proliferation in atherosclerosis. *Circ Res* **117**(10), 835-845.
- Yoshimura, K., Morikage, N., Nishino-Fujimoto, S., Furutani, A., Shirasawa, B. and Hamano, K. 2018. Current status and perspectives on pharmacologic therapy for abdominal aortic aneurysm. *Curr Drug Targets* **19**(11), 1265-1275.
- Yue, J., Chen, L., Cabrera, A.R., Sun, X., Zhao, S., Zheng, F., Han, A., Zheng, J., Teng, X., Ma, L., Ma, Y., Han, D., Zhao, X., Mu, D., Yu, J. and Li, Y. 2010. Measuring tumor cell proliferation with 18F-FLT PET during radiotherapy of esophageal squamous cell carcinoma: A pilot clinical study. *J Nucl Med* **51**(4), 528-534.
- Zampetaki, A., Attia, R., Mayr, U., Gomes, R.S., Phinikaridou, A., Yin, X., Langley, S.R., Willeit, P., Lu, R., Fanshawe, B., Fava, M., Barallobre-Barreiro, J., Molenaar, C., So, P.W., Abbas, A., Jahangiri, M., Waltham, M., Botnar, R., Smith, A. and Mayr, M. 2014. Role of miR-195 in aortic aneurysmal disease. *Circ Res* **115**(10), 857-866.
- Zarrouk, M., Lundqvist, A., Holst, J., Troëng, T. and Gottsäter, A. 2016. Cost-effectiveness of screening for abdominal aortic aneurysm in combination with medical intervention in patients with small aneurysms. *Eur J Vasc Endovasc Surg* **51**(6), 766-773.
- Zhao, S., Kuge, Y., Tsukamoto, E., Mochizuki, T., Kato, T., Hikosaka, K., Nakada, K., Hosokawa, M., Kohanawa, M. and Tamaki, N. 2002.

Fluorodeoxyglucose uptake and glucose transporter expression in experimental inflammatory lesions and malignant tumours: effects of insulin and glucose loading. *Nucl Med Commun* **23**(6), 545-550.

Zhou, J., He, E. and Skog, S. 2013. The proliferation marker thymidine kinase 1 in clinical use. *Mol Clin Oncol* **1**(1), 18-28.

Zhu, C., Cao, L., Wen, Z., Ahn, S., Raithel, E., Forman, C., Hope, M. and Saloner, D. 2019. Surveillance of abdominal aortic aneurysm using accelerated 3D non-contrast black-blood cardiovascular magnetic resonance with compressed sensing (CS-DANTE-SPACE). *J Cardiovasc Magn Reson* **21**(1), 66.

Zhu, C., Leach, J.R., Tian, B., Cao, L., Wen, Z., Wang, Y., Liu, X., Liu, Q., Lu, J., Saloner, D. and Hope, M.D. 2019. Evaluation of the distribution and progression of intraluminal thrombus in abdominal aortic aneurysms using high-resolution MRI. *J Magn Reson Imaging* **50**(3), 994-1001.


Zhu, C., Leach, J.R., Wang, Y., Gasper, W., Saloner, D. and Hope, M.D. 2020. Intraluminal thrombus predicts rapid growth of abdominal aortic aneurysms. *Radiology*, 191723.

Zhu, H., Qu, X., Zhang, C. and Yu, Y. 2019. Interleukin-10 promotes proliferation of vascular smooth muscle cells by inhibiting inflammation in rabbit abdominal aortic aneurysm. *Int J Clin Exp Pathol* **12**(4), 1260-1271.


Zimmermann, W.-H. 2018. Engineered nanoparticles prevent dilation of abdominal aortic aneurysms. *J Am Coll Cardiol* **72**(21), 2606.

Appendix A


Copies of all conference posters associated with this thesis are provided here.



UNIVERSITY OF LEEDS



EPSRC
Engineering and Physical Sciences
Research Council



UNIVERSITY OF HULL

[¹⁸F]Fluorothymidine Positron Emission Tomography/Computed Tomography of Experimental Abdominal Aortic Aneurysms in Murine Models

Richa Gandhi¹, John Wright¹, Joanna Koch-Paszkowski¹, Stephen J Archibald², Christopher Cawthorne³, Marc A Bailey¹, Charalampos Tsoumpas¹

¹ University of Leeds, Leeds Institute of Cardiovascular and Metabolic Medicine, Leeds, United Kingdom; ² University of Hull, PET Research Centre, School of Life Sciences, Hull, United Kingdom; ³ KU Leuven, Leuven, Belgium

Correspondence: r.gandhi@leeds.ac.uk

Background

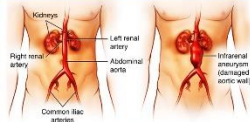


Fig. 1. Normal (left) and aneurysmal (right) abdominal aortae^[1]

- Abdominal aortic aneurysms (AAA) involve
 - Progressive dilatation of the abdominal aorta
 - Asymptomatic disease progression
 - High rupture risk^[2]
- AAA is currently managed by ultrasound screening until the intervention threshold of 5.5 cm^[3]
- A molecular imaging biomarker to stratify patients for different surveillance and treatment regimens is needed




Fig. 2. Ultrasound images of normal (left) and aneurysmal (right) abdominal aortae^[4]

Study aim:
To visualise and quantify AAA-associated cell proliferation using [¹⁸F]fluorothymidine ([¹⁸F]FLT) PET/CT

In vivo [¹⁸F]FLT PET/CT

- Fourteen-week-old apolipoprotein E-knockout mice were infused with saline or angiotensin II (AngII) for 14 or 28 days and underwent 90-min dynamic PET/CT: 14-day saline, n=5; 14-day AngII AAA, n=5; 28-day AngII AAA, n=3
- 3D isocontour regions of interest were manually drawn using Amide software on images reconstructed using the ordered subset expectation maximisation algorithm (2 iterations, 16 subsets)
- [¹⁸F]FLT standardised uptake values (SUVs) were higher in 14- and 28-day AngII AAA than in saline controls; the SUV decreased from day 14 to 28

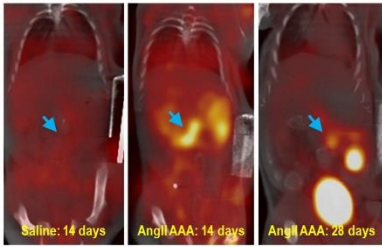


Fig. 3. PET/CT revealed greater [¹⁸F]FLT signal in 14-day AngII AAA (arrow)

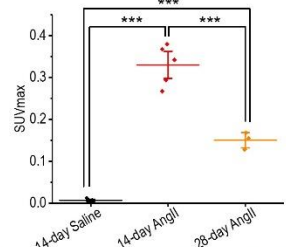


Fig. 4. Greater [¹⁸F]FLT signal was observed in 14-day AngII AAA

[¹⁸F]FLT and TK-1

- [¹⁸F]FLT is retained in cells via phosphorylation by thymidine kinase-1 (TK-1) during DNA synthesis
- Cytosolic accumulation of phosphorylated [¹⁸F]FLT reflects TK-1 activity and cell proliferation^[5]

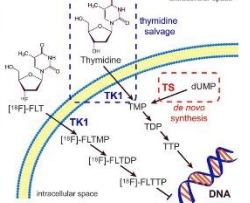


Fig. 5. [¹⁸F]FLT and thymidine uptake pathways^[5]




Fig. 6. Western blotting for TK-1 showed greater protein expression in 14-day AngII AAA than in 28-day AngII AAA.

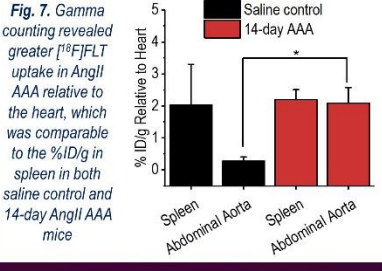


Fig. 7. Gamma counting revealed greater [¹⁸F]FLT uptake in AngII AAA relative to the heart, which was comparable to the %ID/g in spleen in both saline control and 14-day AngII AAA mice

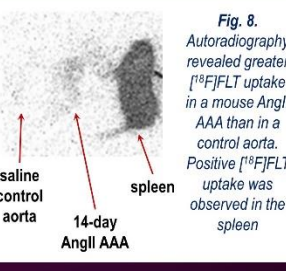


Fig. 8. Autoradiography revealed greater [¹⁸F]FLT uptake in a mouse AngII AAA than in a control aorta. Positive [¹⁸F]FLT uptake was observed in the spleen

Conclusions

- Abdominal aortic [¹⁸F]FLT signal on PET/CT, [¹⁸F]FLT uptake on gamma counting and autoradiography, and TK-1 protein expression demonstrate that [¹⁸F]FLT PET/CT can be used to visualise AAA-associated cell proliferation in the AngII AAA mouse model
- Further validation work to elucidate the time course and molecular mechanisms of AngII AAA are ongoing.
- Future [¹⁸F]FLT PET studies in patients with early-stage AAA are recommended.

References

[1] University of Utah Health. 2017. Abdominal aortic aneurysm. [Image]. Retrieved from: <https://healthcare.utah.edu/healthlibrary/related/doc.php?type=8&id=P08247>

[2] Forsdahl et al. 2009. Circulation, 119, 2202-9.

[3] Moxon et al. 2010. Curr Probl Cardiol, 35, 512-48.

[4] American College of Emergency Physicians. ACEP. 2010. Focus On: Bedside Ultrasound of the Abdominal Aorta. [Online]. [Accessed 6 December 2016]. Available from: <https://www.acep.org/clinical-practice-management/focus-on--bedside-ultrasound-of-the-abdominal-aorta/>

[5] McKinley et al. 2013. PLoS One, 8, e58938.

This research was funded by the David Gamble Award for Secondments in PET-CT Imaging; the EPSRC Centre for Doctoral Training in Tissue Engineering and Regenerative Medicine – Innovation in Medical and Biological Engineering, multidisciplinary collaboration of Faculties at the University of Leeds (grant number EP/L014823/1); and The Academy of Medical Sciences (Clinical Lecturer Starter Grant to MA Bailey). MA Bailey is personally funded by the British Heart Foundation (FS/18/12/33270).

Figure A.1 Poster for the European Molecular Imaging Meeting 2018

Effect of different ROI definitions on the quantification of SUV

Bashair Alhummiyany¹, **Richa Gandhi**¹, Stephen J. Archibald², Christopher Cawthorne³, Marc A. Bailey¹, Charalampos Tsoumpas¹

¹Department of Biomedical Imaging Science, Leeds Institute of Cardiovascular and Metabolic Medicine, University of Leeds, UK

²PET Research Centre, School of Life Sciences, University of Hull, Hull, UK

³KU Leuven, Leuven, Belgium

Contact: r.gandhi@leeds.ac.uk

Background

- The standardized uptake value (SUV) is commonly used in clinical and preclinical PET applications to analyze tracer accumulation within a specified region of interest (ROI)¹.
- The most common ways of calculating SUV are based on the average (SUV_{mean}) or maximum (SUV_{max}) of all voxels within an ROI.
- It has been suggested that applying a threshold to estimate the average SUV within a group of voxels can potentially reduce limitations in the SUV_{max} or SUV_{mean} ²

Aims

- To identify a reproducible threshold value using two different segmentation methods.
- To assess the applicability of using these methods in preclinical PET-CT.

Methods

1. Image acquisition and reconstruction

Fourteen mice (10 with abdominal aortic aneurysms (AAA), 4 controls) underwent 90-min dynamic [¹⁸F]FLT PET-CT acquisitions using the Sedecal Super Argus PET-CT scanner. Images were reconstructed with the 3D OSEM algorithm (2 iterations, 16 subsets).

2. Image analysis using Amide software

- Manual ROIs were drawn using the 3D isocontour tool (Figure 1 A and B)
- Fixed-size ROIs were 4-mm spheres (Figure 1 C and D)

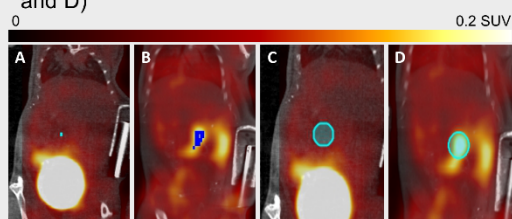


Figure 1. The placement of manual (A, B) and fixed-size ROIs (C, D) on control (A, C) and AAA (B, D) coronal-view PET-CT images

- Amide software was used to compute SUV_{mean} , SUV_{max} , SUV_{40} , SUV_{50} , SUV_{70} , and SUV_{90} .

3. Statistical analysis

Paired sample t-tests were conducted to determine whether a difference existed between pairs of SUV measurements.

References

- Boellaard R. "Standards for PET image acquisition and quantitative data analysis." J Nucl Med 50(S1), 2009
- Lee JR, et al. A threshold method to improve standardized uptake value reproducibility. Nucl Med Comm 21(7) 2000

Results

- SUV_{40} , SUV_{50} , and SUV_{90} for manually drawn vs. fixed-size ROIs showed significant differences (all $P < 0.05$), while SUV_{70} showed no statistically significant difference between the segmentation techniques ($P = 0.72$)

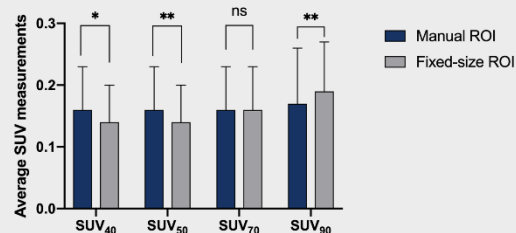


Figure 2. The average SUV measurements when 40%, 50%, 70%, and 90% SUV threshold values were applied to both control and disease models. Error bars represent the standard deviation. Asterisks indicate statistical significance.

- The average volumes of the fixed-size ROIs were relatively larger than those of the manual ROIs, and the volumes of both ROIs decreased with the application of higher threshold values

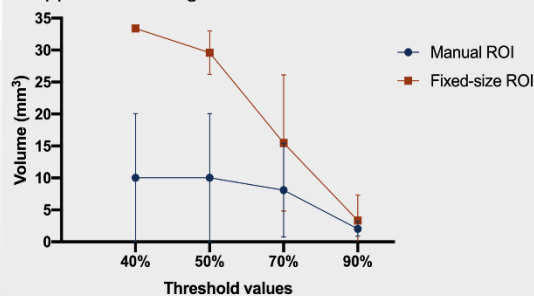


Figure 3. A line graph representing the average volume for each segmentation method when 40%, 50%, 70%, and 90% thresholds were applied. Error bars represent the standard deviation.

Conclusion

- The choice of segmentation tool for ROI definitions in PET image analysis has a direct impact on SUV measurements.
- The implementation of fixed-size ROIs with a 70% threshold appears to provide the most stable SUV measurements in the analysis of aortic lesions in preclinical PET-CT images of mice.

Funding sources: David Gamble Award for Secondments in PET-CT Imaging (MA Bailey); EPSRC Centre for Doctoral Training in Tissue Engineering and Regenerative Medicine – Innovation in Medical and Biological Engineering, multidisciplinary collaboration of Faculties at the University of Leeds (EP/L014823/1; R Gandhi); The Academy of Medical Sciences (Clinical Lecturer Starter Grant to MA Bailey; British Heart Foundation (FS/18/12/33270; MA Bailey)

UNIVERSITY OF LEEDS

UNIVERSITY OF HULL

EPSRC
Engineering and Physical Sciences
Research Council

Aim:

- Abdominal aortic aneurysm (AAA) disease is characterised by a localised dilatation of the abdominal aorta that affects approx. 4% of men aged 65–74 years in the UK.
- AAA risk factors include age, male gender, former/current smoking habits, positive familial history, and high diastolic blood pressure.
- AAA is currently managed with routine ultrasound screening, which does not elucidate the molecular mechanisms that precede physical disease manifestation.
- The aim of this study was to investigate the feasibility of using positron emission tomography/computed tomography (PET/CT) with [¹⁸F]fluorothymidine ([¹⁸F]FLT) to visualise AAA in murine models.

Materials & Methods:

- Fourteen-week-old apolipoprotein E-knockout (ApoE^{-/-}) mice were administered either saline or angiotensin II (AngII) infusions via subcutaneously implanted osmotic mini-pumps for 28 days.
- Ninety-minute dynamic PET/CT under recovery isoflurane was performed on days 14 and 28.
- Radiotracers were administered via intravenous tail vein injections
 - [¹⁸F]fluorodeoxyglucose ([¹⁸F]FDG): 9.79±2.10 MBq
 - [¹⁸F]FLT: 7.63±3.02 MBq (day 14), 9.61±1.34 MBq (day 28)
- Images were reconstructed using the three-dimensional (3D) ordered subsets expectation maximisation (OSEM) algorithm.
- 3D isocontour regions of interest (ROIs) were manually drawn in all abdominal aortic regions.
- Maximum standardised uptake values (SUVs) were calculated over all voxels for each ROI.

Results:

- [¹⁸F]FDG and [¹⁸F]FLT uptake in the inferior vena cava were observed in the first 15 seconds of each scan, indicating successful intravenous tracer delivery.
- Expected tracer biodistribution was observed in control and AAA models:
 - [¹⁸F]FDG: myocardium (**Figure 1**)
 - [¹⁸F]FLT: spleen (**Figure 2**)
- Significantly greater [¹⁸F]FLT uptake was observed in aneurysmal aortae than in control aortae.
 - SUV % differences: 4496.80 (day 14; p<0.001) (**Figure 3**), 430.35 (day 28) (**Figure 4**)
- [¹⁸F]FLT uptake was more consistent than [¹⁸F]FDG (**Figure 5**)
 - Standard deviations: [¹⁸F]FDG, 0.14; [¹⁸F]FLT, 0.04 (day 14) and 0.02 (day 28)
- Aneurysmal aortae showed greater Ki67 positivity than control aortae (**Figure 6**)
 - % difference: 4669.19, p<0.001

Conclusions:

- [¹⁸F]FLT uptake is consistently enhanced in AAA models than in control models in comparison to [¹⁸F]FDG uptake.
- To our best knowledge, this is the first study to demonstrate the potential utility of [¹⁸F]FLT PET/CT in evaluating AAA-associated cell proliferation.
- Further validation work to elucidate the time course and molecular mechanisms of AAA is ongoing.

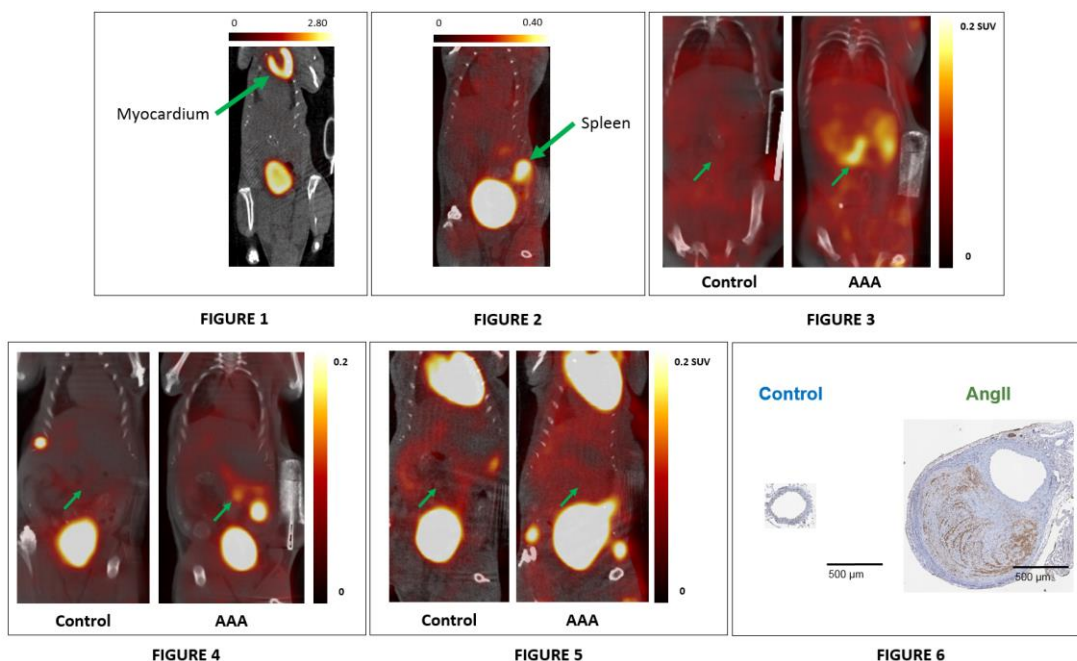


Figure A.3 ePoster contents for the Annual Congress of the European Association of Nuclear Medicine 2018

Appendix B

The results of non-parametric statistical tests are presented here. The Kruskal–Wallis test was used for the data presented in Figures B.1, B.5, B.6, B.7, B.8, and B.9. The Mann–Whitney U test was used for the data presented in Figures B.2, B.3, and B.4. All significant results according to parametric tests remain statistically significant following non-parametric analysis.

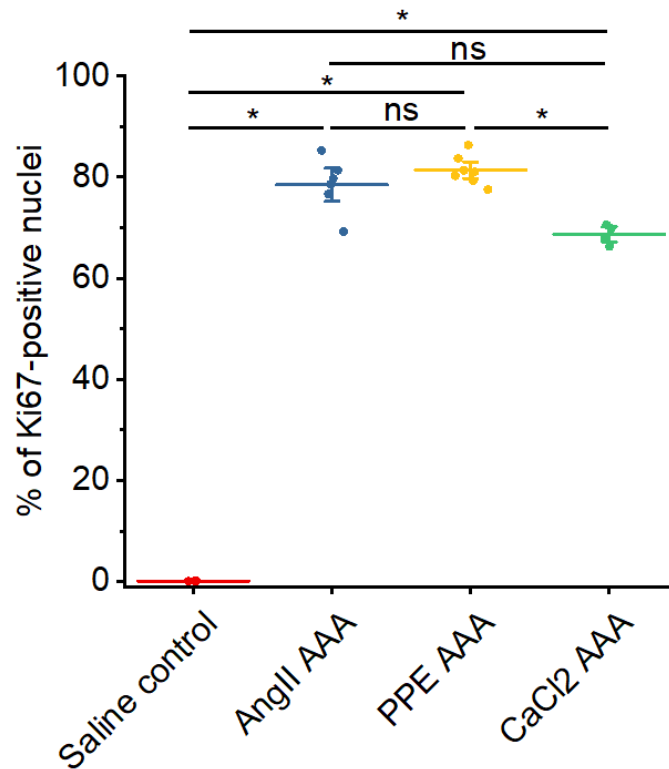


Figure B.1 PPE and AngII AAA tissue reveal the greatest proportions of Ki67-positive nuclei. Proportion of Ki67-positive nuclei in saline controls ($n=3$) and in the AngII ($n=6$), PPE ($n=7$), and CaCl₂ ($n=4$) AAA models. * $p < 0.05$, ns: not significant on Kruskal–Wallis test.

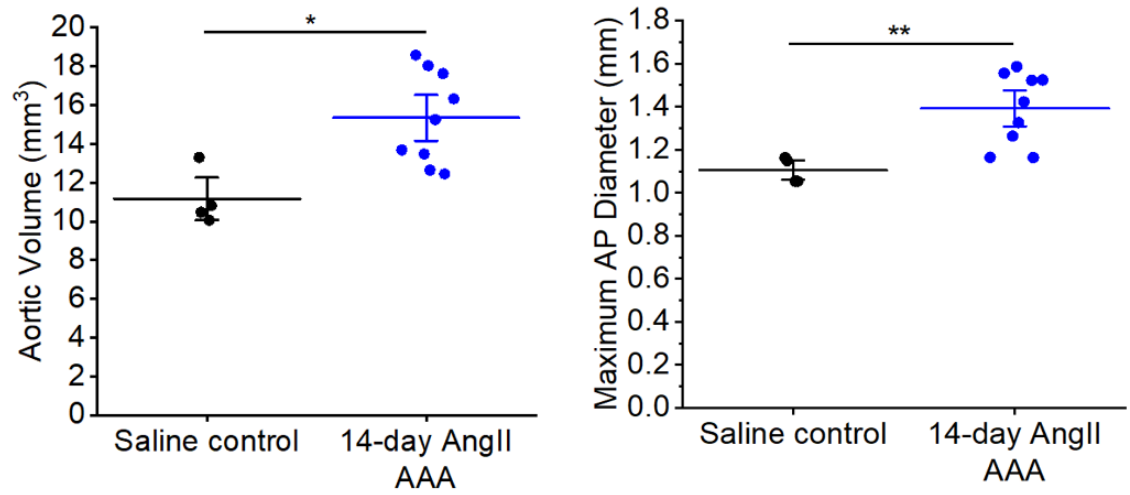


Figure B.2 Aortic volumes and diameters are larger in the AngII AAA model than in saline controls. Aortic volumes and diameters in 14-day AngII AAA ($n=9$) vs. saline control aortae ($n=4$). * $p<0.05$, ** $p<0.01$ on Mann–Whitney U test.

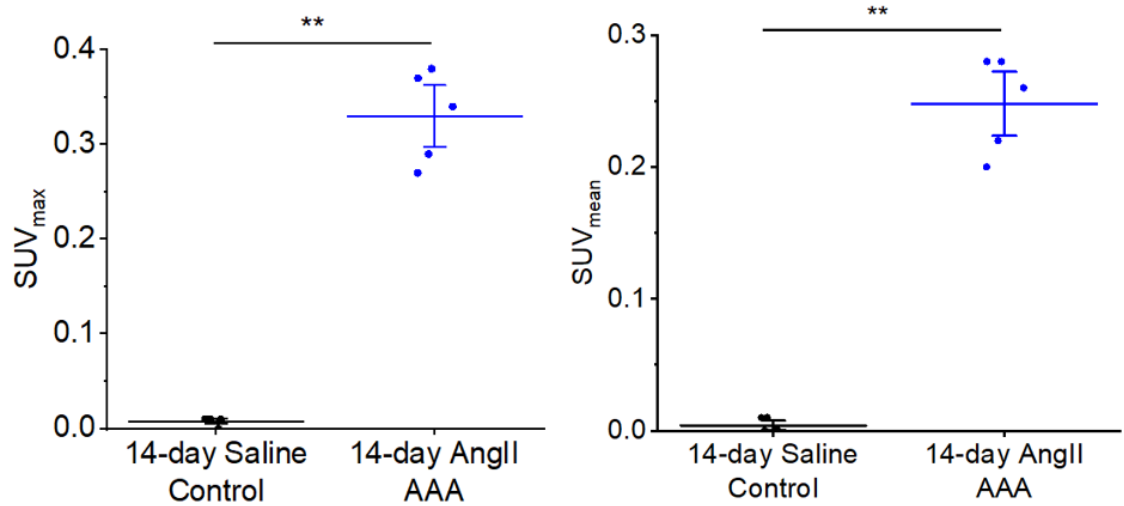


Figure B.3 [¹⁸F]FLT uptake in the abdominal aorta was greater in the 14-day AngII AAA model than in saline controls. Absolute values of SUV_{max} and SUV_{mean} representing 14-day [¹⁸F]FLT uptake in abdominal aortic ROIs 80–90 min post-radiotracer injection in 14-day saline controls ($n=5$) and the 14-day AngII AAA model ($n=5$). ** $p<0.01$ on Mann–Whitney U test.

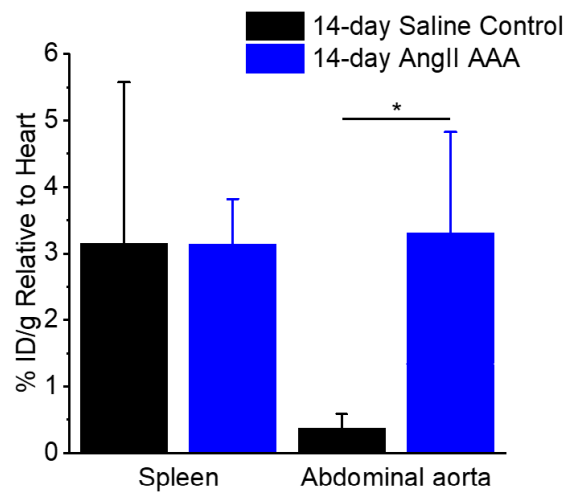


Figure B.4 *Ex vivo* [^{18}F]FLT uptake in the abdominal aorta was greater in the 14-day AngII AAA model than in 14-day saline controls. Decay-corrected *ex vivo* [^{18}F]FLT counts per mass units. Uptake in the spleen and abdominal aorta normalised to uptake in the heart in the 14-day AngII AAA model ($n=9$) and 14-day saline controls ($n=4$). * $p < 0.05$ on Mann–Whitney U test.

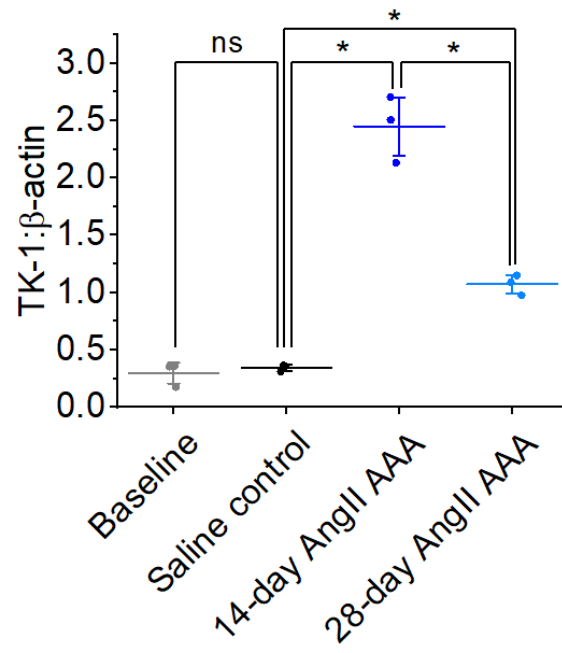


Figure B.5 TK-1 expression was the greatest in 14-day AngII AAA.

Quantitative analysis wherein TK-1 band intensity was normalised to β-actin band intensity. * $p < 0.05$, ns: not significant on Kruskal–Wallis test.

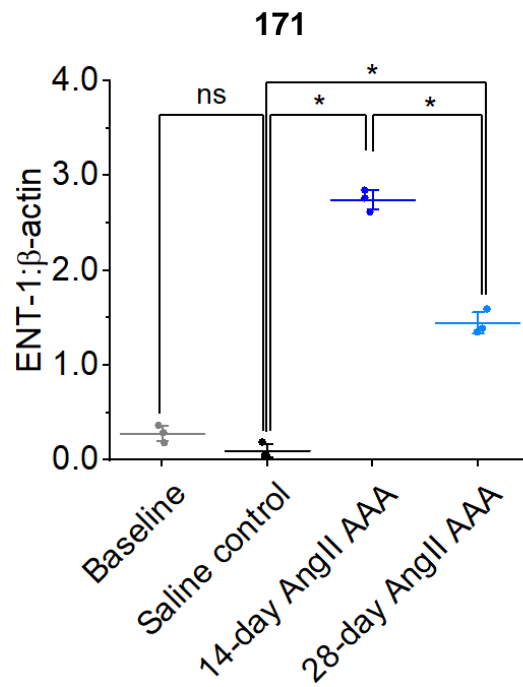


Figure B.6 ENT-1 expression was the greatest in 14-day AngII AAA.

Quantitative analysis wherein ENT-1 band intensity was normalised to β-actin band intensity. * $p < 0.05$, ns: not significant on Kruskal–Wallis test.

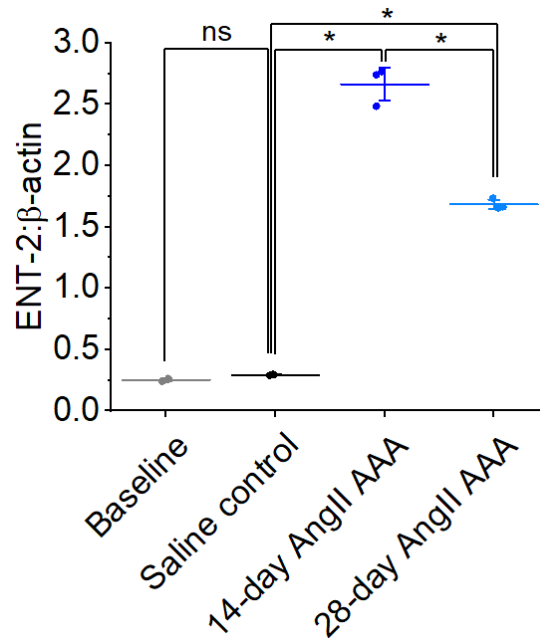


Figure B.7 ENT-2 expression was the greatest in 14-day AngII AAA.

Quantitative analysis wherein ENT-2 band intensity was normalised to β-actin band intensity. * $p < 0.05$, ns: not significant on Kruskal–Wallis test.

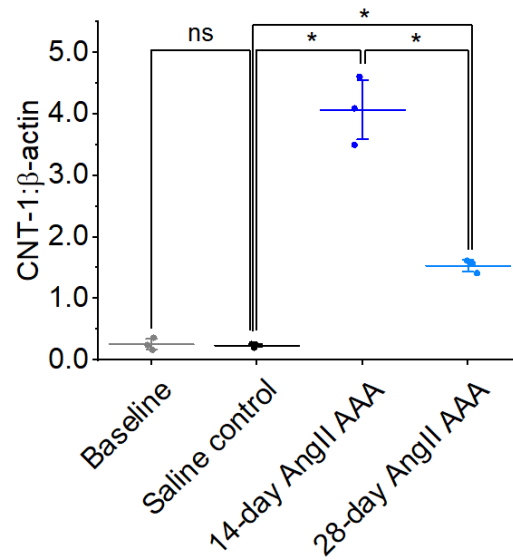


Figure B.8 CNT-1 expression was the greatest in 14-day AngII AAA.

Quantitative analysis wherein CNT-1 band intensity was normalised to β-actin band intensity. * $p < 0.05$, ns: not significant on Kruskal–Wallis test.

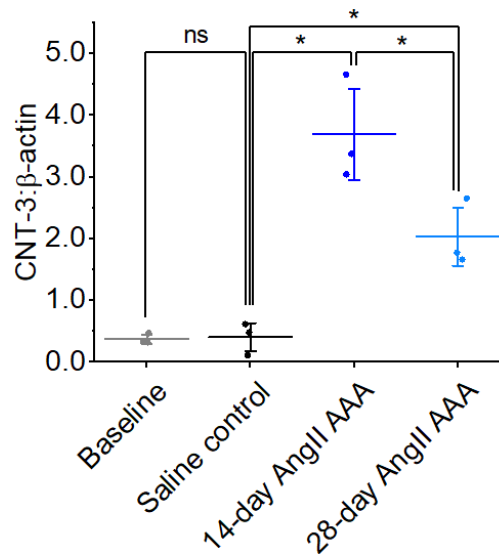


Figure B.9 CNT-3 expression was the greatest in 14-day AngII AAA.

Quantitative analysis wherein CNT-3 band intensity was normalised to β-actin band intensity. * $p < 0.05$, ns: not significant on Kruskal–Wallis test.